Comparison of Different Neural Networks Models for Identification of Manipulator Arm Driven by Fluidic Muscles

Monika Trojanová, Alexander Hošovský

Technical University of Košice, Faculty of Manufacturing Technologies, Department of Industrial Engineering and Informatics, Bayerova 1, 080 01 Prešov, Slovak Republic, email: monika.trojanova@tuke.sk; alexander.hosovsky@tuke.sk

Abstract: The main subject of the study, which is summarized in this article, was to compare three different models of neural networks (Linear Neural Unit (LNU), Quadratic Neural Unit (QNU) and Multi-Layer Perceptron Network (MLP)) to identify of the real system of the manipulator arm. The arm is powered by FESTO fluidic muscles, which allows for two degrees of freedom. The data obtained by the measurements were processed in Python. This program served as a tool for compiling individual dynamic models, predicting measured data, and then graphically interpreting the resulting models. Levenberg-Marquardt (LM) was used as the learning algorithm because it is more suitable for learning neural networks than for example, the Gauss-Newton method.

Keywords: pneumatic artificial muscle (PUS); learning algorithm; neural network; identification; manipulator; fluid muscles; Python

1 Introduction

Automation is currently a highly watched process. By implementing automation into the production process, it is possible to increase work productivity and quality, reduce production costs, or protect employees from working in a hazardous environment [1], [2]. One of the manufacturing activities that can be automated is manipulation. Manipulators can be actuated using various kinds of actuators from electric to hydraulic or pneumatic – in addition to common pneumatic cylinders also pneumatic artificial muscles can be used. The development of the use of pneumatic artificial muscles as one of the atypical forms of propulsion is advancing, where the priority is to achieve the best precision in manipulation. As a result, the system needs to be correctly identified and controlled. [3], [4] Researchers for many years have been devoted to the development and research of artificial muscles. The static and dynamic properties of the artificial muscle have already been described in several articles, e.g. [1], [5], [6], [7]. By recognizing the characteristics of artificial muscles, it is possible to improve their modeling, which can be realized e.g. using different types of neural networks. This was the case in [8], where a hybrid neuron was used to model PUS. The study of dynamics of systems with certain kinematic configuration driven by PAMs can be found in [9], [10]. In both articles, the authors developed and validated the dynamic model of braided pneumatic muscles (also known as McKibben artificial muscle). The effort of all authors of articles is to shift the boundary of knowledge in the field of artificial muscle modeling and subsequent control.

The main objective is to compare the performance of several approaches to experimental identification of the system using neural network. The system is viewed as a SISO system, where the input variable's pressure difference between the muscles and the output variable is joint angle. In addition to MLP model, which is a standard NN model, we used also LNU and QNU models in which the performances were not previously tested for PAM-based system identification.

It is precisely the issue of "correct identification of the system" which this article deals with. The paper contains the outputs from the dynamics identification of a specific manipulator arm, which drives fluidized muscles from the producer FESTO. Three types of neural networks were used for the identification process itself, and their compilation and evaluation took place in the Python working environment. The article is formally divided into two basic parts. The first contains theoretical starting points from the areas of PAMs, neural networks and learning algorithms that were used in the experimental part. In the second part of the article are described: the investigated manipulator, the data used for the identification and the resulting models of the individual neural networks. At the end of the article, the different models are evaluated in terms of their effectiveness and possible further orientation in the field of research is outlined.

2 Pneumatic Artificial Muscles

The inventor of Garasiev, of Russian origin, constructed the first pneumatic artificial muscle (PAM) in the beginning of the 20th Century, which consisted of a rubber hose, in several places surrounded by rings. The rings were interconnected with fibers from non-stretchable material. Since the middle of the last century, McKibben artificial muscles have attracted more attention. This very well-known muscle has been designed with the intent of applying it in medical environment [5], [6]. Since the PAMs have many advantages (low weight, acceptable stiffness, high flexibility, etc.), the development of this type of drive continues to advance. [6]

PAMs work on the principle of changing muscle length when changing the pressure in the muscle. If the muscle is compressed by compressed air, it will shorten from L_0 to L, increasing its volume and muscle diameter from D_0 to D [7]. This contraction κ will develop an external tensile force (Figure 1). The resultant tensile force F_m depends nonlinearly on the pressure in the muscle P_m and the contraction (Equation 1) [11]. The contraction κ is expressed by Equation 2 [12].

$$F_m = f(P_m, \kappa) \tag{1}$$

$$\kappa = (1 - \frac{L}{L_0}) \cdot 100\% \tag{2}$$

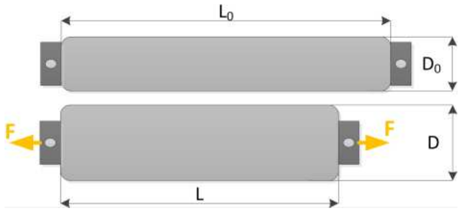

Figure 1
Pneumatic artificial muscle [11]

McKibben's artificial muscles have a relatively low lifetime. The causative factor is the dry friction between the fibers and the tube, so the development tries to eliminate this negative factor. The FESTO fluidic muscles used in the investigated system are designed to eliminate the friction between the strands of the muscle. This is secured by the fact that while the classic artificial muscle has an outer layer, an inner layer and endings [9], [10], the FESTO has joined both layers together.

3 Learning Algorithm and Neural Network Models

Neural networks (NN) allow you to classify or approximate any function using training data. They provide a higher reliability than, for example, expert systems. While expert systems require specific rules for their activity, neural networks can also work with data that contain uncertainties. The ability of neural networks to learn them is similar to statistics, for example, perceptron is the form of a neuron and is similar to a linear model. Neural networks can be taught based on learning algorithms. One type of learning algorithm - the Levenberg-Marquardt method - was chosen for this experiment. This method is mainly used for a higher number of synaptic weights. Using this learning algorithm, the three following NN models were trained: Multi-Layer Perceptron Network with 1 hidden layer, Linear Neural Unit, and Quadratic Neural Unit. [8], [13]

3.1 Levenberg-Marquardt Learning Algorithm

Levenberg-Marquardt (LM) is one of the basic learning algorithms that is similar to Newton's method. LM is an iterative method combining two other methods - the Gauss-Newton method and the Gradient Descent method. This type of learning algorithm is applied to the function in order to minimize it, the solution being of a numerical nature and is very suitable for learning neural networks. [14]

In the following equations, it is expressed how to proceed from Newton's method to the Gauss-Newton method to the Levenberg-Marquardt algorithm itself. From the Newton method shows that the performance index *F(x)* is given by Equation 3, where the individual members A_k and g_k are given by Equations 4 and 5. [15], [16]

$$x_{k+1} = x_k - A_k^{-1} g_k \tag{3}$$

$$A_k \equiv \nabla^2 F(x)\Big|_{x=x_k} \tag{4}$$

$$g_k \equiv \nabla F(x)\Big|_{x=x_k} \tag{5}$$

If F (x) is the sum of square functions and is given by Equation 6, then the gradient $\nabla F(x)$ of the j-th element has the form of Equation 7 or the general shape of the gradient $\nabla F(x)$ in matrix form is given by Equation 8. [16]

$$F(x) = \sum_{i=1}^{N} v_i^2(x) = v^T(x)\, v(x) \tag{6}$$

$$\left[\nabla F(x)\right]_j = \frac{\partial F(x)}{\partial x_j} = 2\sum_{i=1}^{N} v_i(x) \frac{\partial v_i(x)}{\partial x_j} \tag{7}$$

$$\nabla F(x) = 2J^T(x)\, v(x) \tag{8}$$

The essence of the method is assembling of the Jacobian *J(x)*, whose general shape is given by Equation 9. [16]

$$J(x) = \begin{bmatrix} \frac{\partial v_1(x)}{\partial x_1} & \cdots & \frac{\partial v_1(x)}{\partial x_n} \\ \cdots & \cdots & \cdots \\ \frac{\partial v_n(x)}{\partial x_1} & \cdots & \frac{\partial v_n(x)}{\partial x_n} \end{bmatrix} \tag{9}$$

Next it is necessary to find a Hessian matrix, where k,j-th element of this matrix is expressed by Equation 10 or the general matrix form of the Hessian matrix

$\nabla^2 F(x)$ is expressed by Equation 11. If $S(x)$ (Equation 12) is small, then the matrix form of Equation 11 can be adjusted to simpler Equation 13.[16]

$$\left[\nabla F(x)\right]_{k,j} = \frac{\partial^2 F(x)}{\partial x_k \partial x_j} = 2\sum_{i=1}^{N}\left\{\frac{\partial v_i(x)}{\partial x_k}\frac{\partial v_i(x)}{\partial x_j} + v_i(x)\frac{\partial^2 v_i(x)}{\partial x_k \partial x_j}\right\} \tag{10}$$

$$\nabla^2 F(x) = 2J^T(x)J(x) + 2S(x) \tag{11}$$

$$S(x) = \sum_{i=1}^{N} v_i(x)\nabla^2 v_i(x) \tag{12}$$

$$\nabla^2 F(x) \cong 2J^T(x)J(x) \tag{13}$$

If we substitute Equations 8 and Equations 13 into Equation 3, we obtain after Equation 14, which represents the relation for calculating the next element x_{k+1} with using Gauss-Newton method. [16]

$$x_{k+1} = x_k - \left[J^T(x_k)J(x_k)\right]^{-1} J^T(x_k)v(x_k) \tag{14}$$

The Levenberg-Marquardt algorithm (Equation 15) differs from the Gauss-Newton (GN) method because it also contains a unit matrix I and a coefficient μ_k. This parameter brings to the LM algorithm an advantage compared to the GN method because the learning rate is determined based on μ_k value. If μ_k is high, the solution is not satisfactory, and it is not nearby of the optimal solution, so the learning process is slowed. If μ_k is small, it means that the values of parameters are approximated to the optimal solution. [16]

$$x_{k+1} = x_k - \left[J^T(x_k)J(x_k) + \mu_k I\right]^{-1} J^T(x_k)v(x_k) \tag{15}$$

3.2 Linear Neural Unit Model

The essence of the Linear Neural Unit is to find a model of the neuron y_n that can identify the linear dependence between inputs u_i and real y_r outputs. The mathematical model of the LNU is expressed by Equations 16 and 17, where $\boldsymbol{u}$ is the input vector (input), the weight vector is denoted as $\boldsymbol{w}$ and k is the time index. Error of the neuron e expresses to what extent the model represents the real data. The equation for calculating this error is given by the difference between real and model data (Equation 18). [14], [17]

$$y_n(k) = \sum_{i=0}^{n} w_i \cdot u_i(k) = \mathbf{w} \cdot \mathbf{u}(k) \tag{16}$$

$$y_n(k) = [w_0 w_1 \cdots w_n] \cdot \begin{bmatrix} u_0 \\ \vdots \\ u_n(k) \end{bmatrix} = w_0 \cdot u_0(k) + w_1 \cdot u_1(k) + \cdots + w_n \cdot u_n(k) \tag{17}$$

$$e(k) = y_r(k) - y_n(k) \tag{18}$$

3.3 Quadratic Neural Unit Model

The essence of the QNU model is similar to LNU that is to find a model that can identify the functional relationship between inputs and outputs. In this case quadratic dependence is sought. Similar to LNU, the mathematical model of QNU (expressed by Equations 19 and 20) contains a weight vector *w*, a time index *k* and a vector *col u,* that is polynomial. For the neuron error applies the same relationship (Equation 18), where is determined the difference between the real outputs and the model outputs. [14], [17]

$$y_n(k) = \sum_{j=0}^{n} \sum_{i=0}^{n} w_{i,j} \cdot u_i(k) \cdot u_j(k) = w \cdot colu(k) \tag{19}$$

$$y_n(k) = [w_{0,0} w_{0,1} \cdots w_{i,j} \cdots w_{n,n}] \cdot \begin{bmatrix} u_0(k) \cdot u_0(k) \\ u_0(k) \cdot u1(k) \\ \vdots \\ u_i^2(k) \\ u_0(k) \cdot u_0(k) \\ \vdots \\ u_n^2(k) \end{bmatrix} \tag{20}$$

3.4 Multi-Layer Perceptron Network Model

Multilayer Perceptor Network is the last neural network model that has been used to identify the system. This is a well-known network architecture that is characterized by having at least one hidden layer. The base unit - the neuron, which is on the hidden layer, is for this type of network called the perceptron (shown in Figure 2). The intrinsic activity of neuron is expressed as x_i. Output y is obtained by transforming inputs u_i using the activation function φ_i. [13], [17], [18]

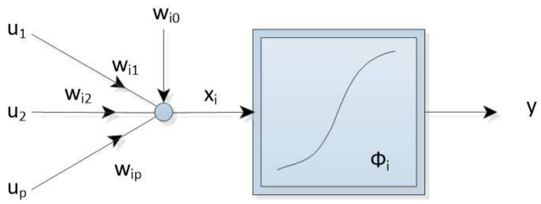

Figure 2
Schema of the perceptron [18]

The two most typical activation functions that are used for MLP networks are a logistic function that is defined at <0; 1> and hyperbolic tangents defined at intervals <-1; 1>. The mathematical formula of the logistic activation function is given by Equation 21 and the hyperbolic tangent by Equation 22. [18]

$$\varphi_i = \text{logistic}(x) = \frac{1}{1+\exp(-x)} \tag{21}$$

$$\varphi_i = \text{tauh}(x) = \frac{1-\exp(-2x)}{1+\exp(-2x)} \tag{22}$$

The MLP network is formed by the parallel interconnection of several perceptrons, and subsequently these neurons are interconnected with the neuron on the output layer. The basic task of the network is the approximation of each nonlinear function. The overall structure of the MLP network with one hidden layer is shown in Figure 3. [17], [18]

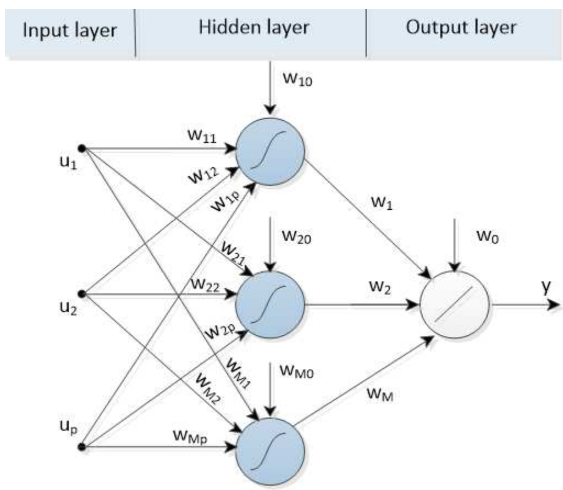

Figure 3
Overall structure of the MLP network with one hidden layer [18]

The output of the multilayer perceptron network can be mathematically formulated based on Equation 23 (the inputs u_j, the weight of the hidden layer w_{ij}, the weight of the output layer w_i, the activation function φ_i and the output y). [17], [18]

$$y = \sum_{i=0}^{M} w_i \varphi_i \left(\sum_{j=0}^{p} w_{ij} u_j \right) \tag{23}$$

Figure 4 shows the structure of a dynamic MLP network with just 1 hidden layer with n number of perceptrons (or neurons). On the input layer there is an input vector that contains data of a dual kind. The input is the measured data, but since it is a dynamic system, the input also forms the y_n data. This type of data is the output of the model from earlier epochs. The sensitivity of each perceptron is expressed by the weight W_i. Within the hidden layer, there are two operations, respectively functions. Synaptic operation is a linear function of the input vector and weights. Somatic operation is a nonlinear activation function given by Equation 24. The output layer contains an output neuron defined by the output data vector y and the weights of this neuron V that form a linear function. [14], [17], [19]

$$\phi = \frac{2}{1+e^{-v}} - 1 \tag{24}$$

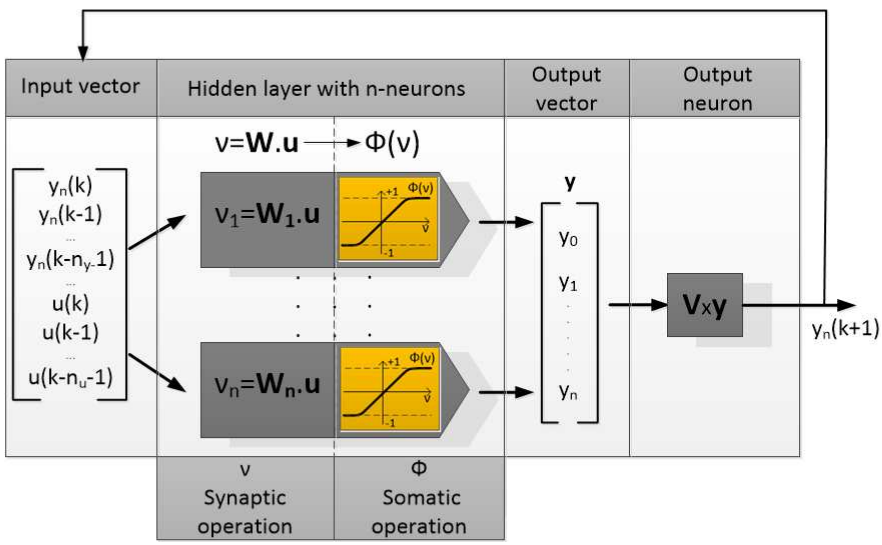

Figure 4
MLP dynamic network with one hidden layer [14]

4 System Description

The main object of the study was the manipulator arm system, actuated by two pairs of FESTO fluidic muscles. In the right part of Figure 5 is the real manipulator arm and in the left part is a principal schematic of the main element manipulator. The most basic parts of the system are two pairs of FESTO MAS-20 muscles. The compressed air is supplied to these muscles by FIAC Leonardo compressor. Chain mechanism (sprocket-chain) and a pair of rotary joints serve to desirably deflect the arm with the load. The flow of pressurized air to and out of the muscles is controlled through four MATRIX EPR-50 pressure regulators. The regulators also incorporate built-in sensors, which ensure simultaneous pressure sensing in each of the muscles. The Kubler 3610 incremental sensor is used to measure joint rotation. The control logic signals were processed by the Humusoft MF624 I / O PCI card, and the Matlab and Simulink modules served to control the arm.

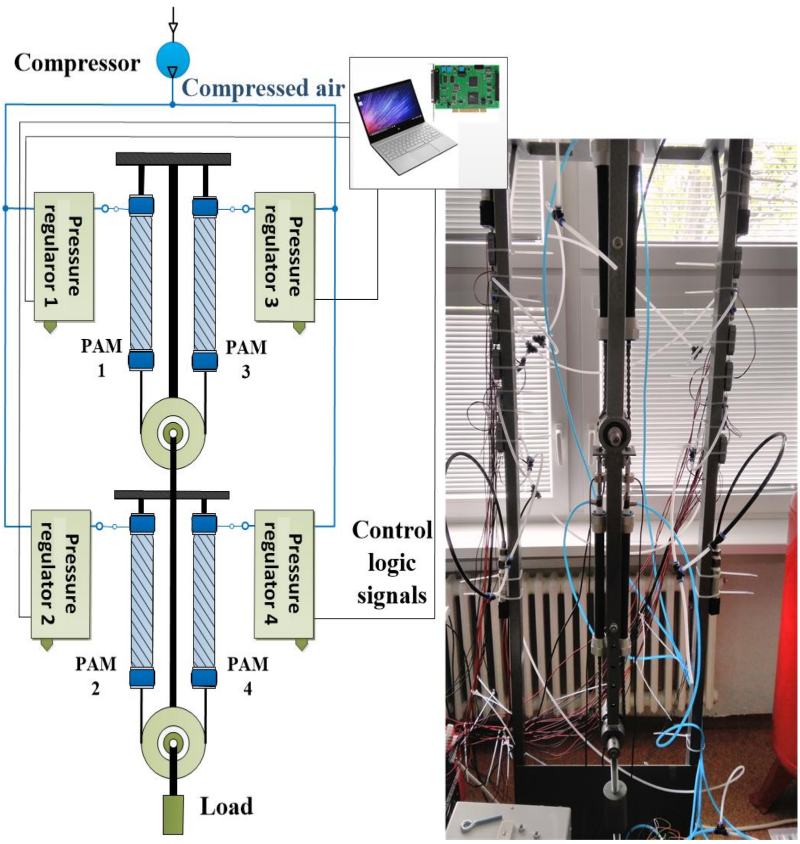

Figure 5
Principled scheme of manipulator with PAMs

5 Experimental Part

The main part of the research is an experimental part. Its essence was to obtain data from the real system (manipulator arm with PAMs) that was used in the learning and testing processes. Neural network models and the learning algorithm, which were theoretically supported first, were created in program IDLEX. The output of the experimental part is the individual models, which are subsequently evaluated on the basis of the SSE and fit parameters and also compared to each other. This process served to identify the dynamics of the manipulator arm. At this stage we tried to identify only the dynamics of one of the axes to simplify the dynamic model by eliminating the presence of dynamic coupling between the joints.

5.1 Training and Test Data

For training and testing of models, measured data were needed. The relationship of interest was between the joint angle (output variable) and pressure difference between the muscles (input variable). A total of 16,667 samples were obtained from one axis of the manipulator arm with a sampling period of 3 ms. The data used in the learning or testing phase has not been sampled (?).

Figure 6 shows the dependence of the pressure difference on the time step used for training and testing. For training (blue curve) the dependence itself has a decreasing character, since triangular excitation signal with a linear decreasing amplitude was used. In this measurement, a pair of muscles was initially pressurized to approximately 300 kPa (i.e. pressure difference was zero). After this the initial set-up, one muscle was discharged, and the other muscle was inflated. For testing (red curve) the data were obtained by generating a random signal with a random amplitude, the curve itself has a random course.

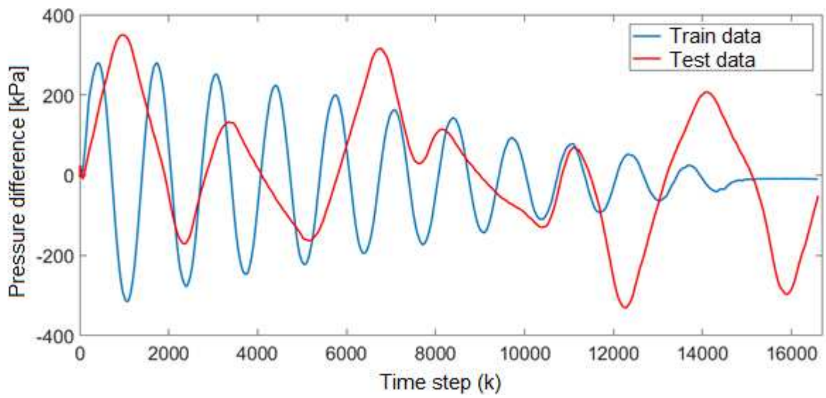

Figure 6

Time dependence of pressure difference for data used in training

5.2 Input Conditions for Models and Individual Models

When compiling individual neural network models in IDLEX, it was necessary to select the input conditions. Using them should ensure the best possible identification of the system. The following parameters were selected for the identification: learning rate μ, number of epochs e, number of inputs nu, number of outputs ny for each model.

A dynamic model with multilayer perceptron network with one hidden layer (MLP) was created, and for this type of network it was also necessary to choose the number of neurons in the hidden layer $n1$. In Table 1 is show an overview of the entry conditions in which the individual models achieved the best results.

Table 1

Comparison of input conditions for individual models

PARAMETERS	LNU	QNU	MLP
LEARNING RATE	0,05	0,02	0,005
NUMBER OF EPOCHS	4	10	10
NUMBER OF INPUTS U	10	7	10
NUMBER OF INPUTS Y	5	1	5
NUMBER OF NEURONS ON THE HIDDEN LAYER	---	---	1

For objective model comparison, it is recommended that the number of inputs and outputs be the same for each model. However, the Quadratic Neural Unit model did not work properly under the same conditions as for LNU or MLP. So, for QNU were chosen such initial conditions, where the model worked the most efficiently.

After setting the entry conditions and creating a program, the learning and testing phases followed showing the results of the models and their graphical interpretations in the program. Each of the models is presented with some pictures: 3 figures relate to the learning phase, the other 3 figures to the test phase. For only the test phase, network weights successful in the learning phase were used. It follows that the graph of the time depending of the pressure difference is depicted in the epoch when the weights were the most suitable.

Figures related to the learning and testing phase show: the first graph shows the time dependence of difference of pressures for real system (blue curve - y_r or y_r*_test*) and for the model (green curve – y or *y_test*). The second graph shows the error between the system and the model (red curve – e or *e_test*). The third graph shows the Sum Squared Error (*SSE* or *SSE_test*) parameter as a function of epoch - the black curve, which expresses the sum of the quadratic errors between the individual data and the diameters of their groups [14].

5.2.1 Linear Neural Unit

Figure 7 graphically interprets the output model of Linear Neural Unit after the learning phase. The picture shows that the LNU model was relatively well taught even in the low number of epochs, as evidenced by the course of the SSE parameter (Figure 9), which has a stable convergence progress. Differences between model and real data can be seen especially at curve vertices where the green curve is unable to reach the position of the blue curve, especially in the negative angles of the joint.

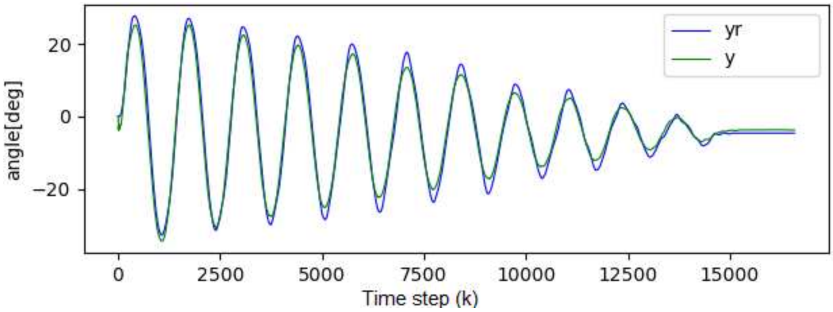

Figure 7
Training LNU

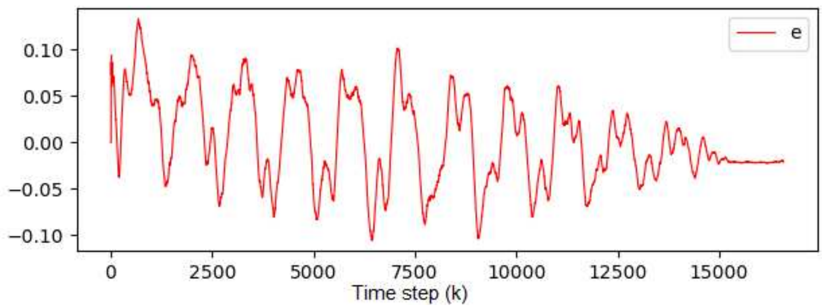

Figure 8
Training LNU – error

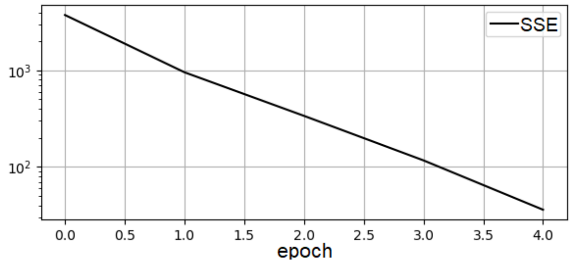

Figure 9
Training LNU – SSE

The results of the test phase are graphically interpreted by Figure 10-Figure 12. While the learning was done on data that had a decreasing character, testing was performed on data with random amplitude, which was reflected in the course of the model. In this case, the difference between the real (blue curve) and the model (green curve) is more pronounced. The SSE_test parameter indicates a wobble.

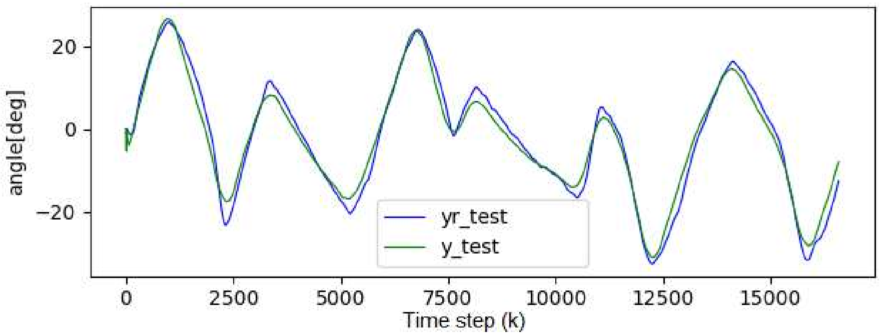

Figure 10
Testing LNU

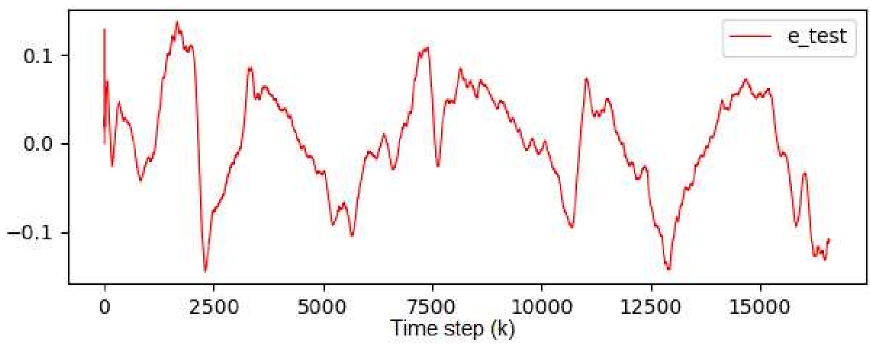

Figure 11
Testing LNU – error

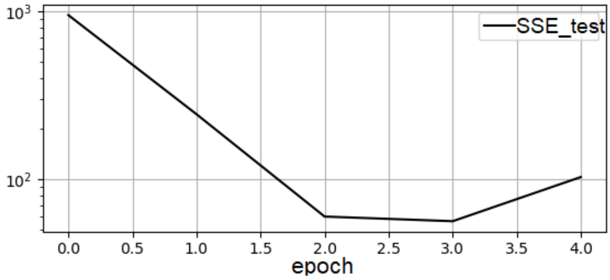

Figure 12
Testing LNU – SSE

5.2.2 Quadratic Neural Unit

In Figure 13 is a graphical representation of the Quadratic Neural Unit output model. The model is shown after training. A higher number of epochs was selected for the QNU learning and testing phase, because it is necessary for proper functioning (Figure 15). Training phase based on either the curve of the model or the progress of the SSE parameter that converges does not look the worst. However, it is not possible to compare this model with LNU and MLP models (they do not have the same initial conditions).

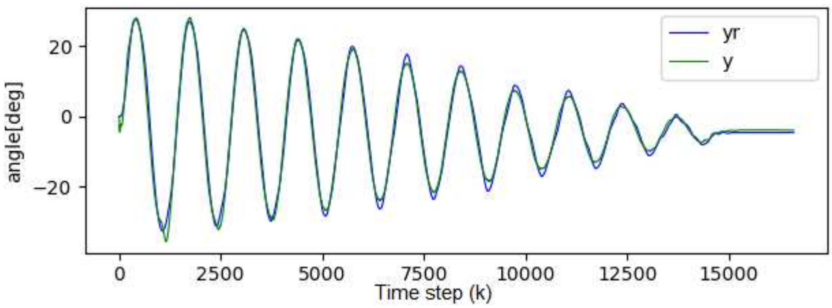

Figure 13
Training QNU

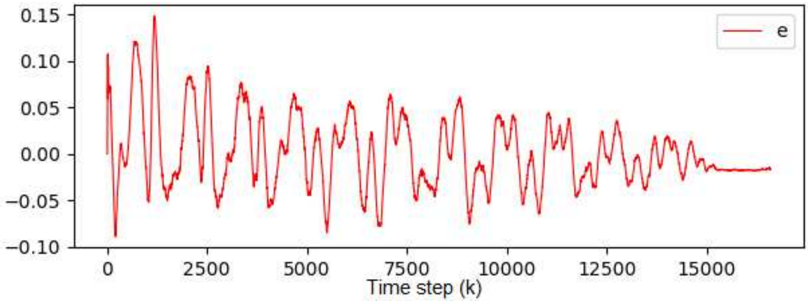

Figure 14
Training QNU – error

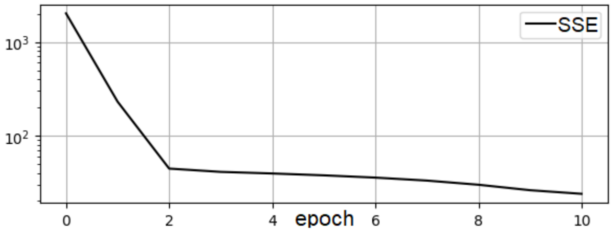

Figure 15
Training QNU - SSE

Although for QNU the most appropriate initial conditions were chosen in which the model achieved the highest possible efficiency, the model worked in the test phase worse than the other two models. The SSE_test parameter (Figure 18), like LNU testing, did not have a purely converging course, and when looking at the course of the green curve it is certain that the model was unable to fit the real data very well at a positive angle (above 20 °) (Figure 16). If the QNU model runs with the same initial conditions as LNU and MLP, the SSE parameter itself would have a chaotic divergence course, and the green curve of the model would not be able to approach towards the model in Figure 13, not even the LNU and MLP model.

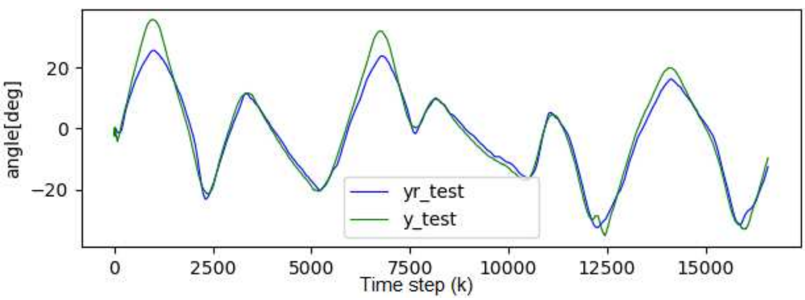

Figure 16
Testing QNU

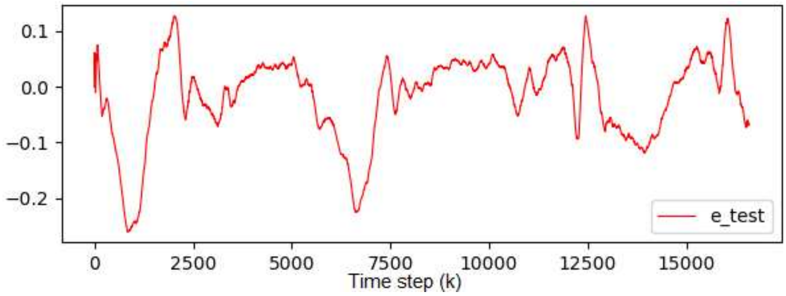

Figure 17
Testing QNU – error

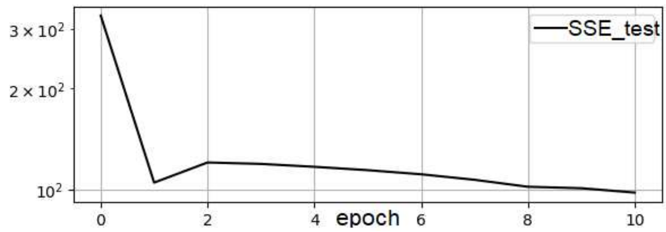

Figure 18
Testing QNU - SSE

5.2.3 Multi-Layer Perceptron Network

The last of the investigated and displayed output model was the MLP. Its graphical interpretation along with the course of real data, errors, and SSE parameters during the training phase is shown in Figure 19-Figure 21. The MLP model (similarly as a model LNU) has also learned well. This is evidenced by the course of the green curve towards the blue. The SSE parameter somewhat fluctuate in the first two epochs, but subsequently dropped significantly and converged.

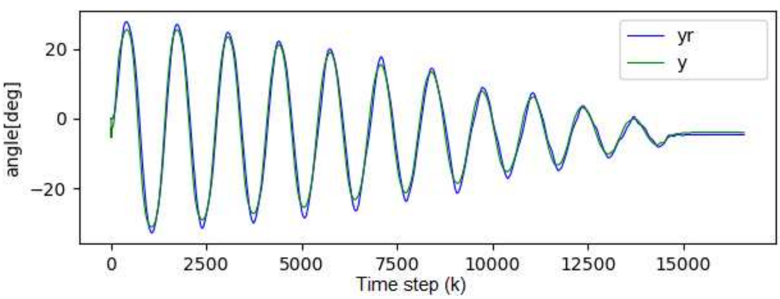

Figure 19
Training MLP

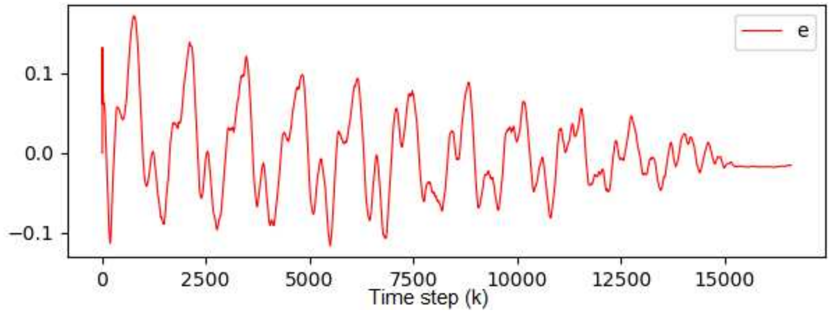

Figure 20
Training MLP – error

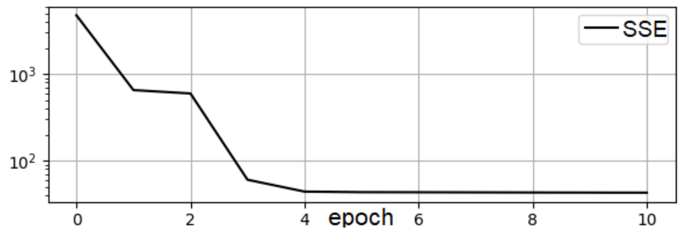

Figure 21
Training MLP - SSE

The multilayer perceptual network, during the testing phase (10 epochs), had parameter SSE_test similar to the parameter SSE for the training phase (Figure 24). In the first epoch, the parameter fluctuates, but then there was a significant decrease and convergence of the SSE_test parameter. The curve, like the QNU model, had a problem in reaching angles above 20 degrees, but below this value, the model was very close to real data (Figure 22).

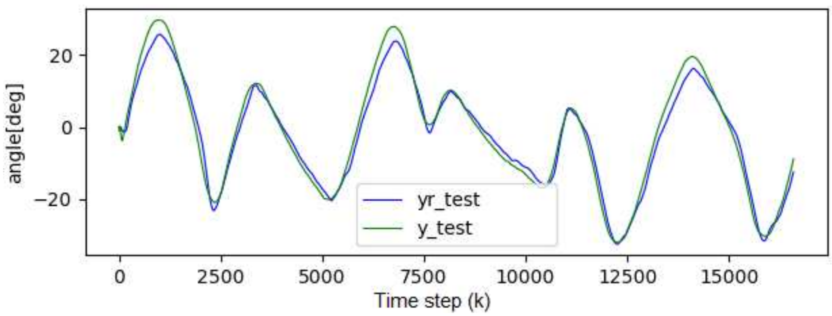

Figure 22
Testing MLP

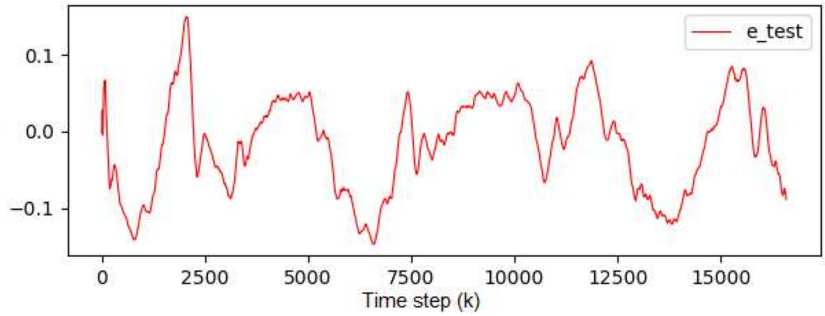

Figure 23
Testing MLP – error

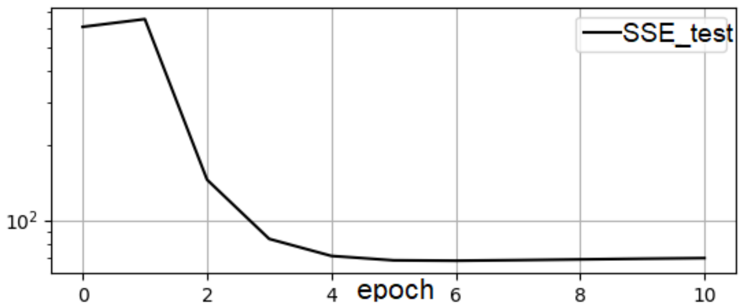

Figure 24
Testing MLP - SSE

5.3 Comparison of Individual Models

The efficacy of the individual models examined in the experimental part was compared based on the fit parameter. It is a parameter that was calculated by the Matlab program after entering the following command: *fit = goodnessOfFit (y, yr, 'NRMSE')*, where y are the values determined by the model and yr are real values. The given command sets the Normalized Root Mean Square Error (NRMSE), which represents the degree of difference between the predicted and the actual model. Equation 25 expresses the mathematical entry of the NRMSE parameter calculation, where *x* are test data, *xref* are reference data and *fit* is a row vector of length *i*. [20], [21]

$$\mathrm{fit(i)} = 1 - \frac{\left\| \mathrm{xref}\left(:,\mathrm{i}\right) - \mathrm{x}\left(:,\mathrm{i}\right) \right\|}{\left\| \mathrm{xref}\left(:,\mathrm{i}\right) - \mathrm{mean}\left(\mathrm{xref}\left(:,\mathrm{i}\right)\right) \right\|} \tag{25}$$

Figure 25 shows individual output models along with real measured data (black curve). The chart also contains a numerically-expressed parameter fit for each model. As above, it was suggested that models should be compared under the same input conditions (input and output), so the QNU will be evaluated only on the basis of how best it would be worked in comparison with the measured data.

The QNU model, which is represented by the green curve, reached 77.80% in fit. This means that it can predict with such precision at the given input conditions. However, the model was not stable and was not the most appropriate for the type of data.

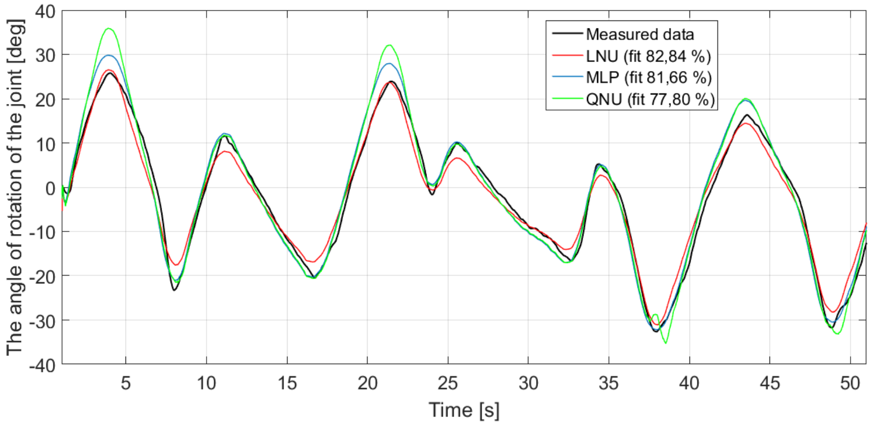

Figure 25
Comparison of output models with real measured data

The MLP model, which is shown in the blue curve, is already comparable to the LNU (red curve) model because it had the same initial conditions. When comparing based on the fit parameter, LNU was better at 82.84%, while MLP reached 81.66%. However, when analyzing the course curves, the MLP network is able to get closer to the top of the measured data than the LNU. Even at negative angles, the MLP is the most accurate in each negative rotation within the three models compared, but in some positive angles, the measured data is exceeded.

Conclusions

Researchers dealing with the modeling, identification and control of pneumatically-powered systems are aware of the highly positive potential due to their use in industry. However, they are constantly confronted with shortcomings; therefore they need to eliminate it. That is the reason, why the effort to advance in research is not regressing. Several authors have already identified similar systems with using the Gauss-Newton method or Incremental back-propagation algorithm as learning algorithms, and as models using genetic algorithms, and different ARX and NARX models. Similarly, the authors of this article attempt to extend the knowledge in the area of identification of pneumatically-actuated systems by experimentally researches, where are comparing different methods – neural networks (eg, the QNU was little explored for PAM).

The aim of this experiment was to identify the dynamics of the system (manipulator arm powered by fluid muscles FESTO) using the pre-selected learning algorithm and 3 different neural network models. The Python program (or its subsystem IDLEX) was used to identify it. The LNU, QNU, and MLP models show that the data are relatively highly linear dependent. Of these, the best models were MLP and LNU, so it would be useful to test them further. The results also show that the use of QNU to identify this system is not the most appropriate. Further testing should be performed measuring to obtain a further set of independent data, and verifying the effectiveness of the models on these data.

Another way to verify the effectiveness of models and their reliability is to create them in another program (e.g. Matlab) and compare the results. In this experimentunsampled data were used, since the correlation analysis showed that sampling of data could lead in the loss of data credibility. The correlation analysis was performed simultaneously for both directions of the manipulator arm joint. In the future, it would be advisable to perform a correlation coefficient analysis especially for each direction of rotation of the joint, which would allow a more accurate identification of the joint rotation above 20 ° in the positive direction.

Acknowledgement

The research is supported by a Grant from the Research Grant Agency within the Ministry of Education, Science, Research and Sport of the Slovak Republic and Slovak Academy of Sciences. Number 1/0822/16 Research of Intelligent Manipulator Based on Pneumatic Artificial Muscles with Three Degrees of Freedom; Number 1/0393/18 Research of Methods for Modeling and Compensation of Hysteresis in Pneumatic Artificial Muscles and PAM-actuated Mechanisms to Improve the Control Performance Using Computational Intelligence as well as the EU Structural Funds Project with ITMS code: 26220220103.

References

[1] Kelasidi, E. et al.: A Survey on Pneumatic Muscle Actuators Modeling. In: International Symposium on Industrial Electronics. June 27-30, 2011, Gdansk: IEEE, pp. 1263-1269

[2] Escobar, F. et al.: Simulation of Control of a Scara Robot Actuated by Pneumatic Artificial Muscles Using RNAPM. Journal of Applied Research and Technology. 2014, Vol. 12, No. 5, pp. 939-946

[3] Piteľ, J. et al.: Pneumatický umelý sval – perspektívny prvok mechatroniky (1). AT&P journal. 2008, Vol. 12, pp. 59-60, ISSN 1336-233X

[4] Piteľ, J. et al.: Pneumatické umelé svaly: modelovanie, simulácia, riadenie. Košice: Technická univerzita v Košiciach, 2015, p. 275, ISBN 978-80-553-2164-6

[5] Wickramatung, K. C. et al.: Empirical Modeling of Pneumatic Artificial Muscle. In: Proceedings of the International MultiConference of Engineers and Computer Scientists 2009. March 18-20, 2009, Hong Kong: IMECS 2009, p. 5

[6] Oliver-Salazar, M. A. et al.: Characterization of pneumatic muscle and their use for the position control of a mechatronic finger. Mechatronics. 2017, Vol. 42, pp. 25-40

[7] Doumit, M. et al.: Development and testing of stiffness model for pneumatic artificial muscle. International Journal of Mechanical Sciences. 2017, Vol. 120, pp. 30-41

[8] Song, CH. et al.: Modeling of pneumatic artificial muscle using a hybrid artificial neural network approach. Mechatronics. 2015, Vol. 31, pp. 124-131

[9] Tang, R. et al.: An Enhanced Dynamic Model for McKibben Pneumatic Muscle Actuators. In: Proceedings of Australasian Conference on Robotics and Automatization. December 3-5, 2012, Wellington, p. 8

[10] Doumit, M. et al.: Analytical Modeling and Experimental Validation of the Braided Pneumatic Muscle. IEEE Transactions on Robotics. 2009, Vol. 25, No. 6, pp. 1282-1290

[11] Chang, M-K. et al.: T-S fuzzy model based tracking control of a one-dimensional manipulator actuated by pneumatic artificial muscles. Control Engineering Practice. 2011, Vol. 19, pp. 1442-1449

[12] Lin, CH-J. et al.: Hysteresis modelling and tracking control for a dual pneumatic artificial muscle system using Prandtl-Ishinskii model. Mechatronics. 2015, Vol. 28, pp. 35-45

[13] Kvasnička, V. et al: Introduction to the theory of neural networks. Slovakia, Bratislava: IRIS. 1997, p. 237, ISBN 9-788-088-77830-1

[14] Bukovský, I.: Nonconventional Neural Architectures and their Advantages for Technical Applications. Faculty of Mechanical Engineering. Praque: Czech Technical University in Praque. 2012, ISBN:978-80-01-05122-1

[15] Tomczyk, K.: Levenberg-Marquardt algorithm for optimization of mathematical models according to minimax objective function of measurement systems. Metrology and Measurement systems. 2009, Vol. XVI (2009), No. 4, pp. 599-606. ISSN 0860-8229

[16] Hagan, M. T. et al: Neural Network Design. ebook

[17] Nelles, O.: Nonlinear system identification: from classical approaches to neural networks and fuzzy models. Germany. Berlin: Springer. 2001, p. 786, ISBN 3-540-67369-5

[18] Karray, F. O. et al: Soft Computing and Intelligent Systems Design: Theory, Tools and Applications. England. Harlow: Addison Wesley. 2004, p. 584, ISBN 0-321-11617-8

[19] Haykin, S.: Neural Networks: A Comprehensive Foundation. India: Pearson Education, 2005, p. 823, ISBN 81-7808-300-0

[20] Rimarčík, M.: Štatistika pre prax. 2007, p. 199, ISBN 978-80-969813-1-1

[21] Ljung, L.: System Identification Toolbox User´s Guide. Natick: The Math Works, 2015, p. 982

Comparing the Reliability of Biomedical Texture Analysis Tools on Different Image Types

Monika Béresová[1]*, Attila Forgács[2,3], Blanka Bujdosó[3], András Székely[4], József Varga[3], Ervin Berényi[1], László Balkay[3]

[1] Div. of Radiology, Department of Medical Imaging, Faculty of Medicine, University of Debrecen, Nagyerdei krt. 98, 4032 Debrecen, Hungary
E-mail: beres.monika@med.unideb.hu; eberenyi@med.unideb.hu

[2] Scanomed Nuclear Medicine Center, Nagyerdei krt. 98, 4032 Debrecen, Hungary; E-mail: forgacs.attila@scanomed.hu

[3] Div. of Nuclear Medicine, Department of Medical Imaging, Faculty of Medicine, University of Debrecen, Nagyerdei krt. 98, 4032 Debrecen, Hungary
E-mail: bujdoso.blanka@kenezy.unideb.hu; jvarga@med.unideb.hu; balkay.laszlo@med.unideb.hu

[4] Kenézy Gyula Hospital, Department of Radiology, Bartók Béla út 2-26, 4031 Debrecen, Hungary; E-mail: andras.szekely@med.unideb.hu

Abstract: The aim of this study was to analyze the reliability of texture index (TI) calculations using two different approaches.
First, we calculated texture parameters on synthetically constructed images using four different biomedical software tools (CGITA, InterView Fusion, Matlab, MaZda). Second, we investigated the reliability of texture parameters, particularly how the texture indices diverge between two similar images with substantially different texture.
We generated five different heterogeneous synthetic images, thereafter, histogram-based and co-occurrence matrix features were calculated. The co-occurrence based indices were computed after two (8 and 64) different gray scale normalizations. For the reliability test, we compared 22 texture indices using a histological slice of the brain and Michelangelo's painting, and the gray level dependence was also analyzed.
The histogram-based parameters of all images and from all software were very similar. Differences were found in the co-occurrence based indices after both gray level image normalizations. The reliability tests showed that from 22 parameters only 5 texture indices changed more than 20%, and at least 64 normalization levels were necessary for acceptable results. Our results underline that in medical multicenter studies it is especially critical to use the same software package. Some parameters do not reliably reflect changes, so texture analysis (TA) should be used with caution.

Keywords: texture analysis; medical imaging; software; comparative study; co-occurrence matrix

1 Introduction

There is an increasing interest in the use of medical imaging to describe tumor tissue characteristics. Radiomics is a new field that intends to capture more information (intensity histogram-based data, shape information, intra-tumor heterogeneity, special texture features) from the image of an organ [1]. Texture analysis (TA) was first introduced in MRI in the nineties [2] and is frequently used for analyzing and differentiating anatomical areas [3]. In addition, TA has become very common in all medical imaging modalities such as ultrasound (US), computed tomography (CT), magnetic resonance imaging (MRI), and positron emission tomography (PET) for the quantification of tumor heterogeneity. Several different methods exist for texture classification, such as statistical methods, filter-based techniques, model-based schemes, and structural approaches [4]. The first application was introduced by Haralick and Shanmugam; they used statistical feature characterization by computing the gray level co-occurrences matrix (GLCM). The co-occurrence matrix represents the relationship between intensity values in a given direction and distance in the image [5].

Despite several attempts to reveal the meaning of different TIs, we still do not fully understand, how the TIs should change when the texture of an image varies, nor how a different image texture could be associated with a TI range [6]. Further research in this topic could be crucial to establish the applicability of any TI in the biomedical area.

On the other hand, many techniques and software solutions have been proposed for the calculation of TIs. There are several software tools frequently used in the medical field such as MaZda [7, 8, 9], Matlab-based CGITA [10], the "GLCM_textureToo" Java tool [11], the ImageJ "Texture Analyzer" plugin [12, 13, 14], several modules of the Matlab "Image Processing Toolbox" [15], TexRad [16], InterView Fusion [17], ABAQUS [18, 19] and FRAGSTATS [20], some of which are free.

MaZda is a special computer program for the calculation of several texture parameters from digitized or medical images. This package contains the B11 program (COST B11 European project) for texture analysis and visualization. MaZda was used by Albuquerque et al. for texture analysis of damaged gray nuclei in amyotrophic lateral sclerosis; by Yan et al. to differentiate renal cell carcinoma, by Orphanidou-Vlachou et al. to quantify brain tumors; and by J MacKay et al. to study bone texture [21, 22, 23, 24].

Matlab is a scientific numerical computing environment and fourth-generation programming language with a wide range of toolboxes. Some frequently cited applications for texture analysis include CT texture analysis by Daginawala et al., the quantitative evaluation of skeletal muscle defects by Liu et al., and the texture analysis of brain MR images by Michoux et al. [25, 26, 27].

CGITA was developed under Matlab by Fang et al., originally used to quantify tumor heterogeneity in molecular images [10, 28]. InterView Fusion is a general-purpose multimodality medical image analysis software developed by Mediso Ltd. It comprises a wide range of functions and special tools that provide detailed, fast and sophisticated evaluation of medical images [29].

Most research groups in this field use in-house software for computing tumor heterogeneity without demonstrating how the reliability of the software was tested [30, 31 32, 33, 34]. Since the algorithms that are used for heterogeneity index (HI) calculations are not always simple, the developed codes should be validated in some manner. In addition, there is no generally accepted concept on how to validate the different HI calculation software from various research groups and vendors. A solution to this issue might be if a collection of synthetic images, constructed with numerous, simple geometrical shapes such as rectangles and circles, were used to define heterogenic patterns, and then applied for software validation.

The aim of this study was to compare the texture analysis calculations of four different biomedical software packages: Matlab, MaZda, CGITA and InterView Fusion. There are several HIs in these packages with the same name, but it is not clear whether the underlying algorithms are identical or not. Manual calculation was regarded as the gold standard for calculating HI values. All calculations were performed on synthetically constructed images. In addition, we also intended to analyze the reliability of HIs based on two carefully selected images, which show similar appearance and shape with different texture content.

2 Materials and Methods

2.1 Synthetic Images

We generated five different image patterns which are modifications of those published by Sugama Chicklore et al. [35]. Their data were defined in a 10x10 matrix. We extended the matrix size to 12x12 to keep the periodicity of the image pixels, thus allowing further extension of the matrix dimensions (Fig. 1a). We also created a homogeneous constant matrix (A0) with the same matrix size. Then we arbitrarily inserted the matrices into a 128*128 image (Fig. 1b), and finally each were converted to DICOM format using Matlab version 2014b (The MathWorks Inc., Natick, MA).

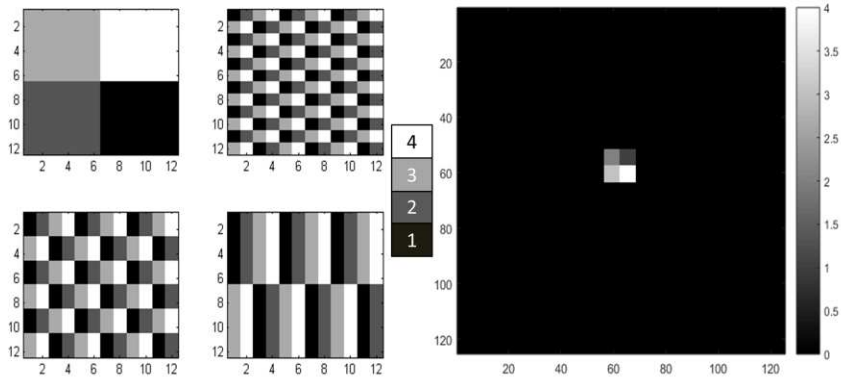

Figure 1a Figure 1b

The proposed A1, A2, A3 and A4 12x12 matrices (1a), and a representative final image that was created by inserting the A1 matrix into a black background (1b). The A1-A4 basic matrices contain only four different pixel values (1-4) and the background area is set to zero in each final image.

2.2 Selected Heterogeneity Indices and the Fundamental Calculation Method

First, we calculated global (histogram-based) and local heterogeneity parameters of the A0, A1, A2, A3 and A4 matrices manually, without applying any software package (manual calculation). The global parameters were histogram-based values, which include the maximum (max), minimum (min), mean, standard deviation (SD), skewness, kurtosis and SD/mean parameters. Additionally, local parameters based on the co-occurrence matrix (coM) were also calculated: contrast, correlation, energy, homogeneity, dissimilarity, and entropy. Mathematical formulas of these parameters are provided in Table 1. Although other textural parameters can also be defined based on the GLCM, we investigated the most frequently used ones [5]. For the comparisons, manual calculation following these formulas was selected as the "gold standard". The GLCM-based HI values were calculated with two different gray scale normalizations (8 and 64 levels), and 2 different directions (corresponding to 0^{o} and 90^{o}). Finally, each GLCM was normalized by dividing it by the sum of all matrix values.

Table 1

Formulas for the texture indices based on the co-occurrence matrix. P_{ij} is the element in the ith row and jth column of the co-occurrence matrix. The μ_i, σ_i, and μ_j, σ_j parameters designate the weighted mean and variance in row i and column j of the co-occurrence matrix, respectively. N is the size of the co-occurrence matrix.

Correlation	$\sum_{i,j=0}^{N-1} P_{i,j} \cdot \left[\frac{(i-\mu_i)(j-\mu_j)}{\sqrt{(\sigma_i^2)(\sigma_j^2)}}\right]$ where $\mu_i = \sum_{i,j=0}^{N-1} i \cdot P_{i,j}$ $\mu_j = \sum_{i,j=0}^{N-1} j \cdot P_{i,j}$ and $\sigma_i^2 = \sum_{i,j=0}^{N-1} P_{i,j} \cdot (i-\mu_i)^2$ $\sigma_j^2 = \sum_{i,j=0}^{N-1} P_{i,j} \cdot (j-\mu_j)^2$		
Contrast	$\sum_{i,j=0}^{N-1} P_{i,j} \cdot (i-j)^2$	**Energy**	$\sum_{i,j=0}^{N-1} P_{i,j} \cdot \lvert \mathrm{i}-\mathrm{j} \rvert$
Dissimilarity	$\sum_{i,j=0}^{N-1} P_{i,j}^2$	**Homogeneity**	$\sum_{i,j=0}^{N-1} \frac{P_{i,j}}{1+\lvert i-j \rvert}$
Entropy	$\sum_{i,j=0}^{N-1} P_{i,j} \cdot (-log_2 P_{i,j})$ or $\sum_{i,j=0}^{N-1} P_{i,j} \cdot (-\ln P_{i,j})$		

2.3 Heterogeneity Index Calculations using Different Software Tools

The heterogeneity parameters of the DICOM images were computed with CGITA, InterView Fusion (ver. 2.02.055), Matlab and MaZda. Of the programs mentioned in the introduction, only these four were available at our institution at the time of our study. The parameters were then compared to the manually calculated values. The 12x12 regions were segmented from the images based on both the vendor-supplied manual ROI definition method, and a semi-automatic segmentation method using a low threshold value; the resulting volumes were found exactly the same.

Based on the available software documentation, we found four different implementations of GLCM generation. CGITA computes local heterogeneity parameters by averaging the two GLCMs from horizontal and vertical (0^o and 90^o) directions [10]. In contrast, InterView Fusion calculates 26 different GLCMs (related to 26 different directions), then the average of these serves as the base for any HI. Matlab has built-in functions such as *graycomatrix()* and *graycoprops();* the direction and the distance can be specified by the user [15]. We used the same directions as in the manual calculations. In MaZda, 20 different options are implemented in the following vector forms: [d 0], [0 d], [d d], [d –d], where d (distance) can take values of 1, 2, 3, 4, or 5.

2.4 Images for Analyzing the Reliability of Heterogeneity Parameters

For these tests 2 images were selected: a sagittal histological section of the brain (Fig. 2a) [36], and Michelangelo's famous painting [37], the Creation of Adam (Fig. 2b). While the appearance and shape of these images is remarkably similar, as revealed by Suk et al. [38], the actual pattern and texture is different. For proper comparison we resampled the original photos to the same pixel size (418x559) and extracted the area of the brain shape from both images by removing the outside pixels using the method described by Zhenjiang et al. [39]; all heterogeneity parameters were calculated within the pixels inside. In this reliability analysis several other TIs were included using a Matlab-based software tool (referred by GLCM_feature) developed by A. Uppuluri [40].

This tool comprises the following 22 TIs: autocorrelation (autoc), contrast (contr), correlation_m (corrm), correlation_p (corrp), cluster prominence (cprom), cluster shade (cshad), dissimilarity (dissi), energy (energy), entropy (entro), homogeneity_m (homom), homogeneity_p (homop), maximum probability (maxpr), sum of squares (sosvh), sum average (savgh), sum variance (svarh), sum entropy (senth), difference variance (dvarh), difference entropy (denth), information measure of correlation1 (inf1h), information measure of correlation2 (inf2h), inverse difference normalized (indnc), and inverse difference moment normalized (indmnc). The detailed definitions of the above parameters can be found in the articles of [41, 42]. We also investigated how the parameters depend on the number of gray scale normalization (with 8, 16, 32, 64, …, 1024 levels) in the case of 6 selected TIs (contrast, correlation, energy, homogeneity, dissimilarity, and entropy).

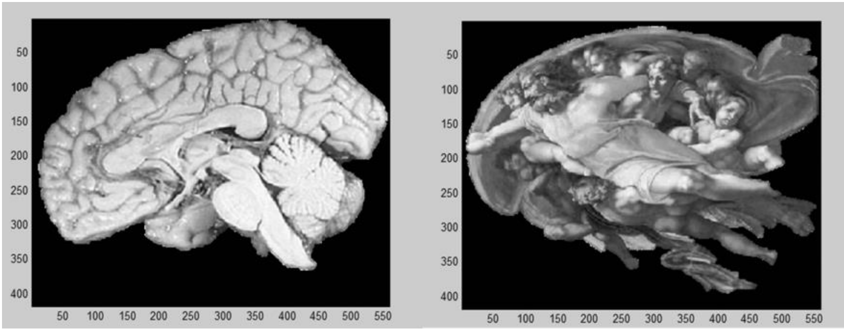

Figure 2a Figure 2b

Segmented histological section of the brain (2a), and Michelangelo's segmented famous painting, the “Creation of Adam” (2b). The pixel size and the colormap are the same for both cases (418x559 and gray scale).

3 Results

3.1 Texture Index Values using Different Software

The ratio of high and low signal intensities and the global data (as listed in section 2.2) were equal in all four inhomogeneous images. The images were structured so that the values of the local parameters, when calculated in the horizontal direction for images A2, A3 and A4, remain the same. The values of the global parameters such as max, min, mean, SD, skewness, kurtosis and SD/mean (Tables 2) for matrices A1-A4 were very similar. With Matlab and CGITA the kurtosis values were significantly different from the manually calculated ones. For the rest of the global parameters the discrepancy was below 0.5% in all cases. From here on all results are given as the percentage differences between the output of the respective software and manual calculation. Differences were even more pronounced in the case of co-occurrence matrix based local parameters (contrast, correlation, energy, homogeneity, dissimilarity and entropy) for both 8 and 64 level gray scale normalization. When we used Matlab and MaZda, calculations were carried out in both [0 1] and [1 0] directions. After 8 level gray scale normalization (Fig. 3), the largest percentage discrepancy was seen for HI values provided by MaZda (both directions), and CGITA.

Parameters	***Matlab***	***MaZda***	***IW-Fusion***	***CGITA***	***Man.***	***Matlab***	***MaZda***	***IW-Fusion***	***CGITA***	***Man.***
	A0					A1, A2, A3, A4				
Mean	100	100	100	100	100	2.500	2.500	2.500	2.500	2.500
Min	100	100	100	100	100	1.000	1.000	1.000	1.000	1.000
Max	100	100	100	100	100	4.000	4.000	4.000	4.000	4.000
SD	n.a.					1.122	1.118	1.120	1.118	1.120
Skewness						0.000	0.000	n.a.	0.000	0.000
Kurtosis						1.640	-1.360	-1.360	1.640	-1.360
SD/Mean						0.449	n.a.	n.a.	0.447	0.448

Table 2

Global HI results for matrices A0 (left), and A1-A4 (right). Some parameters are not available (n.a.) for homogeneous images (Man. = manual calculation).

For matrix A1 the contrast values showed 75-82% deviations with MaZda (both directions), and ~47% with CGITA. When correlation HI was calculated from matrices A2, A3, and A4, we also saw a significant difference between software-aided and manual calculations. The energy parameter yielded a difference of ~50% with MaZda ([1 0] direction) and nearly 70% with CGITA.

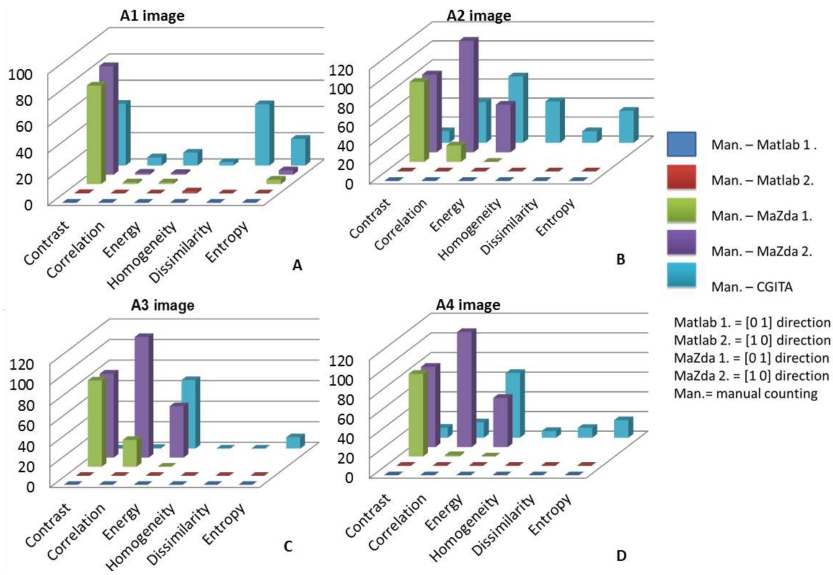

Figure 3

Percentage differences between the values of local parameters (y-axis), provided by the four different software packages, and manual calculation (after 8 level gray scale normalization). Panels A, B, C and D show the results for the four different synthetic images.

Homogeneity and dissimilarity could not be calculated with MaZda. In the case of Matlab (regarding both directions) all HI parameters had a percentage difference from manual calculation less than 0.5%. The eight level, gray scale normalization was not available with InterView Fusion. Homogeneity and entropy showed 5-45% and 10-20% biases, respectively, for all matrices when the 64 level, gray scale normalization was carried out with InterView Fusion (Fig. 4). In case of CGITA, contrast and dissimilarity showed nearly 50% difference for matrix A1, dissimilarity showed a difference greater than 100% for matrix A2, and energy showed a nearly 60% difference for matrices A3 and A4. The largest percentage differences were seen in case of CGITA. Matlab calculations (in both directions) resulted in a maximum difference of 2%. Sixty-four level gray scale normalization was not available in MaZda, and nor contrast, correlation, energy or dissimilarity could be calculated with the built-in modules of InterView Fusion.

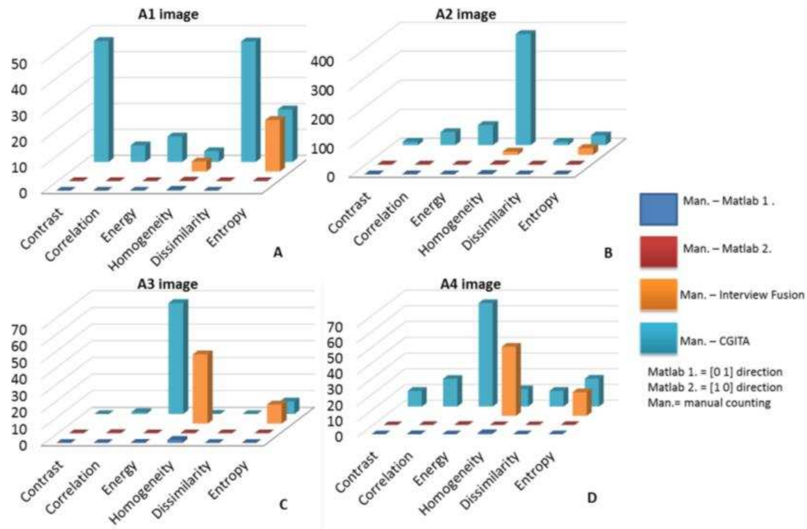

Figure 4

Percentage differences of the values of local parameters (y-axis), provided by the four different software packages from manual calculation (after 64 level gray scale normalization). Panels A, B, C and D show the results for the four different synthetic images.

It can also be stated from Figs 3-4 and Table 2 that all global parameters obtained by the four different software packages were very similar to those calculated manually (<1% deviations), and the values for the four patterns were almost identical, as they must be due to their construction.

In case of local parameters, calculations done with Matlab yielded the smallest difference from the manual calculation. We obtained the most accurate local parameter values using Matlab. Furthermore, for matrices A2, A3, and A4, the local parameters in the horizontal direction gave the same results with Matlab, Mazda and manual calculation, as expected based on the definition of the matrices [43].

For further analysis the absolute values of HIs were also compared for all software and calculation methods. Figs 5, 6 and 7 present each TIs with both normalizations and for all images (A1, A2, A3 and A4). The horizontal axis presents the different software and calculation methods. If a method allowed to generate coM matrix for 2 different directions ([0 1] and [1 0] (which was the case with Manual, Matlab and MaZda), the mean values were also calculated.

From these images we got the same TI values at horizontal direction [0 1] for A2, A3 and A4, corresponding to the definition of these images. Although we found large percentage differences between the software packages, similar monotony (in the order of A1…A4 images) can be seen from Fig. 5 and 6 in case of Manual mean, Matlab mean, MaZda mean, CGITA and InterView Fusion. Entropy and energy (Fig. 7) do not show a similar behavior. The formulas of energy and entropy depend on the *Pij* value of the co-occurrence matrix element rather than the row and column indices (*i,j*), thus gray level normalization had smaller effect on these TIs. This is demonstrated in Fig. 7; the indices from 8 and 64 level normalization are very similar. Fig. 8 presents the percentage difference (PD) of TIs between 8 and 64 gray level normalization for three calculation methods: Manual mean, Matlab mean and CGITA.

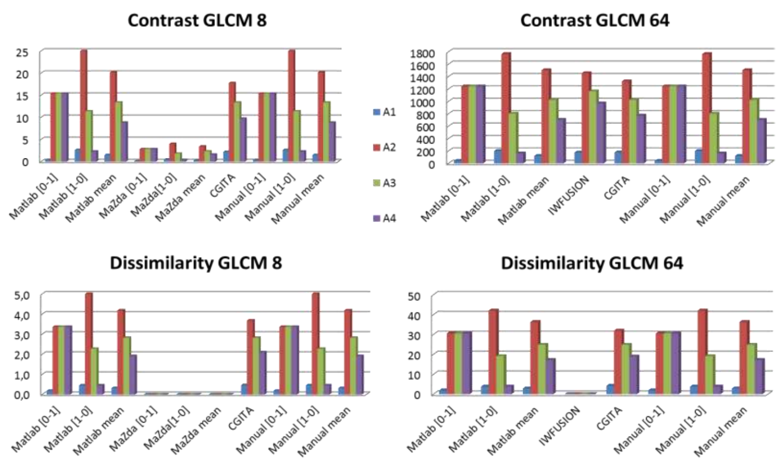

Figure 5

Comparison of contrast and dissimilarity between all software and calculation methods, with both normalizations (8 and 64), and for all images (A1, A2, A3 and A4). The [0 1] and [1 0] symbols stand for the horizontal and vertical directions, respectively.

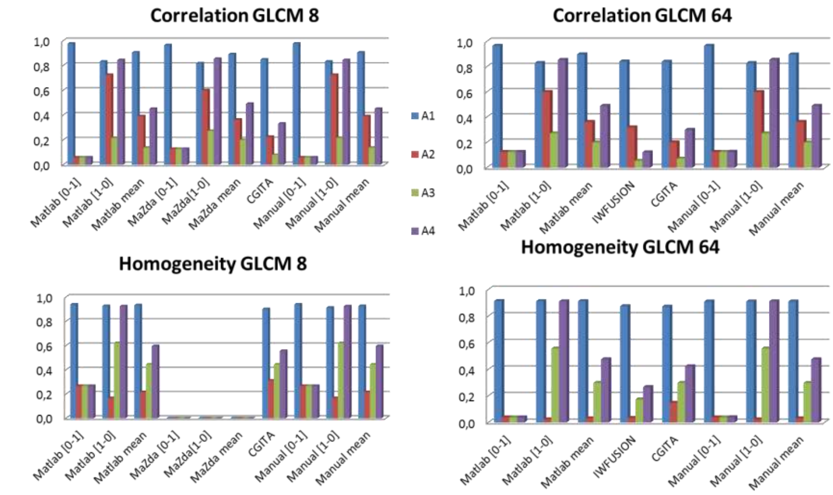

Figure 6

Comparison of correlation and homogeneity between all software and calculation methods, with both normalizations, and for all images

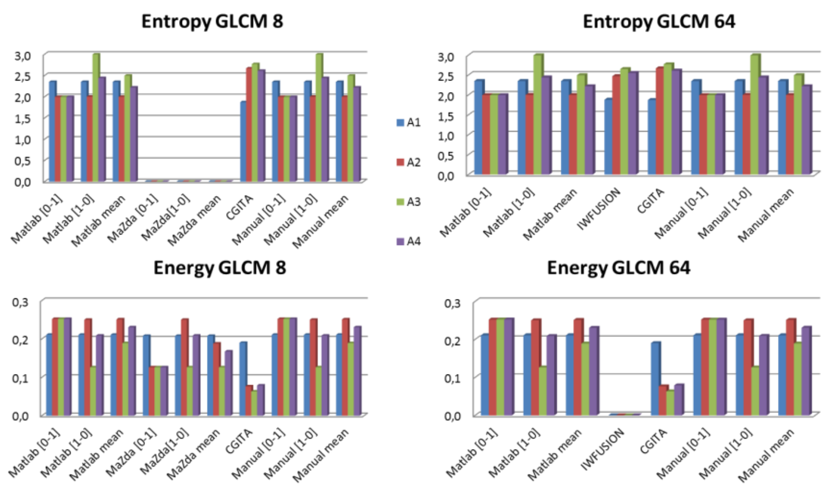

Figure 7

Comparison of energy and entropy between all software and calculation methods, with both normalizations, and for all images

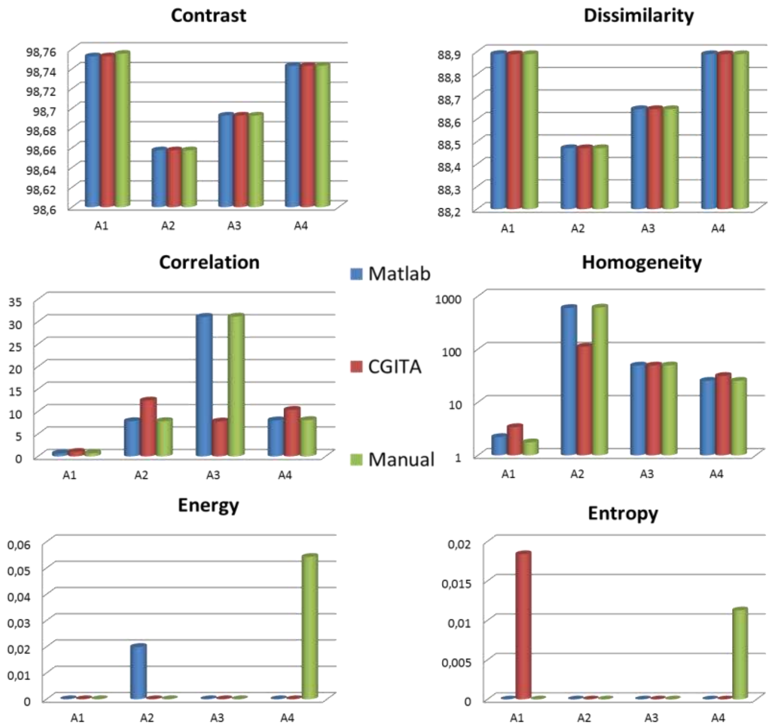

Figure 8
Percentage difference of selected TIs between the 8 and 64 gray level normalization in case of all images, for three calculation methods: Manual mean, Matlab mean and CGITA

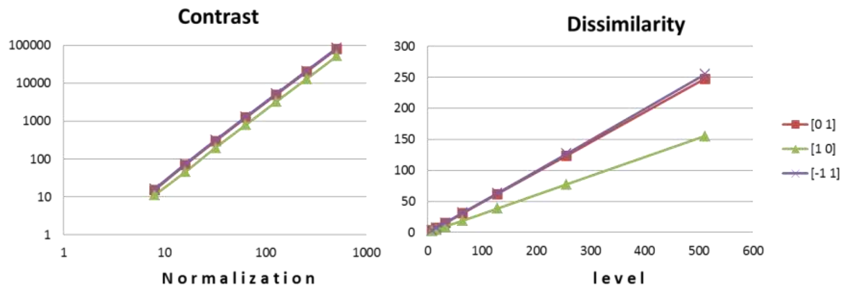

Figure 9
Dependence of contrast and dissimilarity on the normalization level (8 to 512), calculated from the A3 matrix in 3 directions ([0 1], [1 0], [-1 1]. The axes of the contrast plot are scaled in log-log format, allowing for better visualization of the power relationship between the contrast and the normalization level.

MaZda and InterView Fusion are missing from this comparison, because they use a fixed number of gray levels (8 or 64). In Fig. 8 contrast and dissimilarity show very similar tendencies which is due to the similarity of their formulas (Table 1), including the same factor (*i-j*) in the numerator. It can also be noted that the PDs of contrast and dissimilarity are exactly the same for the three calculation methods. The tendency of homogeneity is reversed, since its formula contains the factor (*i-j*) in the denominator. The values of energy and entropy do not depend on the normalization level, as shown in Fig. 7.

We also analyzed the gray level dependences more details in the case of the contrast and the dissimilarity. Fig. 9 shows the TIs from the A3 matrix while the normalization level changed from 8 to 512. The trend is linear and quadratic for dissimilarity and contrast, respectively, corresponding to the power of the (*i-j*) factor in their formulas.

3.2 Results of Reliability Analysis of the Heterogeneity Parameters

Fig. 10 shows the 22 texture index values calculated by the GLCM_feature tool (upper panel) for the histological slice of the brain, and Michelangelo's painting.

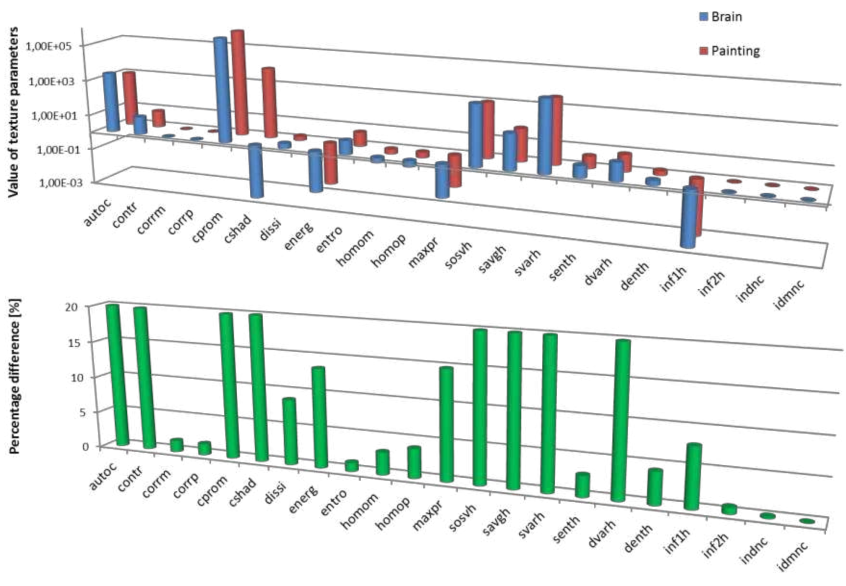

Figure 10

Values of the 22 texture parameters for the histological section of the brain and Michelangelo's painting, and the related percentage differences of the TIs. In the latter case, the scale of the vertical axis is set arbitrarily to 20%, allowing better visualization of the smaller values.

The lower panel presents the percentage differences of the related TIs between the two images. Interestingly, from the 22 co-occurrence based texture parameters, 12 indices did not show relevant differences (less than 10%: corm, corrp, entropy, homom, homop, senth, denth, inf2h, indnc, idmnc, dissi and inf1h). In addition, 5 indices depicted differences in the range of 10-20% (contr, cprom, energy, maxpr, dvarh), and only 5 parameters presented more than 20% dissimilarities (autoc, cshad, sosvh, savgh, svarh). Selecting the contrast, correlation, energy, homogeneity, dissimilarity, and entropy parameters, we also calculated the percentage differences between the two images at distinct gray levels (Fig. 11). This graph confirms that the TI differences did not change when the gray level number was more than 64. In other words, at least 64 normalization levels need to be used for reliable, stable results. These findings suggest that images with similar overall appearance but with different content may have texture indices with very similar values.

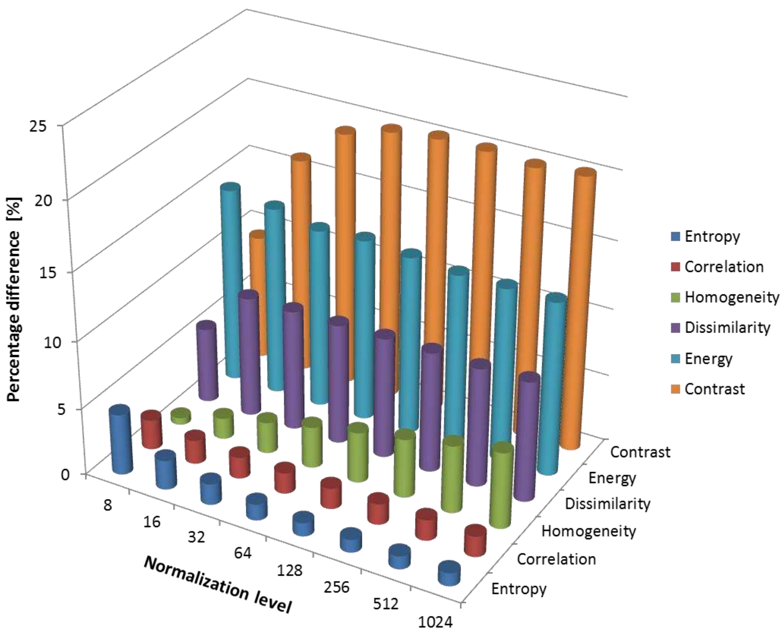

Figure 11

Percentage differences of contrast, correlation, energy, homogeneity, dissimilarity and entropy between the two images, using different numbers of gray levels (from 8 to 1024)

4 Discussion

Texture analysis studies provide additional quantitative information about medical images, which may help with the characterization and differentiation of healthy and pathological areas, and with grading [44, 45, 46, 47]. Several free and commercial software tools such as Matlab, MaZda, InterView Fusion, CGITA, TexRad and ImageJ implement the calculation of heterogeneity parameters; however, in many cases, the implemented calculation algorithms are unknown [8, 10, 15, 29, 48, 49].

In our work, we studied the texture calculation mechanisms of four biomedical software packages; we compared the heterogeneity parameters provided by Matlab, MaZda, CGITA, and InterView Fusion to those calculated manually.

Our aim was to compare various heterogeneity indices, and to highlight possible reasons for the differences. We used 4+1 synthetic images, and we calculated local and global heterogeneity indices after both 8 and 64 level gray scale normalization. Global parameters (histogram-based calculations, Table 2) by all four programs were very similar to the values calculated manually (<0.5%) in case of all five matrices (A0-A4).

We found more differences among the results of local parameters (Figs 3-4). The smallest percentage difference was seen between Matlab and manual calculations for both gray scale normalization settings, in both [0 1] and [1 0] directions. For matrices A2, A3, and A4, Matlab, MaZda and manual calculation yielded similar local parameter values, when choosing horizontal direction of calculation. An explanation for the HI differences may be that the (undocumented) way of averaging when forming multidirectional co-occurrence matrices may also differ. The formulas used for the manual calculations may also differ from those implemented in the software packages tested, although their names may be the same.

For instance, in CGITA, based on the program code, it is clear that the horizontal and vertical calculations are done in a single step, thus a certain averaging takes place [46]. CGITA does not use the built-in Matlab functions for the co-occurrence matrix calculations. InterView Fusion is not an open-source software; thus the particular algorithms are unknown, but based on personal communication we suspect that the co-occurrence matrix calculations are done in 3 dimensions. Not both levels of normalization (8 and 64) are available in all the packages, nor is the definition of the [0 1], [1 0] directions the same, thus the values of heterogeneity parameters provided by the different programs are not comparable. In addition, we analyzed how the selected HIs depend on normalization levels. Our results indicate that contrast and dissimilarity behave alike, because they both include the same factor (i-j) in the numerator (Fig. 5). On the other hand, energy and entropy do not depend on the normalization level. In general, similar monotony (in the order of A1…A4 images) of the texture indices can be seen in

Fig. 5-7, independently of the software or methods applied. In the next step we focused on the reliability of HIs based on two selected images (Fig. 2), a famous painting and a histological brain slice. These two segmented images have the same pixel size and very similar shape, but the actual patterns and textures are quite different. From the calculated 22 TIs, only 5 parameters depict more than 20% dissimilarities, even though we used two images with different texture properties (Fig. 10). Based on our analysis, at least 64 normalization levels need to be used for reliable results (Fig. 11).

Conclusion

CGITA, InterView Fusion, Matlab and MaZda calculate the co-occurrence based heterogeneity indices differently, thus, the results of these calculations are not comparable. Our comparison also underlines that, in medical multi-center studies it is especially critical to use the same software package for all patients. Furthermore, it would be necessary to accept and implement a standard algorithm in such software, so that the results would be truly comparable among different programs. Standardized texture analysis algorithms would then better aid medical diagnostics, therapy planning, follow-up studies and they might provide a non-invasive classification of pathological lesions as well.

Our study also confirmed that some TIs can be very similar in spite of the images having different texture. It means that a single parameter cannot properly characterize a segmented area and using a group of several textural parameters may be more accurate. Some texture parameters are not reliable when distinguishing different changes in patterns, so texture analysis should be clinically validated and used with caution.

Acknowledgements

This work was supported by the „Richter Gedeon Talentum Alapítvány”.

References

[1] Yip SS, Aerts HJ (2016) Applications and limitations of radiomics, Phys. Med. Biol. 61:150-166

[2] Lerski RA, Straughan K, Schad LR, Boyce D, Blüml S, Zuna I (1993) MR image texture analysis - an approach to tissue characterization. Magn. Reson. Imaging. 11: 873-887

[3] Ahmadvand A, Daliri MR (2016) Invariant texture classification using a spatial filter bank in multi-resolution analysis. Image Vis Comput 45:1-10

[4] Maani R, Kalra S, Yang Y-H (2013) Noise robust rotation invariant features for texture classification. Pattern Recognit 46:2103-2116

[5] Haralick RM, Shanmugam K, Dinstein I (1973) Textural features for image classification. IEEE Trans Syst Man Cybern 3:610-621

[6] Brooks FJ (2013) On some misconceptions about tumor heterogeneity quantification. Eur J Nucl Med Mol Imaging 46: 1292-1294

[7] Strzelecki M, Szczypinski P, Materka A, Klepaczko A (2013) A software tool for automatic classification and segmentation of 2D/3D medical images. Nucl Instruments Methods Phys Res Sect A Accel Spectrometers, Detect Assoc Equip. doi: 10.1016/j.nima.2012.09.006

[8] Szczypinski PM, Strzelecki M, Materka A, Klepaczko A (2009) MaZda - a software package for image texture analysis. Comput Methods Programs Biomed 94:66-76

[9] Szczypinski PM, Strzelecki M, Materka A (2007) Mazda - a software for texture analysis. In: 2007 International Symposium on Information Technology Convergence (ISITC 2007). IEEE, pp. 245-249

[10] Fang Y-HD, Lin C-Y, Shih M-J, et al (2014) Development and evaluation of an open-source software package „CGITA” for quantifying tumor heterogeneity with molecular images. Biomed Res Int 2014:248505

[11] Available from:

https://github.com/cmci/GLCM2/blob/master/src/main/java/emblcmci/glcm/GLCM_TextureToo.java [accessed 2018. 03. 20]

[12] Available from: https://imagej.nih.gov/ij/plugins/download/GLCM_Texture.java [accessed 2018. 03. 20]

[13] Baecker V (2010) Workshop: Image processing and analysis with ImageJ and MRI Cell Image Analyzer. Image (Rochester, NY) 1-93

[14] Abramoff MD, Magalhães PJ, Ram SJ (2004) Image processing with ImageJ. Biophotonics Int. 11:36-42

[15] Available from: http://www.mathworks.com/help/images/texture-analysis-1.html [accessed 2017. 03. 20]

[16] Pantic I, Nesic Z, Paunovic Pantic J, et al (2016) Fractal analysis and Gray level co-occurrence matrix method for evaluation of reperfusion injury in kidney medulla. J Theor Biol 397:61-7

[17] J. E. Cabrera: Texture Analyzer https://imagej.nih.gov/ij/plugins/texture.html [accessed 2017. 03. 20]

[18] Wang XC, Mo JL, Ouyang H, et al (2015) Squeal noise of friction material with groove textured surface: an experimental and numerical analysis. J Tribol 138:021401

[19] Bastos FS, Oliveira EA, Fonseca LG, et al (2016) A FEM-based study on the influence of skewness and kurtosis surface texture parameters in human dental occlusal contact. J Comput Appl Math 295:139-148

[20] Yan D, de Beurs KM (2016) Mapping the distributions of C3 and C4 grasses in the mixedgrass prairies of southwest Oklahoma using the Random Forest classification algorithm. Int J Appl Earth Obs Geoinf 47:125-138

[21] de Albuquerque M, Anjos LG V, Maia Tavares de Andrade H, et al (2016) MRI texture analysis reveals deep gray nuclei damage in amyotrophic lateral sclerosis. J Neuroimaging 26:201-6

[22] Yan L, Liu Z, Wang G, et al (2015) Angiomyolipoma with minimal fat: differentiation from clear cell renal cell carcinoma and papillary renal cell carcinoma by texture analysis on CT images. Acad Radiol 22:1115-21

[23] Orphanidou-Vlachou E, Vlachos N, Davies NP, et al (2014) Texture analysis of T1 - and T2 - weighted MR images and use of probabilistic neural network to discriminate posterior fossa tumours in children. NMR Biomed 27:632-9

[24] MacKay JW, Murray PJ, Kasmai B, et al (2016) MRI texture analysis of subchondral bone at the tibial plateau. Eur Radiol 26:3034-3045

[25] Daginawala N, Li B, Buch K, et al (2016) Using texture analyses of contrast enhanced CT to assess hepatic fibrosis. Eur J Radiol 85:511-517

[26] Liu W, Raben N, Ralston E (2013) Quantitative evaluation of skeletal muscle defects in second harmonic generation images. J Biomed Opt 18:26005. doi: 10.1117/1.JBO.18.2.026005

[27] Michoux N, Guillet A, Rommel D, et al (2015) Texture analysis of T2-weighted MR images to assess acute inflammation in brain MS lesions. PLoS One 10:e0145497. doi:10.1371/journal.pone.0145497

[28] Wang H-M, Cheng N-M, Lee L-Y, et al (2016) Heterogeneity of 18 F-FDG PET combined with expression of EGFR may improve the prognostic stratification of advanced oropharyngeal carcinoma. Int J Cancer 138:731–738

[29] Available from: http://www.mediso.hu/products.php?fid=1,10,6&pid=67&feature=all [accessed 2018. 03. 20]

[30] Tixier F, Hatt M, Valla C, et al (2014) Visual versus quantitative assessment of intratumor 18FFDG PET uptake heterogeneity: prognostic value in non-small cell lung cancer. J Nucl Med55:1235-41

[31] Orlhac F, Soussan M, Chouahnia K, et al (2015) 18F-FDG PET-derived textural indices reflect tissue-specific uptake pattern in non-small cell lung cancer. PLoS One 10:e0145063 . doi: 10.1371/journal.pone.0145063

[32] Ganeshan B, Abaleke S, Young RCD, et al (2010) Texture analysis of non-small cell lung cancer on unenhanced computed tomography: initial

evidence for a relationship with tumour glucose metabolism and stage. Cancer Imaging 10:137-43

[33] Hayano K, Kulkarni NM, Duda DG, et al (2016) Exploration of imaging biomarkers for predicting survival of patients with advanced non–small cell lung cancer treated with antiangiogenic chemotherapy. Am J Roentgenol 206:987-993 . doi: 10.2214/AJR.15.15528

[34] Ahn SY, Park CM, Park SJ, et al (2015) Prognostic value of computed tomography texture features in non–small cell lung cancers treated with definitive concomitant chemoradiotherapy. Invest Radiol 50:719-725

[35] Chicklore S, Goh V, Siddique M, et al (2013) Quantifying tumour heterogeneity in 18F-FDG PET/CT imaging by texture analysis. Eur J Nucl Med Mol Imaging 40:133-140

[36] Available from:

https://library.med.utah.edu/WebPath/HISTHTML/NEURANAT/CNS016A.html [accessed 2018. 03. 20]

[37] Available from: https://en.wikipedia.org/wiki/The_Creation_of_Adam#/media/File:Creaci%C3%B3n_de_Ad%C3%A1n_(Miguel_%C3%81ngel).jpg, [accessed 2018. 03. 20]

[38] Suk I, Tamargo RJ (2010) Concealed neuroanatomy in Michelangelo's separation of light from darkness in the Sistine chapel. Neurosurg. 66: 851-861

[39] Zhenjiang L, Yu M, Hongsheng L, Gang Y, Honglin W, Baosheng L (2016) Differentiating brain metastases from different pathological types of lung cancers using texture analysis of T1 postcontrast MR. Magn. Reson. Med. 761410-1419

[40] Available from: https://www.mathworks.com/matlabcentral/fileexchange/22354 [accessed 2018. 03. 20]

[41] Soh L, Tsatsoulis C (1999) Texture Analysis of SAR Sea Ice imagery using gray level cooccurrence matrices. EEE Trans. Geosci. Remote Sens. 372

[42] Available from: http://murphylab.web.cmu.edu/publications/boland/boland_node26.html [accessed 2018. 03. 20]

[43] Castellano G, Bonilha L, Li LM, Cendes F (2004) Texture analysis of medical images. Clin Radiol 59:1061-1069

[44] Peikari M, Gangeh MJ, Zubovits J, et al (2016) Triaging diagnostically relevant regions from pathology whole slides of breast cancer: a texture based approach. IEEE Trans Med Imaging 35:307-315

[45] Rodriguez M, Rehn SM, Nyman RS, et al (1999) CT in malignancy grading and prognostic prediction of non-Hodgkin's lymphoma. Acta Radiol 40:191-7

[46] Henry W (2010) Texture analysis methods for medical image characterisation. Biomedical Imaging. InTech. https://cdn.intechopen.com/pdfs-wm/10175.pdf [accessed 2018.03. 20]

[47] Available from: https://www.ucl.ac.uk/nuclear-medicine/research/researchabstracts/texrad [accessed 2018. 03. 20]

[48] Available from: http://texrad.com/papers-presentations/ [accessed 2018. 03. 20]

[49] Available from: https://code.google.com/archive/p/cgita/ [accessed 2018. 03. 20]

A Laboratory on Visualization of Electrostatic and Magnetic Fields

Kenzhekhan Kabylbekov, Khadisha Abdrakhmanova, Gaukhar Omashova, Pulat Saidakhmetov, Turlan Sultanbek, Nurzhamal Dausheyeva

M. Auezov South Kazakhstan state University, Tawek Khan Avenue, 5, 160012, Shymkent, Kazakhstan, e-mail: omashovag@mail.ru

Abstract: This article presents calculations and visualization of an electric field of a point charge (equipotential lines) and systems of oppositely charged threads, of magnetic field lines of a thin long and straight current-carrying conductor, magnetic field lines inside a cylindrical conductor with evenly distributed current made using the MATLAB language. Calculations of an electric field and potential of a point charge as a function of a distance are provided as well as a potential of a system of oppositely charged threads, magnetic induction of a thin, long current-carrying conductor as a function of a distance and magnetic induction inside the cylindrical conductor are performed. The graphs of these dependencies are drawn.

Keywords: cylindrical conductor; electric field; equipotential lines; magnetic induction; point charge

1 Introduction

At present practically all educational institutions of Kazakhstan are provided with computer hardware and software, interactive boards and internet. Almost all teachers have finished language and computer courses of professional development. So there are all conditions for using computer training programs and models for performing computer laboratory works. Over several years we conducted work on organizing physics usage in the computer laboratory utilizing theresources of the Fizikon Company [1] as well as the resources developed at Al-Farabi Kazakh National University [2]. This topic in general is extremely relevant in the area of modern research. In particular, the problem of the organization of performance of the laboratory work "Visualization of electrostatic and magnetic fields in MATLAB language" was partly covered in the survey of V. P. Dyakonov "MATLAB training course" [34], also in relevant works of H. K. Lam[35], R.-E. Precup[36], A. Ürmös, Z. Farkas[37], J. Saadat, P. Moallem [38], etc. The article is organically continuing the research line on the organization of laboratory works by the authors K. Kabylbekov, Kh. Abdrakhmanova, Zh. Abekova, R. Abdraimov, B. Ualikhanova, T. Tagaev, A. Bitemirova, M. Berdieva, etc. [3-33]. Some of worksheet templates for computer laboratory works are introduced in the educational process of our university and schools of Southern Kazakhstan [3-32]. Students of the specialties 5B060400 and 5B011000-physics are successfully mastering the discipline "Computer modeling of physical phenomena" which is the logical continuation of the disciplines "Information technologies in teaching physics" and "Use of electronic textbooks in teaching physics". The aim of this discipline is to study and learn the program language of the MATLAB [33] system, to help the students get acquainted with its huge opportunities during the modeling and visualization of physical processes. So, the article is devoted to the methodology of organizing the given laboratory works "Calculation and visualization of an electric field of a point charge", "Calculation and visualization of an electric field of a system of two oppositely charged threads", "Calculation and visualization of a magnetic field of a thin and long current-carrying conductor" and "Calculation and visualization of a magnetic field of a cylindrical current-carrying conductor" in the MATLAB language.

2 Results and Discussion

2.1 Laboratory Work № 1. "Calculation and Visualization of an Electric Field of a Point Charge" in the MATLAB Programming Language

The aim of the work: to work out the program of calculation and visualization of an electric field of a point charge.

We will draw equipotential lines of ~~an~~ electric field of a point charge in three-dimensional space and in ~~p~~rojection on the XY plane.

The potential of electric field of a point charge is determined by the expression $\varphi = \frac{1}{4\pi\varepsilon_0}\frac{q}{r}$; Its electric field is determined by the expression $E = \frac{1}{4\pi\varepsilon_0}\frac{q}{r^2}$;

where ε_0 is the electric constant, q is the quantity of a point charge, r is the distance from the charge to the point where the electric field is calculated.

Calculation and visualization program

```
>>x=-6:0.1:6; %input coordinate vectors
>>y=-6:0.1:6; %input coordinate vectors
```

>>q=9*10.^-9; %input a charge quantity

>>e0=8.85*10.^-12; %input an electric constant

>> [X,Y]=meshgrid(x,y); %setting of a grid at knots of which *x иy* coordinates are recorded

%(arrays *X* and *Y).*

>>a=0.5; %input a coordinate

>>r2 = ((X + a).^ 2 + Y.^ 2).^0.5; %calculation of a distance

>>r1 = ((X - a).^ 2 + Y.^ 2).^0.5; %calculation of a distance

>>r=sqrt(r1.^2+r2.^2); %calculation of a distance

>>Z=(q./(4*pi*e0*r)); %calculation of a potential

>>contour3(X,Y,Z,100); %drawing the lines of levels

>>xlabel('X,m') %input the name of the axis

>>ylabel('Y,m') %input the name of the axis

>>title('lines of equal potential′) %input the name of the graph

The result of the program is shown in Figure 1.

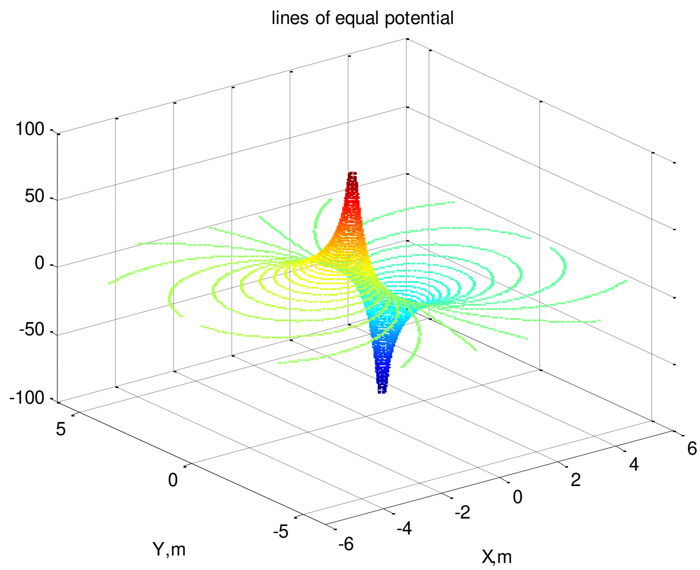

Figure 1
Equipotential lines of a point charge electric field

>>view([0 0 10]) %projection of lines on the plane X-Y

The result of this projection is shown in Figure 2.

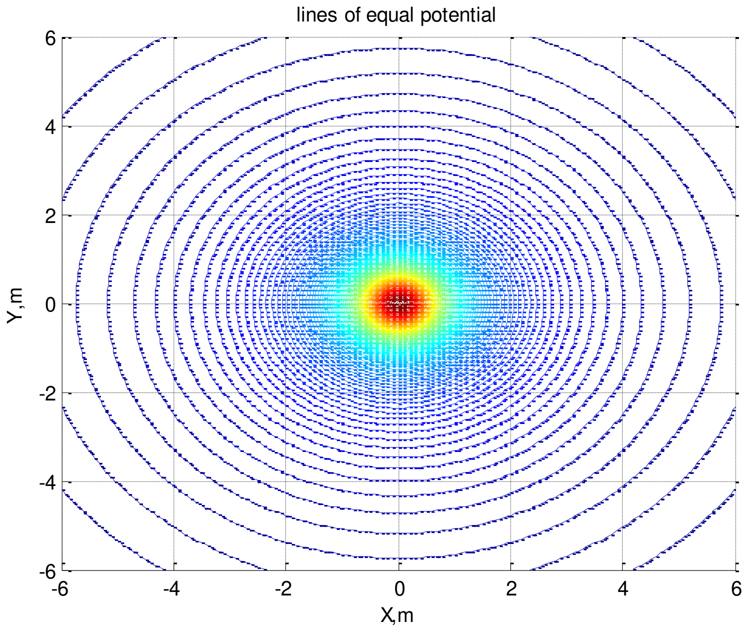

Figure 2
Equipotential lines of a point charge electric field in the projection on the plane X-Y

Equipotential lines of a point charge electric field make concentric circles with density decreasing as the distance from the charge increases.

```
>> E=(q./(4*pi*e0*r.^2)); % calculation of electric field
>> plot(r,E,'k-') %visualization
>> grid on %drawing of  the coordinate grid
>> xlabel('r, sm') %input the name of the axis
>> ylabel('E, V/sm') %input the name of the axis
>> title('E=F(r)') %input the name of the graph
```

The result of the calculation is shown in Figure 3.

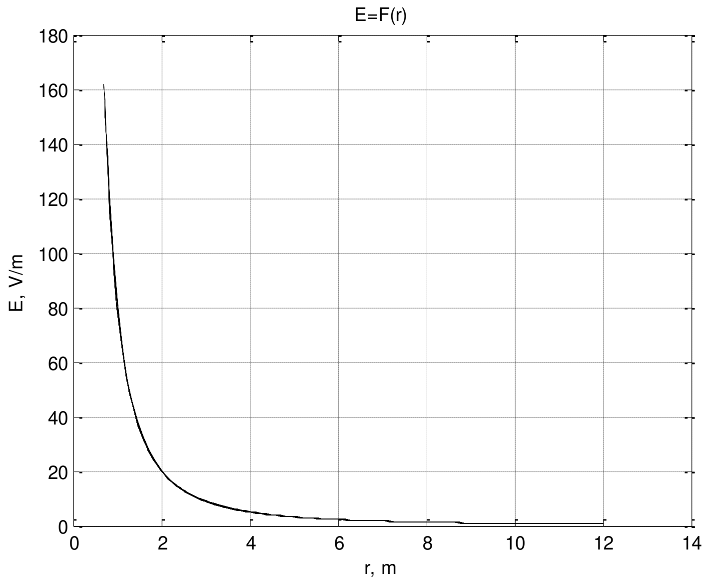

Figure 3
The electric field of a point charge versus distance

```
>> fi=(q./(4*pi*e0*r)); % calculation of a potential
>> plot(r,Z,'k-') % visualization (plotting the graph)
>> xlabel('X,m') % input the name of the axis
>>ylabel('Y,m') % input the name of the axis
>> grid on%drawing of the coordinate grid
```

The result of the calculation is shown in Figure 4.

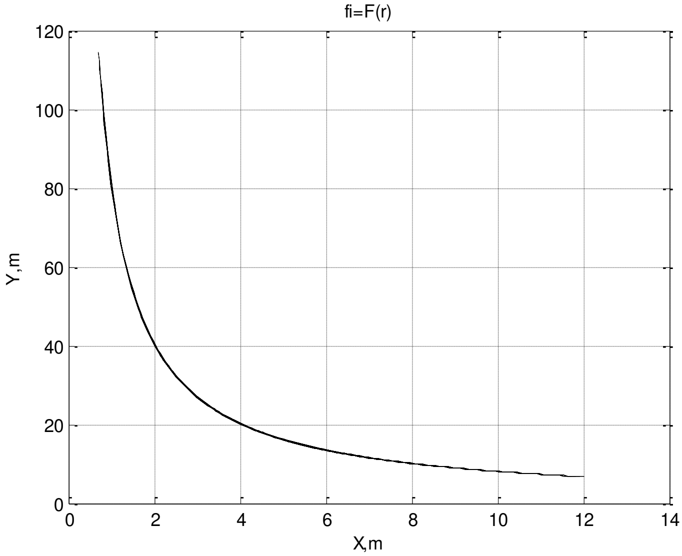

Figure 4
The potential of a point charge electric field versus distance

Comparison of the curves of the electric field (Fig. 3) and potential (Fig. 4) versus distance shows that with increasing of the distance from the point charge its electric field decreases quicker than its potential. At the end of the laboratory work students do this experiment independently for the charge with different quantity and sign.

2.2. Laboratory Work № 2. "Calculation and Visualization of an Electric Field of a System of Two Oppositely Charged Threads" in the MATLAB Program Language

The aim of the work: to work out the program of calculation and visualization of an electric field of a system of two oppositely charged threads.

There are two parallel and infinitely long threads which are evenly and oppositely charged with a linear charge density $+\tau$ and $-\tau$ to be in air (ε=1) (Figure 5). We will draw the diagram of these threads in the cross section plane (the threads are represented by two dots at the distance $2a$ from each other).

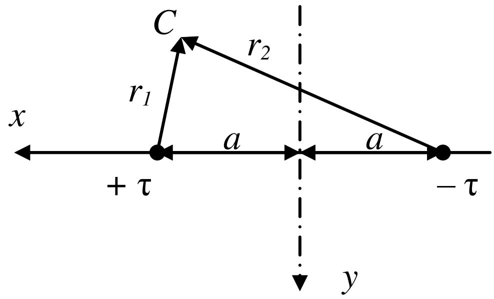

Figure 5
The diagram of the charged threads in the cross section plane

The potential of the system at the point C is equal to the sum of potentials of each charged thread's electric field:

$$\varphi(C) = \varphi_+ + \varphi_- = +\frac{\tau}{2\pi\varepsilon_0\varepsilon}\ln(r_1) - \frac{\tau}{2\pi\varepsilon_0\varepsilon}\ln(r_2) + A = \frac{\tau}{2\pi\varepsilon_0\varepsilon}\ln\left(\frac{r_1}{r_2}\right) + A$$

where τ is the linear charge density of the thread, ε_0 is the electric constant, ε is the dielectric permeability of a medium, r is the module of the radius vector of a point where the potential of an electric field is calculated.

If to accept that $\varphi(x=0) = 0$, i.e. on an axis of symmetry the potential is zero, then A=0. Now we will define the equation of equipotential surfaces. On these surfaces $r_2/r_1=k$ = const. Here k is the parameter of equipotential lines family in the plane of the figure.

We will express r_2 and r_1 in the Cartesian coordinates and derive the equipotential equation in a canonical form relative to coordinates x and y.

$$r_2= ((x+ a)^2 + y^2)^{0,5};\ r_1= ((x–a)^2 + y^2)^{0,5}$$

$$(x+a)^2 + y^2 = k^2 (x–a)^2 + k^2y^2$$

$$(x+a)^2 – k^2 (x – a)^2 + y^2(1 –k^2)= 0$$

$$x^2(1 –k^2) + 2ax(1 +k^2) + a^2(1 – k^2) + y^2(1 – k^2) = 0$$

$$x^2 + 2ax(1 + k^2)/(1 – k^2) + y^2 + a^2 = 0$$

$$(x+a(1 + k^2)/(1 – k^2))^2 + y^2 = (a(1 + k^2)/(1 – k^2))^2 – a^2 = (2ak/(1 – k^2))^2$$

Here we get the equation of a circle in a canonical form:

$$(x–s)^2 + y^2 = R^2(1)$$

where $s=a(k^2+1)/(k^2 – 1)$ is the coordinate of a circle center. $R=a|2k /(1 – k^2)|$ is the circle radius.

We have received expressions for the coordinate of the center and for the radius of the equipotential line with given parameter k, where $k = \exp\left(2\pi\varepsilon_0\varepsilon\phi / \tau\right)$.

According to the equation (1) the lines of equal potential make circles, and the surfaces of equal potential make circular cylinders with geometrical axes displaced relative electric axes. One of these surfaces degenerates to the plane with zero potential (at $k = 1$: $s \rightarrow \pm\infty$; $r \rightarrow \infty$).

The lines of the electric field make the circle arches emerging from the axis with a positive charge and ending on the axis with a negative charge.

If to cut the family of equipotential surfaces with parallel planes which are perpendicular to the charged axes, then in each plane there will be the same picture of lines. The fields having such property are called plane-parallel (or they are called two-dimensional fields).

Defining the picture of the field and use of the uniqueness theorem consequence creates many new tasks to be solved. The number of tasks is determined by the number of pairs of equipotential surfaces, which can be considered as surfaces of conductors.

Let us consider the most important special cases of such tasks.

Calculation and visualization program

```
>>t=2*10.^-9'; % input the linearcharge density of the thread
>>x=-6:0.1:6; % input the vector of an x coordinate
>>y=-6:0.1:6; % input  the vector of an y coordinate
>> [xx,yy]=meshgrid(x,y); %drawing the grid with coordinates x and y at its knots
%(arrays X and Y).
>>a=0.5; % input of a parameter
>>r2 = ((xx + a).^ 2 + yy.^ 2).^0.5; %calculation of the distance from the positively charged  %thread
>>r1 = ((xx - a).^ 2 + yy.^ 2).^0.5; %calculation of the distance from the negatively charged  %thread
>>e0=8.85*10.^-12; %  input  an electric constant
>>zx=(t./(2*pi*e0))*log(r1./r2); %calculation of a system's potential
>>contour3(xx,yy,zx,100); %drawing the lines of  levels
>>xlabel('X,m')
ylabel('Y,m')
```

zlabel(‘fi, V’)

title(title('lines of equal potential′) %input the name of the graph

The result of calculations are shown in Figure 6.

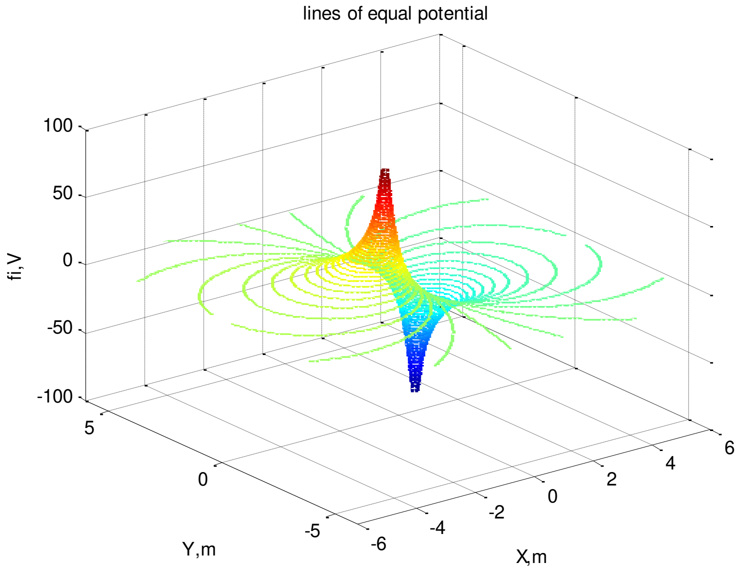

Figure 6

The result of visualization of the field of two oppositely charged threads in three-dimensional space

>>view([0 0 10]) % projection of the field on the *X*-*Y* plane

The result of the projection is presented in Figure 7.

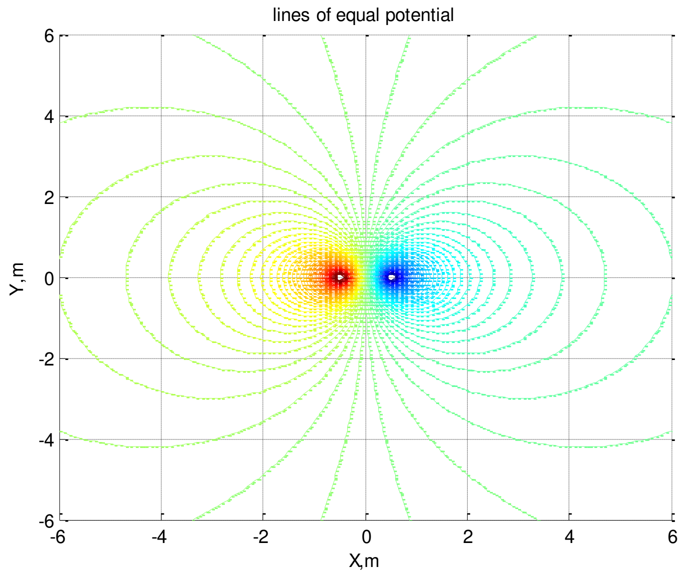

Figure 7
The result of visualization of the field of two oppositely charged threads in the projection on the *X*-*Y* plane

At the end of the laboratory work students do experiment independently by changing the density of charges and the distance between threads.

2.3 Laboratory Work №3. "Calculation and Visualization of a Magnetic Field of an Infinitely Long and Thin cuRrent-Carrying Conductor" in the MATLAB Program Language

The aim of the work: To work out the program of calculation and visualization of a magnetic field of an infinitely long and thin current-carrying conductor.

Let an electric current of I = 2 A to flow through an infinitely long and thin conductor. It is necessary to calculate the magnetic induction around the conductor as a function of the distance b from the center of its axis.

Induction of a magnetic field of an infinitely long current-carrying conductor as a function of the distance b from the center of its axis is calculated by the formula:

$$B = \frac{2\mu_0 I}{4\pi b}$$

where μ_0 is the magnetic constant, I is the electric current, b is the distance between the center of the conductor axis and the point where the magnetic induction is calculated.

Calculation and visualization program

```
>> x=-6:0.1:6;% input  the vector of an x coordinate
>>y=-6:0.1:6; % input  the vector of an y coordinate
>> I=2; % input  the current magnitude
>> m0=4*pi*10e-7; % input  the magnetic constant
>> r=sqrt(x.^2+y.^2);%calculation  r
>> b=0:0.1:1; % input  the distance vector
>> B=2*m0*I./(4*pi*b); %calculation of the magnetic induction magnitude
>> plot(b,B,'k-') %visualization (plotting the picture of a magnetic field)
>> grid on%drawing the coordinate grid
>> xlabel('b, m') %input the name of the axis
>> ylabel('B, Tl') %input the name of the axis
>> title('B=F(b)') %input the name of the graph
```

The result of the calculation is given in Figure 8.

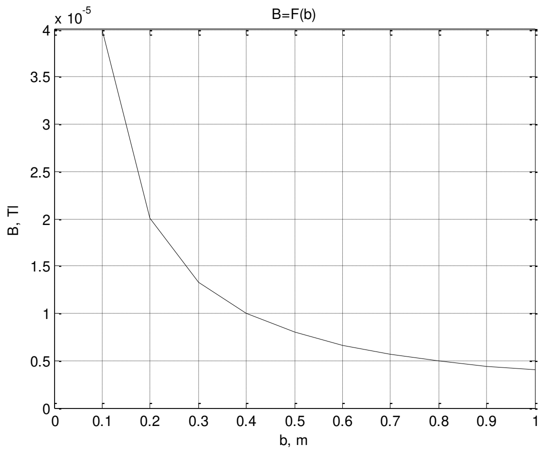

Figure 8

Magnetic induction of an infinitely long current-carrying conductor as a function of the distance *b* from the center of its axis

Figure 8 shows that the magnetic induction of the thin and infinitely long current-carrying conductor decreases as $1/b$ with increase of the distance b from the conductor axis.

The program of visualization of magnetic field lines in colored three-dimensional space:

>> [X,Y]=meshgrid(x,y)% drawing the grid with coordinates *x* and *y* at its knots %(arrays *X* and *Y).*

>> r2 = ((X + 0.2).^ 2 + Y.^ 2).^0.5; %calculation of the distance

>> r1 = ((X - 0.2).^ 2 + Y.^ 2).^0.5; %calculation of the distance

>> r=sqrt(r1.^2+r2.^2); %calculation of the distance

>> Z=2*m0*I./(4*pi*r); %calculation of the magnetic induction

>> contour3(X,Y,Z,100); %drawing the lines of levels

>> xlabel('x,m') %input the name of an *x* axis

>> ylabel('y, m') %input the name of an *y* axis

>> zlabel('B, Tl') %input the name of an *z* axis

>> grid on%input the coordinate grid

The result of visualization is shown in Figure 9.

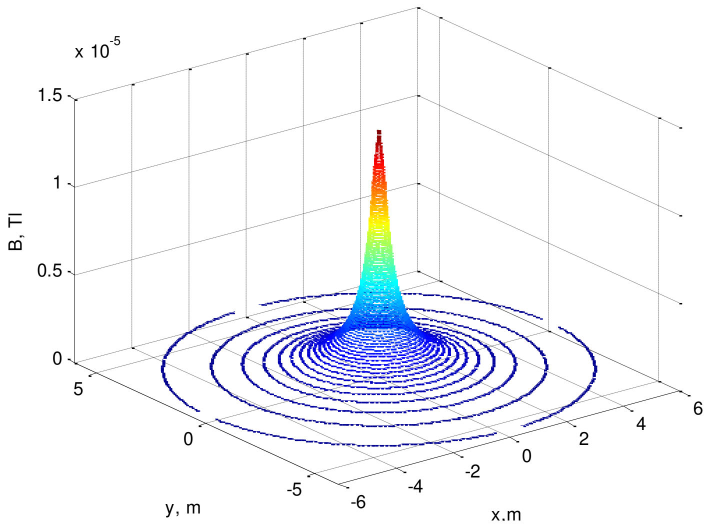

Figure 9

The lines of the magnetic induction of a thin and long current-carrying conductor

>> view([0 0 100]) %projection on *X-Y* plane of support

>> gtext('B') %input the text in the figure

The result of the projection is presented in Figure 10.

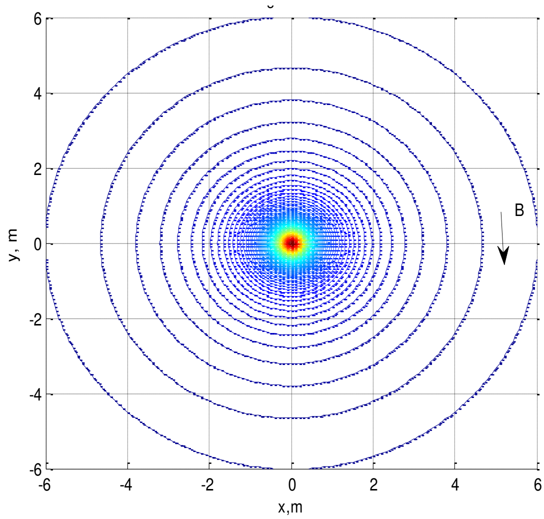

Figure 10
The projection of lines of the magnetic induction of a thin and long current-carrying conductor on *X-Y* plane

Figure 10 shows that the magnitude of the magnetic induction of a long straight current-carrying conductor decreases with increase of the distance *b,* namely from $4\cdot10^{-5}$ T at b=0.1m to $0.5\cdot10^{-5}$ T at b=0.8m. Figures 9, 10 show that lines of magnetic induction are concentric circles around the center of the conductor. The density of lines decreases with removal from the conductor that verifies the idea that induction magnitude decreases with increase of the distance from the conductor axis.

At the end of laboratory work students do experiments independently by changing the magnitude and direction of the current through the conductor.

2.4 Laboratory Work № 4. "Calculation and Visualization of a Magnetic Field of a Long Cylindrical Current-Carrying Conductor" in the MATLAB Program Language

The aim of the work: To work out the program of calculation and visualization of a magnetic field inside and outside of a long cylindrical current-carrying conductor.

Let the electric current of I = 7.0 A evenly distributed with density $j = \dfrac{4I}{\pi d^2}\, A/m^2$ to flow through the cylindrical conductor with diameter of d = 6.0 mm.

Hence, we find out the magnetic field strength inside the cylindrical conductor using the formula $H_i = \frac{jr}{2}$, where *r* is the distance between the cylinder centre and its surface; outside the conductor - $H_o = \frac{jd^2}{8r}$, where $j = \frac{4I}{\pi d^2}$ is the current density or $H_o = \frac{I}{2\pi r_o}$, where r_o is the distance from outside surface of the cylinder to the point where the magnetic field strength is calculated.

a) Program of calculation and visualization of a magnetic field strength inside the conductor:

```
>> d=6e-3; I=7; % input parameters
>> j=4*I./(pi*d.^2) % calculation of a current density
j =  2.4757e+005 % result
>> r=d./ 2 % calculation of a conductor radius
r =   0.0030 % result
>> x=-r:0.01*r:r; % input the vector of x coordinate
>>y=-r:0.01*r:r; % input the vector of y coordinate
>> [X,Y]=meshgrid(x,y) % drawing the grid with coordinates x and y at its knots
% (arrays X и Y).
>> r1 = ((X - 0.2).^ 2 + Y.^ 2).^0.5; % calculation of the distance
>>r2 = ((X + 0.2).^ 2 + Y.^ 2).^0.5; % calculation of the distance
>>r=sqrt(r1.^2+r2.^2); % calculation of the distance
>> H=j*r./2; % calculationof a magnetic field strength magnitude inside the conductor
>>Z=H; % redenotation
>>plot(r,H,'k-') % visualization
>> xlabel('r,m') % input the name of x axis
>> ylabel('r,m') % input the name of y axis
>> title('H=F(r') % input the name of the graph
>> grid on% input the coordinate grid
```

The result of calculation is shown in Figure 11.

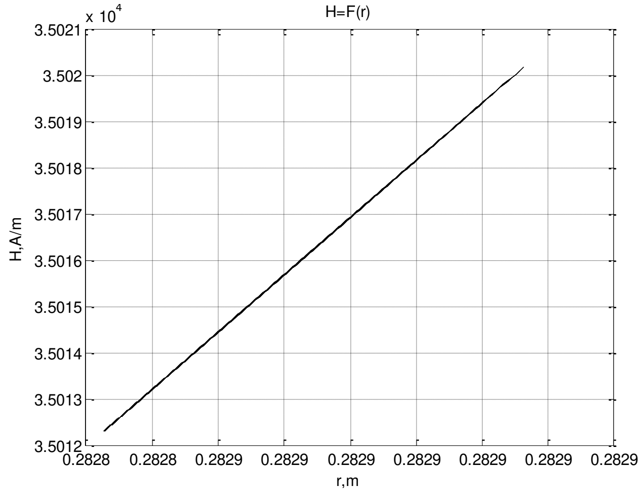

Figure 11

The magnetic field strength versus distance r between the points inside the cylinder and its surface.

>> contour3(X,Y,Z,100); % drawing the lines of levels

>> xlabel('x,m') % input the name of x axis

>> ylabel('y, m') % input the name of y axis

>> zlabel('H, A/m') % input the name of z axis

The result of visualization is shown in Figure 12.

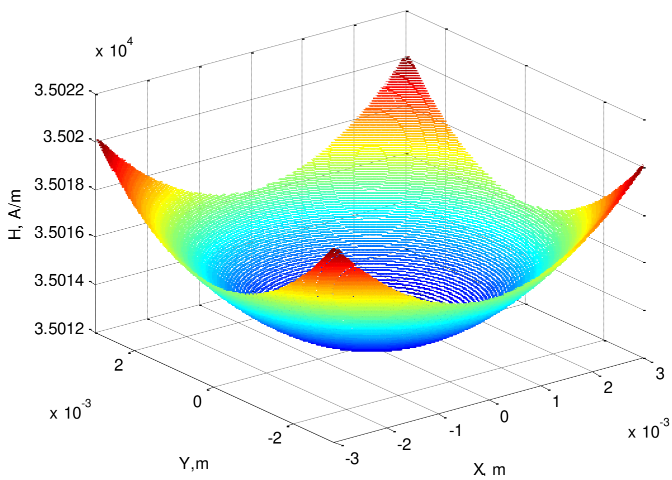

Figure 12

The lines of the magnetic field strength inside the cylindrical current-carrying conductor

view([0 0 100]) % projection on X-Y plane of support.

The result of projection is given in Figure 13.

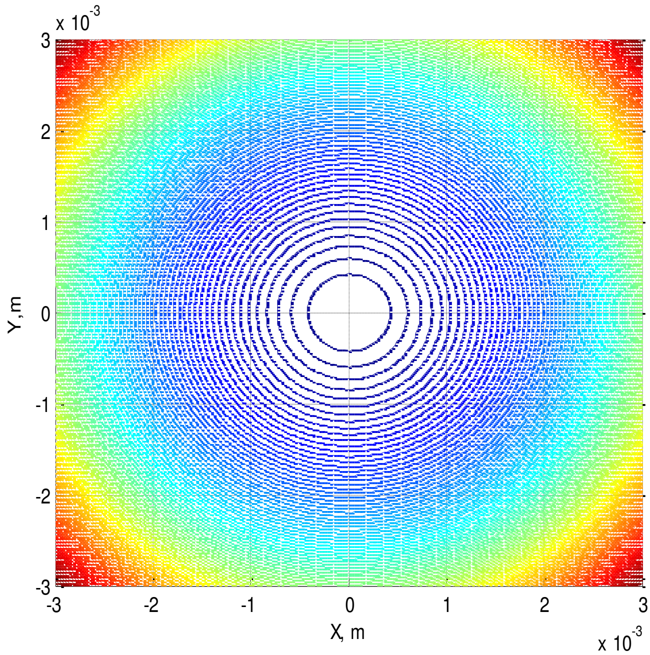

Figure 13
The projection of lines of the magnetic field strength inside the cylindrical current-carrying conductor on the X-Y plane

Figure 13 shows that the density of lines of magnetic field strength increases with the approach to the surface of the conductor that demonstrates that the magnitude of the magnetic field strength increases proportionally to distance *r* from the center of the conductor to its surface.

b) Program of calculation and visualization of a magnetic field strength outside the conductor:

```
>> rc= r:0.1*r:10*r; % input vector of distance
>> Hc=j*d.^2./(8*rc); % calculation of the field strength magnitude in dependence on the distance
>>plot(rc,Hc,'k-'); % visualization
>>grid on % drawing the coordinate grid
>>xlabel('r,m') % input the name of x axis
>>ylabel('H,A/m') % input the name of y axis
>>title('H=F(rc)') % input the name of the graph
```

The result of this program is shown in Figure 14.

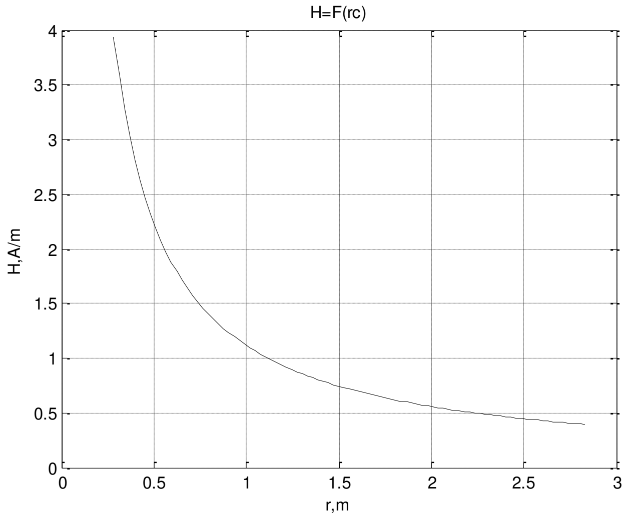

Figure 14
The magnetic field strength versus distance outside the cylindrical conductor

The magnetic field strength outside the cylindrical conductor decreases in proportion to the distance of a considered point from the conductor surface, as in the case of a long current-carrying conductor. The picture of the lines of magnetic field strength outside the cylindrical conductor is similar to the picture of the lines of magnetic field strength of the infinitely long current-carrying conductor. Students conduct this part of work by themselves.

Conclusions

The survey presents calculations and visualization of an electric field of a point charge (equipotential lines) and systems of oppositely charged threads, of magnetic field lines of a thin long and straight current-carrying conductor, and magnetic field lines inside of a cylindrical conductor with evenly distributed current made using the MATLAB language. Calculations of an electric field and potential of a point charge as a function of a distance are provided as well as a potential of a system of oppositely charged threads, magnetic induction of a thin, long current-carrying conductor as a function of a distance and magnetic induction inside the cylindrical conductor are performed. The graphs of these dependencies are drawn. So, the article is a fundamental research and gives a methodology of organization and performance of the laboratory work “Visualization of electrostatic and magnetic fields in the MATLAB language”.

References

[1] CD of the open JSC "Phizicon". «The open hysics1.1», 2001

[2] QIP.RU, available at: http://elektronika.newmail.ru

[3] Kabylbekov, K. A., Saidahmetov, P. A., Arysbaeva, A. S.: Worksheet template for organization the independent performance of computer laboratory works, Proceedings of the National Academy of Sciences of the Republic of Kazakhstan, Series of Physics and Mathematics, Almaty, 2013, No. 6, pp. 82-89

[4] Kabylbekov, K. A., Saidahmetov, P. A., Baidullaeva, L. E., Abduraimov, R. A.: Technique of use of computer models for photo-effect and Compton effect studying, worksheet template for organization the performance of computer laboratory works, Proceedings of the National Academy of Sciences of the Republic of Kazakhstan, Series of Physics and Mathematics, Almaty, 2013, No. 6, pp. 114-121

[5] Kabylbekov, K. A., Saidahmetov, P. A., Turganova, T. K., Nurullaev, M. A., Baidullaeva, L. E.: Model of a lesson on converging and diverging lenses, Proceedings of NAN RK, series physical-mat., Almaty, No. 2, 2014, pp. 286-294.

[6] Kabylbekov, K. A., Ashirbaev, H. A., Saidahmetov, P. A., Rustemova, K. Zh., Baidullaeva, L. E.: Worksheet template for organization the performance of computer laboratory work on study the diffraction of light, Proceedings of the National Academy of Sciences of the Republic of Kazakhstan, Series of Physics and Mathematics, Almaty, No. 1 (299), 2015, pp. 71-77

[7] Kabylbekov, K. A., Ashirbaev, H. A., Takibaeva, G. A., Saparbaeva, E. M., Baidullaeva, L. E., Adineeva, SH. I.: Worksheet template for organization the performance of computer laboratory work on study the motion of charged particles in a magnetic field, Proceedings of the National Academ of Sciences of the Republic of Kazakhstan, Series of Physics and Mathematics, Almaty, No. 1(299), 2015, pp. 80-87

[8] Kabylbekov, K. A., Ashirbaev, H. A., Saidakhmetov, P. A., Baigulova, Z. A., Baidullaeva, L. E.: Worksheet template for organization the performance of computer laboratory work on study the Newton's ringes, Proceedings of the National Academy of Sciences of the Republic of Kazakhstan, Series of Physics and Mathematics,Almaty, No. 1(299), 2015, pp. 14-20

[9] Kabylbekov, K. A., Ashirbaev, H. A., Sabalakhova, A. P., Dzhumagalieva, A. I.: Worksheet template for organization the performance of computer laboratory work on study the phenomenon of light interference, Proceedings of the National Academy of Sciences of the Republic of Kazakhstan, Series of Physics and Mathematics, No. 3 (301), Almaty, 2015, pp. 131-136

[10] Kabylbekov, K. A., Ashirbaev, H. A., Sabalakhova, A. P., Dzhumagalieva, A. I.: Worksheet template for organization the performance of computer

laboratory work on study the Doppler-effect, Proceedings of the National Academy of Sciences of the Republic of Kazakhstan, Series of Physics and Mathematics, No. 3(301), Almaty, 2015, pp. 155-160

[11] Kabylbekov, K. A., Ashirbaev, H. A., Arysbaeva, A. S., Dzhumagalieva, A. I.:Worksheet template for organization the performance of computer laboratory work on study physical phenomena, Modern high technologies, No. 4, Moscow, 2015, pp. 40-43

[12] Kabylbekov, K. A., Saidahmetov, P. A., Ashirbaev, Kh. A., Omashova, G. Sh., Berdalieva, J.:Worksheet template for organization the performance of computer laboratory work on study electromagnetic oscillations,Proceedings of the National Academy of Sciences of the Republic of Kazakhstan, Series of Physics and Mathematics, No. 1(305), Almaty, 2016, pp. 111-116

[13] Kabylbekov, K. A., Saidakhmetov, P. A., Omashova, G. Sh., Berdalieva, J., Dzhumagalieva, A. I.:Worksheet template for organization the performance of computer laboratory work on study the interaction between two infinitely long parallel current-carrying conductors,Proceedings of the National Academy of Sciences of the Republic of Kazakhstan, Series of Physics and Mathematics, No. 1(305), Almaty, 2016, pp. 135-140

[14] Kabylbekov, K. A., Saidakhmetov, P. A., Omashova, G. Sh., Suttibaeva, D. I., Kozybakova, G. N.:Worksheet template for organization the performance of computer laboratory work on studyisobaric process, Proceedings of the National Academy of Sciences of the Republic of Kazakhstan, Series of Physics and Mathematics, Almaty, No. 2, 2016, pp.92-97

[15] Kabylbekov, K. A., Omashova, G. Sh., Saidakhmetov, P. A., Nurullaev, M. A., Artygalin, N. A.:Worksheet template for organization the performance of computer laboratory work on studythe Carnot cycle, Proceedings of the National Academy of Sciences of the Republic of Kazakhstan, Series of Physics and Mathematics, Almaty, No. 2, 2016, pp. 98-103

[16] Kabylbekov, K. A., Saidahmetov, P. A., Ashirbaev H. A., Abdubaeva, Ph. I., Doskanova, A. E.:Study of the work done by gas on computer model, The Herald of NAN PK, No. 2, 2016, pp. 83-88

[17] Kabylbekov, K. A., Saidahmetov, P. A., Omashova, G. Sh., Serikbaeva, G S., Suyerkulova, Zh. N.: Worksheet template for organization the performance of computer laboratory work on study simple harmonic motions,Proceedings of the National Academy of Sciences of the Republic of Kazakhstan, Series of Physics and Mathematics, Almaty, No. 2, 2016, pp. 84-91

[18] Kabylbekov, K. A., Madjarov, N. T., Saidakhmetov, P. A.: An Independent design of research assignments for computer laboratory work on thermodynamics, Proceedings of the IX International scientific-methodical

conference “Teaching natural Sciences (biology, physics, chemistry), mathematics and computer science”, Tomsk, 2016, pp. 93-99

[19] Kabylbekov, K. A., Saidakhmetov, P. A., Omashova, G. Sh.: Organization of computer laboratory work on study of inductor reactance in an ac circuit, Proceedings of NAN RK, No. 1, Almaty, 2017, pp. 77-82

[20] Kabylbekov, K. A., Saidahmetov, P. A., Omashova, G. Sh., Ashirbaev, H. A., Abekova, J. A.: Organization of computer laboratory works on study of the isotherms of a real gas, Proceedings of the National Academy of Sciences of the Republic of Kazakhstan, Series of Physics and Mathematics, Almaty, No. 1, 2017, pp. 77-83

[21] Kabylbekov, K. A., Saidahmetov, P. A., Omashova, G. Sh.: Organization of computer laboratory works on study of the phenomenon of beats,Proceedings of the National Academy of Sciences of the Republic of Kazakhstan, Series of Physics and Mathematics, Almaty, No. 2, 2017, pp. 104-110

[22] Kabylbekov, K. A., Omashova, G. h., Spabekova, R. S., Saidakhmetov, P. A., Serikbaeva, G., Arysbaeva, A. S.: Worksheet template for organization the performance of computer laboratory work on studythe isothermal process, Herald of the National Academy of Sciences of Kazakhstan, No. 3, Almaty, 2017, pp. 19-207

[23] Kabylbekov, K. A., Omashova, G. Sh., Spabekova, R. S., Saidakhmetov, P. A., Abdrakhmanova, Kh. K., Arysbaeva, A. S.: Independent design of assignment for performance of a computer lab to study isochoric process, Proceedings of the National Academy of Sciences of the Republic of Kazakhstan, Series of Physics and Mathematics, Almaty, No. 3, 2017, pp. 127-134

[24] Kabylbekov, K. A., Omashova, G. Sh., Spabekova, R. S., Saidakhmetov, P. A., Serikbaeva, G. S., Aktureeva, G.: Organization of computer laboratory works on study the turn-on and turn-off current of the power supply by using MATLAB software package, Proceedings of the National Academy of Sciences of the Republic of Kazakhstan, Series of Physics and Mathematics, Almaty, No. 3, 2017, pp. 139-146

[25] Kabylbekov, K. A., Omashova, G. Sh., Spabekova, R. S., Saidakhmetov, P. A., Serikbaeva, G. S., Aktureeva, G.: Organization of computer labs for the study of velocity and height distribution of molecules from the Earth's surface by using MATLAB software package, Herald of RK NAS, Almaty, No. 3, 2017, pp. 111-119

[26] Kabylbekov, K. A., Ashirbayev, H. A., Abdrakhmanova, Kh. K., Dzhumagalieva, A. I., Kydyrbekova, J. B.: Organization of laboratory work on study of electric and magnetic fields by using MATLAB software package, Proceedings of the National Academy of Sciences of the Republic

of Kazakhstan, Series of Physics and Mathematics, Almaty, No. 3(313), 2017, pp. 206-212

[27] Kabylbekov, K. A., Spabekova, R. S., Omashova, G. Sh.,Abzhapparov, A. A., Polatbek, A., Serkebayeva, S. G.: The use of the software package MATLAB for solving problems on bifurcated electrical circuits, Herald of NAS RК, Almaty, 2017, No. 4, pp. 101-108

[28] Kabylbekov, K. A., Saidullaeva, N., Pazylova D. T., Ashirbaev, H. A., Alikulova, A. O.: Design of ambiguous tasks and tasks with missing data for performance the computer labs, Proceedings of the National Academy of Sciences of the Republic of Kazakhstan, Series of Physics and Mathematics, Almaty, 2017, No. 4, pp. 19-25

[29] Kabylbekov, K. A., Saidullaeva, N., Pazylova, D. T., Tagaev, N., Alikulova, A. O.: Organization of computer laboratory works on study of power delivered to the external load circuit,Proceedings of the National Academy of Sciences of the Republic of Kazakhstan, Series of Physics and Mathematics, Almaty, 2017, No. 4, pp. 5-10

[30] Kabylbekov, K. A., Saidahmetov, P. A., Omashova, G. Sh.,Tokzhigitova, A. A., Abdykerova, J. R.: Organization of computer laboratory works on study the dependence of the inductor reactance on the alternating current frequency, Proceedings of the National Academy of Sciences of the Republic of Kazakhstan, Series of Physics and Mathematics, 2017, No. 4, pp.259-266

[31] Kabylbekov, K. A., Ashirbaev, H. A., Abdrakhmanova, Kh. K., Dzhumagalieva, A. I., Kadyrbekova, J. B.: Organization of the performance of the laboratory work "Modeling the electric field of a system consisting of a dielectric square and a long charged conductor" by using MATLAB software package, Proceedings of the National Academy of Sciences of the Republic of Kazakhstan, Series of Physics and Mathematics, Almaty, 2017, то. 4, pp. 252-259

[32] Saidullaeva, N., Spabekova, R., Omashova, G., Kabylbekov, K.,Tagaev, N., Bitemirova, A., Berdieva, M.:Model of a blank form for computer laboratory work on research of the speed selector, Journal of Theoretical and Applied Information Technology, 15th July 2017, Vol. 95, No. 13, pp. 2999-3009, JATIT & LLS

[33] Kabylbekov, K. A., Abdrakhmanova, Kh. K., Abekova, Zh. A., Abdraimov, R. T., Ualikhanova, B. S.: Calculation and visualization of a system-an electron in a deep square potential well, with use of the software package of MATLAB, Proceeding of the III International Scientific and Practical Conference «Topical researches of the World Science» (June 28, 2017, Dubai, UAE), No. (23) Vol. 1, July 2017, pp. 7-13

[34] Dyakonov, V. P.: MATLAB training course, SPb., Peter, 2001, 533 p

[35] Lam, H. K., Leung, F. H. F., Tam, P. K. S. Stable and robust fuzzy control for uncertain nonlinear systems, IEEE Transactions on Systems, Man and Cybernetics, Part A: Systems and Humans, Vol. 30, No. 6, pp. 825-840, 2000

[36] Precup, R.-E., Preit, S., Faurb, G. PI predictive fuzzy controllers for electrical drive speed control: Methods and software for stable development, Computers in Industry, Vol. 52, No. 3, pp. 253-270, 2003

[37] Ürmös, A., Farkas, Z., Sándor, T., Nemcsics, A. Application of self-organizing maps for technological support of droplet epitaxy, Acta Polytechnica Hungarica, Vol. 14, No. 4, pp. 207-224, 2017

[38] Saadat, J., Moallem, P., Koofigar, H. Training echo state neural network using harmony search algorithm, International Journal of Artificial Intelligence, Vol. 15, No. 1, pp. 163-179, 2017

Connections between Spatial Ability and Visual Imagery Preferences

Csaba Csíkos[1] and Andrea Kárpáti[2]

[1] Eötvös Loránd University (ELTE), Department of Mathematics, Faculty of Primary and Pre-School Education
Kiss János altábornagy utca 40, 1126 Budapest, Hungary
e-mail: csikos.csaba@tok.elte.hu

[2] Eötvös Loránd University (ELTE), Centre for Science Communication and UNESCO Chair for ICT in Education, Faculty of Science
Pázmány sétány 1/A, 1117 Budapest, Hungary
e-mail: andrea.karpati@ttk.elte.hu

Abstract: The aim of the current study is to reveal the types of connections between spatial ability and visual imagery preferences. Participants in the study were 114 students from five Universities in Hungary. Two measurement tools were administered: (1) The OSIQ questionnaire (30 items, 15 items on object imagery, and 15 on spatial imagery), and (2) A spatial ability test. The score achieved on spatial imagery items of the OSIQ test has a significant correlation with performance on the spatial ability test ($r = 0.46$; $p < 0.001$), while score on the object imagery items has a neutral correlation with spatial ability ($r = -0.07$; $p = 0.46$). This tendency in the strengths of correlations was independent of the type of study (engineering students and visual art pre-service teachers) and of gender. Results have relevance for designer training, skills identification and talent identification.

Keywords: spatial ability; visual imagery; OSIQ; visual skills development

Connections between Spatial Ability and Visual Imagery Preferences

Development of spatial abilities is crucial in training, for a wide range of professions. Research on factors influencing developmental levels may improve training programs, by means of providing data for more targeted, skills enhancements. Our study aims to reveal connections between spatial ability and visual imagery preferences and experiences, in two tertiary student populations: engineering students and pre-service teachers of art, with a background in design. Whereas possessing an appropriate level of spatial ability is crucially important in several fields of tertiary education, the role of visual imagery preferences and their connections with spatial ability is an issue for critical discussion. The phenomenon of visual imagery preferences in itself deserves further clarifications, since there are at least two main types of imagery towards which preferences can be defined and measured. Object imagery and spatial imagery are the two broad categories; the first referring to colorful, vivid images, while spatial imagery refers to schematic drawings.

1 Introduction

1.1 Spatial Ability and its Importance in Tertiary Education

Spatial ability has long been recognized as an important intelligence factor, a field of talent recognition and development, and a set of skills necessary for academic expertise indifferent fields of tertiary education.

Research on spatial ability has a long tradition, under different paradigms, including the Piagetian tradition and the factor-analytical studies of intelligence. Piaget presumes that man organizes reality into coherent and stable patterns at certain points of cognitive development which are structurally different from those at other points – an idea of developmental stages influencing research on visual language of children and youth for decades [27, 17]. Piaget identified sensorimotor, preoperational, concrete and formal operational stages in the perception of and manipulation with space as well [16].

In factor-analytic studies of human intelligence, a wide variety of tests were used to measure a broad range of abilities labeled under the umbrella of spatial ability (see [26, 11, 6, 9] for overviews). The common base for the divergent definitions of spatial ability can be identified in the ability to manipulate images mentally. In Carroll's overview [11], spatial ability consists of several different first-order intelligence factors such as visualization and other, speed-related factors. More recent findings on the structure of intelligence challenged the traditional division of fluid and crystallized factors, and [18] suggest that image rotation – considered as the core part of spatial ability – also deserves a separate intelligence factor, besides the verbal and perceptual components.

In spite of the widely recognized importance of spatial ability as a distinct intelligence factor, school curricula and talent recognition instruments often fail to involve spatial ability as befitting its importance [21]. As [14] emphasized, the assessment of spatial intelligence (one important branch of intelligence in Gardner's multiple intelligences paradigm) should take the form of manipulative tasks, as opposed to linguistic ones. Measures of academic potential (like the Scholastic Aptitude Test) do not assess spatial ability, despite its crucial role in STEM (science, technology, engineering and mathematics) subjects [1]. This may be a reason why many university students in STEM subjects, start their studies with a deficient spatial ability. As a consequence, they face problems in acquiring visual representations required by art and geometry and fail to decode spatial visualizations in science textbooks. There have been weaknesses reported in spatial ability even among first year engineering students [15].

The importance of an appropriate level of spatial ability in engineering studies is emphasized by [34] and it is highlighted in the European Space for Higher Education documents [10]. In a study on the relation of spatial skills and areas of study, engineering students tend to provide better performance in different spatial ability tests than students of visual arts and humanities [38]. Another population of special interest with regard to the role of spatial ability in tertiary education is the pre-service teacher population, especially in the fields of mathematics and visual arts and design. Pre-service and in-service mathematics teachers' performance on 3D visualization tasks was hindered by their frequently observed misconceptions when trying to transform 3D situations to two dimensional problems [13].

Diagnosing deficiencies of spatial performance inspired researchers to address the issue of skills development in higher education and beyond. It is still an unresolved problem if and to what extent spatial ability can be improved in adulthood by means of adequate instructional strategies and tasks. In an experiment, computer-based real-world tasks were applied to improve spatial ability, but no significant between-group differences were found [25]. In other skill enhancement experiments, there were some promising findings published on the potentials of improving spatial ability among engineering students [29, 36]. At the same time, these efforts emphasize the importance of spatial ability development in adulthood. Nevertheless, it has been revealed that enriching activities are needed over a long period of time in order to gain long-term development effects [31].

1.2 Visual Imagery Preferences

According to the MIT Encyclopedia of the Cognitive Sciences [22], mental imageries are mental processes that can be connected to either generating, transforming or inspecting images (what we see with our inner eyes). The measurement of imagery rely on people's subjective statements considered to be true for themselves, thus an established means of measuring imagery preferences and experiences is the self-report questionnaire methodology. For instance, adults and even teenagers may give unbiased judgments on their own skills and abilities, and who else would better know what an individual prefers (i.e., choosing between a work of architecture and painting) than the individuals themselves. There were six items used among young children (from grades 3 to 12) on their 'spatial experience' [12]. In that study, spatial experience did not prove to be a significant predictor of spatial ability.

One of the widely used self-report questionnaires on visual imagery is the Object-Spatial Imagery Questionnaire [4] which contains 30 statements on the individual's visual imagery preferences and experiences. Obviously, measuring preferences and experiences in a cognitive domain by definition accomplishes the measurement of cognitive and learning styles, too. An extended version of the OSIQ questionnaire, OSIQV [3] covers three cognitive style factors: two visual and one verbal factor.

The taxonomy of cognitive styles must be briefly mentioned here as it is closely related to OSIQ, the questionnaire that we also used in our study. This taxonomy would certainly involve a discussion on the verbalizer-visualizer dichotomy, and there are two types of visualizers revealed [24]. Some people rely on vivid, colorful images in their thinking, while others prefer to use schematic drawings. This division of visualizers was incorporated in the OSIQ theoretical framework where the object imagery scale refers to the first, while the spatial imagery scale to the second type of visualization. A comprehensive, new model of cognitive styles with three pillars were introduced [5]: object imagery, spatial imagery, and verbal style. Why is it preferential to study cognitive styles in a tertiary education context? Blazhenkova and Kozhevnikov provide a detailed analysis of different aspects from which cognitive styles can be discussed: e.g., from the aspect of the brain areas involved in cognitive processing, different cognitive styles have their brain region correlates. Other aspects from which cognitive styles can be distinguished and defined are the psychological representations involved and the sequential nature of the related psychological processing.

In their study of visual artists, scholars of humanities and scientists, differences in object and spatial imagery scores were found [4]. As expected, visual artists obtained much higher object imagery scores, while scientists scored much better in spatial imagery tasks. As for the connection between object or spatial imagery scores and spatial ability, significant correlations (above .3) were found for spatial imagery scores, and non-significant correlations for object imagery [7].

The relevance of studies on connections between mental imagery scores and spatial ability can be justified from at least two aspects. First, the instructional strategies and tasks that are used in tertiary education may effectively foster students' spatial ability. At least in a diagnostic assessment setting, some expected correlations between OSIQ scores and different task genres were found [37]. Another, even broader aspect of relevance is the possible predictive value of either the mental imagery scores or the level of spatial ability. Mental imagery scores may well predict an individual's ability level and dispositions necessary to be successful a profession requiring the production and/or processing of different types of visualizations or to qualify for such university degree programs at all. Moreover, the level of spatial ability (that correlates with spatial imagery) has also some important correlations with personality traits, for example, with the openness personality factor [39].

1.3 Research Questions

Based on the literature review, and in accordance with the main aim of the current investigation (revealing correlations between training types and developmental level of spatial abilities), the following research topics have been formulated.

First, are spatial ability and visual imagery preferences of tertiary student interdependent? Provided that both psychological constructs can be reliably measured, we aim to investigate their relationships with two background variables: type of study and gender.

Second, in accordance with the main motive and title of the current research, we suggest that the nature or magnitude of the connections between spatial ability and visual imagery preferences are influenced by the background variables.

In line with these research topics, we hypothesized that:

- Both spatial ability and visual imagery preference can be reliably measured among engineering and arts and design pre-service teachers. Besides the two main factors of OSIQ, we presumed to identify other clusters of items (e.g., items related to color perception and preference).
- Engineering students will tend to have higher scores on the spatial imagery than on the object imagery subscale, while art and design pre-service teachers will have results in the opposite direction.
- Engineering students are expected to have better performance on the spatial ability test.
- Spatial ability is likely to have stronger correlation with the spatial imagery than with the object imagery subscale.
- The strength of correlations is thought to be the same regardless of the type of study.
- Males are expected to have better performance on the spatial ability test, while the results on the OSIQ scales would show mixed findings in relations to gender.
- Since there are more male engineering students, the study-type-effect and the gender effect are supposed not to interact with each other, i.e., both factors were supposed to have their own independent effect on both the OSIQ scores and on spatial ability performance.

These hypotheses derived from the two main research topics have driven our data analysis and the presentation of the results.

2 Methods

2.1 Sample

The students involved were recruited from five tertiary institutions of Hungary. The main characteristics of the sample composition are presented in Table 1.

Table 1
Characteristics of the sample

Institution and field of study	N	Male + female participants
Nyíregyháza College of Education	8	4 + 4
Óbuda University	46	41 + 5
Kecskemét College	28	1 + 27
Moholy-Nagy University of Art and Design	11	0 + 11
University of Pécs	21	13 + 8
Σ	114	59 + 55

The training program, infrastructure and student population of the universities and colleges selected are not fully representative of Hungarian institutions with similar training programs. While the University of Pécs has an accredited engineering program similar to others in Hungary, the Moholy-Nagy University of Art and Design is a unique and worldwide recognized institution that trains designers and teachers of art and design, who all possess an M.A. degree in an area of design, before entering the teacher training course. Students, however, are representative of the three university-level art and design teacher training institutions of Hungary.[1] The other two training sites are representative of college level art teacher education in Hungary. The Kecskemét and Nyíregyháza Teacher Training Colleges accepts students with a B. A. in Education (a primary teacher's degree) into their M. A. degree course in Art Education through a less competitive examination procedure.

Students tested were randomly selected from among those in the same degree course at each institution. However, the number of students attending each course is different and so are the chances of having been selected for the sample. At the University of Pécs, the sample was selected from 240 engineering students. At the Kecskemét and Nyíregyháza Teacher Training Colleges, students represent a cohort of 30 art education teacher trainees. At Moholy-Nagy University of Art and Design, all but four second-year Art and Design Education M. A. students were included in the sample.

---

[1] Besides Moholy-Nagy University of Art and Design, Budapest, the Hungarian University of Fine Arts, Budapest and the Faculty of Arts at the University of Pécs offer M. A. degree courses on Art and Design Education for M. A. degree holders in Art or Design.

2.2 Measures

Two tests were used in this investigation. A spatial ability test developed by Séra, Kárpáti and Gulyás [35], for an English description, see [28], and a questionnaire on visual imagery preferences [4].

2.2.1 Spatial Ability Test

The test measured two large skills clusters: spatial manipulation and perception. The subgroups evaluated were visualization, imagination, psychomotor components and visual memory. Item types were as follows

*A) Perception of space (*recognition and interpretation of 2D images representing spatial relations*)*

- Perception of spatial relations (e. g. location, direction, positioning, relative size)
- Interpretation of the structure and composition of spatial objects (e. g. positive and negative relations, juxtaposition, rules of illusionary representation of space)
- Reconstruction of spatial objects (e. g.: depiction of a geometric shape based on its floor plan, estimating size based on plans and sections, reading reduced images: silhouettes, maps, technical drawings, explanatory charts, representations of processes)

In all three item groups, the aspect of time was also present in tasks challenging spatial memory, mental rotation and manipulation, imagination of movement in space etc.)

B) Creation of 2D spatial images: representation, transformation, manipulation

- Rotation, alteration, mirroring and construction of images representing spatial relations. Two tasks are shown on Figure 1 to illustrate item types.

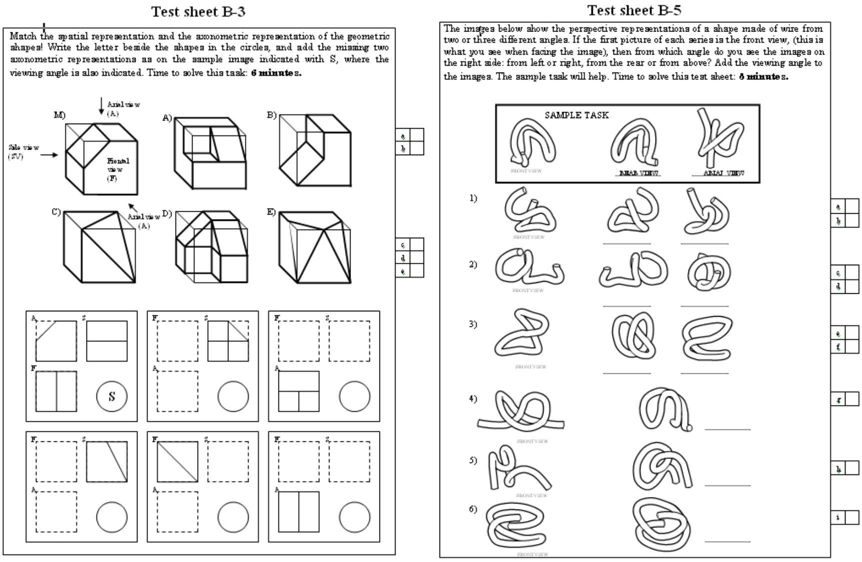

Figure 1(a) and 1(b)
Two tasks of the Spatial Ability Test by [30, p. 67]

The Spatial Ability Test proved to be a reliable measure: Version A (56 items) and Version B (47 items) had Cronbach's α coefficients .81 and .93, respectively. The mean score on Version A was 52.19%, while on Version B 50.79%. Items of the test have been successfully used in the Visual Culture subtests of the Hungarian Competence-Based Assessment of Student Skills [39].

2.2.2 OSIQ

Object-Spatial Imagery Questionnaire (OSIQ) measures individual differences in representing and processing visual imagery. It consists of an *object imagery scale* that reveals preferences for representing and processing colorful, pictorial visualizations of objects individual objects and a *spatial imagery scale* that shows the degree of preferences for schematic images, spatial relations amongst objects, and spatial transformations. The developmental process of the OSIQ questionnaire on visual imagery preferences is detailed in Blajenkova, Kozhevnikov and Motes (2006).

The reliability of OSIQ proved to be appropriate for the purposes of the current study. For the whole questionnaire (30 items), Cronbach's α coefficients was .77, while for the two subscales reliability was .86 (object imagery) and .80 (spatial imagery).

2.3 Procedure

The tests were administered within a one-week period to volunteering university and college students. In all institutions, OSIQ was administered first, followed by the Spatial Abilities Test.

3 Results

The results are presented in three consecutive sections. Section 3.1 discusses the results on the spatial ability test and the connections between spatial ability and background variables. Then results of the OISQ questionnaire are addressed in 3.2. In Section 3.3 the connections between the two psychological construct, and how these are influenced by background factors will be presented.

3.1 Spatial Ability Level

The level of spatial ability, i.e. the total score performed on the Spatial Ability Test is presented in Table 2 according to the type of study, and in Table 3, according to gender.

Table 2
Results on the Spatial Ability Test according to the type of study

Type of study	N	M	SD
Engineering students	66	57.71	19.73
Visual art and design pre-service teachers	47	43.03	23.71
Total	113	51.61	22.58

Our results suggest that engineering students outperformed visual art and design pre-service teachers in their spatial ability level. The difference is significant ($t = 3.59$; $p = 0.001$).

Table 3
Results on the Spatial Ability Test according to gender

Gender	N	M	SD
Male	58	56.53	19.76
Female	55	46.42	24.32
Total	113	51.61	22.58

Gender differences proved to be also significant with male students' advantage ($t = 2.43$; $p = 0.02$).

3.2 Visual Imagery Preferences

Table 4 and Table 5 present the results on visual imagery preferences for both subscales and for study type (Table 4) and gender (Table 5). Please note that for 15 items with five-level Likert-scale, the minimum total score is 15, and maximum is 75.

Table 4

Results on OSIQ according to the type of study

		Object imagery		Spatial imagery	
Type of study	N	M	SD	M	SD
Engineering students	67	50.55	9.13	51.69	7.00
Visual art and design pre-service teachers	47	55.74	8.83	42.64	8.80
Total	114	52.69	9.33	47.96	8.95

Independent-samples t-test showed significant differences in both scales of the questionnaire: $t = 3.03$; $p = 0.001$ for object imagery, and $t = 6.11$, $p < 0.001$ for spatial imagery.

Table 5

Results on OSIQ according to gender

		Object imagery		Spatial imagery	
Gender	N	M	SD	M	SD
Male	59	49.25	9.06	51.32	7.79
Female	55	56.38	8.18	44.35	8.77
Total	114	52.69	9.33	47.96	8.95

Gender differences proved to be significant in both subscales: $t = 4.40$; $p < 0.001$ for object imagery, and $t = 4.50$; $p < 0.001$ for spatial imagery. Since there is connection between the type of study and gender in the current sample, the relative weight of these two factors will be analyzed separately in section 3.4.

3.3 Item Clusters in OSIQ

Cluster analysis is a multivariate technique of analysis that groups variables into similarity clusters. The aim of using this method rather than confirmatory factor analysis is that cluster analysis relies on manifest variables only. Manifest variables are actually the students' answer scores, and the tendency in similarities and dissimilarities in their answers are shown in the dendrogram. Figure 3 shows the results of cluster analysis using the furthest neighbor method based on Pearson correlations.

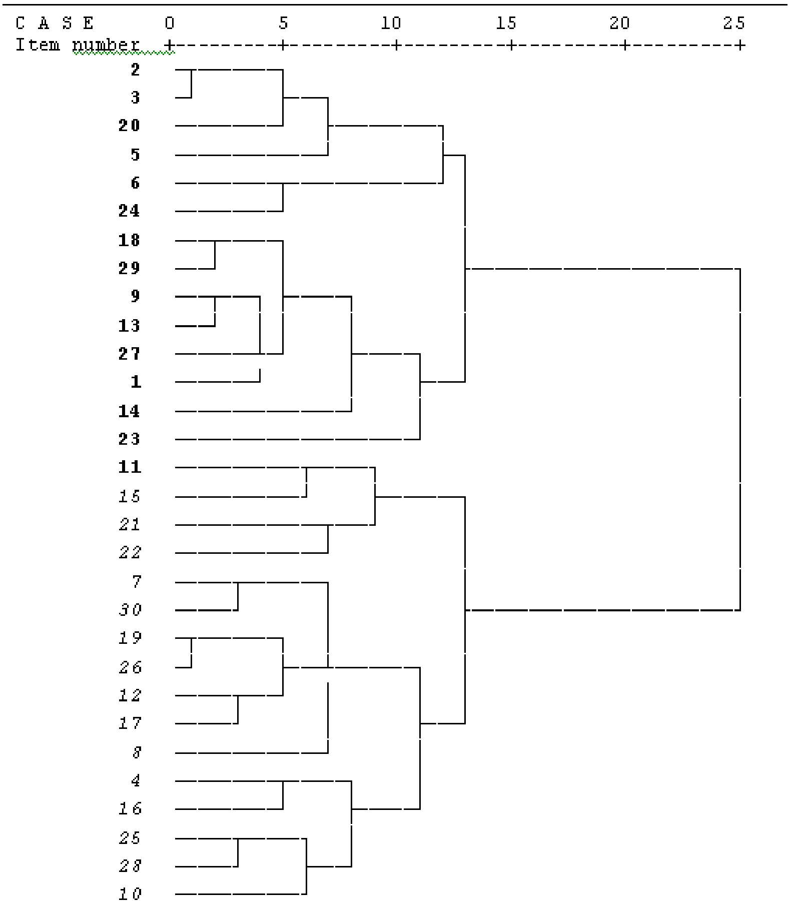

Figure 2

Dendrogram of the OSIQ items based on Pearson-correlation using the furthest neighbor method

Note: spatial imagery item numbers are in bold, and object imagery item numbers are in italic

The immediate visualization in Figure 2 reveals two distinct clusters: one containing spatial imagery items (with the exception of Item 11), and another cluster with object imagery items only. This immediate visualization is further approved by the analysis of significant correlations, since the last seven vertical lines represent non-significant connections. Consequently, Item 11 forms a separate cluster together with the Item 15, and this two-component cluster has no significant connections to other similarity groups. Item 11 is a rather long sentence claiming that 'I [the respondent] normally do not experience many spontaneous vivid images; I use my mental imagery mostly when attempting to solve some problems like the ones in mathematics.' Item 15 expresses preference for architecture as opposed to genres of visual arts. The peculiar place of Item 11 in this dendrogram may point to a didactical problem of making students aware of the role of mental imagery in problem solving in art and design as well as geometry. This division of items according to content proves the validity or the questionnaire and also supports our previous results.

Figure 2 shows other similarity groups, i.e., clusters where the vertical line is at most on scale level 6. For instance, Items 19 and 26 belong to such a similarity group, and both items contain the terms ‘remember’ with the words visual or visually. Similarly, Items 12 and 17 refer to vivid and clear mental images. Similarly, among the spatial imagery items, Items 2 and 3 refer to professions closely associated with spatial imagery, and Items 18 and 29 concern graphic abilities.

3.4 Connections between Spatial Ability and Visual Imagery Preferences

As revealed in previous studies and hypothesized in the current research, there may be significant correlations between the level of spatial ability and visual imagery preferences. Since both measures provide interval scale level scores, Pearson-correlation coefficients were computed and shown in Table 6.

Table 6

Correlation coefficients between spatial ability and visual imagery in the whole sample and in two subsamples

Whole sample	**Object imagery**	**Spatial imagery**
Spatial ability	-0.07	0.46
Object imagery		-0.13
Engineering students	Object imagery	Spatial imagery
Spatial ability	0.11	0.27
Object imagery		0.01
Pre-service teachers	Object imagery	Spatial imagery
Spatial ability	-0.09	0.45
Object imagery		0.02

Note: Correlation coefficients highlighted in bold are significant, other coefficients are non-significant at p = 0.05 level

Table 6 suggests that independently of the type of study the students pursue, there is a significant correlation between their spatial ability and spatial imagery. There is no significant correlation either between spatial ability and object imagery or between object and spatial imagery. The latter non-significant coefficients indicate the independence of the two OSIQ subscales, and therefore, validate the correlation between spatial imagery and spatial ability.

With respect to gender, similar patterns were revealed. It means that for both male and female students, the correlation between spatial ability and spatial imagery was significant, while the other two types of correlations were non-significant.

Consequently, the connection revealed for the whole sample by a massive .46 correlation coefficient is stable independently of either study type or gender.

To examine the cumulative role of the type of study and gender, a two-way analysis of variance has been conducted. This type of analysis reveals effects (if any) of two background variables, and examines whether the effects occur independently of each other. According to two-way ANOVA, interestingly, neither the type of study nor gender has a significant effect on *spatial ability* in itself (due to the small intersectional subsamples). However, the interaction of the two background factors proved to be significant with eta-squared coefficient = 7.2%. (Eta-squared coefficients are estimates of the explained variances on spatial ability). In itself, the magnitude of explained variance in this case can be considered medium sized. On the contrary, having examined the cumulative role of study type and gender, significant gender effect was found on *object imagery* (eta-squared = 3.7%), and the type of study had also a significant effect on spatial imagery (eta squared = 9.1%). In neither case the interaction of the two factors was significant.

This result, however, needs further research as several other spatial ability studies report gender-related performance differences. Gender played a significant role when computer-based real-world tasks were applied to improve spatial ability [25]. In a recent study of the same age group [9], a group of 202 female and male university undergraduates were administered three performance tests and three imagery questionnaires. Men obtained higher scores than women on the performance tests while no significant gender differences were observed on the imagery questionnaires. Women obtained higher scores than men on the Object scale of the Object-Spatial Imagery and Verbal Questionnaire. Gender differences were also observed between the correlations obtained for the performance test, with higher correlations for men. Other studies, comparing spatial imagery with a performance test also found significant gender differences [6].

4 Discussion

In this section, we review our research questions and hypotheses in light of the results of the current survey.

Engineering students had significantly better scores on the spatial ability test. Their good spatial ability level may be due to their training program involving more exercises in mental imaging. Training in spatial creation of art teachers generally lacks mental manipulation in space and focuses on realistic representation only. Therefore, their performance on this test is inferior to those of engineering students in mental manipulation tasks. This type of Pre-service training is later reflected in the teaching practice of art teachers: instead of developing a balanced curriculum of mental and creative spatial tasks, thus preparing students for vocations and everyday life situations requiring mental operations in space, they focus on representing space in a realistic manner.

This type of representation, however, is less and less required both in the world of work and in leisure time activities while mental operations gain importance in jobs like engineering and Information Technology as well as in free time activities like finding our way during a web search or in a city, reading a map. Spatial orientation tasks requiring mental rotation, completion and transformation range from reading and producing technical drawings to learning through simulations and playing computer games.

Our findings are in line with [4] who claim that 'compared to visual artists and humanities professionals, scientists, reported higher spatial imagery ratings; however, compared to scientists and humanities professionals, visual artists reported higher object imagery ratings' (p. 239).

Spatial ability was hypothesized to have stronger correlation with the spatial imagery than with the object imagery subscale. This hypothesis is supported by our results. Engineering students scored higher on the spatial imagery than on the object imagery subscale, and pre-service art and design teachers scored better in object imagery. Engineering students were also more successful in the Spatial Ability Test. This supports the predictive, discriminant, and ecological validity of both of our measures.

Connections between the two tests employed were strong. Good performance in our Spatial Ability Test predicted preference for spatial imagery as identified by the OSIQ questionnaire. This result does not mean that both measures may be used for the detection of the level of spatial abilities – for the screening of mental and psychomotor abilities needed for the study of engineering or art education, discipline-specific measures should be used. (The Spatial Ability Test has repeatedly been employed for identifying students in need of special training in an area of spatial perception or manipulation at the University of Technology in Budapest).

Strong connection between results in the test and the self-report questionnaire indicates a preference for a certain mode of visualization. If a group of pre- or in-service art educators have a strong preference for object imagery, it may indicate that they are likely to favor expressive and representational tasks versus analytical, design-oriented ones. Art teachers in secondary education should not have such a preference as their students need a balanced education in both technical and expressive skills. Therefore, pre- and in-service trainers should emphasize planning and design tasks to reveal their creative potentials and thus motivate for their inclusion in the curriculum.

The strength of correlations between the OSIQ scales and spatial ability was the same regardless of the type of study. Consequently, different types of studies may not have a specified effect on the connections between visual imagery preferences and spatial ability.

In line with previous research, males were expected to have better performance on the spatial ability test. In the OSIQ scales, we expected mixed findings in relations to gender, but the preference of engineering students for spatial imagery and the art education students for object imagery was significant. There is a significant correlation between their spatial ability and spatial imagery. There is no significant correlation either between spatial ability and object imagery or between object and spatial imagery. The latter non-significant coefficients indicate the independence of the two OSIQ subscales, and therefore, validate the correlation between spatial imagery and spatial ability. With respect to gender, similar patterns were revealed. It means that for both male and female students, the correlation between spatial ability and spatial imagery was significant, while the other two types of correlations were non-significant.

The connection between OSIQ scores and spatial ability results revealed for the whole sample by a massive .46 correlation coefficient is stable independently of either study type or gender. The type of study had also a significant effect on spatial imagery. Since there are many more male engineering students, the study-type-effect and the gender effect were thought not to interact with each other, i.e., both factors were supposed to have their own independent effect on both the OSIQ scores and on spatial ability performance. Gender differences, however, proved to be significant in both subscales.

4.1 Theoretical and Practical Relevance

Theoretical relevance of this research involves the establishment of connections between spatial ability and visual imagery preferences – a result that may be relevant for empirical aesthetics studies of personality traits and environmental effects affecting the development of taste. The level of perception of and creation in space is apparently connected to preferring certain visualizations. We have shown that spatial manipulations and visual preferences are connected in the mind, and the strength of connection depends on the type of training. Practical relevance of our research includes methodological aspects, the possibility of using a self-reported paper-and-pencil questionnaire to diagnose visual imagery preferences (and henceforth some aspects of spatial ability), and to provide an easy to administer measure for profession counselors. The Spatial Ability Test proved to be a reliable measure to identify outstanding spatial ability among engineering student, and the OSIQ showed interrelations with preferences of spatial imagery. Current research emphasizes the importance of spatial skills in STEM education [26, 28]. The joint use of these instruments promotes talent identification that may result in more efficient development.

The development of spatial ability can and should be supported by educational practices that are not oriented toward searching for gifted persons, but are oriented toward different gifted behaviors [8]. Spatial ability as supported by Gardner's multiple intelligence paradigm, is one of the important fields where gifted behavior can be observed and recognized. Identification of outstanding (or deficient) spatial ability is especially important for future and in-service art and design educators, who are supposed to develop spatial skills and abilities of their students, thus preparing them for a range of technological vocations and professions. When identified as lacking adequate spatial abilities, students may enter remedial courses that are likely to improve their spatial skills considerably [30]. Our results may help in early talent recognition and identification of spatial ability.

4.2 Limitations

The limitations of this research come from at least two sources. First, the sample is not representative of all types of engineering instruction offered by Hungarian universities and colleges. Architecture students were not involved – a cohort that may have more balanced skill structure, integrating both object and spatial imagery. Second, the indirect nature of any self-report questionnaire must be taken into account when interpreting the results of our study.

Although our Spatial Ability Test has repeatedly proven to be a reliable instrument, assessing spatial skills with two-dimensional, paper-and-pencil tasks has some ecological validity issues. For example, gender differences may be different, if tasks are to be performed in real space with authentic instruments. In such a situation, females were superior at static object-location memory tasks [32]. We also improved ecological validity through the introduction of three-dimensional, movable images produced by the open-source, internationally used GeoGebra software and launched studies on age-related and gender differences in a virtual environment resembling real-life situations in terms of changeability of viewpoints. (See [19], for a description of interactive, mobile, three-dimensional testing instruments.)

4.3 Implications for Future Research

Until the advent of neuroscience research, educators of artists and engineers had been convinced that individual differences in mental imagery, as well as the investigations of individual preferences for processing visual versus verbal information, were based on imagery as an undifferentiated, unitary construct and therefore individuals could simply be classified as good or bad imagers [33]. However, neuroscience research has proven the existence of distinct imagery subsystems [23]. In the current study, the nature and strength of connections between two types of measures have also been revealed.

Training programs have to consider such differences and, if necessary, ensure that the less developed mode of representation and encoding is enhanced through discipline-relevant developmental tasks [2]. This is especially true for art teacher education, where object imagery seems to be in the focus, while in art education programs focusing on ‘real world’ needs, spatial imagery of students has to be developed as well. Therefore, future art teachers have to be taught to develop curricula that support the encoding and processing of visual information in different ways.

In order to train students with high level spatial imagery skills, art educators have to develop their own spatial ability as well. Their spatial imagery will support the representations of the spatial relations amongst objects and their parts, locations and movements in space and other complex spatial transformations. These may of course be easily created in a computer assisted design environment – but only if the person at the keyboard has a clear mental vision about the desirable image. Additionally, a new factor, i.e. possible dynamic changes in the relationship between spatial ability and visual imagery preferences should also be addressed. It may be done by means of either longitudinal studies or design experiments. Both possibilities are available and feasible already from lower secondary school grades.

On the other hand, engineering students seem to need more training in visual creativity to develop their object imagery capacity. Object imagery supports the representations of objects in terms of their form, size, shape, color and brightness as they are perceived. For future architects and industrial designers or engineers, this capacity helps create convincing for their prospective customers visualizations of inventions or novel technical solutions.

Acknowledgements

Research presented in this paper is related to the "Moholy-Nagy Visual Modules - teaching the visual language of the 21th century" project of the MTA-ELTE Visual Culture Research Group (2016-2020). The study was funded by the Content Pedagogy Research Program of the Hungarian Academy of Sciences and by a grant from the Hungarian Scientific Research Fund (OTKA81538) awarded to the first author.

The authors express their gratitude to Emil Gaul, Ákos Gocsál, Anikó Illés, József Strohner and Péter Tóth for their support in data collection and useful comments concerning the applicability of the spatial ability test in tertiary education.

References

[1] Andersen, L.: Visual-spatial ability: important in STEM, ignored in gifted education. Roeper Review, 36, pp. 114-121, 2014

[2] Babály, B. and Kárpáti, A.: The Impact of Creative Construction Tasks on Visuospatial Information Processing and Problem Solving. Acta

Polytechnica Hungarica, (13)7, pp. 159-180, 2016, http://uni-obuda.hu/journal/Babaly_Karpati_71.pdf

[3] Blajenkova, O., Becker, M. and Kozhevnikov, M.: Object-spatial imagery and verbal cognitive styles in children and adolescents: Developmental trajectories in relation to ability. Learning and Individual Differences, 21, pp. 281-287 (2011)

[4] Blajenkova, O., Kozhevnikov, M. and Motes, M. A.: Object-spatial imagery: A new self-report imagery questionnaire. Applied Cognitive Psychology, 20, pp. 239-263, 2006

[5] Blazhenkova, O. and Kozhevnikov, M.: The new object-spatial-verbal cognitive style model: theory and measurement. Applied Cognitive Psychology, 23, pp. 638-663, 2009

[6] Blazhenkova, O. and Kozhevnikov, M.: Visual-object ability: A new dimension of non-verbal intelligence. Cognition, 117, pp. 276-301, 2010

[7] Borst, G. and Kosslyn, S. M.: Individual differences in spatial mental imagery. The Quarterly Journal of Experimental Psychology, 63, pp. 2031-2050, 2010

[8] Brown, S. W., Renzulli, J. S., Gubbins, E. J., Siegle, D., Zhang, W. and Chen, C.-H.: Assumptions underlying the identification of gifted and talented students. Gifted Children Quarterly, 49, pp. 68-79, 2005

[9] Campos, A.: Gender differences in imagery. Personality and Individual Differences, 59, pp. 107-111, 2014

[10] Carrera, C. C., Saorín Pérez, J. J., de la Torre Cantero, J. and Marrero González, A. M.: Engineers' spatial orientation ability development at the European Space for Higher Education. European Journal of Engineering Education, 36, pp. 505-512, 2011

[11] Carroll, J. B.: Human cognitive abilities: A survey of factor-analytic studies. Cambridge: Cambridge University Press, 1993

[12] Chan, D. W.: Gender differences in spatial ability: Relationship to spatial experience among Chinese gifted students in Hong Kong. Roeper Review, 29, pp. 277-282, 2007

[13] D. Moore-Russo, J. M., Viglietti, M., Chiu, M. and Bateman, S. M.: Teachers' spatial literacy as visualization, reasoning, and communication. Teaching and Teacher Education, 29, pp. 97-109, 2013

[14] Gardner, H. and Hatch, T.: Multiple intelligences go to school: educational implications of the theory of multiple intelligences. Educational Researcher, 18, pp. 4-10, 1989

[15] Garmendia, M., Guisasola, J. and Sierra, E.: First-year engineering students' difficulties in visualization and drawing tasks. European Journal of Engineering Education, 32, pp. 315-323, 2007

[16] Hardiman, G. and Zernich, T.: Some considerations of Piaget's cognitive-structuralist theory and children's artistic development. Studies in Art Education, 21, pp. 12-19, 1980

[17] Hurwitz, A. and Day, M.: Children and Their Art. New York: Harcourt, Brace and Jovanovich, 1994

[18] Johnson, W. and Bouchard, T. J. Jr.: The Structure of Human Intelligence: It is verbal, perceptual, and image rotation (VPR), not fluid and crystallized. Intelligence, 33, pp. 393-416, 2005

[19] Kárpáti, A., Babály, B. and Budai, L.: Authentic assessment of spatial abilities through interactive, online 2D and virtual 3D tasks. International Journal of Arts Education, 13, pp. 94-124, 2014

[20] Kárpáti, A.: Child Art of the Z Generation - A Multimedia Model of Visual Skills Development. In: Benedek, A. and Nyíri, K. (Eds.): How to Do Things With Pictures. Skill, Practice, Performance. Frankfurt/M.: Peter Lang Verlag, pp. 57-74, 2013

[21] Kell, H. J. and Lubinski, D.: Spatial ability: a neglected talent in educational and occupational settings. Roeper Review, 35, pp. 219-230, 2013

[22] Kosslyn, S. M. and Rabin, C. S.: Imagery. In Wilson, R. A. and Keil, F. C. (Eds.): The MIT Encyclopedia of the Cognitive Sciences, Boston: MIT Press. pp. 387-389, 1999

[23] Kosslyn, S. M.: Image and brain: The resolution of the imagery debate. Cambridge, MA: MIT Press, 1994

[24] Kozhevnikov, M., Hegarty, M. and Mayer, R. E.: Revising the visualizer-verbalizer dimension: evidence for two types of visualizers. Cognition and Instruction, 20, pp. 47-77, 2002

[25] Lajoie, S. P.: Individual differences in spatial ability: Developing technologies to increase strategy awareness and skills. Educational Psychologist, 38, pp. 115-125, 2003

[26] Lohman, D. F.: Spatial abilities as traits, processes and knowledge, In R. J. Sternberg (Ed.), Advances in the psychology of human intelligence. Hillsdale, NJ: Erlbaum, pp. 181-248, 1981

[27] Lowenfeld, V.: Creative and Mental Growth. New York: Macmillan Co, 1947

[28] Lubinsky, D.: Spatial ability and STEM: A sleeping giant for talent identification and development. Personality and Individual Differences, 49, pp. 344-351, 2010

[29] Martín-Gutiérrez, J., Luís Saorín, J., Contero, M., Alcañiz, M., Pérez-López, D. C. and Ortega, M.: Design and validation of an augmented book

for spatial abilities development in engineering students. Computers & Graphics, 34, pp. 77-91, 2010

[30] Menenghetti, C., De Beni, R., Gyselinck, V. and Pazzaglia, F.: The joint role of spatial ability and imagery strategy in sustaining the learning of spatial descriptions under spatial interference. Learning and Individual Differences, 24, pp. 32-41, 2013

[31] Miller, D. I. and Halpern, D. F.: Can spatial training improve long-term outcomes for gifted STEM undergraduates? Learning and Individual Differences, 26, pp. 141-152, 2013

[32] Montello, D. R., Lovelace, K. L., Golledge, R. G. and Self, C. M.: Sex-Related Differences and Similarities in Geographic and Environmental Spatial Abilities. In: Annals of the Association of American Geographers. 89, pp. 515-534, 1999

[33] Paivio, A.: The empirical case for dual coding. In: J. C. Yuille (Ed.): Imagery, memory and cognition. Hillsdale, NJ: Lawrence Erlbaum Associates, pp. 307-332, 1983

[34] Potter, C. and van der Merwe, E.: Perception, imagery, visualization and engineering graphics. European Journal of Engineering Education, 28, pp. 117-133, 2003

[35] Séra, L., Kárpáti, A. and Gulyás, J.: A térszemlélet [Spatial ability] Pécs: Comenius Bt., 2006

[36] Sorby, S., Casey, B., Veurink, N. and Dulaney, A.: The role of spatial training in improving spatial and calculus performance engineering students. Learning and Individual Differences, 26, pp. 20-29, 2013

[37] Thomas, P. R. and McKay, J. B.: Cognitive styles and instructional design in university learning. Learning and Individual Differences, 20, pp. 197-202, 2011

[38] Williams, C. B. Gero, J., Lee, Y. S. and Paretti, M.: Exploring spatial reasoning ability and design cognition in undergraduate engineering students. In: Proceedings of the ASME 2010 International Design Engineering Technical Conferences & Computers and Information in Engineering Conference. Montreal: American Society of Mechanical Engineers, pp. 669-676, 2010

[39] Woodfield, R., Jessop, D. and McMillan, L.: Gender differences in undergraduate attendance rates. Studies in Higher Education, 31, pp. 1-22, 2006

Application of Catalan Numbers and the Lattice Path Combinatorial Problem in Cryptography

Muzafer Saračević[1], Saša Adamović[2], Enver Biševac[1]

[1] Department of Computer Sciences, University of Novi Pazar, Dimitrija Tucovića bb, 36300, Novi Pazar, Serbia, (muzafers, e.bisevac)@uninp.edu.rs

[2] Faculty of Informatics and Computing, Singidunum University in Belgrade, Danijelova 32, 11000 Belgrade, Serbia, sadamovic@singidunum.ac.rs

Abstract: This paper analyzes the properties of Catalan numbers and their relation to the Lattice Path combinatorial problem in cryptography. Specifically, analyzes the application of the appropriate combinatorial problem based on Catalan-key in encryption and decryption of files and plaintext. Accordingly, we use Catalan numbers for generating keys and within the experimental part we have applied the NIST (National Institute of Standards and Technology) statistical battery of tests for assessing the quality of generated keys was applied. A total of 12 quality assurance tests for Catalan-key were applied. A Java application is presented which allows the encryption and decryption of plaintext based on the generated Catalan-key and combinatorial problem of movement in integer network or Lattice Path. Experimental study yields the comparison of results in text encryption speed for combinatorial encryption methods (such as: Ballot Problem, Stack permutations and Balanced Parentheses) in comparison with Lattice Path method (in Java programming language).

Keywords: cryptography; Catalan numbers; Lattice path; combinatorial problems; encryption

1 Introduction

The subject of this research paper refers to the testing of Catalan numbers and the possibility of their use in cryptography. In addition, this research paper also illustrates the application of Lattice Path combinatorial problems which are based on the properties of Catalan numbers, used for encrypting and decrypting files and plaintext. The idea emerged, based on our previous research in the field of combinatorial problems, number theory and Catalan numbers. The pseudo-random numbers are of paramount importance in these procedures, particularly in key generation [1].

Number theory is most important in the process of key generation and also in the design of the cryptographic algorithm and in the cryptographic analysis [2, 3].

By using Catalan-key in encryption and decryption of files and plaintext, the basic idea is realized: generation of a long and unpredictable binary sequence of symbols from an alphabet on the basis of a short secret key, selected in a random manner. In this case, we will present the Lattice Path combinatorial encryption methods. In this way, a effective system performance for encryption is achieved [4].

2 Related Work

Applied number theory has numerous applications in cryptography, especially in the field of the integer sequences. Previous cryptographic algorithms were designed by using the integer sequences of the Fibonacci sequence and Lucas numbers.

Monograph [5] lists the concrete applications of these numbers with the possible solutions in terms of representation of Catalan numbers. This monograph contains a set of tasks that describe over 60 different interpretations of Catalan numbers. Some can be enumerated: the triangulation of polygons, paired brackets problem, a binary tree, steak permutations, Ballot problem, Lattice Path or the problem of motion through an integer grid, etc. In [6], the enumeration and generation of generalized Dyck words (path) based on Catalan numbers is discussed.

Paper [7] proposes cryptographic algorithms based on integer sequences of Catalan numbers as new methods of encryption. In the proposed encryption method, by using Catalan numbers, a large random number "n" is set as a secret key for encryption text in one file. The binary notation of Catalan number C_n, corresponding to the agreed upon secret key. In the mentioned paper, the proposed encryption methods use a logical XOR operation (exclusive-OR) on bits of *ASCII* binary code of messages.

More precisely, in the mentioned paper, the binary records of Catalan numbers and the messages, as well as, the XOR operations between them, simulate a One-Time Password (OTP) code. From the point of cryptanalysis, the proposed algorithm uses Catalan numbers, where it seems that they are resistant to the most known sorts of attacks. Identical characters in plain text are coded with different crypto characters. Thereby, "brute force attack" and the complete key search are difficult to perform. The time for encryption or decryption is independent of the characters in the data block.

Paper [8] presents an advanced technique for encryption based on values that satisfy properties of Catalan numbers. Key generation is based on a series of

Catalan numbers. The primary key value is fixed and defined by the user. In addition, each subsequent key value is double the previous one. The objective of the algorithm is to make cryptanalysis more difficult and to strengthen the algorithm. This paper emphasizes another important application of Catalan numbers, that is, the application in cryptosystem design, with techniques of recursive key generation.

Catalan numbers have the property of reclusiveness and their generation can be efficiently implemented with dynamic programming. Paper [9] gives a proposal of a *Vigenere* cipher modification, with the help of Catalan numbers and double transposition. In this paper, this method is based on Catalan numbers and it is presented as a mathematical method, which is used to create the initial cryptanalysis key with an emphasis on stronger key properties (balance and unpredictability).

From the point of view of cryptanalysis, it is emphasized that such a key is more difficult to detect, due to its specific properties and sequences that correspond to Catalan numbers.

3 The Basic Properties of Catalan Numbers

Catalan numbers (C_n) represent a sequence of numbers which are primarily used in computational geometry and in solving many combinatorial problems. Catalan numbers, $n > 0$, present a series of natural numbers, which appear as a solution to a large number of known combinatorial problems [5] (the number of possible paths in a discrete grid of n x n, problem of balanced parenthesis, stack permutations, binary trees, triangulation of polygons, etc.).

Catalan numbers are defined as [5]:

$$C_n = \frac{(2n)!}{(n+1)!n!} \tag{1}$$

Now we are going to analyze the values which are generated in the C_n set. For the purposes of Catalan numbers validity verification, we will use the binary notation. The basic feature that must be fulfilled is *bit property balance,* in the binary form for a certain number from the C_n set (we will referee to this property as *bit-balance* property).

For example, for the basis $n=29$ we have the space of keys $C_{29}=1,002,242,216,651,368$, i.e. the values that satisfy the property of Catalan number. By increasing the n basis, the key space is also drastically increasing. In order to provide a stronger, i.e. a more resistant mechanism of cryptanalysis encryption, it is necessary to choose keys whose value base is mainly greater than $n=30$.

Catalan number property [5]: A number can be labeled as a Catalan number when its binary form consists of numbers equal to "1" and "0" and starting with "1". If a binary notation of a Catalan number is connected with another mode of writing, most often with the mode of balanced parentheses, then "1" represents an open parenthesis and "0" represents a closed parenthesis, and it can be said that each opened parenthesis closes, or every bit 1 has its pair and that is the bit 0.

This property is known as a Dyck word. The Dyck words interpretation of Catalan numbers, so that C_n is the number of ways to correctly match n pairs of parentheses. C_n is the number of monotonic lattice paths along the edges of a grid (Lattice) with $n \times n$ square cells, which do not pass above the diagonal.

A monotonic path is one which starts in the lower left corner, finishes in the upper right corner, and consists entirely of edges pointing rightwards or upwards. Counting such paths is equivalent to counting Dyck words or number of *valid Dyck path*. Coordinate X stands for "move right" and Y stands for "move up".

A Dyck path of semilength n is a lattice path from (0,0) to (2n,0) consisting of n up steps of the form (1,1) and n down steps of the form (−1,1) which never goes below the x-axis y=0. Every Dyck word w of length ≥ 2 can be written in a unique way in the form $w = Xw_1Yw_2$ with Dyck words w_1 and w_2 [5].

Also, in [6] the definition is given for Dyck path of semilength n, which can be seen as a Dyck word, this is a word in {0,1} such that any prefix contains at least as many 1's as it contains 0's. Seeing a 1 as an opening parentheses and a 0 as a closing bracket, Dyck words can be seen as *well-formed parentheses systems*.

Dyck words definition [6]: Let B = {0, 1} be a binary alphabet and $X_1X_2 \ldots X_n \in B^n$. Let h: B → {−1, 1} be a valuation function with

$$h(0)=1,\ h(1)=-1 \text{ and } h(X_1X_2\ldots X_n) = \sum_{i=1}^{n} h(x_i)$$

A word $X_1X_2 \ldots X_n \in B2^n$ is called a Dyck word if it satisfy conditions:

- $h(X_1X_2 \ldots X_i) \geq 0$, for $1 \leq i \leq 2n - 1$
- $h(X_1X_2 \ldots X_{2n}) = 0$, where n is the semi-length of the word

In papers [10, 11, 12, 13] we performed generation testing of all the numbers for a given basis n which fulfill the above mentioned Catalan number properties. Based on the given analyzes, we can perform basic characteristics of keys generation based on Catalan number properties:

1. The condition of balance property must be fulfilled
2. It can serve as pseudo-random number generator (PRNG)
3. It can be used for realization of sequential algorithms
4. Based on the key belonging to the n basis, or $2n$-length key, appropriate n-permutations can be made

4 Application of Catalan Numbers and the Lattice Path Combinatorial Problem in File Encryption

Catalan numbers have found widespread use in solving many combinatorial problems. In [5, 6], concrete applications of these numbers are given, with possible solutions, when it comes to representation over certain combinatorial problems. The number of combinations and the manner of Catalan number generation represent a solution for certain combinatorial problems.

The binary notation of a Catalan number can be graphically represented in the integer network (another name, discrete grid or *Lattice Path*) which consists of a number of points in the Cartesian coordinate system. The problem is related to the number of calculations of the paths for movement through the integer network. The number of possible valid paths in the network is directly determined by the calculating formula for the C_n set of Catalan numbers. The pathways consist of *2n* steps with the initial point *(0,0)* and the end point *(n, n).* If we want to present the binary record of Catalan number in the form of movement through the integer network, then bit 1 represents movement to the right and bit 0 represents movement to the up.

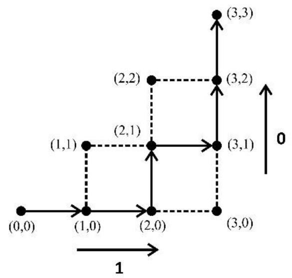

Figure 1

Lattice path based on the Catalan-key K3 = 110100

As shown in the figure, each path in the integer network can be encoded with specific order of vector movement to the right (1,0) and vector movement to the up (0,1). The selection of position movements (label 1, of the total number of *2n* movements) uniquely determines the path in the integer network, because the remaining positions represent the movement to the right (label 0). Thus, if we apply a valid Catalan number, the direction through integer network will do exactly *2n* movements, starting from the center point (0,0), and finishing it at the end point *(n,n)*.

We will check whether the movement in the integer network actually corresponds to Catalan number property. Based on the general case, a restriction has been introduced on the network of the size n × n and it thus, determines how many shortest paths exist in the integer network.

The path never crosses its diagonal. The main requirement is that each subsequent step must be closer to the target point. The number of possible paths in the network of dimension *n* is determined by Catalan number for the basis *n*, and the binary values in the C_n set are determining different combinations of the paths in the network. The presented movement procedure through the integer network based on the *binary* key record can serve as an idea for the system formation of plaintext encryption.

The encryption process based on discrete lattice can be applied to text messages (*String variant*), but also it can be applied to binary messages (*ASCII Text to Binary*). In addition, due to a better understanding, we will show the process of text encryption where the values are taken as a string record (the transposition cipher is obtained), and in the experimental part of this paper, we will present an example of taking an open text in a binary form (the substitution cipher is obtained). Based on the position of bits 0 and 1 in the binary key record, the elements in the text can have two states:

1. *Free element* – a character from the message which is not encrypted, or more precisely, which is not transferred in the cipher text. The free element is conditioned by the appearance of bit 1 (in the key), and it awaits its pair, bit 0.
2. *Engaged element* – a character from the message that is encrypted and transferred in the cipher text. This is an element that is conditioned by the appearance of bit 0 (in the key). In this way, the element is "closed" (transferred in the cipher text because bit 0 has appeared and it closes the corresponding bit 1).

The Code for encryption process based on movement through *LatticePath:*

```
n=0, A[n]=1; segment = 60;
1. count = file.length() / segment;
2. for (j = 0; j < count; j++) {
3. in.read(text, 0, segment);
4. EndPoint = segment - 1;
5. for (i=n; i>=0; i--) {
6. if (A[i] == 1) {
   path[Free] = text[EndPoint];
   Free ++;
   EndPoint --;
   }
7. else {
   ciphertext[Engaged] = path[Free-1];
   Engaged ++; Free --;
   path[Free] = 0;  }
   }
```

```
8. out.write(ciphertext);
   }
```

Explanation of source code:

(1) Splits the message (a file) on n-bit segments (fits to the basis of the n key); (2) The cycle for inclusion of the file segments starting from 0th up to the last segment; (3) In each segment, the reading of the elements is performed, from the first up to the last element in the segment; (4) Minimizing the position of the bits in the segment; (5) The cycle for reading the bits in the key; (6) if it is bit 1 then movement to the right follows (increasing the number of the free characters, and reducing the number of steps to the end point); (7) if it is bit 0 then movement to the up follows (takes character, which means that it increases the number of engaged characters and reduces the number of free ones); (8) at the end, when all the segments of the message are completed, the complete ciphertext is printed.

Example 1: The given key **K=877268**, which possesses the Catalan number property based on the binary record $(877268)_{10} = (11010110001011010100)_2$ for the given plaintext **P=SINGIDUNUM**. Moving through the integer network based on the binary representation of the key, starting from the source to the end point, we get the ciphertext *C=INIGSDNUMU*.

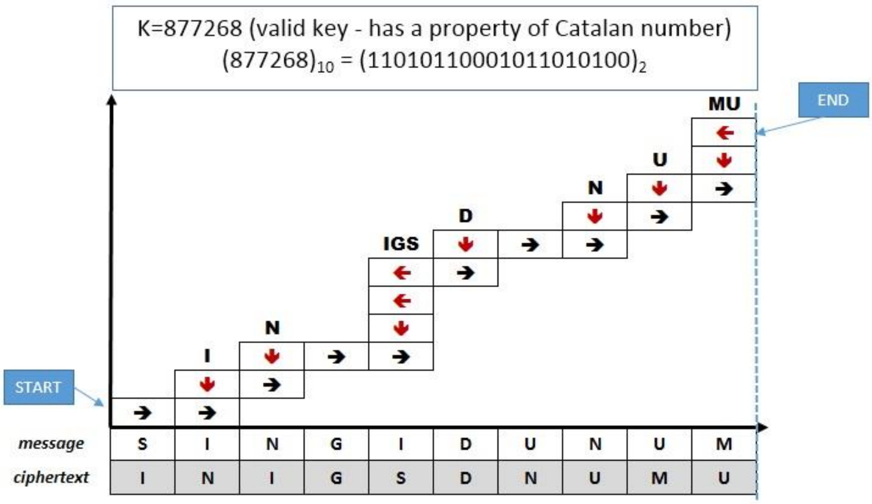

Figure 2

Encryption based on the principle of movement through a discrete grid

From the aforementioned process, we can identify two basic rules of movement: (1) Movement through the integer network never crosses its diagonal; (2) In every next step, the movement must be further from the START and closer to the END point.

Table 1

State of the characters in P = "SINGIDUNUM" based on Lattice Path

Bit in key	**Free elements - occurrence of bit 1**	**Engaged element - occurrence of bit 0**	**Parameters of the counter**
1	S		EndPoint=19, Free=1, Engaged=0
1	S, I		EndPoint=18, Free=2, Engaged=0
0	S,	I	EndPoint=17, Free=1, Engaged=1
1	S,N,	I	EndPoint=16, Free=2, Engaged=1
0	S,	I, N	EndPoint=15, Free=1, Engaged=2
1	S, G	I, N	EndPoint=14, Free=2, Engaged=2
1	S, G, I	I, N	EndPoint=13, Free=3, Engaged=2
0	S, G	I, N, I	EndPoint=12, Free=2, Engaged=3
0	S	I, N, I, G	EndPoint=11, Free=1, Engaged=4
0		I, N, I, G, S	EndPoint=10, Free=0, Engaged=5
1	D	I, N, I, G, S	EndPoint=9, Free=1, Engaged=5
0		I, N, I, G, S, D	EndPoint=8, Free=0, Engaged=6
1	U	I, N, I, G, S, D	EndPoint=7, Free=1, Engaged=6
1	U, N	I, N, I, G, S, D	EndPoint=6, Free=2, Engaged=6
0	U	I, N, I, G, S, D, N	EndPoint=5, Free=1, Engaged=7
1	U,U	I, N, I, G, S, D, N	EndPoint=4, Free=2, Engaged=7
0	U	I, N, I, G, S, D, N, U	EndPoint=3, Free=1, Engaged=8
1	U, M	I, N, I, G, S, D, N, U	EndPoint=2, Free=2, Engaged=8
0	U	I, N, I, G, S, D, N, U, M	EndPoint=1, Free=1, Engaged=9
0		I, N, I, G, S, D, N, U, M, U	EndPoint=0, Free=0, Engaged=10

We can conclude that the characters are taken from the plaintext at the moment when we get an ordered pair of 1 and 0. As long as the corresponding bit 1 does not get its pair of bit 0, the character has the status of "free", specifically it is not transferred in the ciphertext. The moment it gets its pair, the character will receive the status "engaged" and it is transferred to the ciphertext. Decryption is performed in reverse order of reading the binary key record, starting from the last bit and ending at the first bit in the key. In this case, (1,0)→(0,1) applies, and the occurrence of bit 0 indicates an open pair and 1 closed pair.

Example 2: Now let us take a value (for the key) that does not have Catalan number property, specifically for that value the rule of bit balance does not apply. We will try to use that key in the encryption of the text based on the movement through the integer network.

Case 1: The given key is *K=877011*, for which we can determine that it does not possess Catalan number property based on the binary record $(877011)_{10} = (11010110000111010011)_2$. And in the given plaintext *P=SINGIDUNUM.* Moving through the integer network, starting from the source point we cannot get to the end point, or more precisely, we cannot successfully complete the process.

From this case, we can see that the problem originated in the 11th step, more accurately, the problem is in the 11th bit in the key (bit 0), because it does not have its pair $(877011)_{10} = (1101011000\boxed{\mathbf{0}}111010011)_2$

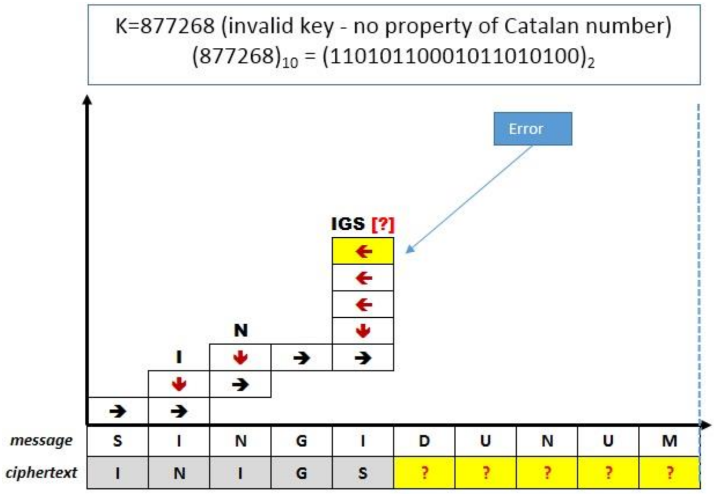

Figure 3
Unsuccessful encryption based on the key that is not Catalan (case 1)

Case 2: The given key is *K=877267*, for which we determined that it does not possess the bit balance property based on its binary record $(877267)_{10}$ = $(11010110001011010011)_2$. And in the given plaintext *P=SINGIDUNUM*. Moving through the integer network, starting from the source point we cannot get to the end point. In this case the movement exceeds the space of the network.

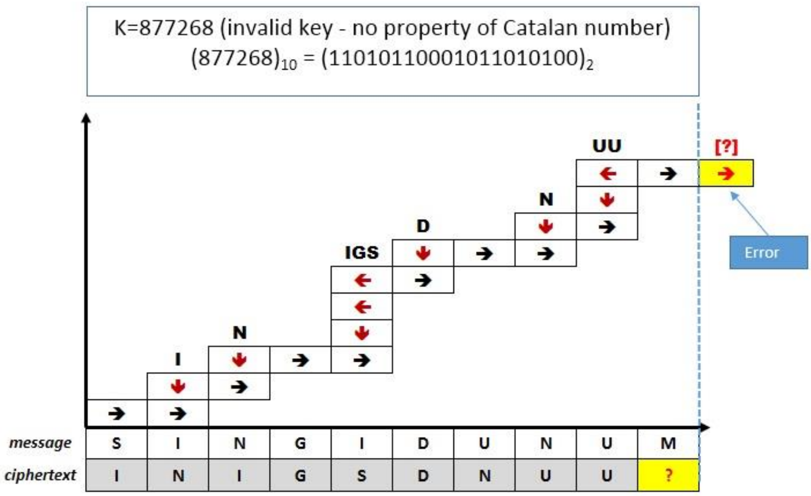

Figure 4
Unsuccessful encryption based on the key that is not Catalan (case 2)

From this case, we can see that the problem originated in the 20th step, more accurately, the problem is in the 20th bit in the key (bit 1), because it does not have its pair $(877267)_{10} = (1101011000101101001\boxed{\mathbf{1}})_{2.}$

In both cases we can conclude that the balance conditions are not fulfilled, and they are the basis for determining Catalan number properties.

This basic rule has caused the two basic conditions of movement through the integer network not to be fulfilled:

1. In the first case, the condition which requires that with every next step it has to be closer to the end point and that it must start and finish within the points that determine the diagonal is not fulfilled.
2. On the other hand, in the second case the introduced restriction on the network size $n \times n$ is not complied, so moving outside is impossible because it is exactly determined how many shortest paths there are in the integer network that never exceed its diagonal, and that is the C_n number.

The conclusion is that the key that does not possess Catalan number properties is not functional in the movement of the integer network. It is noteworthy that this process of encryption can be applied to the textual format of the message (string transposition) and reading the message in the binary form can be performed, hence the application of the described process in the binary message record is conducted.

Example 3: Given is the plaintext *P="SINGIDUNUM"*. If we apply convertor *ASCII Text to Binary* on *P*, then we get set of bits: *01010011 01001001 01001110 01000111 01001001 01000100 01010101 01001110 01010101 01001101.*

If we apply the key $K = (930516)_{10} = (11100011001011010100)_2$ based on which we will perform a permutation of bits from the message, then we will get the following binary record of the ciphertext: *C=01001001011010000 10001100110010101100011010000100101001001000 1100110110101001011.*

If we apply the *Binary to ASCII Text* convertor to the ciphertext C, we will get the textual record of the ciphertext *C="IhFecBRFmK"*.

In this way, we get the stronger ciphertext, that is, one character is replaced by some completely different symbol depending on the obtained permutation of the bits. In this case, we do not have the classical transposition code as in the previous examples; instead we have the code of substitution or replacement.

It is important to mention that here a conventional substitution is not realized, because one character from the message is not always replaced with the same character in the ciphertext. The mode of replacement depends on the key itself and its length, as well as from the disposition of the bits in a key. Also, it depends on the length of the message and the size of the message segments that are taken in the encryption process.

If from the previous example we compare the plaintext P="*SINGIDUNUM*", and the obtained ciphertext C="*IhFecBRFmK*", we can see that the first character "*I*" is replaced with "h", and the second character "*I*" with "*c*". It is the same case with the character "*U*", where the first has been replaced with "*R*" and the second one with "m". In this manner we provide a stronger encryption mechanism.

Paper [14] is related to investigating properties of Catalan numbers and their possible application in the procedure of data hiding in a text, more specifically in the area of steganography. The objective of this paper is to explain and investigate the existing knowledge on the application of Catalan numbers, with an emphasis on dynamic Catalan-key generation and their application in data hiding.

Based on many other research papers, we can observe that *Lucas–Catalan–Fibonacci* numbers are used, which are far superior compared to *Fibonacci* technique for data hiding. In the papers [15,16], new techniques for data hiding are suggested that use combinations of *Catalan–Fibonnaci* and *Catalan–Lucas* numbers sequences, which represents an improvement compared to the existing techniques for data hiding.

5 Experimental Work with Case Studies

Our Java software solution for this case study consists of three segments [4,11]. The first phase involves finding Catalan numbers (keys) based on the given n basis. This phase involves the next steps: (1) On the input n is assigned, (2) On the basis of n, the set C_n (space of keys) is calculated, (3) Selecting one Catalan number (key) from the C_n set, (4) The selected key is converted from the decimal to the binary record.

For implementing the Java software solution for *LatticePath* encryption method, it is important to note that we did not use a ready-made Java classes from the two standard APIs (JCA, JCE).

For details regarding the used Java classes, GUI and application functionality for *LatticePath* encryption method see our paper [11].

The form of the *Java GUI application* has the following options:

- Loading a Catalan-key
- Loading a file with text
- *LatticePath* encryption
- *LatticePath* decryption
- Checking the number of valid Catalan-keys for given n
- Generating the Catalan-keys that have Catalan number properties

The condition to start generating the entire space of Catalan-keys for a particular *n* basis is to determine the file in which the entire space of Catalan-keys will be recorded. After that, generation and recording of keys starts. This process may take time, depending on the input of *n*.

When starting a Java application, the first step is loading the Catalan-key from an external file. There is an algorithm for generating a complete space of Catalan-keys for a specific *n* basis. We use the method of manual taking of one of those values and storing them in the file *Cat-Key.TXT*.

After that, we include the active Catalan-key. We can create multiple Catalan-keys, but in one process we have to determine which key is active for the encryption or decryption process.

After loading the Catalan-key, the next step is loading the plaintext. After successful loading of the key and the message, the "*LatticePath encryption*" button becomes enabled. By clicking the button "*LatticePath decryption*", we can decrypt ciphertext and compare it to the message.

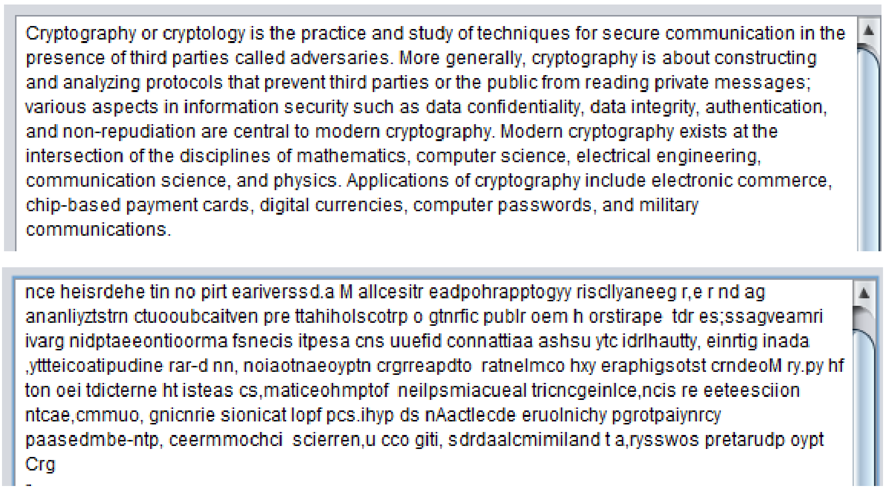

Figure 5

Example of *LatticePath* encryption of plaintext and displaying the ciphertext

Paper [11] examines the possibilities of applying of appropriate combinatorial problems in encryption and decryption of files and plaintext. A comparison is given for combinatorial encryption methods based on Catalan-key, such as: *Ballot Problem, Stack permutations* and *Balanced Parentheses*.

Table 2 shows the comparison of results in text encryption speed for these combinatorial encryption methods and Lattice Path method (in *Java* programming language).

Table 2

Comparison of different combinatorial encryption methods based on Catalan-key

Length of text (in characters, with spaces)	Text encryption methods (time in seconds)			
	Lattice Path combinatorics	*Stack permutations*	*Ballot Problem*	*Balanced Parentheses*
1000	0.001	0.001	0.001	0.001
5000	0.003	0.004	0.004	0.004
30000	0.024	0.026	0.025	0.025
50000	0.040	0.041	0.040	0.041
100000	0.085	0.087	0.085	0.087
500000	0.407	0.417	0.411	0.419
1000000	0.989	0.995	0.991	0.996

6 NIST Statistical Test Battery for the Catalan-Key

Considering that we use a Catalan number for key generation, we will apply the NIST (*National Institute of Standards and Technology*) statistical battery of tests for assessing the quality. The NIST's package of tests consist of multiple statistical tests that have been developed for testing the randomness of binary sequences that produce software or hardware on the basis of random or pseudo-random numbers. These statistical tests focus on the different types of inconsistencies that might exist in the sequence. Some tests are divided into subtests [17]. A total of 12 quality assurance tests for Catalan-key were applied.

For an input parameter we took the key that satisfies the property of Catalan number ε = *11101101011001010010100111111010100100100100011101110101000101001 0 01101111001010101000010110101100000*.

1) The objective of the test for examining the frequency in the series, based on an analysis of the relationship of 1s and 0s in a series of bits, more precisely, is to observe the equality of 1 of 0 occurrences. An approximate number of ones and zeroes is necessary in the sequence, which means that Catalan number property or the bit balance property is always a good result for this test. All subtests derived from this test are directly dependent on its successfulness. The invoke of this test is done through the method ***Frequency(n)*** where *n* is the bit length of the sample. The method uses the parameter ε (a series of bits in the key).

```
FREQUENCY TEST - COMPUTATIONAL INFORMATION:

 (a) The nth partial sum = 6
 (b) S_n/n               = 0.006000

SUCCESS       p_value = 0.849515
```

Since $P \geq 0.01$, it is considered that the sequence is random.

2) The test for examining the frequency in the block shows the ratio of 1s and 0s in n-bit blocks. The purpose of this test is to detect equality number of 1s and 0s in each n-bit block. This test is invoked through the method ***BlockFrequency(M,n)*** where M is the length of every block, and n is the length of the bit sample. The same as with the test for testing frequency in the series, this test uses the parameter ε.

```
BLOCK FREQUENCY TEST - COMPUTATIONAL INFORMATION:

(a) Chi^2 = 1.718750
(b) # of substrings = 7
(c) block length = 128
(d) Note: 104 bits were discarded

SUCCESS              p_value = 0.973758
```

The test displays that the sequence is random, since $P \geq 0.01$.

3) The test for examining the successive repetition of the same bits in the series refers to the total number of successive repetitions of a number in the series. The purpose of the test is to determine whether the number of consecutive repetitions of 0s and 1s matches the expected random sequence. This test is invoked through the method ***Runs(n)*** where n is the length of the bit sample. As an additional parameter, input ε is used.

```
RUNS TEST - COMPUTATIONAL INFORMATION:

 (a) Pi                         = 0.503000
 (b) V_n_obs (Total # of runs) = 465
 (c) V_n_obs - 2n pi (1-pi)
      ----------------------- = 1.564499
      2 sqrt(2n) pi (1-pi)

SUCCESS              p_value = 0.026930
```

It is considered that the sequence is random, because the result is $P \geq 0.01$.

4) The test for examining the longest consecutive repetition of units in n-bit blocks determines whether the length of the longest continuous repetition matches the length which is expected in the series of random numbers. This test is invoked through the method ***LongestRunOfOnes(n)*** where n is the length of the bit sample. The test is set in the way that for M (the length of each block) three values are used: M = 8 (where n is minimum 128), M = 128 (where n is minimum 6272), and M = 104 (where n is minimum 750,000). In this case, the test is M = 8. As an additional parameter, the input ε is used.

```
LONGEST RUNS OF ONES TEST - COMPUTATIONAL INFORMATION:

 (a) N (# of substrings)  = 125
```

```
 (b) M (Substring Length) = 8
 (c) Chi^2                = 3.500324
                   F R E Q U E N C Y
<=1    2    3   >=4  P-value Assignment
 26   47   22   30   SUCCESS p_value = 0.320720
```

The test result shows that $P \geq 0.01$, so the sequence is considered random.

5) The test for examining the state of the binary matrix refers to the verification of the linear dependence between the subseries of fixed length from the original series. The test is invoked through the method ***Rank(n)*** where *n* is the length of the bit sample. The method uses the parameter ε (series of bits in the key record).

```
RANK TEST - COMPUTATIONAL INFORMATION:
 (a) Probability P_32 = 0.288788
 (b)             P_31 = 0.577576
 (c)             P_30 = 0.133636
 (d) Frequency   F_32 = 0
 (e)             F_31 = 1
 (f)             F_30 = 0
 (g) # of matrices    = 1
 (h) Chi^2            = 0.731373
 (i) NOTE: 0 BITS WERE DISCARDED.
SUCCESS      p_value = 0.693720
```

It is considered that the sequence is random, because the result is $P \geq 0.01$.

6) The test for examining the discrete Fourier transform aims to detect periodic functions. In the tested series, the aim is to indicate deviation from a random assumption (refers to the highest value set of discrete Fourier transform). The intention is to find out whether the number of the highest values exceeding *95%* is significantly different from the remaining *5%.* This test is invoked through the method ***DiscreteFourierTransform(n)*** where *n* is the length of the bit sample.

```
FFT TEST - COMPUTATIONAL INFORMATION:
 (a) Percentile = 95.000000
 (b) N_l        = 475.000000
 (c) N_o        = 475.000000
 (d) d          = 0.000000
SUCCESS             p_value = 1.000000
```

7) The test for examining the non-overlapping samples is based on the analysis of the frequency of occurrence of all possible *n*-bit patterns where there is no overlapping in the entire examined series. The test detects whether the number of non-overlapping patterns is approximately equal to the number expected for the series of random numbers. This test is invoked through the method ***NonOverlappingTemplateMatching (m,n)*** where *m* is the length of the bits and *n* is the length of the bit sample.

```
NONPERIODIC TEMPLATES TEST - COMPUTATIONAL INFORMATION
LAMBDA = 0.228516   M = 125      N = 8  m = 9  n = 1000
F R E Q U E N C Y - Template W_1 W_2 W_3 W_4 W_5 W_6 W_7 W_8
Chi^2   P_value Assignment Index
1.769891 0.987272 SUCCESS   148
128 Templates = SUCCES, 20 Template = FAILURE
```

8) The test for examining the overlapping samples examines the frequency of occurrence of all possible *n*-bit patterns where overlapping occurs in the entire examined sequence. The test should detect whether the number of overlapping patterns is approximately equal to the number expected for the series of random numbers. The test is invoked through the ***OverlappingTemplateMatching (m,n)*** where *m* is the length of the bits and *n* is the length of the bit sample.

```
OVERLAPPING TEMPLATE - COMPUTATIONAL INFORMATION:
 (a) n (sequence length)       = 1000
 (b) m (block length of 1s)    = 9
 (c) M (length of substring)   = 1032
 (d) N (number of substrings) = 0
 (e) lambda [(M-m+1)/2^m]      = 2.000000
 (f) eta                       = 1.000000
F R E Q U E N C Y
0   1   2   3   4 >=5   P-value Assignment
0   0   0   0   0   0   SUCCESS
```

9) The test for examining the linear complexity determines whether the sequence is sufficiently complex to be considered random. This test is invoked through the method ***LinearComplexity (M, n)*** where *M* is the length of every block, and *n* is the length of the bit sample. The method uses an additional parameter *ε*.

```
LINEAR COMPLEXITY - COMPUTATIONAL INFORMATION:
M (substring length)     = 500
N (number of substrings) = 2
F R E Q U E N C Y
```

```
C0   C1   C2   C3   C4   C5   C6    CHI2     P-value
Note: 0 bits were discarded!
0    0    0    2    0    0    0  2.000106 0.919689
```

Since $P \geq 0.01$, it is considered that the sequence is random.

10) The serial test is used to determine the frequency of all possible overlapping of the *n*-bit sequence in the entire sequence. This test is invoked through the method ***Serial (m, n)*** where *m* is the length of every block, and *n* is the length of the bit sample. Also, here an additional parameter *ε* is used.

```
SERIAL TEST - COMPUTATIONAL INFORMATION:
 (a) Block length    (m) = 16
 (b) Sequence length (n) = 1000
 (c) Psi_m               = 146324.928000
 (d) Psi_m-1             = 97500.608000
 (e) Psi_m-2             = 64765.376000
 (f) Del_1               = 48824.320000
 (g) Del_2               = 16089.088000
SUCCESS            p_value1 = 0.011201
SUCCESS            p_value2 = 0.949014
```

Since P_1 and $P_2 \geq 0.01$, it is considered that the sequence is random.

11) The test for examining the approximate entropy examines the frequency of occurrence of all possible overlapping of *n*-bit patterns in the series. The aim is to compare the frequency of overlapping blocks with the expected results. This test is invoked through the method ***ApproximateEntropy (m, n)*** where *m* is the length of every block, and *n* is the length of the bit sample.

```
APPROXIMATE ENTROPY TEST - COMPUTATIONAL INFORMATION:
 (a) m (block length)      = 10
 (b) n (sequence length)   = 1000
 (c) Chi^2                 = 973.830581
 (d) Phi(m)                = -5.747581
 (e) Phi(m+1)              = -5.953813
 (f) ApEn                  = 0.206232
 (g) Log(2)                = 0.693147
Note: The blockSize = 10 exceeds recommended value of 4
SUCCESS            p_value = 0.867027
```

12) The test for examining the random summations determines whether the cumulative sum of the partial sequences that occur in the series which are tested is too big or too small in relation to the expected behavior of this cumulative sum of random sequences. The test is invoked through the method ***CumulativeSums (mode, n)*** where there is *mode = 0* or *mode = 1*, and *n* is the length of the bit sample.

```
CUMULATIVE SUMS (FORWARD) TEST - COMPUTATIONAL INFORMATION:

(a) The maximum partial sum = 14
SUCCESS      p_value = 0.997649

CUMULATIVE SUMS (REVERSE) TEST - COMPUTATIONAL INFORMATION:

(a) The maximum partial sum = 20
SUCCESS      p_value = 0.941731
```

We find out that P_1 and $P_2 \geq 0.01$, more precisely, for the *forward* and the *reverse* test, so it is considered that the sequence is random.

Conclusion and Further Work

From the achieved results, we can say that we have given a few new applications for Catalan numbers, primarily as a generator of pseudo-random numbers in combination with several combinatorial problems, with the purpose of text encryption and decryption. We emphasized the application of movement through the integer network methods in text encryption. Within the theoretical part of the research the tested basic Catalan number properties are mentioned, and the focus was on the bits balance property in the binary notation of Catalan number.

We then provided examples and experimental results of text encryption speed for some combinatorial encryption methods (such as: Ballot Problem, Stack permutations and Balanced Parentheses) in comparison with Lattice Path method.

An experimental study is given that includes specific algorithms for LatticePath encryption and decryption, which are implemented in the Java programming language. The implemented GUI application has all the necessary elements for easy and efficient file encryption and decryption, loading of Catalan-keys, displaying the content of the encoding text, key generation, etc. In the experimental section of this paper, we applied the NIST statistical test battery to assess the quality of the keys based on Catalan number properties.

The proposed methods can be further improved and adapted to the modern approaches in cryptography. Some studies are dealing with the application of number theory in the realization of visual cryptography algorithms and in solving the problem of sharing secrets. The visual cryptography is primarily based on cryptographic methods that perform encryption and data hiding within a set of images, and the reconstruction of the protected or encrypted data is done by a direct, visual examination. Additionally, number theory finds increasing application in the realization of basic cryptographic techniques dealing with secure data exchange.

Beside steganography and visual cryptography, some other suggestions for future work in the field of application of Catalan numbers in cryptography can be given. In [18] the authors give the possibility of applying Catalan numbers in quantum cryptography. In many scientific studies, papers and monographs, when discussing the future of cryptography, quantum cryptography is indicated, which emerged as a result of discoveries in the field of quantum computing [19]. It is very important to mention that quantum cryptography and DNA, in the near future, will present the basis for the protection of confidential documents. According to that, a proposal for future work could relate directly to the application of Catalan numbers in quantum cryptography and the improvement of existing algorithms and methods.

With regard to the fact that cryptography is a very dynamic and widespread field, this paper covers only part of the mathematical concepts and provides a contribution for the application of number theory, in the field of cryptography.

References

[1] Horak, P., Semaev, I., Tuza, I. Z. An application of Combinatorics in Cryptography, Electronic Notes in Discrete Mathematics, 2015, Vol. 49, pp. 31-35

[2] Higgins, P. M. Number Story: From Counting to Cryptography, Springer Science & Business Media, Berlin, Germany, 2008

[3] Lachaud, G., Ritzenthaler, C., Tsfasman, M. A. Arithmetic, Geometry, Cryptography, and Coding Theory, American Mathematical Society, United States, 2009

[4] Saračević, M. Application of Catalan numbers and some combinatorial problems in cryptography (Bachelor's thesis), Faculty of Informatics and Computing, Singidunum University in Belgrade, 2017

[5] Koshy, T. Catalan Numbers with Applications, Oxford University Press, New York, 2009

[6] Duchon, P., On the enumeration and generation of generalized Dyck words, Discrete Mathematics, 2000, Vol. 225, No. 3, pp. 121-135

[7] Amounas, F., El-Kinani, E. H., Hajar, M. Novel Encryption Schemes Based on Catalan Numbers, International Journal of Information & Network Security, 2013, Vol. 2, No. 4, pp. 339-347

[8] Srikantaswamy, S. G., Phaneendra, H. D. A Cryptosystem Design with Recursive Key Generation Techniques, Procedia Engineering, 2012, Vol. 30, pp. 170-173

[9] Pratama, G. M., Tamatjita, E. N. Modifikasi algoritma vigenère cipher menggunakan metode Catalan number dan double columnar transposition, Journal Compiler, 2015, Vol 4, No 1, pp. 31-40

[10] Mašović, S., Saračević, M., Stanimirović, P. Alpha-Numeric notation for one Data Structure in Software Engineering, Acta Polytechnica Hungarica: Journal of Applied Sciences, 2014, Vol. 11, No. 1, pp. 193-204

[11] Saračević, M., Koričanin, E., Biševac, E. Encryption based on Ballot, Stack permutations and Balanced Parentheses using Catalan-keys, Journal of Information Technology and Applications, 2017, Vol. 7, No. 2, pp. 69-77

[12] Saračević, M. Methods for solving the polygon triangulation problem and their implementation (PhD thesis), Faculty of Science and Mathematics, University of Niš, 2013

[13] Stanimirović, P., Krtolica, P., Saračević, M., Mašović, S. Decomposition of Catalan numbers and Convex Polygon Triangulations, International Journal of Computer Mathematics, 2014, Vol. 91, No. 6, pp. 1315-1328

[14] Saračević, M., Hadžić, M., Koričanin, E. Generating Catalan-keys based on dynamic programming and their application in steganography, International Journal of Industrial Engineering and Management, 2017, Vol. 8, No. 4, pp. 219-227

[15] Pund-Dange, S., Desai, C.G., Data Hiding Technique using Catalan-Lucas Number Sequence, Indian Journal of Science and Technology, 2017, Vol. 10, No. 4, pp. 12-17

[16] Aroukatos, N., Manes, K., Zimeras, S., Georgiakodis, F. Data hiding techniques in steganography using Fibonacci and Catalan numbers. In Information Technology: New Generations (ITNG), Ninth International Conference, 2012, pp. 392-396

[17] Rukhin, A., Soto, J., Nechvatal, J., Smid, M., Barker, E. A statistical test suite for random and pseudorandom number generators for cryptographic applications. NIST Special Publication, USA, 2010

[18] Cohen, E., Hansen, T., Itzhaki, N. From entanglement witness to generalized Catalan numbers, Scientific Reports, 2016, Vol.6, Art. No: 30232

[19] Kościelny, C., Kurkowski, M., Srebrny, M. Modern Cryptography Primer: Theoretical Foundations and Practical Applications, Springer Science & Business Media, Berlin, Germany, 2013

Simulated Medical Ultrasound Trainers A Review of Solutions and Applications

Csaba Urbán[1], Péter Galambos[1], György Györök[2], and Tamás Haidegger[1,3]

[1]Antal Bejczy Center for Intelligent Robotics (IROB), EKIK, Óbuda University, Bécsi út 96/b, H-1034 Budapest, Hungary, {csaba.urban, peter.galambos, tamas.haidegger}@irob.uni-obuda.hu

[2]IROB Székesfehérvár, Alba Regia Technical Faculty, , Óbuda University, Bécsi út 96/b, H-1034 Budapest, Hungary, gyorgy.gyorok@irob.uni-obuda.hu

[3]Austrian Center for Medical Innovation and Technology (ACMIT), Viktor-Kaplan-str. 2, A-2700 Wiener Neustadt, Austria

Abstract: Ultrasound is one of the most widely employed real-time diagnostic imaging modalities in modern medicine. To use it efficiently, and to correctly interpret the images, the medical staff needs to acquire sophisticated skills. In this article, a review is provided on the devices and methods of modern ultrasonography training employing high-end information technology tools. It spans from the most critical moments, examination, to image-based training methods. Hardware and software based solutions are introduced along their current limitations. A comprehensive overview is provided about the most popular ultrasound simulators based on a common set of criteria, including their basic features, simulation methods, training concept and the supported scanning protocols. Tutors shall be able to make better informed decisions based on the enlisted characteristics of the various systems. The principles of simulation methods and techniques are also discussed in details along with the challenges of the field.

Keywords: medical imaging; ultrasound diagnostics; ultrasound simulation & training

1 Introduction

Medical ultrasound (US) has quickly gained popularity as a primary diagnostic imaging modality, since it is non-invasive and widely available. It played a major role in the rapid advancement of Computer-Integrated Surgery [1]. The US devices developed in the last years are getting smaller and more portable, relying on revolutionary multi-transducer matrices and crystal arrays; however their usage, and especially the interpretation of the images still relies heavily on the personal qualities of the human sonographer. The necessary skills require solid routine gained through extensive, hands-on training. Consequentially, during the basic medical doctoral (M.D.) education, and especially during the US practitioner training, it has utmost importance to acquire the necessary skills and experience in a controlled environment, to allow credentialing in a comparable manner. During regular examinations, there are specific, important US protocols, which are inconvenient to perform on humans e.g., the transthoracic echocardiography (TTE) or the transesopageal echocardiography (TEE). In such cases, the use of US simulators is recommended, and they allow the sonographers to focus on efficient tasks execution.

Medical US was originally developed to explore and study the anatomy and function of human organs. However, this imaging technique can also be applied for instrument tracking and as a guidance tool in a wide range of interventions [2–4]. More recently, US has been successfully employed for treatment as well, especially with the application of High-Intensity Focused Ultrasound (HIFU) [5].

The first US examinations were performed in the early 1970s, when the underlying technology allowing to detect the reflected ultrasound waves from internal human organs has become affordable. Over the years, the field of US imaging has evolved rapidly, whereupon this modality has become one of the cheapest and most diversely used for medical imaging diagnostics. The goal of the ongoing development on one hand is to produce clearer US images with higher resolution (finer details), and on the other hand to decrease the size of the US devices to improve portability. One of the most important breakthroughs in medical US imaging was the advent of the color Doppler US method, which is a non-invasive technique to directly measure the blood flow within the heart or in any other organ that the US wave can reach [6].

Since there are no known harmful side effects (e.g., ionizing radiation) of the diagnostic US (except for some specific cases, like the local heating in a certain wave range), it is routinely employed in numerous clinical procedures, named ultrasound-guided interventions. For example, during a breast biopsy, US can be used as a real-time needle tracker tool to guide the physician to the target anatomical structure along the planned trajectory. Efficient software algorithms are also able to support interventional radiology with automated segmentation [7]. Novel ”ultrasound-on-a-chip” and similar manufacturing techniques promise further improvements, such as integration with robot-assisted minimally invasive surgery and more creative utilization in the near future [8, 9].

Since the proper evaluation of a US image requires years of practice, it is important to train the sonographers in a practical and lifelike environment. There are several studies giving recommendations about the number of examination to be performed during their training period:

- 20 mentored examinations are recommended for sentinel node biopsy [10];
- 25 for fetal echocardiography [11];
- 300 for critical care [12];
- 480 for echocardiography [13];

- the European Association of Cardiovascular Imaging (ESC) also recommends hundreds.

Unfortunately, these high numbers may still not be enough to develop the proper US-based diagnostic skills. In an earlier publication, it was shown that after the recommended number of cases on the physical simulator, some physicians had problems performing real-life examinations (effect of over-training) [14]. It can be concluded that the education of medical US is a major challenge, and computer-driven US trainers could provide the expected enhancement. Studies showed that physicians who received not just theoretical, but simulator-based training as well, cloud significantly improve their skills in the evaluation of US images [15]. Another study involving 262 clinical fellows showed that performance depends on the number of years spent as a resident, and on the number of scans performed during these years. However, the number of didactic hours spent on US did not lead to measurable improvement in the residents' performance beyond 15 hours per year [16].

Simulated US training devices (relying on sophisticated human phantoms or completely simulated tool–tissue interaction) have become a financially and practically appealing solution for many medical educational institutions [17]. Systematic skill measurement (i.e., measuring the learning curve [18]) and credentialing (offering certificates for skill training) are also key advantages present. In 2013, the Consortium for the Accreditation of Sonographic Education endorsed a new US simulator based training program to help standardizing assessments and educations [19].

During the last few years, numerous experimental US trainer projects have been launched with the aim to develop commercial devices, primarily for teaching schools.

This paper provides a survey of the State-of-the-Art US training solutions. In the Section 2, the latest available training practices are introduced, then the main simulator development directions and categories are reviewed in Section 3 and last, in Section 4, a technological overview is provided.

2 A review of computer-driven training approaches

US training has a long tradition. Widely recognized organizations, like the Society and College of Radiographers, the Radiological Society of North America and The British Medical Ultrasound Society [20], are committed to education, development and standardization of US procedures. They published a handbook ”Guidelines for Professional Ultrasound Practice” recently[1], as the most important source of information for both experienced sonographers and other medical practitioners. This book provides a general and organ-specific overview of US examinations. The first part contains information about the safety of the medical US, ergonomic practice, including patients with high Body Mass Index (BMI), examination times, and last but not least contains guidelines on how the sonographer should perform the intimate examinations professionally.

[1] https://www.bmus.org/policies-statements-guidelines/professional-guidance/guidelines-for-professional-ultrasound-practice

The need for high throughput education and training became clear for US, but until 1995, no international, and very few relevant national recommendations were published. In 1995, the World Health Organization (WHO) published the first training manual in this topic [21]. The rapid development of US equipment and indications for the extension of this medical imaging procedure into therapy indicated the need for a new ultrasonography manual. In 2011, the WHO published a new manual for medical US [21], which presents the requirements towards the practitioners', and describes important guidelines ranging from the basic physics of US to the detailed description of each organ's or body part's examination. It starts with general rules and recommendations, the list of general indications for B-Scan and duplex techniques, patient positioning, coupling agents and the interpretation of the US images of different body parts, the choice of the proper transducer, the preparations and the scanning technique described. The normal and the pathological findings are also discussed accompanied by rich visual illustration [21].

These manuals demonstrate what shall be the baseline knowledge for medical practitioners. Based on the clinical experience and practical competencies, a multi-level concept of US practice would be feasible. The European Federation of Societies for Ultrasound and Biology proposed the following minimal training requirements divided into 3 levels [22]:

- Level 1 practitioners are required to perform common examinations safely and accurately, they also have to recognize and differentiate normal anatomy, common abnormalities and pathologies;
- Level 2 extends Level 1 requirements with recognizing and diagnosing almost all pathologies, performing basic, non-complex US-guided invasive procedures;
- Level 3 is the most advanced level of practicing, where performing special US examinations and advanced US-guided invasive procedures is required.

US scanning protocols in emergency (ER) care also belong to the critical part of the training, since in trauma care (e.g., patients in shock, respiratory distress, and cardiac arrest), typically US can provide the fastest, yet reliable diagnostic support [23]. The major emergency US protocols include the followings: ACES, BEAT, BLEEP, Boyd Echo, EGLS, Elmer/Noble, FALLS, FAST, Extended-FAST (eFAST), FATE, FEEL-Resuscitation, FEER, FREE, POCUS, RUSH-HIMAP, RUSH, Trinity and UHP, covered by large international professional organizations [24–26].

One of the main problems for novice practitioners is the mental mapping from 2D US slices to 3D anatomy [27]. Computer-based simulators have an important role, here with the main advantage of the wide range of available cases, which are stored in a "case database". Manufacturers create their own databases, which consist of many simulation scenarios grouped to modules by the simulated organ or body part. With these, typical, yet very important US procedures can also be simulated [28–31]. Using US simulators together with case databases, a highly standardized educational program can be developed, and objective requirements can be set for assessment. Another major advantage of these simulators is the ability to show a virtual 3D model of the examined anatomic region. These 3D models help to build the *mental model* of the anatomy, which is one of the core skills the sonographer must acquire. The virtual feedback allows to verify the mental model, mapping the 2D ultrasound plane to 3D anatomic structures and vice versa [32]. There are fundamental US examinations, like echocardiography, where it is challenging to identify the critical parts of the heart [33], because there is very little contextual information. In other cases, like intravascular US examination, there is a completely different workflow to be employed [32].

A virtual model can visualize anatomic parts in 3D, which opens up numerous training concept variations to the practitioners. A virtual scene allows to decrease the level of complexity by hiding the irrelevant organs, and showing the more important information in greater details. Most simulators show not just the scan plane, but importantly, the surface of the virtual patient, bones, skin, etc. as well.

In the past few years, Augmented Reality (AR) applications emerged in the medical field, and this domain is also contributing to an unprecedented boost in medical education technology. In [34], two methods were compared, how AR can be used for US training. Many modern computer-based US simulators aim to resolve this by showing a 3D model of the examined anatomy, but these are still rendered on a 2D screen. At the high end, e.g., EchoPixel's True 3D Viewer allows to visualize and interact with tissues and organs in a completely open 3D space [35].

3 Methods for Simulated Ultrasound

Since computer-based simulators do not use real US probes and realistic phantom models, the output image shown during the training falls behind reality. A high fidelity and fast method is required to synthesize the simulated US slices, depending on the position and orientation of the dummy probes. In the literature, three major methods can be found to generate US-like images [32], and the following subsections give a brief explanation of the different approaches:

- interpolative;
- generative image-based and
- generative model-based method.

3.1 Interpolative method

The interpolative simulation of US is the most widely employed method to produce synthetic US output. In this case, the 2D images are interpolated from pre-acquired, rendered 3D US volumes. The quality of these interpolated images can be very high, since they are derived from real US source. At the same time, the quality of the results depends on the probe's orientation, because US images have view-dependent qualities. Accordingly, in the off-line pre-process phase, undesirable artifacts should be removed, and during the on-line simulation, the simulated image should be enhanced to include the proper view dependent features [36]. If the acquired 3D ultrasound volume contains artifacts, it is difficult to replace them with correct data. A viable workaround could be to acquire several volumes from different viewpoints, yet a high number of volumes is required. The US simulators employing this technique may require an algorithmic solution to collect 3D volumes from real patients that can be managed by free hand scanning [32]. During the acquisition, the transducer puts pressure on the skin, resulting in tissue deformation, but there are efficient algorithms and models to correct these [37]. Compared to other methods, the major advantage is the simplicity of the implementation, leading to a real-time realization [32].

3.2 Generative image-based method

Generative image-based methods synthesize US images from other modalities, like Computed Tomography (CT) or Magnetic Resonance Imaging (MRI). These are typically aimed for for non real-time applications (e.g., transducer design) to simulate wave propagation. To enable the use these methods in real-time applications, the synthesis of US-like slices from other types of images needs to be optimized; broken down into pre-processing and run-time phases. Shams et al. presented a novel method in which the pre-processing phase produces detailed fix-view 3D scattering images, and the run-time phase generates view-dependent US artifacts [38]. An acoustic model was also developed of the US in the run-time phase. Combining the scattering images with the generated ones by the acoustic model results in real-time US images. In [39], a CT-based tissue model for US simulation was presented, which relies on an estimation of the transfer function from a 2D CT slice into a tissue model applicable to US simulation. This approach also requires an offline preprocessing phase to produce the necessary inputs for the simulation algorithm, such as the acoustic map, back-scattering map and the attenuation coefficient map. In the case of CT, the correlation between the Hounsfield units and acoustic impedance was derived in [36, 38], and used to simulate absorption, reflection and transmission. The main advantage of this CT-based method is that large patient datasets are already available.

3.3 Generative model-based method

To simulate small and moving anatomies, such as the heart, the generative methods based on CT do not provide information at the expected level of details. To overcome this problem, computer modeling the anatomy is one solution. In the literature, numerous heart models can be found, however most of them are static. The dynamics of the heart cannot be handled realistically with static geometric models, thus in [40], a time-varying mathematical model was presented for vessel-representations of the human heart, and in [41], time-varying MR volumes were used to construct a heart model. One major drawback of model-based simulation is a very complicated procedure to generate new cases. Ontologies can also be used to construct high-fidelity heart models for US simulation, however, those cannot be generalized easily [40].

4 Available products and technologies

In this Section, commercial US simulators are surveyed to highlight the most important characteristic of the training products currently available. In order to give a comparative review, discussion is based on the following common set of criteria:

- the basic features provided;
- US simulation method employed;
- training concept *(where known)*;
- supported US scanning protocols;
- user interface and interaction;
- clinical validation/development status;
- DICOM compatibility.

Table 1 presents a comprehensive overview of the commercially available systems to the authors' best knowledge. Beside these rather concrete aspects, the user interface is also critical, thus the properties and issues related to the user experience are addressed. The user interface necessarily consists of an input and output device; in this context, input devices are the different kind of dummy transducers, and the output devices are mainly visual displays. Probe tracking is an integral feature of the simulators, and thus each system incorporates orientation and position sensors, but tracking technology and methods vary [42]. For example, the CAE Vimedix and Schallware simulators use an expensive electromagnetic system to record the probe pose relative to the mannequin, while the SonoSim simulator's probe is based on a more affordable RFID positioning technology to acquire location information [43].

In the following subsections, the most popular systems are reviewed based on the above mentioned criteria.

4.1 Vimedix

Vimedix is a recent US education platform (developed by CAE Healthcare, Montreal, QC) (Fig. 1). It contains 3 base modules running on a common software platform: Vimedix Cardiac, Vimedix Abdo and Vimedix Obstetrics / Gynaecology (Ob/Gyn). The Cardiac and Abdo modules support the TTE and TEE, furthermore they also support Color Doppler, Continuous Wave Doppler and Wave Doppler of the Heart simulations. These modules, particularly the TTE and the TEE, require a detailed, anatomically correct solid beating model of the heart. To serve these requirements, a model-based generative simulation was necessary, that can also replicate artifacts and give an opportunity to find the appropriate acoustic windows [28, 32, 44].

It provides male and female multi-purpose mannequins, a phased array, transq-esophageal and curvilinear transducers (Fig. 1). With these devices, most of the real-life and frequent US examinations can be simulated. The Vimedix training software's

Table 1
Summary of the commercial ultrasound simulator systems

Simulator	Simulation methods	Training material	Basic feature set
Vimedix	Generative model-based simulation	Cardiac, Abdo, Ob/Gyn, E-Learning	Doppler, 3D AR, Bi-Plane and M-Mode
SonoSim	Generative image-based method (Pre-recorded 3D US by free hand)	Modular format: course, knowledge assessment, hands-on training with numerous cases	virtual human patient, Power Doppler, Real-Time Assessment and Performance Tracking
Schallware	Generative image-based method (By free hand)	Internal medicine, ER, Ob/Gyn, fetal heart cases	B Mode, M Mode, 4D B Mode, Colour Doppler, ROI
UltraSim, Compact-Sim	Interpolative method (Pre-recorded 3D US)	Abdomen, Ob/Gyn, Breast, Vascular, Neck and ER	B-mode, Color and Spectral Doppler, Intuitive control panel
ScanTrainer	Interpolative method (Pre-recorded 3D US)	Transvaginal, Trans-abdominal, Ob/Gyn, FAST, eFAST	B Mode, M Mode, Doppler, haptic probes, virtual patients

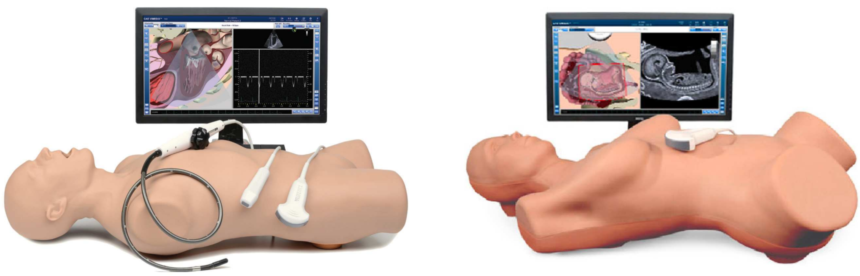

Figure 1
The Vimedix Cardiac, Abdo (left) and the Vimedix Ob/Gyn platforms [28].

Cardiac/Abdo module has over 150 pathological cases validated through numerous scientific publications, and the Ob/Gyn module has over 40 pathologies from the first and second trimester of pregnancy.

Both modules support 3D augmented reality with animated anatomy that can be moved and rotated in 3D to learn structure identification and spatial orientation. The Vimedix displays this animated model side-by-side with the simulated US images to enhance the efficiency of the training (Fig. 2).

Vimedix also provides measurement functionalities, including length, diameter, circumference and area of structures. Report functionality is also supported, which is consistent with typical scanning protocols and workflows. DICOM compatibility may also be an important feature, yet there is no public information about it.

Figure 2
The Vimedix simulation software. The 3D animated anatomy (left) is matched with the simulated US image(right) [45].

CAE Healthcare developed an online training solution and an interactive learning management system called ICCU E-Learning, which contains more than 30 hours of multimedia and interactive content. Since it is an online solution, it is accessible from any platform, including mobile devices [46].

4.2 SonoSim Ultrasound Training Solution

The SonoSim Ultrasound Training Solution (SonoSim Inc., Santa Monica, CA) provides an integrated hands-on US training, didactic instruction and assessment. This laptop-based solution can be used without complex and expensive mannequins that makes it altogether light and portable (Fig. 3).

Since basically this is a mannequin-free simulation platform, a photorealistic 3D virtual human body model is used to represents the anatomical structures. The orientation of the US probe is mapped onto this virtual human body, and the virtual US beam is showed based on the probe's pose in real-time. This feature is extended with an optimal US window acquisition guidance, which helps the practitioner to choose the appropriate US window for each anatomic structure. SonoSim uses a freehand method and a special acquisition system to collect US volumes from real human patients. These are stored and post processed to build the case database, which can be used by the simulator to show US images [47].

The content of the US training modules is organized as follows:

- Advanced Clinical Module;
- Anatomy and Physiology Modules;
- Core Clinical Modules;
- Procedure Modules.

Figure 3
SonoSim's solution can be used without a mannequin, as it provides a virtual patient instead [48].

All of these have numerous submodules, which contain well-defined simulation cases, like Ob/Gyn, Focused Assessment with Sonography in Trauma (FAST) cases, etc., starting with an overview of the role of the given case, then describing the affected anatomic structures, the optimal transducer selection, further demonstrating the appropriate patient positions and the imaging techniques. SonoSim has another solution, called LiveScan, which allows to involve both live volunteers and mannequins into US training. In this setup, RFID tags are used to designate the anatomic locations on the human volunteers or on the mannequins (Fig. 4). The SonoSim LifeScan solution provides important additional cases like Critical Care (RUSH), eFAST, Cardiac Resuscitation Cases, etc. The training of these cases was shown to be efficient with mannequins and human volunteers [49]. With the SonoSim Case-Builder, customized US training cases can also be created [31, 50].

Figure 4
The SonoSim LifeScan solution may involve human volunteers for higher fidelity. RFID tags (circle red) are used to designate the key anatomic locations [49].

The SonoSim simulator shows the simulated US image and the related virtual anatomic structure on a split screen (Fig. 3). This kind of data representation is efficient to develop the sonographer's mental mapping between the 2D US image and the 3D anatomy. SonoSim provides one US probe to simulate all the cases from its database. Compared to the Vimedix, this makes the SonoSim's simulator more portable and affordable. There is no information available about the clinical validation of SonoSim, but based on the testimonials, this simulator is popular and widely used in clinical education. Information about DICOM compatibility is not provided, however the real-life patient volumetric US data is stored in DICOM format [51].

4.3 Schallware ultrasound simulator

The Schallware US simulator (Schallware GmbH, Berlin, Germany) provides mannequin-based US simulation for general practice, emergency cardiology and gynecology (Fig. 5). These modules are produced at the company's internationally recognized affiliate clinics with a special Schallware US free hand acquisition system, and distributed with a tutorial including documented patient cases. During the acquisition process, they used up to 2000 raw B-scans to construct one 3D volume, in order to gain optimal resolution. This pathology database contains more than 400 cases from real patients, including a medical history, questions leading to a diagnosis and comments on US findings. The major scanning protocols like TTE, TEE, FAST, eFAST, Focused Echocardiography in Emergency Life support (FEEL), etc. are also included in the repertoire. The simulator supports all the major US visualization types, such as B Mode, M Mode, Colour Doppler and 4D Colour Doppler. Some cases with accompanied MRI and CT images are also available (Fig. 6).

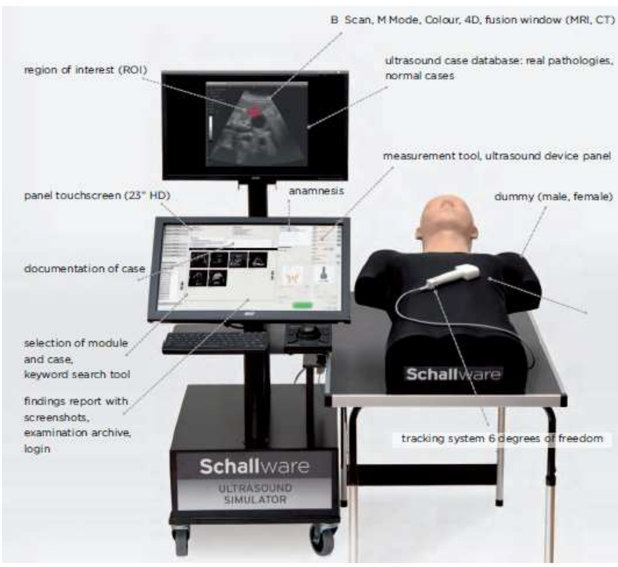

Figure 5
The mannequin-based Schallware US simulator [30].

The Schallware simulator was designed with two displays (Fig. 5), the top screen displays the US image, while the bottom touch screen exhibits the related information, like the documentation of the case, the anamnesis, the measurement tools, the module selector and the reporting functions. The dummy probe repertoire satisfies the most common clinical demands (Fig. 7).

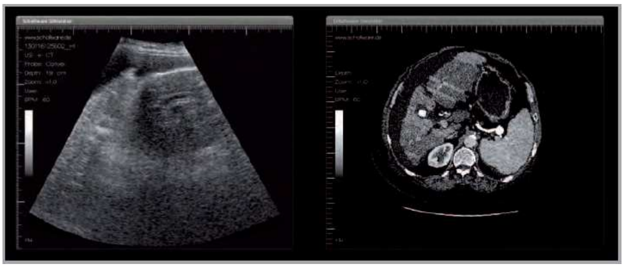

Figure 6
CT/MRI synchronized to US data employed with Schellware US simulators [30].

Figure 7
The Schallware's dummy probe repertoire (convex, linear, sector, transvaginal probe and TEE endoscope) satisfies the most common training needs [30].

4.4 UltraSim and CompactSim

UltraSim and CompactSim (MedSim Inc., Ft. Lauderdale, FL) are mannequin-based US simulators (Fig. 8). These provide a wide range of training modules, the major case repertoire covers abdominal, Ob/Gyn, transvaginal Ob/Gyn, breast, vascular, neck and ER medicine with FAST scanning protocol. The modules built from US volumes acquired from real patients, and consist of two case classifications: curriculum and practice. Each case is organized around a task list used to perform the examination, which are based on standard echocardiography guidelines and internal anatomical landmarks. The curriculum offers complete task lists, lesson plans containing a proper introduction, learning objectives, demonstration lesson, teaching tips and a didactic content outline. These modules allow to directly measure and monitor the practitioners' skills and progress by performing automatic skill assessment. The major imaging features are the B-mode, Color and Spectral Doppler modes [52].

Compared to the previously described simulators, it has a traditional scanning station with a generic control panel. This unique setup with an intuitive control panel allows to practice US knobology. The main US imaging functions (e.g., preset, depth, focus, Time Gain Compensation, frequency, freeze, etc.) are configurable from the control panel with mechanical knobs, like in the case of real devices.

The MedSim provides 3 dummy US probes: the 3.5 MHz is used for abdominal, Ob/Gyn and ER examinations, the 7.5 MHz linear probe is used for breast, neck and Color Doppler studies of the carotid vessels and the 5.0 MHz transvaginal probe is used for Ob/Gyn examinations.

(a)
The UltraSim simulator scanning station [52].

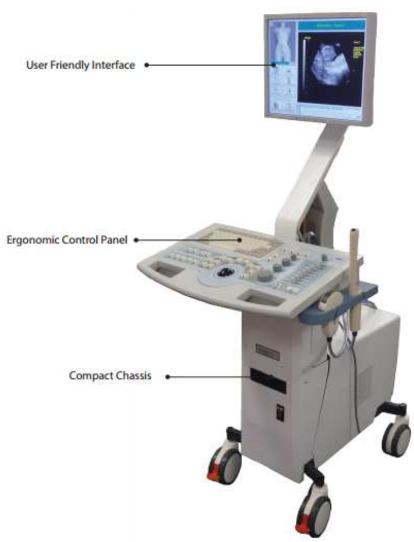

(b)
The CompactSim simulator scanning station.

Figure 8
With their traditional design and realistic control panel, the UltraSim systems provide unique appearance among the commercial simulators [52].

4.5 ScanTrainer

The ScanTrainer (MedaPhor Ltd., Cardiff, UK) provides two mannequin-free platforms for US training: a transvaginal and a transabdominal simulator. The first one allows to perform Ob/Gyn and ER, the second allows general examinations. ScanTrainer uses a curriculum-based training concept with real patient scans, and provides a comprehensive metric-based assessment. The MedaPhor's subscription-based cloud service offers two unique features: the ScanTrainer Case Generator service allows tutors and specialists to upload and publish their own patient scan and self-created cases and the ScanTrainer Case Library offers a cloud-based, continuously growing library with more than 500 normal and abnormal cases. ScanTrainer provides two separate simulation devices (Fig. 9): the transvaginal simulator uses an endo-cavity haptic probe, and the transabdominal simulator uses a special floor-mounted haptic device. These replace the need for a mannequin, and provide a realistic scanning experience. The simulator platform uses two displays: one for the US image and the settings panel and another for the virtual human patient (Fig. 10). ScanTrainer offers a large variety of configuration options, like depth, focus, time gain compensation, measurement and reporting features [53].

Figure 9
The ScanTrainer US training system with the transvaginal (tabletop) and the transabdominal simulator modules [53].

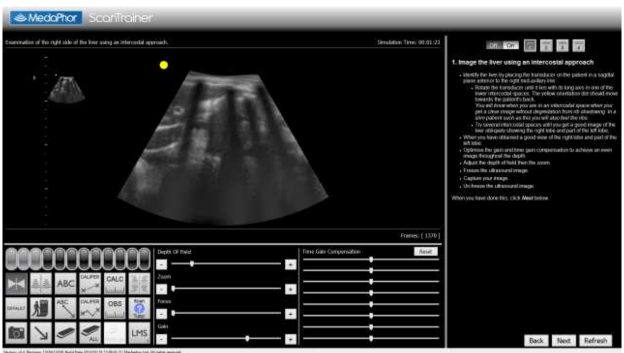

Figure 10
The ScanTrainer's main screen with the US image and the control panel. Features like zoom, time gain compensation, depth, measurement tools are also displayed on this screen [53].

4.6 Portable alternatives

As mentioned in the first section, US devices developed in the last years are getting smaller, giving place to hand-held, portable US devices that still produce clinical quality US images. These are less expensive than the traditional US stations, thus they are more affordable for educational purposes as. Clarius Inc. (Burnaby, BC) is a U.S.A. Food and Drug Administration (FDA) approved hand-held wireless device with linear and convex transducers [54] (Fig. 11). These are designed for clinicians to perform daily bedside US examination. To display the images provided by Clarius, a mobile application (with Android and IOS support) is required to connect via wireless. Its high resolution US images, the DICOM compatibility, the automated gain and frequency setting and the waterproof magnesium shell make this device competitive on the market [55].

Figure 11
The Clarius hand-held wireless US scanner. The convex probe used to examine organs with depth of 3–30 cm, and the linear type used to examine organs with depth of 1–7 cm, while the Endocavity is mostly for Ob/Gyn [55].

Another practical US tool is coming from TELEMED (Fig. 12), in the form of a computer-based US system. It supports numerous imaging modes such as B-Mode, M-Mode, Color and Power Doppler. Their broad range of transducers repertoire allows to perform the most common important examinations. It requires a laptop and a software provided by TELEMED to display the output images [56].

More recently, various (Asian) developers appeared with even smaller and lighter US tools, however, their certification (CE or FDA) is still pending, thus they are omitted from this review. Nevertheless, it is clear that cheaper alternatives can be provided for US training, relying only on a mobile phone or other smart devices.

A new concept appeared on the market, the iNNOGING (iNNOGING Medical Ltd., Israel), which employs the model-based generative method for remote evaluation and diagnosis of US [57]. Particularly, their software converts data from any US device into a 3D representation of the scanned area, that then can be manipulated, analyzed and evaluated using a same transducer, offering dynamic, real-time examination of the pre-recorded data set. Arguably, this technology could well be used in training as well.

Conclusion

Since medical ultrasound is a generally employed, non-invasive and relatively cheap imaging modality, it is important to train practitioners how they can use them properly and effectively. It is also critical to teach to evaluate the images produced. During the MD education, US simulators can be used to practice from the basic to expert examination techniques. There are many great US simulators available on the

Figure 12
The TELEMED's computer-based US system [56].

market, relying on advanced computer modeling. Some simulators are mannequin-based (linked to a physical examination phantom), while others replace the mannequins with virtual patient displayed to the practitioner. Another differentiating property of these is the simulation method they rely on. *Interpolative methods* use pre-acquired US volumes to produce the simulated 2D US image, while the *generative image-based methods* synthesize US-like images from CT or MRI, and the *generative model-based methods* use precise mathematical models to simulate the US images of different organs. These are mainly used in the case of moving anatomies, such as the heart. As an alternative solution, the recently emerged hand-held US scanners could be taken into consideration as a direct competition to the traditional simulators. These are less costly, while they can already provide clinical-grade image quality. Since US simulators have been clearly shown to help the practitioners to gain practical experience, their use greatly reduces the risk associated with US-based procedures, and can improve the clinical outcome. In the near future, with the further spread of computer-based methods, the standardization of these training devices and adjacent curricula is expected.

Acknowledgment

The research was supported by the Hungarian OTKA PD 116121 grant. This work has been partially supported by ACMIT (Austrian Center for Medical Innovation and Technology), which is funded within the scope of the COMET (Competence Centers for Excellent Technologies) program of the Austrian Government. T. Haidegger and P. Galambos are supported through the New National Excellence Program of the Ministry of Human Capacities. Partial support of this work comes from the Hungarian State and the European Union under the EFOP-3.6.1-16-2016-00010 project. T. Haidegger is a Bolyai Fellow of the Hungarian Academy of Sciences.

References

[1] Arpád Takács, Dénes Ákos Nagy, Imre Rudas, and Tamás Haidegger. Origins of surgical robotics: From space to the operating room. *Acta Polytechnica Hungarica*, 13(1):13–30, 2016.

[2] David M. Sella. Ultrasound-Guided Procedures. *American J. of Roentgenology*, 196(2):221–221, February 2011.

[3] B. R. Douglas, J. W. Charboneau, and C. C. Reading. Ultrasound-guided intervention: expanding horizons. *Radiologic Clinics of North America*, 39(3):415–428, May 2001.

[4] American Institute of Ultrasound in Medicine. Selected Ultrasound-Guided Procedures, 2014. Accessed: 2018-10-01. http://www.aium.org/resources/guidelines/usguidedprocedures.pdf.

[5] Mathias Hoeckelmann, Imre J Rudas, Paolo Fiorini, Frank Kirchner, and Tamas Haidegger. Current capabilities and development potential in surgical robotics. *Intl. J. of Advanced Robotic Systems*, 12(5):61, 2015.

[6] Alexander L Klibanov and John A Hossack. Ultrasound in radiology: from anatomic, functional, molecular imaging to drug delivery and image-guided therapy. *Investigative radiology*, 50(9):657, 2015.

[7] Tamas Ungi, Derek Sargent, Eric Moult, Andras Lasso, Csaba Pinter, Robert C McGraw, and Gabor Fichtinger. Perk tutor: an open-source training platform for ultrasound-guided needle insertions. *IEEE Transactions on Biomedical Engineering*, 59(12):3475–3481, 2012.

[8] Renáta Elek, Tamás D Nagy, Dénes Á Nagy, Bence Takács, Péter Galambos, Imre Rudas, and Tamás Haidegger. Robotic platforms for ultrasound diagnostics and treatment. In *Systems, Man, and Cybernetics (SMC), 2017 IEEE Intl. Conference on*, pages 1752–1757. IEEE, 2017.

[9] Seth Billings, Nishikant Deshmukh, Hyun Jae Kang, Russell Taylor, and Emad M Boctor. System for robot-assisted real-time laparoscopic ultrasound elastography. In *Medical Imaging 2012: Image-Guided Procedures, Robotic Interventions, and Modeling*, volume 8316, page 83161W. Intl. Society for Optics and Photonics, 2012.

[10] Dayalan Clarke, Robert G. Newcombe, and Robert E. Mansel. The learning curve in sentinel node biopsy: The ALMANAC experience. *Annals of Surgical Oncology*, 11(3):211–215, 2004.

[11] Miguel A. Quiñones, Pamela S. Douglas, and et al. ACC/AHA clinical competence statement on echocardiography. *J. of the American Society of Echocardiography*, 16(4):379–402, 2003.

[12] Luca Neri, Enrico Storti, and Daniel Lichtenstein. Toward an ultrasound curriculum for critical care medicine. *Critical Care Medicine*, 35(5):S290–304, 2007.

[13] D. Ehler, D. K. Carney, A. L. Dempsey, R. Rigling, C. Kraft, S. A. Witt, T. R. Kimball, E. J. Sisk, E. A. Geiser, C. D. Gresser, A. Waggoner, and ASE. Guidelines for cardiac sonographer education: recommendations of the American Society of Echocardiography Sonographer Training and Education Com-

mittee. *J. of the American Society of Echocardiography: Official Publication of the American Society of Echocardiography*, 14(1):77–84, 2001.

[14] B. S. Hertzberg, M. A. Kliewer, J. D. Bowie, B. A. Carroll, D. H. DeLong, L. Gray, and R. C. Nelson. Physician training requirements in sonography: how many cases are needed for competence? *American J. of Roentgenology (AJR)*, 174(5):1221–1227, May 2000.

[15] H. Maul, A. Scharf, P. Baier, M. Wüstemann, H. H. Günter, G. Gebauer, and C. Sohn. Ultrasound simulators: experience with the SonoTrainer and comparative review of other training systems. *Ultrasound in Obstetrics & Gynecology: The Official J. of the Intl. Society of Ultrasound in Obstetrics and Gynecology*, 24(5):581–585, October 2004.

[16] Thomas G. Costantino, Wayne A. Satz, Sarah A. Stahmer, and Anthony J. Dean. Predictors of success in emergency medicine ultrasound education. *Academic Emergency Medicine: Official J. of the Society for Academic Emergency Medicine*, 10(2):180–183, February 2003.

[17] Árpád Takács, Péter Galambos, Péter Pausits, Imre J Rudas, and Tamás Haidegger. Nonlinear soft tissue models and force control for medical cyber-physical systems. In *IEEE Intl. Conf. on Systems, Man, and Cybernetics (SMC)*, pages 1520–1525. IEEE, 2015.

[18] Norbert Suhánszki and Tamás Haidegger. Objective surgery–advanced robotic devices and simulators used for surgical skill assessment. *Magyar Sebészet (Hungarian J. of Surgery)*, 67(6):340–352, 2014.

[19] Vivien Gibbs. A proposed new clinical assessment framework for diagnostic medical ultrasound students. *Ultrasound*, pages 113–117, December 2013.

[20] Society and College of Radiographers and British Medical Ultrasound Society. Guidelines for professional ultrasound practice, December 2015.

[21] Harald Lutz and Elisabetta Buscarini. *Manual of diagnostic ultrasound*, volume 1. World Health Organization, Guttenberg Press Ltd., 2. edition, 2011.

[22] European Federation of Societies for Ultrasound in Medicine and Biology. Minimum training requirements for the practice of medical ultrasound in Europe.

[23] Juan A. Asensio and Donald D. Trunkey. *Current Therapy of Trauma and Surgical Critical Care*. Elsevier, 2 edition edition, June 2015.

[24] Daniel A. Lichtenstein. BLUE-protocol and FALLS-protocol: two applications of lung ultrasound in the critically ill. *Chest*, 147(6):1659–1670, 2015.

[25] Dina Seif, Phillips Perera, Thomas Mailhot, David Riley, and Diku Mandavia. Bedside Ultrasound in Resuscitation and the Rapid Ultrasound in Shock Protocol. *Critical Care Research and Practice*, 2012.

[26] C. Hrymak, E. Weldon, and C. Pham. The educational impact of a formalized RUSH (Rapid Ultrasound in Shock) protocol in emergency medicine residency ultrasound training. *Canadian J. of Emergency Medicine*, 18(S1):61–62, 2016.

[27] Mary Hegarty, Madeleine Keehner, Cheryl Cohen, Daniel R Montello, and Yvonne Lippa. The role of spatial cognition in medicine: Applications for selecting and training professionals. *Applied spatial cognition*, pages 285–315, 2007.

[28] CAE Healthcare Ltd. VIMEDIX Abdo and Cardiac, 2017. Accessed: 2018-10-01. https://caehealthcare.com/media/files/TechSheets/Vimedix-Cardiac-Abdo-Techsheet.pdf.

[29] U/S Library of Modules | Simbionix, 2017. Accessed: 2018-10-01. http://simbionix.com/simulators/us-mentor/us-library-of-modules/.

[30] Schallware. Schallware Product Sheet, 2017. Accessed: 2018-10-01. https://www.schallware.com/downloads.

[31] SonoSim Inc. SonoSim - What are my content choices?, March 2017. Accessed: 2018-10-01. http://sonosim.com/what-are-my-content-choices/.

[32] Tobias Blum, Andreas Rieger, Nassir Navab, Helmut Friess, and Marc Martignoni. A review of computer-based simulators for ultrasound training. *Simulation in Healthcare: J. of the Society for Simulation in Healthcare*, 8(2):98–108, April 2013.

[33] Michael Weidenbach, Florentine Wild, Kathrin Scheer, Gerhard Muth, Stefan Kreutter, Gernoth Grunst, Thomas Berlage, and Peter Schneider. Computer-based training in two-dimensional echocardiography using an echocardiography simulator. *J. of the American Society of Echocardiography: Official Publication of the American Society of Echocardiography*, 18(4):362–366, April 2005.

[34] T. Blum, S. M. Heining, O. Kutter, and N. Navab. Advanced training methods using an Augmented Reality ultrasound simulator. In *8th IEEE Intl. Symposium on Mixed and Augmented Reality*, pages 177–178, 2009.

[35] EchoPixelTech, March 2017. Accessed: 2018-10-01. http://www.echopixeltech.com/.

[36] Dror Aiger and Daniel Cohen-Or. Real-Time Ultrasound Imaging Simulation. *Real-Time Imaging*, 4(4):263–274, August 1998.

[37] B. Flack, M. Makhinya, and O. Goksel. Model-based compensation of tissue deformation during data acquisition for interpolative ultrasound simulation. In *2016 IEEE 13th Intl. Symposium on Biomedical Imaging (ISBI)*, pages 502–505, April 2016.

[38] Ramtin Shams, Richard Hartley, and Nassir Navab. Real-time simulation of medical ultrasound from CT images. *Intl. Conf. on Medical image computing and computer-assisted intervention (MICCAI)*, 11:734–741, 2008.

[39] Sjur Urdson Gjerald, Reidar Brekken, Lars Eirik Bø, Torbjørn Hergum, and Toril A. Nagelhus Hernes. Interactive development of a CT-based tissue model for ultrasound simulation. *Computers in Biology and Medicine*, 42(5):607–613, May 2012.

[40] Gerd Reis, Bernd Lappé, Sascha Köhn, Christopher Weber, Martin Bertram, and Hans Hagen. Towards a Virtual Echocardiographic Tutoring System. In *Visualization in Medicine and Life Sciences*, pages 99–119. Springer, Berlin, Heidelberg, 2008.

[41] Martin Bertram, Gerd Reis, Rolf H. van Lengen, Sascha Köhn, and Hans Hagen. Non-manifold Mesh Extraction from Time-varying Segmented Volumes Used for Modeling a Human Heart. In *7th Joint Eurographics / IEEE VGTC Conference on Visualization*, pages 199–206, 2005.

[42] Alfred M Franz, Tamas Haidegger, Wolfgang Birkfellner, Kevin Cleary, Terry M Peters, and Lena Maier-Hein. Electromagnetic tracking in medicine—a review of technology, validation, and applications. *IEEE transactions on medical imaging*, 33(8):1702–1725, 2014.

[43] S. Farsoni, L. Astolfi, M. Bonfè, S. Spadaro, and C. A. Volta. A Versatile Ultrasound Simulation System for Education and Training in High-Fidelity Emergency Scenarios. *IEEE J. of Translational Engineering in Health and Medicine*, 5:1–9, 2017.

[44] Omair Shakil, Bilal Mahmood, Robina Matyal, Jayant S. Jainandunsing, John Mitchell, and Feroze Mahmood. Simulation Training in Echocardiography: The Evolution of Metrics. *J. of Cardiothoracic and Vascular Anesthesia*, 27(5):1034–1040, October 2013.

[45] CAE Healthcare Ltd. Vimedix User Guide v1.16, 2016. Accessed: 2018-10-01. https://caehealthcare.com/media/files/User_Guides/Vimedix-116-User-Guide.pdf.

[46] CAE Healthcare Ltd. CAE ICCU Ultrasound Education – CAE Healthcare, 2016. Accessed: 2018-10-01. https://caehealthcare.com/ultrasound-simulation/iccu.

[47] K Petrinec. *Patient-Specifc Interactive Ultrasound Image Simulation Based on the Deformation of Soft Tissue*. PhD thesis, University of California, 2013. http://web.cs.ucla.edu/ dt/theses/petrinec-thesis.pdf.

[48] SonoSim Inc. The SonoSim Ultrasound Training Solution, 2017. Accessed: 2018-10-01. http://sonosim.com/our-solution/.

[49] SonoSim Inc. SonoSim LiveScan – Ultrasound Training, 2016. Accessed: 2018-10-01. https://sonosim.com/livescan/.

[50] SonoSim Inc. SonoSim CaseBuilder, 2017. Accessed: 2018-10-01. https://sonosim.com/casebuilder/.

[51] K. Petrinec, E. Savitsky, and D. Terzopoulos. Patient-Specific Interactive Simulation of Compression Ultrasonography. In *2014 IEEE 27th Intl. Symposium on Computer-Based Medical Systems*, pages 113–118, May 2014.

[52] MedSim Inc. UltraSim, 2016. Accessed: 2018-10-01. http://www.medsim.com/ultrasim.html.

[53] MedaPhor. ScanTrainer Platforms, 2016. Accessed: 2018-10-01. https://www.medaphor.com/scantrainer/platforms/.

[54] Heather Mack. Clarius Mobile Health gets FDA clearance for app-based, wireless ultrasound scanners, 2016. Accessed: 2018-10-01. http://www.mobihealthnews.com/content/clarius-mobile-health-gets-fda-clearance-app-based-wireless-ultrasound-scanners.

[55] Clarius. Clarius Product Specifications, 2016. Accessed: 2018-10-01. https://www.clarius.me/product/specs/.

[56] Telemed. Telemed | Ultrasound Medical Systems, 2016. Accessed: 2018-10-01. http://www.pcultrasound.com/index.html.

[57] A. K. Leichman. Ultrasound breakthrough allows doctors to examine patients remotely, Israel21c, 2018. Accessed: 2018-10-31. https://www.israel21c.org/breakthrough-system-turns-ultrasound-images-into-virtual-3d-models/.

Fuzzy Logic-based Maximum Power Point Tracking for a Solar Electric Vehicle

Thameur Obeidi[1,2], Cherif Larbes[2], Adrian Ilinca[1], Gul Filiz Tchoketch Kebir[1,2]

[1]Wind Energy Research Laboratory, Université du Québec à Rimouski, 300, allée des Ursulines, Rimouski, QC, Canada, G5L 3A1, Thameur.Obeidi@uqar.ca, Adrian_Ilinca@uqar.ca, GulFiliz.TchoketchKebir@uqar.ca

[2] Laboratoire des Dispositifs de Communication et de Conversion Photovoltaïque, Département d'Électronique, École Nationale Polytechnique, 10, Avenue Hassen Badi, El Harrach, Alger 16200, Algeria, cherif.larbes@g.enp.edu.dz

Abstract: A maximum power point tracking (MPPT) system, for a very high-efficiency photovoltaic array applied to a solar-powered vehicle, was studied in this work. Photovoltaic energy is a promising alternative energy; however, its high initial cost, it is essential to improve the energy conversion efficiency. Regarding a particular incident solar insolation and temperature, there is a specific voltage at which maximum power may be harvested (Maximum power point, MPP). The Maximum Power Point is therefore achieved at a specific voltage that depends on insolation and temperature. A proper maximum power point tracking system is particularly important for solar-powered vehicles relating to the rapid change of insolation due to the dynamic motion of the vehicle. In this paper, the emphasis is on the potential of energy conversion improvement of a PV system, associated with a moving vehicle via the use of a fuzzy based maximum power point tracking algorithm.

Keywords: Maximum Power Point Tracking (MPPT); the fuzzy controller; Photovoltaic Dynamic Tracking (PVT); solar electric vehicle

1 Introduction

The development of photovoltaic (PV) cells, small and large PV systems has accelerated during recent years. Application of photovoltaic energy has been studied on different systems, namely, satellite power systems, solar power generation, solar battery charging stations, and solar vehicles (cars, ships, and airplanes). Since space, weight, and cost are limiting and defining factors for solar vehicles, it is desirable to harvest maximum energy from installed photovoltaic cells. The present work emphasizes the improvement of power conversion using state of the art high-performance fuzzy logic based MPPT algorithm. Every photovoltaic cell array has an optimum operating point, called the maximum power point (MPP), which varies depending on cell temperature and incident insolation level. In this paper, a fuzzy controller is used recently in the PV system of a solar vehicle, the performance of this controller is tested and compared to that of a Perturb and Observe (P&O) controller [1, 2, 3, 4] under Matlab-Simulink environment. The other novelty of this controller is the use of a Buck instead of Boost and the use of Gaussian forms instead of Triangular forms in the membership functions.MPPT methods portrayed in the literature [2-29] used different techniques and algorithms which widely differ in performance: convergence speed, implementation complexity, accuracy, and most importantly the cost of implementation of the whole set-up. Regarding to previous study [23, 28], it was presented nineteen different MPPT methods including: “Hill Climbing/P&O method” [5, 7, 19, 21, 25], “Incremental Conductance Method” [6, 8, 21, 26, 27], “Fractional Open-Circuit Voltage Method” [19, 22], “Fractional Short-Circuit Current Method” [21, 22, 25], “Artificial Intelligence-Based MPPT Algorithms” [5, 11, 20, 21, 25], “Current Sweep Method” [5, 20], “DC-Link Capacitor Droop Control method” [5, 20], “Load Current or Load Voltage Maximization method” and “dP/dV or dP/dI Feedback Control technique” [5, 6]. Additional MPPT techniques have been studied as “Linearized I-V Characteristics Method” [8], “Ripple Correlation Control Method” [5, 21, 22], “Current Compensation Method”, “Constant Voltage and Current Method”, “Parasitic Capacitance Method” [5, 8, 21], “Sliding Mode Control MPPT Technique”, “Curve-Fitting Method”, “Forced Oscillation Technique”[5, 12], “Particle-Swarm-Optimisation-Based MPPT” [5, 21] and “Hybrid Methods” [5, 6, 13].

MPPT methods have also been applied to solar vehicles. A new Maximum Power Point Tracking (MPPT) control algorithm based on the Incremental Conductance (IncCond) has been applied for a single high-performance gas-solar cell for hybrid and electric vehicle applications [6, 14, 32, 33]. This work concluded that the proposed MPPT algorithm secures a 1.5ms response time under rapid insolation changes. The application of an improved perturbation control method to a Solar Autonomous Underwater Vehicle (SAUV) has been studied in [15, 16, 17, 34, 35]. Particular attention is paid to the equalization charging control method based on an improved P&O controller on a series of Lithium-Ion battery strings. Another study [36, 37] illustrated the efficiency of a maximum power point tracker for compound curve photovoltaic arrays applied to solar-powered vehicles. The article presented an open loop algorithm aiming at maximum power point tracking and use of synchronous rectification in a boost converter to improve the overall circuit efficiency. The application of a modified quadratic maximization MPPT algorithm to a moving vehicle has been studied in [30, 31, 38, 39, 40] together with its performance validation using the Sandia dynamic test protocol. It concluded that the traditional P&O method has a slow restart tracking of the maximum power. It resulted from the literature review that a diversity of MPPT algorithms has been developed for the improvement of energy conversion. Its performances (convergence speed, implementation complexity, accuracy, and cost of implementation) are variable and subject to improvement. The paper is organized as follows: regarding the second section, we have studied the specificities of PV fields mounted on solar vehicles. The third section is devoted to the energy production chain from the solar panels and up to battery via the DC-DC converter which houses the controller programmed to track the MPP (MPPT) where the study will focus on the comparison of two algorithms. The classic P&O and the FL algorithm proposed to improve the performance of the controller (MPPT); section four comes with the simulation parameters to concretize the simulation of the two models studied in the previous section; the results are discussed in the fifth section.

2 Specificity of Photovoltaic Arrays in a Solar Electric Vehicle

A typical simple configuration of a solar electric vehicle (EV) is shown in Figure 1 [6, 11]. The outputs of individual PV panels are combined and connected to a common DC/DC converter linked to the battery pack. The DC bus voltage is then converted to AC voltage through an inverter to control the machine traction.

However, most solar panels on solar-powered electric vehicles are curved to fold into the aerodynamic shape of the vehicle such that all PV arrays require an MPPT controller for best conversion efficiency. Figure 2 schematizes the different arrays. The MPPT algorithm applies differently to arrays as they are submitted to different incident irradiance and temperature at the same time. Therefore, the imposed voltage for each array is different in order to extract maximum output power.

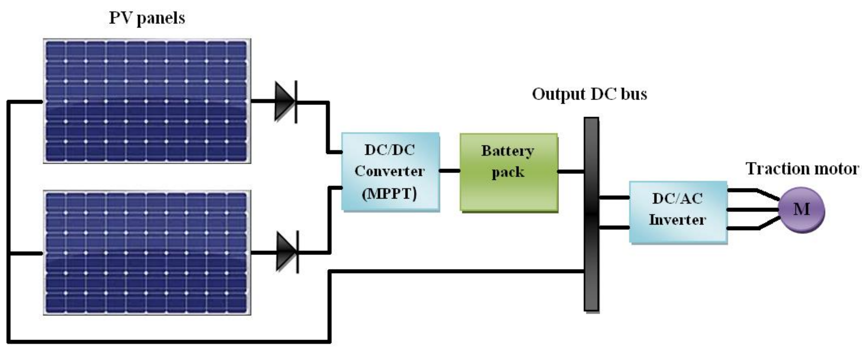

Figure 1

Simple block diagram representation of a solar electric vehicle [11]

3 Elements of Solar Vehicle Power System

A typical solar vehicle power system consists of an array made up of a given number of serially connected photovoltaic cells [1, 6, 7], a parallel-connected battery pack acting as an energy buffer and a DC-DC converter to match the voltage of the solar array with the one of the batteries (Figure 2). The conversion ratio of the converter is varied by a controller to constantly adjust the operating voltage of the solar panel to its point of maximum power (MPP), it is being operated as a Maximum Power Point Tracker (MPPT).

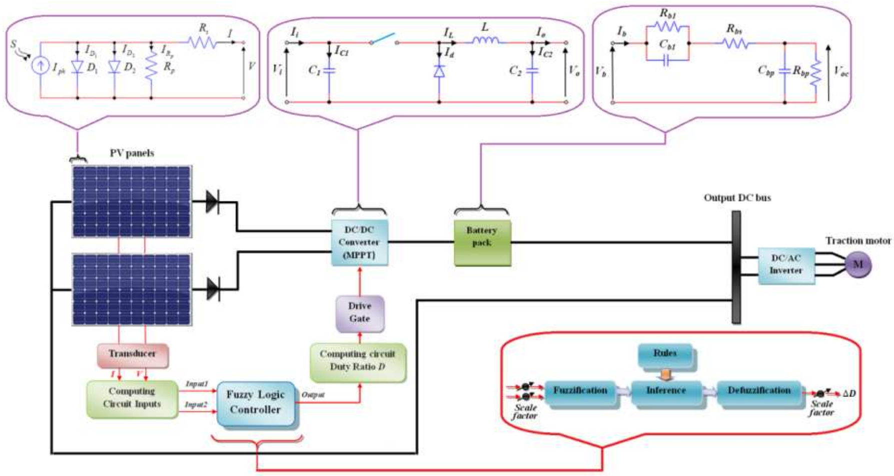

Figure 2
MPPT component architecture for Solar Electric Vehicle with Fuzzy Controller

3.1 Solar Arrays

The photovoltaic (PV) cell model used contains two diodes [14, 18, 29] and is based on the general equation (1). The complete photovoltaic module consists of z photovoltaic cells connected in series:

$$I = S.I_{ph}(T) - I_{s1}\left[e^{\frac{q(V+IzR_s)}{zn_1kT}} - 1\right] - I_{s2}\left[e^{\frac{q(V+IzR_s)}{zn_2kT}} - 1\right] - \frac{V+IzR_s}{zR_p} \tag{1}$$

Where:

$$I_{ph}(T) = I_{ph}\big|_{(T=298\,K)}\left[1+(T-298)\cdot(5\cdot10^{-4})\right] \tag{2}$$

$$I_{s_1} = K_1T^3e^{-\frac{E_g}{kT}} \tag{3}$$

$$I_{s_2} = K_2 T^{\frac{5}{2}} e^{-\frac{E_g}{kT}} \tag{4}$$

In equations (1-4), I and V are respectively the output current and output voltage of the photovoltaic cell, S is the irradiance and T is the absolute temperature in Kelvin. $I_{ph}(T)$ is the generated photo-current, I_{s_1} and I_{s_2} are the diodes reverse saturation currents, n_1 and n_2 the diode ideality factors, R_s the series resistance and R_p the parallel resistance. E_g is the band-gap energy of the semiconductor, *q* is the elementary charge constant ($1.602 \cdot 10^{-19}$C), $K_1 = 1.2 \ A/cm^2K^3$, $K_2 = 2.9 \times 10^5 \ A/cm^2K^{5/2}$ and *k* the Boltzman constant (1.38×10^{-23} J/K).

3.2 Principle and Motivation for MPPT

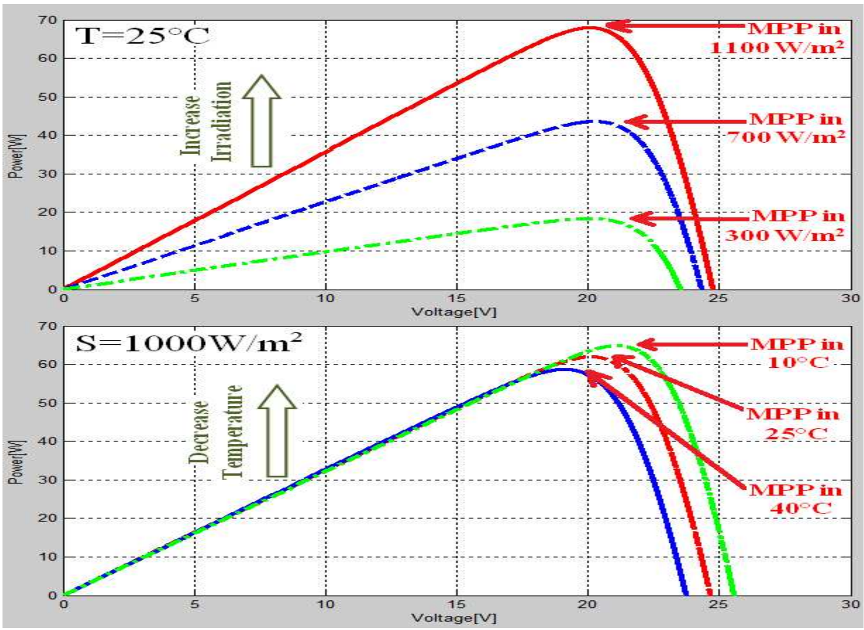

Figure 3

Variation of MPP with changing irradiance and temperature

As illustrated in Figure 3, the harnessed power from photovoltaic arrays, P, does not only depend on its operating voltage V (and load value), but also on incident temperature and irradiance. The point of maximum power indicated as MPP (Maximum Power Point) is the desired operating point for a photovoltaic array to obtain maximum efficiency. In these circumstances, a maximum power point tracking (MPPT) mechanism can help to significantly increase the power output of a solar power system by adjusting the system parameters (like load or operating voltage V) in such a way that the operating voltage V will always be approximately equal to the optimum operating voltage V_{MPP}. In the case of solar-powered electric vehicles, the use of MPPT is of high importance as it gives an opportunity to boost power and efficiency, despite rapidly varying incident parameters (irradiance and temperature) due to vehicle mobility and aerodynamically curved solar arrays. MPPT helps in securing high power availability without the need for solar panel oversizing in which case, vehicle weight is unnecessarily increased and overall performance diminished [2, 32].

3.3 DC-DC Converter

Photovoltaic systems are generally connected to static converters (DC-DC) driven by preprogramed controllers to continuously analyze the output of the solar panel. MPPT controllers continuously analyze instantaneous power output and adjust the parameters with an aim to maximum energy whatever are the load and atmospheric conditions [16, 20, 32]. In this work, the MPPT device consists of a buck converter between the PV module and the load (Figure 2). Mathematical equations modeling the buck converter are as follows:

$$\frac{V_o}{V_i} = D \tag{5}$$

$$I_o = I_L - C_2 \frac{dV_o}{dt} \tag{6}$$

$$I_L = \frac{1}{D}\left(I_i - C_1 \frac{dV_i}{dt} \right) \tag{7}$$

$$V_i = \frac{1}{D}\left(V_o + L \frac{dI_L}{dt} \right) \tag{8}$$

It is understood from equation (5) and from Figure 4 below, that an increase in conversion duty ratio results in an increase in the output voltage of the buck converter and vice-versa [16, 21, 33, 44].

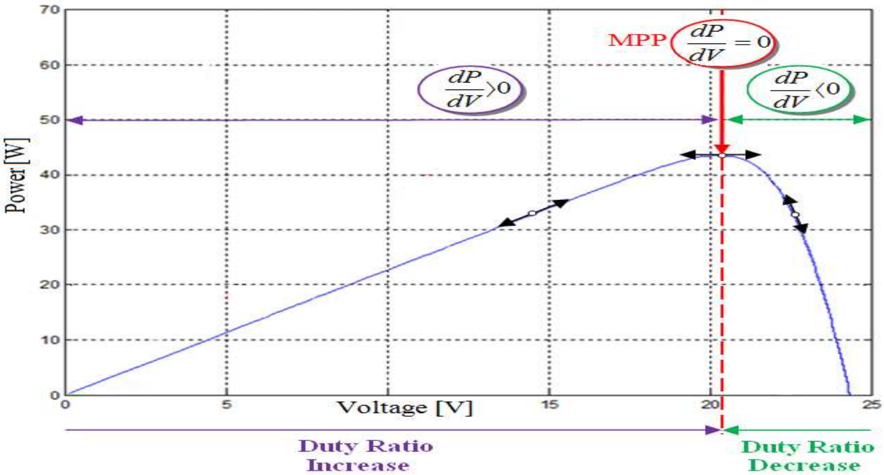

Figure 4

Direction change of the duty ratio D of the buck converter for tracking the MPP

3.4 Solar Vehicle Lead-Acid Batteries

In a photovoltaic power supply system for a car, batteries are used as an energy buffer due to the variability of solar array production and power demand from the vehicle. Using the batteries to store the electrical power from the solar panels in the form of chemical energy makes the generated energy readily available whenever it is needed, independent of the current weather conditions. An equivalent electrical circuit model for the batteries has been established to analyze the dynamic performance and the steady-state behaviour of the whole power system. We use an equivalent electrical circuit model as shown in Figure 2 that includes equivalent components for all major operating characteristics of a lead-acid battery. The representation in Figure 2 illustrates the characteristics of a lead-acid battery in a comprehensive yet very simplified way. Reference [39, 40] proposes additional mathematical expressions used to adjust the model's components to represent the variation with temperature of the battery’s characteristics. They do not account for other parameters such as the state of the charge or the electrolyte level, which are additional factors influencing the battery's characteristics. The component values of the battery were modeled in the literature [16, 43, 44, 45], to realize an approximate overvoltage of 27 V at the maximum charging current of 9.5 A. Knopf [29] uses a battery pack consisting of a series of 9 independent 12 V GNB batteries with a specified capacity of 45 Ah each. This adds up to a theoretical operating voltage of 108 V. The actual operating range (V_{min}; V_{max}) of the batteries lies between 90 V and 125 V. The lead-acid battery model can be mathematically expressed in the frequency domain representing the equivalent input impedance of a lead-acid battery:

$$Z(s) = \frac{V_b}{I_b} = R_{bs} + \frac{R_{b1}}{R_{b1}C_{b1}s + 1} + \frac{R_{bp}}{R_{bp}C_{bp}s + 1} \tag{9}$$

The form of equation (9) can be written as:

$$Z(s) = \frac{a_2 s^2 + a_1 s + a_0}{b_2 s^2 + b_1 s + b_0}$$

$$\begin{cases} a_2 = R_{bs}R_{b1}R_{bp}C_{b1}C_{bp} \\ a_1 = R_{bs}R_{b1}C_{b1} + R_{bs}R_{bp}C_{bp} + R_{b1}R_{bp}c_{bp} + R_{bp}R_{b1}C_{b1} \\ a_0 = R_{bs} + R_{b1} + R_{bp} \\ b_2 = R_{b1}R_{bp}C_{b1}C_{bp} \\ b_1 = R_{b1}C_{b1} + R_{bp}C_{bp} \\ b_0 = 1 \end{cases} \tag{10}$$

Equation (9) and parametric definitions (10) were used previously [15, 19, 30] to model lead-acid batteries. The following numerical definitions were used to complete the model: R_{bs}=0.0013 Ω, R_{b1}=2.84 Ω, R_{bp}=10e^3 Ω, C_{b1}=2.5 mF, C_{bp}=2*45*9*12*36000/ (125^2- 90^2) =4.650 KF.

3.5 MPPT of a Solar Electric Vehicle with Fuzzy Logic and P&O Controllers

3.5.1 MPPT of a Solar Vehicle with P&O Controller

The performance of our MPPT applied to a solar-powered vehicle is compared to one of the most conventionally used, a P&O MPPT algorithm [2, 20, 22, 26, 37]. The P&O algorithm used for comparison is illustrated in Figure 5. The P&O method works as follows: the system is perturbed by increasing or decreasing the array operating voltage and observing its impact on the output power as shown in Figure 5. V and I are measured to calculate the present array output power P(k). This value for P(k) is compared to the value obtained from the previous measurement P(k-1). If the output power has increased since the last measurement, the perturbation of the output voltage will continue in the same direction as in the last cycle. If the output power has decreased since the last measurement, the perturbation of the output voltage will be reversed in the opposite direction of the last cycle. The operating voltage V is perturbed with every MPPT cycle and as soon as the MPP is reached, V will oscillate around the ideal operating voltage V_{MPP}. These oscillations will result in a power loss which value depends on the step of a single perturbation. If the step width is large, the

MPPT algorithm will be responding quickly to sudden changes in operating conditions with the trade-off increased losses under stable or slowly changing conditions. If the step width is very small, the losses under stable or slowly changing conditions will be reduced, but the system will be only able to respond very slowly to rapid changes in temperature or irradiance.

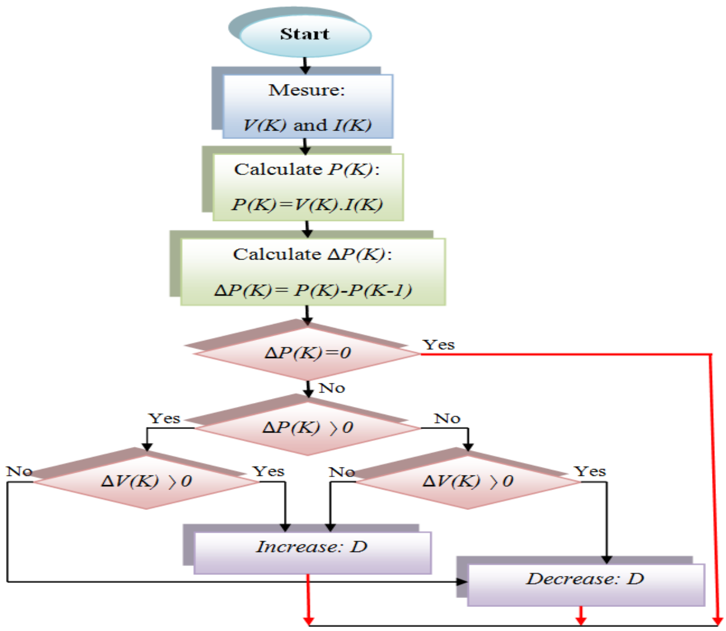

Figure 5

Flowchart of the P&O MPPT algorithm used for comparison

3.5.2 MPPT of a Solar Vehicle with Fuzzy Logic Controller

The Fuzzy Logic Control (FLC) is a rule-based algorithm which has the advantages of working with imprecise inputs, it does not need an accurate mathematical model and it can handle nonlinearity as well. Because of advantages like (1) Flexible operation, (2) Convenient user interface, (3) ease of implementation and (4) Qualified validation, the Fuzzy method is preferred in implementation for MPPT [38]. FLC constitutes four parts, which include fuzzification, inference, rule base, and defuzzification as shown in Figure 6.

In these parts, Fuzzy inference and designing of fuzzy rules decide the optimal performance of the system [41, 42]. But then, to design Fuzzy rules abundant knowledge and high amount of training is needed. The inputs to an MPPT fuzzy logic controller are usually an error E and a change in error ΔE. The user has the flexibility of choosing how to compute E and ΔE. Since dP/dV vanishes at the MPP.

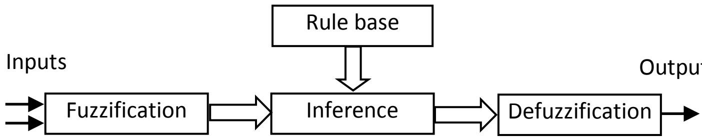

Figure 6
Block diagram of fuzzy logic controller

The common approaches made in FLC based MPPT are to reduce the error in the systems. In most of the cases, the error and difference in error are calculated based on the Equations (11) and (12).

$$E(K) = \frac{P(K) - P(K-1)}{I(K) - I(K-1)} \tag{11}$$

$$CE(K) = E(K) - E(K-1) \tag{12}$$

Where 'K' refers to iteration number, 'CE' is the change in error, 'E' is the error, 'P' is the power and 'I' is the current. Table 1 explaining the rules for determining the error and the change in error is given. In Fuzzy implemented MPPT, the variable duty cycle is considered for an effective tuning of a duty cycle [50, 51]. For instance, the error (E) and the change in error (CE) associated with the duty cycle is calculated. If the error value is PB (Positive Big) and the change in error value is PS (Positive Small), the rules are predefined in the lookup table.

Table 1
Fuzzy logic rule table/lookup table

E / CE	NB	NS	ZE	PS	PB
NB	ZE	ZE	PB	PB	PB
NS	ZE	ZE	PS	PS	PS
ZE	PS	ZE	ZE	ZE	NS
PS	NS	NS	NS	ZE	ZE
PB	NB	NB	NB	ZE	ZE

Decision on the duty 'ZE (zero)' has to be added with control variable for next cycle. Similar, the process is continued until the optimal location is reached. The key tool to choose fuzzy logic control is for its better accuracy, the ability to detect the error in quick time and tracking speed. The representation of membership function error 'E', change in error 'CE' and calculation of output variable duty variable 'D' is shown in Figure 7.

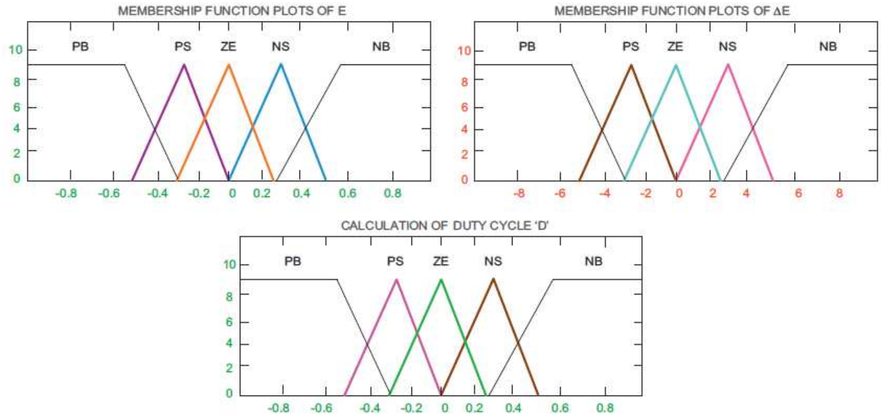

Figure 7

Membership function plots for E, ΔE, and calculation of duty cycle 'D'

The Fuzzy Logic based MPPT is based on the following algorithm:

1) The derivative of the P(V) function is used to locate the actual operation point p_i. Based on the result, the controller decides whether to increase or decrease the voltage, through the applied load to the duty ratio ΔD.

2) The second derivative of the P(V) function expresses the rate of approach or distancing of the point p_i from the MPP. These data are used by the controller for fast search of MPP. A fuzzy logic controller consists of three main operations: "fuzzification", "inference" and "defuzzification". The input sensory (crisp or numerical) data are fed into the fuzzy logic rule-based system where physical quantities are represented into linguistic variables with appropriate membership functions. These linguistic variables are then used in the antecedents (IF-Part) of a set of fuzzy "IF-THEN" rules within an inference engine to result in a new set of fuzzy linguistic variables or consequent (THEN-Part). During the fuzzification part, the controller instantaneously measures the voltage V(k) and current I(k) of a photovoltaic array and calculates output power as P(k)=I(k)V(k). The controller analyses $input_1(k)$, which expresses the slope of the current operating point on the P-V curve and $input_2(k)$: which expresses the rate of change of approach or distancing of the point p_i. The fuzzy logic controller takes instantaneous measurements of these two points then decides and calculates the output, ΔD(k) which is actually the change of the duty ratio of the MOSFET power switch. The input and output variables of the fuzzy logic controller must be expressed in terms of membership functions. Determination of the range of the fuzzy linguistic variables that compose the membership functions of input and output variables of the fuzzy logic controller is based on automation specialists experience, as described in the literature [39, 46].

Unlike commonly used FLC described previously, in this paper the FLC uses Gaussian form in membership functions. The Gaussian functions facilitate obtaining smooth, continuously differentiable hypersurfaces of a fuzzy model. They also facilitate theoretical analysis of fuzzy systems as they are continuously differentiable and infinitely differentiable, i.e. they have derivatives of any grade [47, 48, 49].

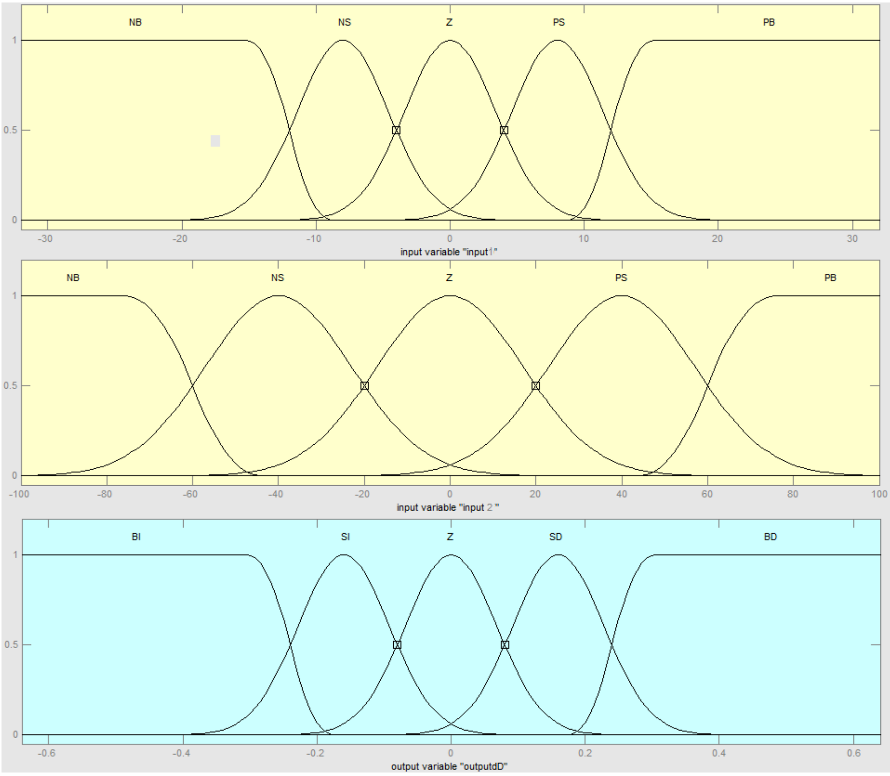

Figure 8

Membership functions of the two entries and the output: (a) Input1, (b) Input2 and (c) Output dD with five sets of linguistic Gaussian variables

The inputs and the outputs as sets of linguistics variables are expressed as follows:

<u>Input1:</u> NB: Negative Big, NS: Negative Small, Z: Zero, PB: Positive Big, PS: Positive Small.

<u>Input2:</u> NB: Negative Big, NS: Negative Small, Z: Zero, PB: Positive Big, PS: Positive Small.

<u>Output</u>: BD: Big Decrease, SD: Small Decrease, S: stabilize, BI: Big Increase, SI: Small Increase.

The value of $Input_1$, $Input_2$ and Output are normalized by an input scaling factor [4]. In this system the input scaling factor has been designed such that:

$Input_1$ values are between -32 and 32

$Input_2$ values are between -100 and 100

Output values are between -62 and 62

The inference method works in such a way that a change in the duty ratio of the buck chopper leads to the voltage V_{MPP} corresponding to the MPP. Following the study of an exhaustive number of combinations of input variables and analysis of the corresponding outputs, we came up with the decision inference rules illustrated in Figure 9.

1. If (input1 is NB) and (input2 is NB) then (outputdD is S) (1)
2. If (input1 is NS) and (input2 is NB) then (outputdD is S) (1)
3. If (input1 is Z) and (input2 is NB) then (outputdD is SD) (1)
4. If (input1 is PS) and (input2 is NB) then (outputdD is SI) (1)
5. If (input1 is PB) and (input2 is NB) then (outputdD is BI) (1)
6. If (input1 is NB) and (input2 is NS) then (outputdD is S) (1)
7. If (input1 is NS) and (input2 is NS) then (outputdD is S) (1)
8. If (input1 is Z) and (input2 is NS) then (outputdD is SI) (1)
9. If (input1 is PS) and (input2 is NS) then (outputdD is SI) (1)
10. If (input1 is PB) and (input2 is NS) then (outputdD is BI) (1)
11. If (input1 is NB) and (input2 is Z) then (outputdD is BD) (1)
12. If (input1 is NS) and (input2 is Z) then (outputdD is SD) (1)
13. If (input1 is Z) and (input2 is Z) then (outputdD is S) (1)
14. If (input1 is PS) and (input2 is Z) then (outputdD is SI) (1)
15. If (input1 is PB) and (input2 is Z) then (outputdD is BI) (1)
16. If (input1 is NB) and (input2 is PS) then (outputdD is BD) (1)
17. If (input1 is NS) and (input2 is PS) then (outputdD is SD) (1)
18. If (input1 is Z) and (input2 is PS) then (outputdD is S) (1)
19. If (input1 is PS) and (input2 is PS) then (outputdD is S) (1)
20. If (input1 is PB) and (input2 is PS) then (outputdD is S) (1)
21. If (input1 is NB) and (input2 is PB) then (outputdD is BD) (1)
22. If (input1 is NS) and (input2 is PB) then (outputdD is SD) (1)
23. If (input1 is Z) and (input2 is PB) then (outputdD is SI) (1)
24. If (input1 is PS) and (input2 is PB) then (outputdD is S) (1)
25. If (input1 is PB) and (input2 is PB) then (outputdD is S) (1)

Figure 9
Proposed Fuzzy Rules decisions

In this work, the Mamdani fuzzy inference method has been used with Max-Min operation fuzzy composition law. This method allows the definition of minimum and maximum input impact for all operating scenarios as illustrated in Figure 10.

Following "inference" operation, the controller outputs expressed as a linguistic variable curve. "Defuzzification" methods are then used to calculate and decode the linguistic variable to a numerical value. In this work, we make use of a Centroid Method, which determines the crisp controller Output as the value of the center of gravity of the final combined fuzzy set.

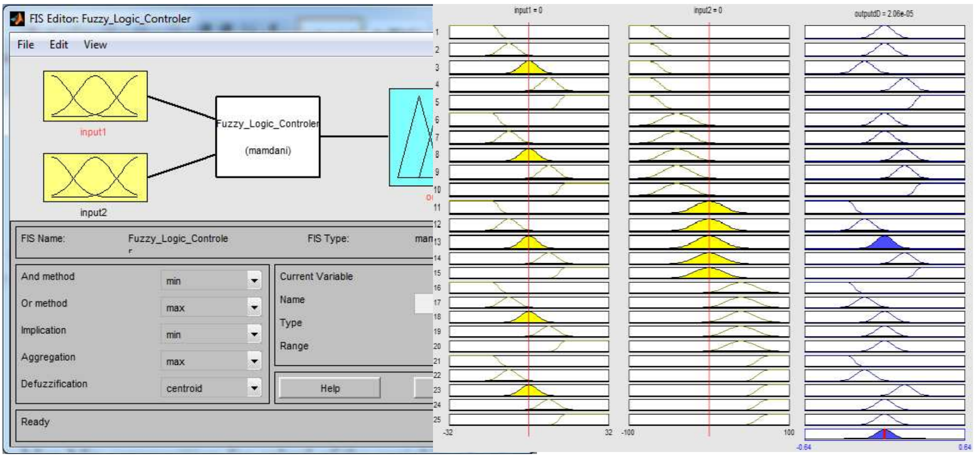

(a) *(b)*

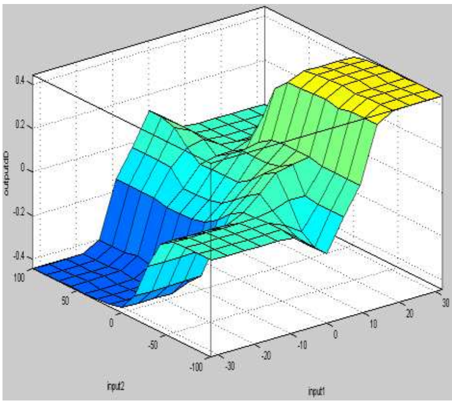

(c)

Figure 10
a) MATLAB representation of the Mamdani fuzzy logic controller; b) Output values depending on possible combinations of Input variables; c) Surface representation used for computation of the Output variable ΔD (center of gravity)

4 Simulation Model

The mathematical representation of the PV-powered section of the electric vehicle expressed through equations (1-4) with specific parametric definition given as follows: 5 series of connected solar panels consisting of 56 photovoltaic cells in series such that referring to Figure 2: z=56, $R_p=30\,\Omega$, $R_s=15.10^{-3}\,\Omega$, $E_g=1.1$ eV, $n_1=1$; $n_2=2$, $k=1.380\times10^{-23}$ J/K, $q=1.602\times10^{-19}$ C, $I_{ph}\big|_{(T=298\cdot K)}=3.25A$.

The buck converter is modeled by equations (5-8) with specific parametric values: $C_1 = C_2 = 5.6$ mF, L= 3.5 mH.

The solar car load block lead acid battery has been modeled by equations (9–10) with initial output voltage V_b=95 V and the following numerical definitions: R_{bs}= 0.0013 Ω, R_{b1}= 2.84 Ω, R_{bp}=10e^3 Ω, C_{b1}=2.5 mF, C_{bp}=2*45*9*12*36000/ (125^2-90^2) =4.650 KF.

The initial output of the MPPT was set to d=0.1(fuzzy logic), d=0.5(P&O).

The initial input of the MPPT was set to P=0 W and V=0V (fuzzy logic), P=0W and V=0V (P&O).

The parameters described above were integrated into the Simulink blocks shown in Figure 9 and Figure 10

Figure 9 describes the PV system implementing the P&O algorithm using Model-Based Design in order to control the Buck converter, and harvest the maximum power.

In Figure 11 the same blocks are maintained whereas the block of P&O was replaced by fuzzy logic Block.

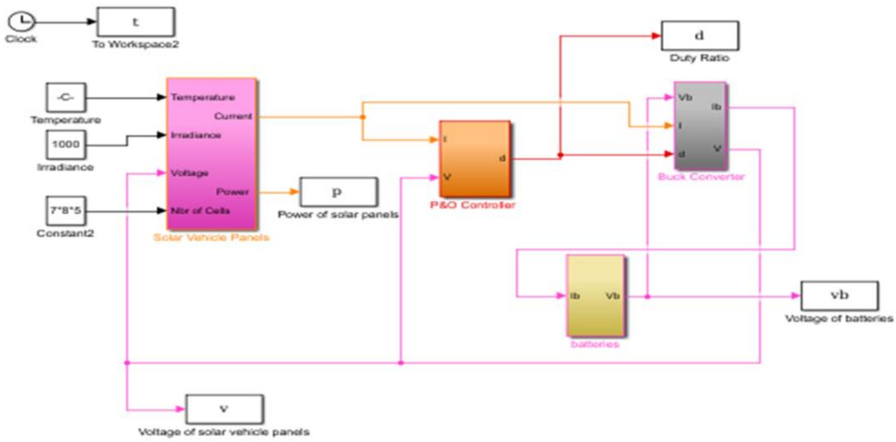

Figure 11

Solar vehicle PV system simulated in Matlab/Simulink with P&O controller

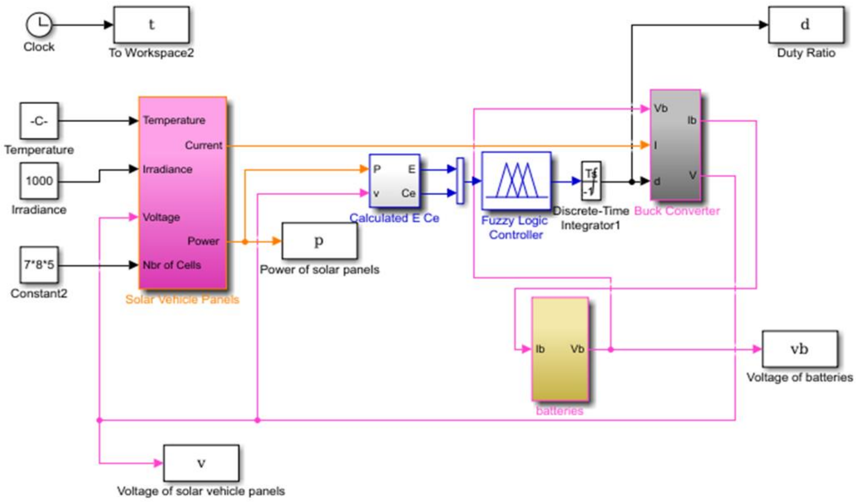

Figure 12
Solar vehicle PV system simulated in Matlab/Simulink with a fuzzy logic controller

5 Simulation Results

In an attempt to evaluate the performance improvement of a fuzzy logic based MPPT applied to a solar vehicle system, we analyzed its power extraction capabilities and stability versus the traditional P&O controller. In this simulation, the model of a solar vehicle was run with a fuzzy logic controller and a P&O controller under different climatic conditions, relevant to the movement of a solar vehicle, i.e., with rapid changes of irradiance and temperature.

5.1 Simulation Results for a Fast Increase of Irradiance

The first performance comparison between the fuzzy controller and conventional P&O controller was for a fixed temperature of 25ºC and a virtually instantaneous increase of irradiance from 100 Wm^{-2} to 1100 Wm^{-2} that occurs at t=25 s (Figure 13).

As expected, we note that with the rapid irradiance increase, the harnessed power also increased. In the case of the P&O controller, we note that there is a very harsh overshoot of the power signal. The power signal for the P&O controller rapidly increases and then abruptly drops to increase progressively to a seemingly steady state of maximum power. However, when zoomed in, we note that the P&O controller generated signal actually oscillates about a mean and is not stable. Similar overshoots are obtained for operating voltages for solar panels and solar batteries in the case of the P&O controller. This leads, not only to reduce energy being harvested but also to cyclic recurrent electric changes on the elements with possible lifecycle reduction. We note a much better performance of the fuzzy logic based controller. First of all, in the case of all signals (voltage and power), the steady state signal is very stable. Furthermore, we note that the response time to detect MPP and achieve maximum power harvest is shorter compared to the P&O controller with limited overshoot.

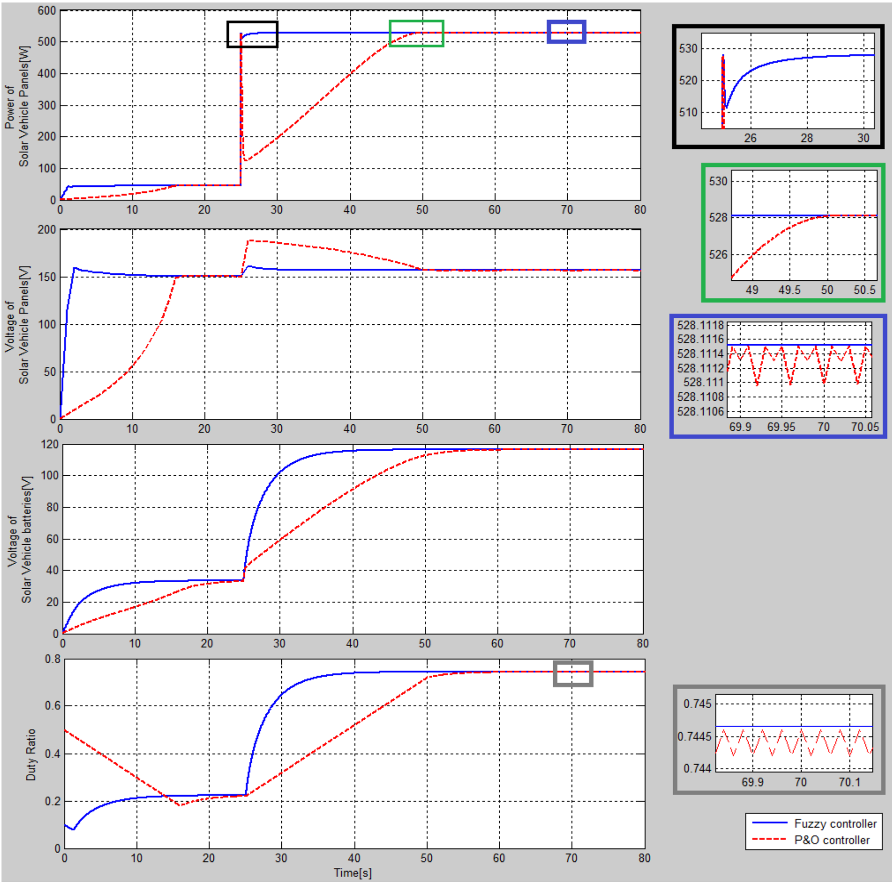

Figure 13

Performance comparison between P&O and a fuzzy logic controllers for an instantaneous increase of irradiance from 100 Wm^{-2} to 1100 Wm^{-2} at t=25 s for fixed temperature of 25°C

5.2 Simulation Results for a Fast Decrease of Irradiance

In this case, we compare the relative performance of fuzzy logic controller with a conventional P&O controller for a fixed temperature of 25°C and a virtually instantaneous decrease of irradiance from 1000 Wm^{-2} to 400 Wm^{-2} at t=25 s (Figure 14).

Similar advantages are noticed for the fuzzy logic controller with shorter time response for maximum power point identification and power stabilization. However, the performance disparity between the two controllers is less than the previous case of the rapid increase in irradiance. In this case, the major advantage of the fuzzy logic controller is during the steady-state operation with an increase of power and voltage stability and overshoot reduction.

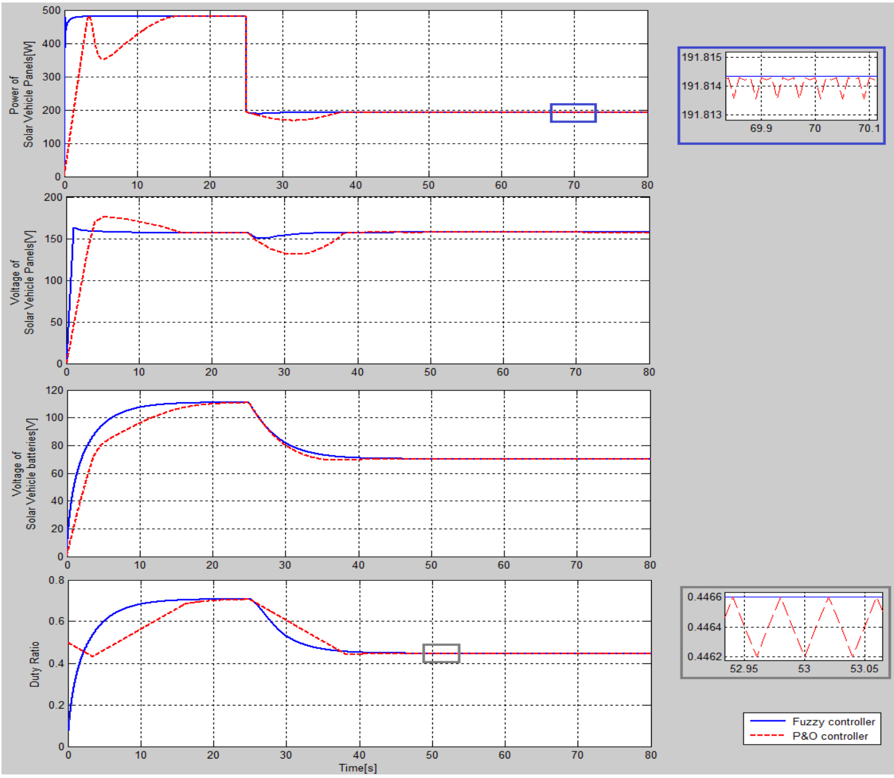

Figure 14

Performance comparison between P&O and a fuzzy logic controller for an instantaneous decrease of irradiance from 1000 Wm^{-2} to 400 Wm^{-2} at t=25 s for a fixed temperature of 25ºC

5.3 Simulation Results for a Fast Increase in Temperature

Because of the influence of the temperature, which acts negatively on the efficiency of photovoltaic systems, it is essential to study the behavior of the two controllers for abrupt variations of temperature. The two controllers FL and P&O will be subject to an instantaneous increase of temperature from 10°C to 50°C at a fixed irradiance of 1000 Wm^{-2} (Figure 15).

The performances of FL controller are definitely more appreciable with a better response time and overshoot reduction and less oscillation in steady state.

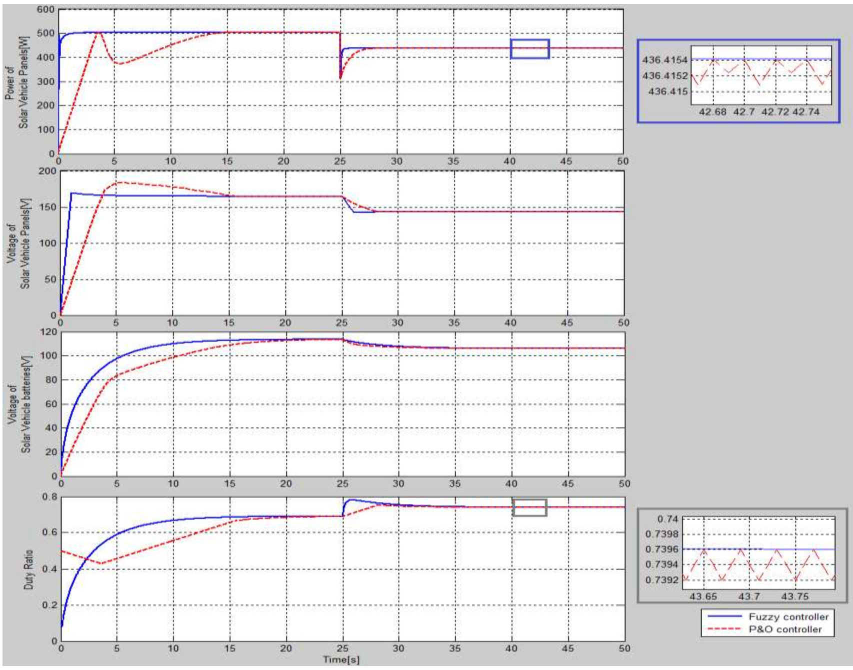

Figure 15

Performance comparison between P&O and a fuzzy logic controller for an instantaneous increase of temperature from 10ºC to 50ºC (at t=25 s) at a fixed irradiance of 1000 Wm^{-2}

5.4 Simulation Results for a Fast Decrease in Temperature

In a second test, where the temperature falls abruptly from 60°C to 05°C with a fixed irradiance of 1000 Wm^{-2}, the same performances described above are noticed with a better time of response, a limited overshoot and reduced oscillations in the steady state. This state represents a precious gain of time and energy for the vehicle that changes position all the time of which sudden changes in irradiance and temperature are always expected (Figure 16).

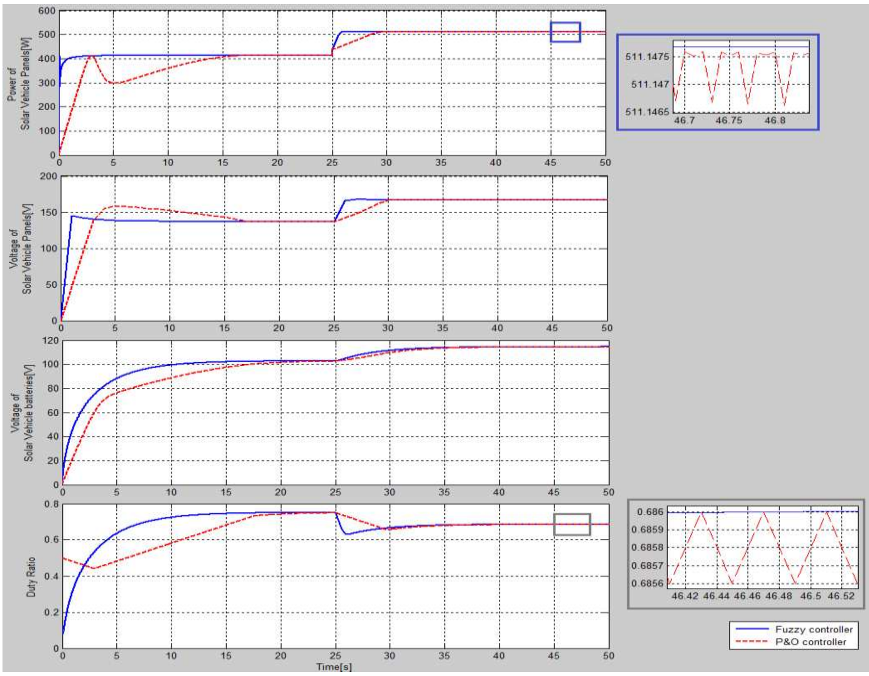

Figure 16

Performance comparison between P&O and a fuzzy logic controller for an instantaneous decrease of temperature from 60ºC to 5ºC (at t=25 s) at a fixed irradiance of 1000 Wm^{-2}

Conclusion

The initial cost of solar energy is a major issue in relation to its huge potential for greater development. Maximum power extraction is an important parameter to reduce the total cost of PV systems and enables better paybacks of PV projects. In this paper, we focused our analysis on solar-powered vehicles. A rapidly adapting MPP algorithm is required to harness the maximum power and make such applications technologically and cost effective. We proposed a new fuzzy logic method to achieve a faster and more stable power output from PV modules. In order to emphasize the performance of this new controller, a Matlab-Simulink® model was built and simulations were run for various operational scenarios. The results were compared with a commonly used P&O controller. Simulation results prove a high efficiency, in maximum power tracking, of a fuzzy logic controller. The simulations showed that most significant performance differences were achieved with rapidly varying parameters that influence power output (temperature and irradiance). Moreover, the fuzzy logic-based controller, as compared to the P&O controller, shows better performance in maximum power tracking time, and stability and robustness in all cases. Better stability and a robust performance from the fuzzy logic based controller, offers significant advantages in the mitigation of power fluctuations.

Acknowledgment

The authors would like to thank Dr. Khaled Ragab (UQAC University, Chicoutimi, QC, Canada) for his efforts in revising the academic written English of this article.

References

[1] Cheddadi, Y., et al: Design and verification of photovoltaic MPPT algorithm as an automotive-based embedded software. Solar Energy 171: 414-425. 2018

[2] Karami, N., et al: General review and classification of different MPPT Techniques." Renewable and Sustainable Energy Reviews 68: 1-18. 2017

[3] Makhsoos, A., et al: Design, simulation and experimental evaluation of energy system for an unmanned surface vehicle." Energy 148: 362-372. 2018

[4] Yilmaz, U., et al: PV system fuzzy logic MPPT method and PI control as a charge controller." Renewable and Sustainable Energy Reviews 81: 994-1001 (2018)

[5] Anurag, A., et al: A review of maximum power-point tracking techniques for photovoltaic systems. International Journal of Sustainable Energy, 2016. **35**(5): pp. 478-501

[6] Shweta Pandey, Prasanta Kumar Jena: A Review on Maximum Power Point Tracking Techniques for Photovoltaic Systems. International Research Journal of Engineering and Technology (IRJET). Volume: 04 Issue: 06 | June -2017

[7] Onat, N: Recent developments in maximum power point tracking technologies for photovoltaic systems. International Journal of Photoenergy, 2010

[8] M. Oulcaid, H. El Fadil, A. Yahya, F. Giri: Maximum Power Point Tracking Algorithm for Photovoltaic Systems under Partial Shaded Conditions. IFAC-PapersOnLine. Vol. 49, Issue 13, 2016, pp. 217-222

[9] Won, C.-Y., et al: A new maximum power point tracker of photovoltaic arrays using fuzzy controller. In Power Electronics Specialists Conference, PESC'94 Record. 25th Annual IEEE. 1994. IEEE

[10] Ahmed M. Othman, Mahdi M. M. El-arini, Ahmed Ghitas, Ahmed Fathy: Realworld maximum power point tracking simulation of PV system based on Fuzzy Logic control. Volume 1, Issue 2, December 2012, pp. 186-194

[11] Patcharaprakiti, N., S. Premrudeepreechacharn, and Y. Sriuthaisiriwong: Maximum power point tracking using adaptive fuzzy logic control for grid-connected photovoltaic system. Renewable Energy, 2005. **30**(11): pp. 1771-1788

[12] Juntao Fei, Yunkai Zhu: Adaptive fuzzy sliding control of single-phase PV grid-connected inverter. PLoS ONE 12(8): e0182916. https://doi.org/10.1371/journal.pone.0182916. August 10, 2017

[13] Subhash E. Apatekar, Akireddy Shravankumar, Ch. Anitha: Maximum Power Point Tracking using Fuzzy Logic Control for Grid-Connected Photovoltaic System & Operation of PV Cells under Partial Shading Conditions. International Conference on Recent Trends in Engineering Science and Technology (ICRTEST 2017) Volume 5, Issue 1 (Special Issue 21-22 January 2017)

[14] Cheikh, M. A., et al: Maximum power point tracking using a fuzzy logic control scheme. Revue des energies Renouvelables, 2007. **10**(3) pp. 387-395

[15] Sadeq D. Al-Majidi, Maysam F. Abbod, Hamed S. Al-Raweshidy: A novel maximum power point tracking technique based on fuzzy logic for photovoltaic systems. International Journal of Hydrogen Energy. Volume 43, Issue 31, 2 August 2018, pp. 14158-14171

[16] Salameh, Z. M., M. A. Casacca, and W. A. Lynch: A mathematical model for lead-acid batteries. IEEE Transactions on Energy Conversion, 1992. 7(1): pp. 93-98

[17] Leszek Kasprzyk: Modelling and analysis of dynamic states of the lead-acid batteries in electric vehicles. Eksploatacja i Niezawodnosc – Maintenance and Reliability 2017; 19 (2): 229-236

[18] Larbes, C., et al: Genetic algorithms optimized fuzzy logic control for the maximum power point tracking in photovoltaic system. Renewable Energy, 2009. **34**(10): pp. 2093-2100

[19] Mohamed Amine Haraoubia, Najib Essounbouli, Abdelaziz Hamzaoui: Optimisation of fuzzy controller for tracking the maximum power point in PV systems. IEEE 2015 3rd International Renewable and Sustainable Energy Conference (IRSEC)

[20] Khaligh, A. and O. C. Onar: Energy harvesting: solar, wind, and ocean energy conversion systems. 2017: CRC press

[21] Kamarzaman, N. A. and C. W. Tan: A comprehensive review of maximum power point tracking algorithms for photovoltaic systems. Renewable and Sustainable Energy Reviews, 2014. 37: pp. 585-598

[22] Jaldeep Kumar, Prakash Bahrani: Comprehensive Review on maximum power point tracking methods for SPV system. International Research Journal of Engineering and Technology (IRJET) Volume 04, Issue 12 | Dec-2017

[23] Esram, T. and P. L. Chapman: Comparison of photovoltaic array maximum power point tracking techniques. IEEE Transactions on energy conversion, 2007. 22(2): pp. 439-449

[24] Manel Hlaili and Hfaiedh Mechergui: Comparison of Different MPPT Algorithms with a Proposed One Using a Power Estimator for Grid Connected PV Systems. International Journal of Photoenergy. Volume 2016, Article ID 1728398, 10 pages

[25] Hua, C. and C. Shen: Comparative study of peak power tracking techniques for solar storage system. In Applied Power Electronics Conference and Exposition, 1998. APEC'98. Conference Proceedings 1998. Thirteenth Annual. 1998, IEEE

[26] Fernando Lessa Tofoli. Dênis de Castro Pereira. Wesley Josias De Paula: Comparative Study of Maximum Power Point Tracking Techniques for Photovoltaic System. in International Journal of Photoenergy 2015(3):1-10 February 2015

[27] Reisi, A. R., M. H. Moradi, and S. Jamasb: Classification and comparison of maximum power point tracking techniques for photovoltaic system: A review. Renewable and Sustainable Energy Reviews, 2013. 19: pp. 433-443

[28] Priety, Vijay Kumar Garg: A review paper on various types of MPPT techniques for PV system. International Journal of Engineering & Science Research. IJESR/May 2014/ Vol-4/Issue-5/320-330

[29] Knopf, H: Analysis, simulation, and evaluation of maximum power point tracking (MPPT) methods for a solar powered vehicle. 1999, Portland State University Portland

[30] Athanasios G. Sarigiannidis, Spyridon A. Stathis, Antonios G. Kladas: Performance evaluation of MPPT techniques for PV array incorporated into Electric Vehicle roof. IEEE, 2015 International Conference on Renewable Energy Research and Applications (ICRERA)

[31] Swokowski, E. W: Analyse. 1993: De Boeck Supérieur

[32] Wolfs, P. and Q. Li: A current-sensor-free incremental conductance single cell MPPT for high performance vehicle solar arrays. in *Power Electronics Specialists Conference, 2006. PESC'06. 37th IEEE*. 2006. IEEE

[33] Sheifali Gupta. Ankit Aneja. Hitesh Mittal. Aditya Jai: Performance and Cost Optimised MPPT for Solar Powered Vehicle. International Journal of Advanced Research in Computer Engineering & Technology (IJARCET) Volume 2, Issue 12, December 2013

[34] Yuli, H. and W. Jiajun: Study on power generation and energy storage system of a Solar Powered Autonomous Underwater Vehicle (SAUV) Energy Procedia, 2012. 16: pp. 2049-2053

[35] Ali Razmjoo, Mohammad Ghadimi, Mehrzad Shams, Hoseyn Shirmohammadi: Design and Built a Research AUV Solar Light Weight. International Journal of Energy and Power Engineering. 2015; 4(5) 268-274

[36] Skaale, I., D. J. Patterson, and H. Pullen: The development of a new maximum power point tracker for a very high efficiency, compound curve photovoltaic array for a solar powered vehicle. Renewable Energy, 2001. 22(1-3): pp. 295-302

[37] K. Someswara Rao, V. Mahesh, Jammula. Kalyan Chakravarthi, Syed Khutub Uddin: Design and Development of Green Car. ISSN (Print): 2319-3182, Volume 3, Issue 4, 2014

[38] Ram, J. P., et al: A comprehensive review on solar PV maximum power point tracking techniques. Renewable and Sustainable Energy Reviews 67: 826-847, 2017

[39] Amitava Chatterjee. Ranajit Chatterjee. Fumitoshi Matsuno. Takahiro Endo: Augmented Stable Fuzzy Control for Flexible Robotic Arm Using LMI Approach and Neuro-Fuzzy State Space Modeling. in IEEE Transactions on Industrial Electronics 55(3):1256 -1270, April 2008

[40] Tamás Haidegger, Levente Kovács, Radu-Emil Precup, Balázs Benyó, Zoltán Benyó, Stefan Preitl: Simulation and control for telerobots in space medicine. Acta Astronautica, Vol. 81, Issue 1, December 2012, pp. 390-402

[41] Petr HušEk, Otto Cerman: Fuzzy model reference control with adaptation of input fuzzy sets. Knowledge-based Systems. Volume 49, September, 2013, pp. 116-122

[42] Sasa Vrkalovic, Teodor-Adrian Teban, Ioan-Daniel Borlea: Stable Takagi-Sugeno Fuzzy Control Designed by Optimization. Control Designed by Optimization, International Journal of Artificial Intelligence, Vol. 15, No. 2, pp. 17-29, 2017

[43] Ko, S.-H. and R.-M. Chao: Photovoltaic dynamic MPPT on a moving vehicle. Solar Energy, 2012. **86**(6): pp. 1750-1760

[44] Ismail Nakir. Ali Durusu. Hakan Akca. Ali Ajder: A New MPPT Algorithm for Vehicle Integrated Solar Energy System. in Journal of Energy Resources Technology 138(2) November 2015

[45] Salameh, Z. and D. Taylor: "Step-up maximum power point tracker for photovoltaic arrays". Solar energy, 1990. **44**(1): pp. 57-61

[46] Casacca, M. A. and Z. M. Salameh: Determination of lead-acid battery capacity via mathematical modeling techniques. IEEE Transactions on Energy Conversion, 1992, 7(3): pp. 442-446

[47] Ahsanullah Soomro, Wenguo Xiang, Kamran A Samo: Development of a simplified method for the determination of ampere-hour capacity of lead–acid battery. Energy & Environment, November 28, 2017

[48] Lu, C.-F., C.-C. Liu, and C.-J. Wu: Dynamic modelling of battery energy storage system and application to power system stability. IEEE Proceedings-Generation, Transmission and Distribution, 1995, **142**(4): pp. 429-435

[49] Xiaokang Xu, Martin Bishop, Donna G. Oikarinen, Chen Hao: Application and modeling of battery energy storage in power systems. CSEE Journal of Power and Energy Systems (Volume 2, Issue 3, Sept. 2016)

[50] Bühler, H: *Réglage par logique floue*. 1994: Presses polytechniques et universitaires romandes

[51] Piegat, A: (2013) Fuzzy modeling and control, Physica

Multi-Scenario Multi-Objective Optimization of a Fuzzy Motor Controller for the Szabad(ka)-II Hexapod Robot

István Kecskés, Péter Odry

University of Dunaújváros, Táncsics Mihály utca 1/A, 2401 Dunaújváros, Hungary; kecskesi@uniduna.hu, podry@uniduna.hu

Abstract: The aim of this research was to develop a robust motor controller for the Szabad(ka)-II hexapod robot. A Fuzzy-PI controller that utilized a lookup table was chosen because of its reported promising performance and its ability to be embedded in the microcontrollers of the robot. The variables of the controller were defined by a particle swarm optimization method to minimize the five quality objectives related to the walking of the robot. The preferences of the five objectives were successfully expressed by a biased-weighted geometric mean utility function. The resulting optimal solutions were significantly altered by changing the bias and exponential weights of preferences. Therefore, we checked the robustness of the solution against the controller's variables as a secondary objective.

Keywords: multi-scenario; multi-objective optimization; fuzzy control; robot dynamic simulation

1 Introduction

This work presents advanced research for control optimization related to the Szabad(ka)-II hexapod walker robot (Fig. 1), therefore, it is closely aligned with previous research results. The author's previous publication provides detailed information about the Szabad(ka)-II mechatronic device, its structure, sensors, motion requirements, modeling and control challenges.

This paper focuses on the issue of motion quality formulation, and the effects of the changing of preference weights between the objectives. Robust optimization is performed on a fuzzy-based motor controller, while walking quality is defined as a multi-scenario and multi-objective, in a specific simulation environment.

The Szabad(ka)-II is an 18 degree of freedom (DOF) hexapod walker robot. All the 18 joints are driven by 12 V DC gear motors. The embedded electronics executes the control algorithm real-time with a sampling frequency of 500 Hz.

The dynamic simulation model of the Szabad(ka)-II was developed and validated based on measurements performed on a real robot [1]. The cyclic trajectory data were generated offline specifically for the intended walking scenario. The trajectory curve of the tripod hexapod walking [2] has been researched and optimized together with a PI motor controller [3]. The optimization of the Fuzzy-PI motor controllers has also been researched [4].

In this study, the optimization of the motor controller differs from previous research in the following aspects:

- Developing and optimizing a Fuzzy-PI controller that can be embedded into real robot controllers (one Texas Instruments MSP430F2618 microcontroller for each leg). The fuzzy output is calculated by a previously generated lookup table, which has a constant number of dimensions and resolution, see details in [5].
- The simulation has multi-scenario properties. The multi-scenario approach is important to develop a universally optimal and robust motor controller for the intended use of the robot. See the details in Subsection 2.1.

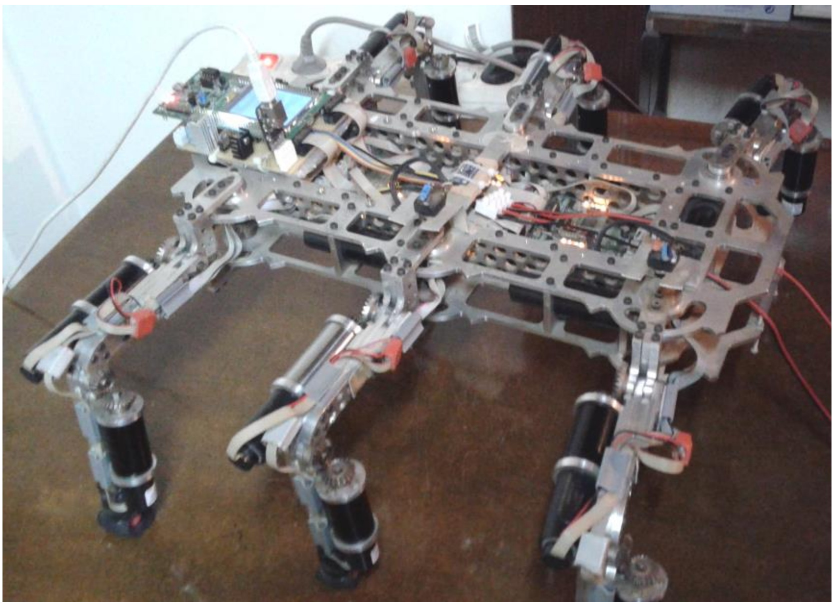

Figure 1
Szabad(ka)-II hexapod robot

The analyzed and optimized system is a multi-scenario multi-objective (MSMO) simulation system. These two properties are described in the second chapter. The third chapter describes the fuzzy-PI motor controller, and the fourth chapter summarizes the experimental results.

1.1 Multi-Objective Optimization Algorithms

Over the past decade, a number of multi- and many-objective evolutionary algorithms have been proposed. The most cited procedure is the Nondominate Sorting Genetic Algorithm (NSGA) [6] and its extended version, the NSGA-II method [7], which is currently the most widely read article in this field of science. The authors of the NSGA have provided two sets of test problems. Besides the popular NSGA series, there are several evolutionary multi-optimization search methods, such as Multi-Objective Particle Swarm Optimization (MOPSO) [8], Cuckoo Search [9], Ant colony optimization (ACO) [10], and Multi-objective Differential Evolution (MOnDE) [11].

A multi-objective optimization process has several objective functions, and when searching for the optimum solution, the criteria involve finding the best fitness values while making compromises between the objectives. This topic has been addressed well in several studies [12] [13] [14].

The utility function is a specific type of objective function that is used to summarize (aggregate) the original objectives into a single figure of merit" [15] based on any predefined preferences - this is also called scalarization. When the aggregation of the objectives into a single utility function value can be defined unambiguously, then it represents the best solution [16].

One common approach is to combine the objective functions into a single function using weights, and the problem then becomes a matter of how to determine the appropriate weights [17]. However, in case of a real system optimization, it is often difficult to define the importance of these aspects relative to each other and, in addition, how they can be aggregated numerically.

1.2 Controller Multi-Objective Optimization

Structural and control optimization issues in complex dynamic systems are commonly multi-objective problems, as seen in hexapod robots [4] [18] [19], turbojet engines [20] [21], servo motor controllers [22] [23] [24], smart grids [25], train speed controllers [26], vehicle design [27], or building energy consumption problems [28].

Multi-objective optimization is commonly used for controllers where more than one quality objectives are defined. Adaptive PID and PI controllers are optimized using Multi-Objective Generic Algorithm in [22]. Cascaded DC motor controllers are optimized using multi-objective optimization evolutionary algorithms (MOEAs) selecting different solution on the Pareto-set in [29]. Optimal PID controllers are developed by NSGA-II algorithm, and compared to the traditional Ziegler Nichols methods in [30] and [23].

Complex, nonlinear and stochastic systems, such as, a hexapod robots or smart grids are frequently controlled by fuzzy or neuro-fuzzy systems. A multi-objective genetic algorithm is commonly used to find the optimal fuzzy controller, e.g., in [25] and [31] the set of solutions was found on the Pareto front. The results were compared using the same fuzzy controller optimized by a mono-objective genetic algorithm in [25]. Multi-objective Particle Swarm Optimization is also used for motor controller optimization [24].

In the cited optimization research group, the Pareto solution is determined without researching any further robustness or additional criteria to select the final solution. For example, in [30] the solution is selected based on only the primary objective from the Pareto set of two-objectives without any further investigation or explanation. In papers where weighted aggregation is performed to create single-objective from multi-objectives, the weights are not mentioned explicitly [26], or defined empirically.

1.3 Multi-Scenario in Optimization

A scenario in this context means a bunch of modifications in the input or parameterization of the system handled and optimized in parallel mode (e.g., a walker robot is walking, running, turning or sneaking). Scenarios are also referred to as 'situations' or 'modifications' in literature, but in event-based controlling, a scenario is not the same as an event.

The multi-scenario is similar to the multi-objective property. Commonly, the aggregation of scenarios is performed similarly to or together with the multi-objectives. The main purpose of the scenario-oriented approach is to be able to deal with a series of small multi-criteria design problems as opposed to a single large multi-criteria problem [32]. The increase of optimum robustness is the most common additional criteria aimed for in the multi-scenario approach, such as in [32] and [33]. In [34], the multi-scenario optimization was used to reach a robust optimum by dealing with uncertainty.

The MSMO approach has already been developed for theoretical problems [35] but it still appears as a new research area for issues related to motion quality of robot systems.

2 Multi-Scenario Multi-Objective Quality Definition of a Walker Robot

To the best of the authors' knowledge, there are no specific and applicable quality definitions for walker robot control problems. Practically, there are no definitions for the required quality aspects, nor is it clear to what extent the aspects should be optimized. In our definitions, goodness is divided into simpler elements, which are established by common sense and empirical experience. Thus, the quality description is multi-objective.

2.2 Multi-objective Quality Definition

A multi-objective optimization process has several objective functions, and when searching for the optimum solution, the criteria involve finding the best fitness values while compromising between the objectives [12] using any preference between them.

The determination of the robot walking quality is not a trivial task. However, the most commonly seen criteria are the maximum traction and the minimum power consumption [36]: “In rough terrain, traction should be maximized. In benign terrain, power consumption should be minimized.”

The walking quality or driving quality definition is multi-objective. Previously, five quality objectives were defined for the Szabad(ka)-II robot walking [4]; see Table 1. In addition to the energy consumption and maximum walking speed, the vibration and jerks that appear in dynamics are addressed. The minimization of such high accelerations or rigid collisions is generally examined in robotics [37].

Table 1
Hexapod walking objectives

Quality Goal	**Objective (to be minimize)**	**Symbol**
achieve the maximum walking speed	the reciprocal value of mean velocity in the X direction	f_5
minimize the electrical energy consumption	electric energy consumption for walking one meter	f_4
minimize the torque on the joints and gears, thus minimizing the jerks in the motor current	root mean square of torque measured in the 18 joints	f_1
minimizing the robot’s body acceleration in all three-dimensional directions	root mean square of magnitude of 3D body acceleration	f_2
minimizing the robot’s body angular acceleration in all three-dimensional directions	root mean square of magnitude of 3D body angular acceleration	f_3

2.2 Multi-Objectives Aggregation

Some type of manual selection is required for the Pareto solution sets that result from the multi-objective optimizer algorithms [15], because only one solution at a time can be implemented in the real application.

The fitness values are calculated by aggregating these five (M=5) objectives by a so-called utility function. We propose a bias-weighted utility function and the production operation for the aggregation (geometrical mean). This function has a bias (b_m) and exponent (e_m) weights for each objective. The bias weights can reduce the strong influence of near zero values, while the exponent weights express the relative importance between the objectives. Equation (1) describes this utility function resulting in the scalar fitness value (f_{SC}) for one simulation scenario. The X represents the design variables, which are optimized by the optimizer algorithm.

$$f_{SC}(X)=\prod_{m=1}^{M}\left(b_m+f_m(X)\right)^{e_m} \tag{1}$$

The well-defined quality formulation and proper weighting of the objectives are important [4]. In this study, these quality definitions are used. However, the preferences between these objectives are defined carefully and empirically. Different variations of these preferences are presented in Section 3.2.

2.3 Multi-Scenario Simulation

A driving solution is sought that provides robust and universally optimal behavior for all possible movements or walking tasks of the walker robot. The scenario-oriented approach offers an advantageous solution to this issue, as stated in the conclusion of [27]: The all-situation problem can thus be decomposed into several scenarios to form multiple objective functions, where these scenarios can be typical cases of all possibilities (generally an infinite number of situations). The main criteria in the selection of these targets and the determination of the number of scenarios should be a diversity of the required maneuvers as much as possible.

There is no guidance on how to select and how many scenarios are necessary, e.g., in [38], there are only two scenarios. The selected six typical scenarios for the Szabad(ka)-II robot demonstrate the possible intended use (which is just an example, because this robot was built for research purposes). In the selection of these scenarios, we considered the possible types of motions that the real robot can perform in the given laboratory conditions.

Table 2 lists the six scenarios and their parameters used for the optimization of the Szabad(ka)-II robot fuzzy controllers. The *load* means a real cargo, mounted on the robot body.

This ellipse-based leg trajectory was first published in [39]. The 3D leg trajectory curves are generated based on a half-ellipse. The *width*, the *stride*, the *height*, and the *radius* parameters are predefined or calculated from other scenario requirement parameters, such as *withers* or *turn*. These parameters differ for each scenario, as shown in Table 2.

Table 2
Parameters of six walking scenarios

Scenario description				Trajectory parameters			
ID	**Gait**	**Speed**	**Load**	**Turn**	**Time**	**Radius**	**Withers**
1.	Tripod normal	Fast	0 kg	0	1.5 s	0.16 m	0.15 m
2.	Tripod normal	Slow	0 kg	0	2.2 s	0.16 m	0.15 m
3.	Tripod normal	Fast	2 kg	0	1.5 s	0.145 m	0.20 m
4.	Tripod normal	Slow	2 kg	0	2.2 s	0.145 m	0.20 m
5.	Tripod slope	Fast	0 kg	0	1.5 s	0.20 m	0.14 m
6.	Turn right	Fast	0 kg	0.5	1.5 s	0.16 m	0.15 m

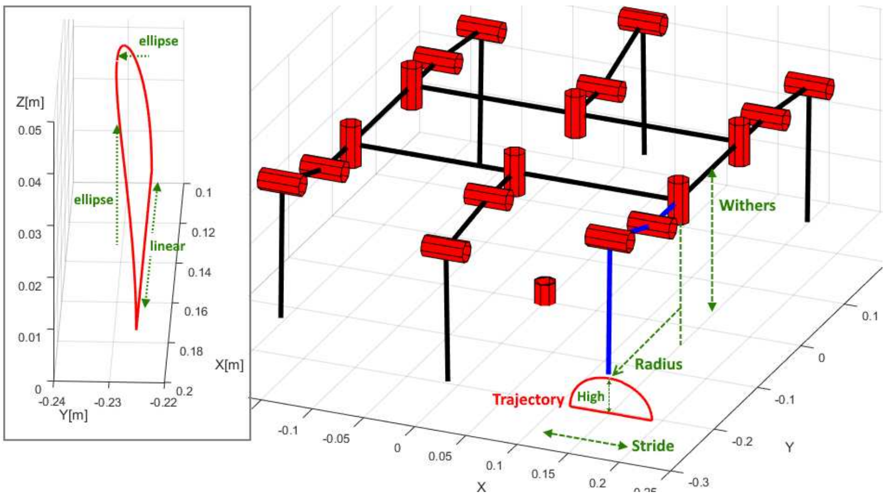

Figure 2
Ellipse based leg trajectory for the tripod hexapod walking of the Szabad(ka)-II robot

Each of the six legs received the same curves with inverted phases according to the tripod walking. This curve is adjusted only with the parameter *turn* if the robot performs a turn. The joint trajectories are calculated from this leg trajectory using inverse kinematics, which was described in a previous publication [1].

2.4 Multi-Scenario Aggregation

Parallel execution of these scenarios ($K=6$) provides a multi-scenario objective function that is primarily a multi-objective function. Multi-scenario problems are regularly solved by aggregating all the objectives of all scenarios into a large multi-criteria problem, which is confirmed by previous studies [27], [35]. The global scalar fitness values (f_G) are calculated with the geometrical mean applied for the scenario's fitness values (f_{SC}); see equation (2).

$$f_G(X) = \sqrt[K]{\prod_{k=1}^{K} f_{SC}(X,k)} \qquad (2)$$

2.5 Simulation Model

The kinematic model describes the movement, while the dynamic model shows the forces and torque effects on the robot body and engine, as well as the electrical activity of the motor. The kinematic and dynamic models are essential for the effective development of robots, especially if the controllers are under research, which is confirmed by several of the studies [40], [41], [19].

The current simulation model was described in paper [1] (it includes a detailed kinematic and dynamic model of the real Szabad(ka)-II robot). This model includes the kinematics and dynamics of the 18 DOF robots, model of the DC motor and gearboxes, model of the PWM amplifiers, model of the encoders and current sensors, model of the ground contacts, and model of the controllers embedded in the robot electronics. Fig. 3 illustrates the simulation model implemented in Simulink.

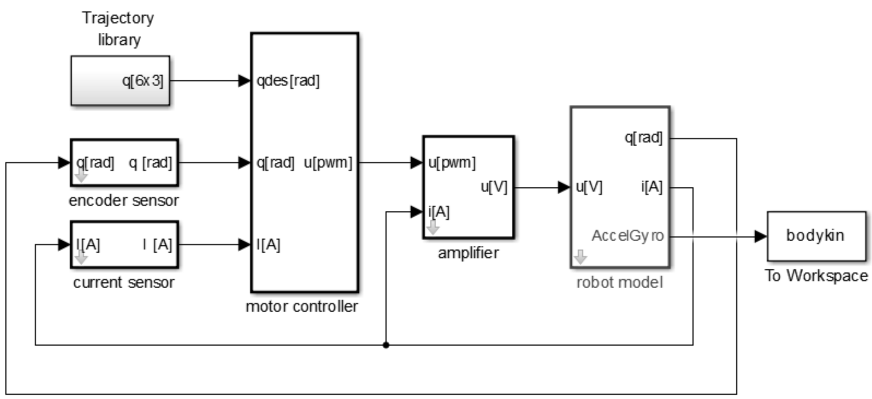

Figure 3
Simulink model of the Szabad(ka)-II robot – the root level. More details are given in [1]

2.6 Optimization Algorithm

In previous research [4], the examined motor controllers were optimized together with the parameters of the leg trajectory of the Szabad(ka)-II robot. The particle swarm optimization (PSO) method was chosen from 12 heuristic optimization methods through a benchmark-based selection and with the help of specific test functions [4]. The applicability of swarm-based optimizations of the hexapod robot structure and its walking are summarized in reference [42].

Therefore, in this study, we used the already developed algorithm of the PSO (original implementation available in [43]). Fig. 4 illustrates the block diagram of the implemented optimization system in a Matlab/Simulink environment. This implementation is capable of parallelizing iterations, storing iteration results immediately after its calculation and analyzing the evolution during the work. These functionalities are especially developed for long term optimizations (when calculations last more than days or weeks).

The Matlab code is available in webpage [44].

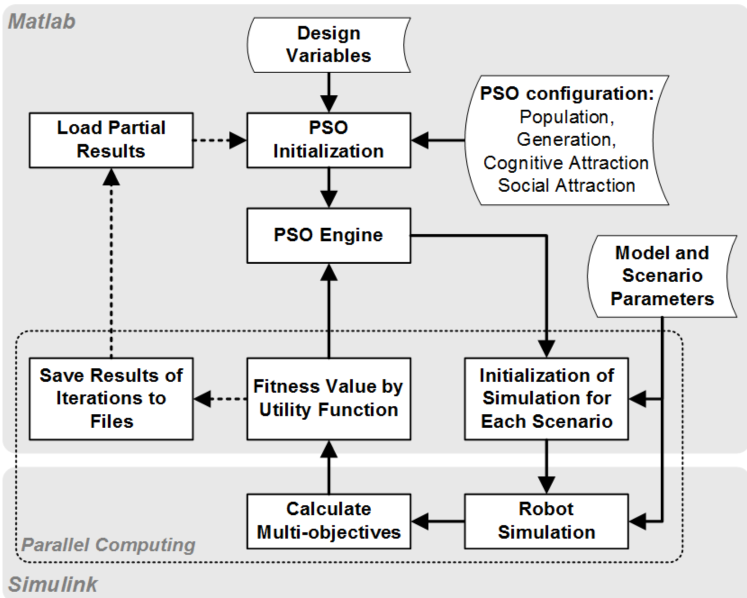

Figure 4
Block diagram of the PSO optimization system in a Matlab/Simulink environment for the MSMO robot simulation

3 Fuzzy-PI Motor Controller

The main advantage of the Fuzzy Logic System is that it can extract heuristic rules that contain if-then statements from human experience [38]. Fuzzy Logic Systems are introduced to learn the behaviors of the unknown dynamics of the robot and wheel actuators due to their universal approximation properties. In this way, the external disturbances and approximate errors can be efficiently counteracted by employing smooth, robust compensators [45].

The fuzzy controller can provide a more comprehensive solution compared to the PID controller [46]. This is confirmed by our previous studies:

- A fuzzy-PI motor controller with three input variables was constructed and compared with a previously used PI controller for the Szabad(ka)-II walker robot [4].
- A fuzzy route controller was introduced and compared with a simple PID route controller [40].
- A fuzzy-I motor controller was developed and optimized to ensure better control performance to protect the Szabad(ka)-II walker robot's electromechanical equipment against high peaks or jerks, and was compared to a PID controller. [41]

3.1 Motor Controller of Szabad(ka)-II Robot

In this context, the fuzzy-PI controller type is a PI controller, where the P - proportional tag is defined by a Fuzzy Logic Controller (fuzzy); see Fig. 5. This control system includes the following:

- The fuzzy controller is implemented as a lookup table (LUT), published in [5]. Therefore, its name became "fuzzy LUT" in this context. This controller has two inputs: the angle error and the motor current.
- Each motor current is measured by the robot's microcontroller with a 12-bit resolution AD converter.
- The desired joint angles are predefined (see Section 2.3) and sent from a Matlab program implemented in the PC client side.
- The measured joint angles are calculated based on an encoder sensor mounted on the motor.
- The I integrator tag's output is added to the P proportional tag and results in the control voltage. This voltage drives a PWM amplifier with a 10-bit resolution DA converter.

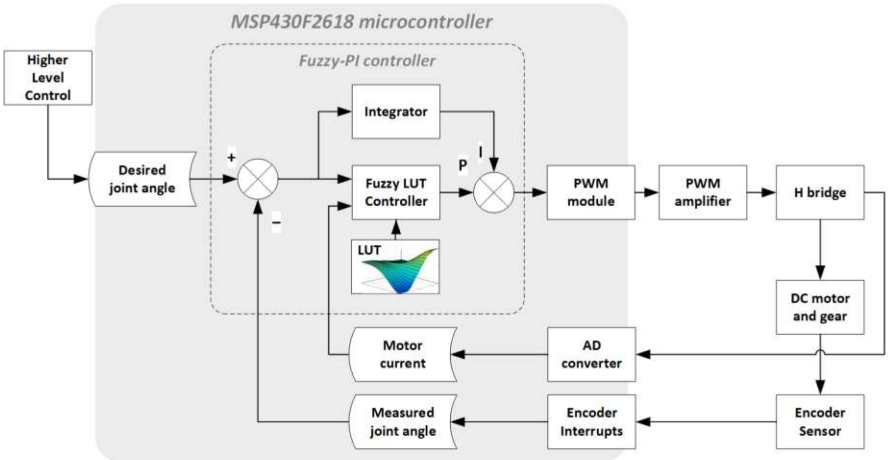

Figure 5

Block diagram of the Fuzzy-PI motor control design and implemented for 18 joints of the Szabad(ka)II robot

3.2 Fuzzy Controller

The aim of the fuzzy-P controller is the same as the proportional tag of a traditional PID controller. However, this fuzzy controller is capable of taking into account the motor current and ensuring softer behavior for high motor currents. Moreover, when the motor current is extremely high, inverse output can be ensured to protect the electro-mechanical system. These requirements are represented by the six fuzzy rules; see Table 3 and Fig. 6.

Fig. 7 shows the surface that is established by the proposed rules, which will be transformed to a LUT in the embedded implementation. It demonstrates the nonlinear control behavior along the two input variables.

Table 3

Rules of the proposed fuzzy-P controller

Rules					**Comment**
	ErrorAngle	*MotorCurrent*	*Voltage*	*Weight*	
1.	Zero	-	Null	0.5	direct P controlling rules for normal behavior
2.	Pos	-	Pos	1	
3.	Neg	-	Neg	1	
4.	Zero	small	Null	0.5	inverse P controlling rules for protection again high motor current
5.	Neg	large	pos-ex	1	
6.	Pos	large	neg-ex	1	

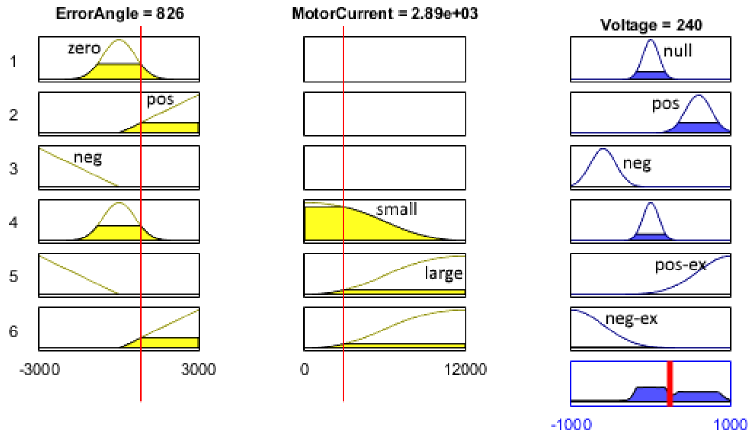

Figure 6
Demonstration of the rules of the proposed fuzzy-P controller

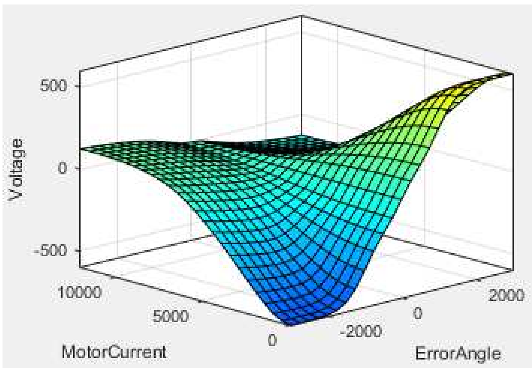

Figure 7
Surface of the proposed fuzzy-P controller – the basis of the fuzzy lookup table in the embedded implementation

This kind of controller was previously tested under extreme mechanical situations [47] and proposed to protect the robot in such situations. An adaptive control mechanism is proposed in [47] by changing the rule's weights in the fuzzy controller: "The suggested solution of mechanism control lies in the turning on or turning off of some membership functions in the fuzzy control. Changing the weight of the rules in the control algorithm we can modify the characteristics of the controller so as to be optimal in the case of drop test and walking as well."

In this study, the weights of the fuzzy rules are optimized by the PSO to increase the multi-objective walking quality during multi-scenarios.

3.3 Design Variables

In this context, the parameters that are changed by the optimizer algorithm are called design variables, and the other parameters that influence the objectives but are not changed by the optimizer are called design parameters. In this case, there are some constant design parameters, and there are some that differ between the scenarios (considered as scenario design parameters).

In this study, the optimal motor controller is searched for by the previously designed leg trajectories and walking algorithm. The fitness function is multi-objective as introduced in Section 1.1.

Table 3 lists the selected design variables ($N=9$) related to the fuzzy-PI motor controller. The minimum and maximum values are selected empirically and based on the previous experience given in [4]. The symmetric rules (2-3 and 5-6) are handled together as proposed by [4]. The unit of inputs and outputs are in integer coded format inherited from the ADC and DAC, but the transfer multipliers are mentioned in Table 4 in the Unit and Domain column. The fuzzy output membership function domain includes three functions that are convertible to each other without adding or removing any parameters (triangular – *trimf*, gaussian – *gaussmf*, and Π-shaped membership function - *pimf*). This is important in the optimization algorithm, for a constant number of design variables.

Table 4
Design variables – selected fuzzy controller parameters to be optimized

Abbr.	**Variable Description**	**Min. Value**	**Max Value**	**Unit and Domain**
I	Integrator tag	*0.1*	*1*	*V/rad*
FI1R	Fuzzy input 1 (*Aerr*) range	*1500*	*6000*	*Rad/10430*
FI2R	Fuzzy input 2 (*Im*) range	*6000*	*24000*	*A/2079*
FOR	Fuzzy output 1 (*P*) range	*500*	*2000*	*V/(511/11.3)*
FOMF	Fuzzy output membership function	*1*	*3*	*1: trimf* *2: gaussmf* *3: pimf*
FW1	Fuzzy rule 1 weight	*0.1*	*1*	
FW23	Fuzzy rule 2 and 3 weight	*0.1*	*1*	
FW4	Fuzzy rule 4 weight	*0.1*	*1*	
FW56	Fuzzy rule 5 and 6 weight	*0.1*	*1*	

4 Results

4.1 Optimization Results

The PSO method was applied to increase the MSMO walking quality of the Szabad(ka)-II robot by searching for the best motor controller. The MSMO fitness evaluation and aggregation were described in Chapter 2. The design variables of the motor controller and their boundaries were defined in Section 3.3.

The PSO algorithm has its own parameters, which were defined based on previous experiences [4], [42], [3]. These parameters include the cognitive attraction of *0.5*, Social Attraction of *1.5*, generation number of *25*, and the population number of *25*. However, in this phase the population and generation numbers were set relatively small compared to the final optimization instance. Here, the aim was to research the method, to make the multiple runs of the optimization faster during the development, and to run one final larger optimization for the real implementation at the end. I.e. the larger sized optimization reach the global optimum with higher probability [48], but not obligatory [49].

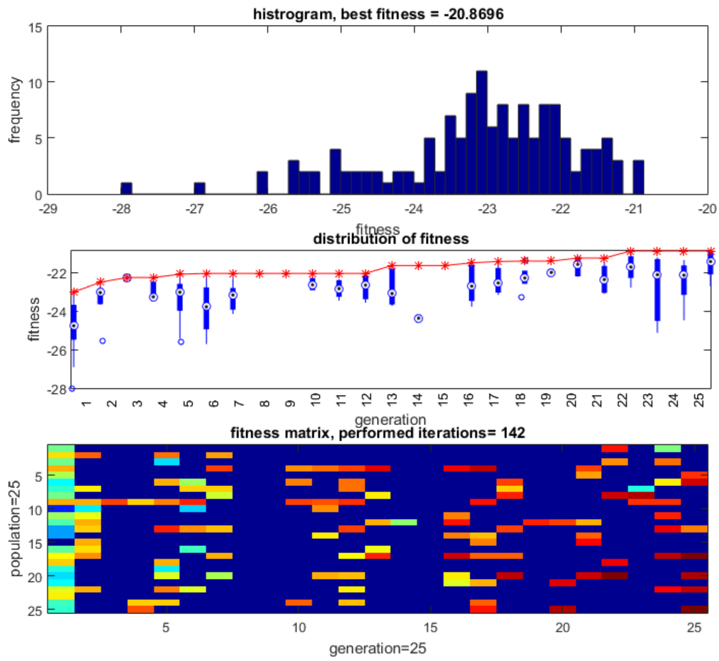

Figure 8
Statistical results of the PSO (case A) for the fuzzy-PI controller evaluated by the MSMO approach. The top graph shows the distribution of the global fitness values (f_G) occurring in the optimization, the middle graph shows its distribution for each generation, and the bottom graph shows its distribution over generations and populations

Fig. 8 graphically shows the statistical analysis of the first optimization (A case). It confirms that the PSO during the generations continuously found a better solution, as it the maximum curve (red curve) illustrates in the middle graph. On the other hand, there is no proof that the best solution from the tested 142 iterations - considered “optimum” - is the real global optimum. However, the global optimum within a weaker tolerance is expected based on the previous research [4].

The given optimum is given in Table 6, while the fuzzy controller surface for the A case is illustrated in Fig. 8.

The preference weights for the MSMO fitness evaluation according to equation (1) are listed in Table 4 (A case). The explanations for these preference weights are described in next subsection.

4.2 Various Preferences of Multi-Objective

There is no universal guidance for predefining the preferences between the objective methods as introduced in Chapter 2. In this section, we analyze the effect of changing the preferences to the optimum values.

Table 5 lists the tested preference values, where the preferences for the A and B cases are generated randomly, while the C case preferences are set manually to default values (bias $b=0$, exponent $e=1$).

Table 5

Multi-objective preference changes by modifying the weights of the utility function

Utility Function Case	**Bias weight of utility function (b_m)**	**Exponent weight of utility function (e_m)**
A	[0.9 0.8 0.24 0.5 0.8]	[0.1 0.7 0.3 0.3 0.1]
B	[0.4 0.7 0.3 0.4 1]	[0.2 0.6 0.8 0.1 0.2]
C	[0.0 0.0 0.0 0.0 0.0]	[1.0 1.0 1.0 1.0 1.0]

Table 6 lists the given optimum for these three cases. We can observe significant differences between the cases for most of the design variables.

Table 6

Calculated optimums of the design variables by the three different multi-objective preferences (note: global fitness values are not comparable between the cases because of the different utility functions)

Design Variables	**Result A**	**Result B**	**Result C**
I	0.171	0.160	0.607
FI1R	5837	5400	5629
FI2R	20111	18693	18242
FOR	781	500	527
FOMF	2 (gaussmf)	3 (pimf)	3 (pimf)

FW1	0.187	0.347	0.581
FW23	0.961	0.972	0.889
FW4	0.789	0.592	0.702
FW56	0.927	0.814	0.188
Global fitness (f_G)	*20.8696*	*59.5132*	*1396908*

Fig. 9 shows the fuzzy surfaces for these three optimums. The observable significant differences of these surfaces also confirm that the different preference weights lead to different solutions.

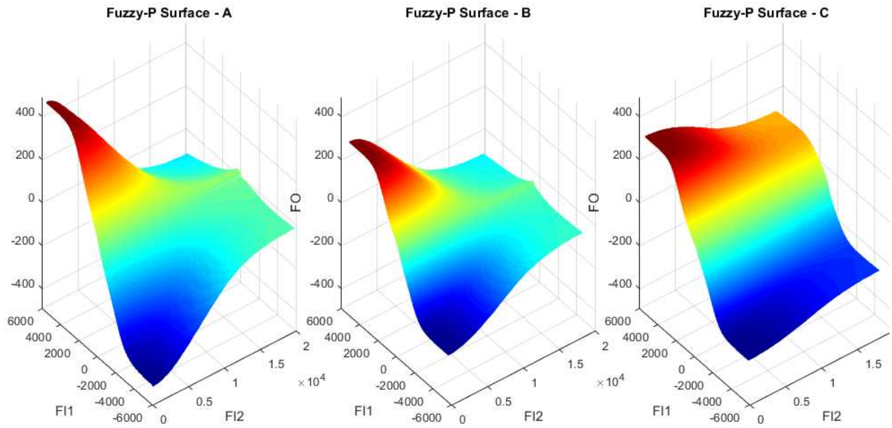

Figure 9
Optimal fuzzy-P surfaces for the A, B, and C optimization cases

4.3 Robustness Comparison

Robust optimization refers to the process of finding optimal solutions for a particular problem that have the least variability to probable uncertainties [50]. The robustness index introduced by [51] is used to evaluate and compare our optimums, because the robustness is aimed as the secondary performance metric in addition to the primary multi-objectives, similar to in [28].

Robustness index (*Ri*) is determined to be the largest eigenvalue of the sensitivity Jacobian matrix ($J_k \in R^{N\times M}$), which calculated between the design variables ($X \in R^N$) and the objective function values ($F \in R^M$, $F=\{f_1,\ldots f_M\}$), for one scenario (k), see equation 3.

$$Ri(X,k)=\max\left(\sqrt{diag\left(J_k \cdot J_k^{\,T}\right)}\right)=\max\left(\sqrt{diag\left(\frac{\partial F}{\partial X}\cdot\frac{\partial F}{\partial X}^{T}\right)}\right) \tag{3}$$

The robustness indices are calculated for each of the six scenarios in each of the three cases. The values and distribution of these robustness indices are illustrated in the left panel of Fig. 10. The smaller values represent more robust or less sensitive optimums for the changes of the design variables. Solution A shows a slightly higher median value (red line) but with the lowest maximum, solution B has the highest maximum, and solution C has the lowest median value. It is difficult to select the most robust solution because the robustness properties deviate between the scenarios.

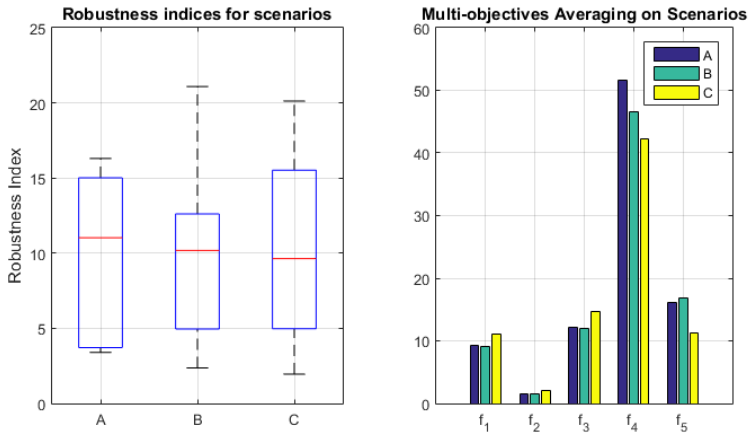

Figure 10

Comparison statistics of the three optimization cases: the left graph shows the distribution of the robustness indices (lower is more robust), the right graph shows the average values of the multi-objectives (lower is better)

The right panel of Fig. 10 illustrates the how the five objectives (defined in Table 1) differ between the three cases. The plotted values are averaged over the six scenarios. This analysis confirms that the preferences weights are influenced by the relation between the objectives. For example, in case A, the exponent for f_4 was small (e_4=*0.1*), while it was high in case C (e_4=*1.0*), furthermore f_4 shows a better value in case C.

Conclusions

We studied the issues related to the heuristic optimization of motor controllers for a walker robot, using a dynamic simulation model. Defining and quantifying the quality of the hexapod robot walking as a multi-objective problem and how to aggregate the multi-objectives into a scalar fitness value using preference weights were explored. Integrating the multi-scenario simulation approach was also examined in this optimization system.

The optimization results (three example solutions of the fuzzy-PI controller) show high divergences between the optimums for defining different preferences between the objectives. The preferences are implemented in a utility function with bias and exponent pair weights for each objective.

The manual selection of these weights opens another optimization issue, which we believe, is the important part of the entire system. The sensitivity or robustness analysis can be used as an external quality aspect to select the appropriate preferences. The method proposes an automatic definition of the preference weights by the optimum robustness against the design variables, design parameters or multi-scenarios.

This robust optimization approach could be applied, not only to mobile robots (legged, wheeled or train structures), but in other fields of engineering systems, such as, optimization problems of smart-grids, turbo-jet engines, or bridge structures. In the aforementioned systems, quality can be defined using more objectives; moreover, the intended use could both include additional scenarios and be simulated with multi-scenarios. The robustness of optimum against situation variability can be considered as a secondary objective, since in reality, several scenarios may occur.

Acknowledgements

This work/publication is supported by the EFOP-3.6.1-16-2016-00003 project and is co-financed by the European Union.

References

[1] I. Kecskes, E. Burkus, F. Bazso, P. Odry: “Model validation of a hexapod walker robot”, *Robotica,* Vol. 35, No. 2, 2017, pp. 419-462, DOI: 10.1017/S0263574715000673

[2] D. Grzelczyk, et al.: “Kinematics, Dynamics and Power Consumption Analysis of the Hexapod Robot During Walking with Tripod Gait”, *International Journal of Structural Stability and Dynamics*, Vol. 17, No. 9, (17 pages), 2017, DOI: 10.1142/S0219455417400107

[3] I. Kecskes, L. Szekacs, J. C. Fodor, P. Odry: “PSO and GA optimization methods comparison on simulation model of a real hexapod robot”, *IEEE 9th International Conference on Computational Cybernetics (ICCC)*, 2013, pp. 125-130, DOI: 10.1109/ICCCyb.2013.6617574

[4] I. Kecskes and P. Odry: “Optimization of PI and Fuzzy-PI Controllers on Simulation Model of Szabad (ka)-II walking robot”, *Int. J. Adv. Robot. Syst.*, Vol. 11:186, 2014, DOI: 10.5772/59102

[5] I. Kecskés, L. Székács, P. Odry "Lookup table based fuzzy controller implementation in low-power microcontrollers of hexapod robot Szabad (ka)-II." *3rd International Conference & Workshop Mechatronics in Practice and Education–MECHEDU,* 2015

[6] Srinivas Nidamarthi and Kalyanmoy Deb: "Muiltiobjective optimization using nondominated sorting in genetic algorithms", *Evolutionary Computation,* Vol. 2, No. 3, 1994, pp. 221-248

[7] Kalyanmoy Deb, et al.: "A fast and elitist multiobjective genetic algorithm: NSGA-II", *IEEE Transactions on Evolutionary Computation,* Vol. 6, No. 2, 2002, pp. 182-197

[8] Konstantinos E. Parsopoulos, Michael N. Vrahatis: "Multi-objective particles swarm optimization approaches", *Multi-objective optimization in computational intelligence: Theory and practice, Chapter II. IGI Global*, 2008, pp. 20-42

[9] Alexander Teske, Rafael Falcon, Amiya Nayak: "Efficient detection of faulty nodes with cuckoo search in t-diagnosable systems", *Applied Soft Computing*, Vol. 29, 2015, pp. 52-64

[10] Ines Alaya, Christine Solnon, Khaled Ghedira. "Ant colony optimization for multi-objective optimization problems", *19th IEEE International Conference on Tools with Artificial Intelligence (ICTAI 2007)* 2007, DOI: 10.1109/ICTAI.2007.108

[11] Awad Noor H., Mostafa Z. Ali, Rehab M. Duwairi: "Multi-objective differential evolution based on normalization and improved mutation strategy", *Natural Computing,* Vol. 16, No. 4, 2017, pp. 661-675

[12] J. Brank, et al. eds.,: "Multiobjective optimization: Interactive and evolutionary approaches", *Theoretical Computer Science and General Issues, Springer Science,* Vol. 5252, 2008, DOI: 10.1007/978-3-540-88908-3

[13] R. T. Marler, J. S. Arora: "Survey of multi-objective optimization methods for engineering", *Structural and multidisciplinary optimization*, Vol. 26, No. 6, 2004, pp. 369-395

[14] Eckart Zitzler: "Evolutionary algorithms for multiobjective optimization: Methods and applications", Vol. 63, Ithaca: Shaker (1999)

[15] Andrew L. Nelson, Gregory J. Barlow, Lefteris Doitsidis: "Fitness functions in evolutionary robotics: A survey and analysis." *Robotics and Autonomous Systems*, Vol. 57, No. 4, 2009, pp. 345-370

[16] R. Timothy Marler, Jasbir S. Arora: "Survey of multi-objective optimization methods for engineering", *Structural and multidisciplinary optimization,* Vol. 26, No. 6, 2004, pp. 369-395

[17] Michael A. Gennert, Alan L. Yuille: "Determining the optimal weights in multiple objective function optimization", *Second International Conference on Computer Vision (ICCV)* 1988, DOI: 10.1109/CCV.1988.589974

[18] L. Kubler, C. Henninger, P. Eberhard: "Multi-criteria optimization of a hexapod machine", *Advances in Computational Multibody Systems*, Volume 14, Issues 3-4, pp. 225-250, DOI:10.1007/s11044-005-4311-z

[19] E. Burkus, J. C. Fodor, P. Odry, "Structural and gait optimization of a hexapod robot with particle swarm optimization", *IEEE 11th International Symposium on Intelligent Systems and Informatics (SISY)* 2013, pp. 147-152 DOI:10.1109/SISY.2013.6662559

[20] Rudolf Andoga, et al.: "Innovative approaches in modeling control and diagnostics of small turbojet engines", *Acta Polytechnica Hungarica*, Vol. 10, No. 5, 2013, pp. 81-99

[21] Hanz Richter: "A multi-regulator sliding mode control strategy for output-constrained systems", *Automatica* Vol. 47, No. 10, 2011, pp. 2251-2259

[22] Moulay Rachid Douiri, Mohamed Cherkaoui: "Evolutionary Multi-objective Optimization Based Proportional Integral Controller Design for Induction Motor Drive", *Multi-disciplinary Trends in Artificial Intelligence, (MIWAI 2012), Lecture Notes in Computer Science,* Vol. 7694. Springer, Berlin, Heidelberg, 2012

[23] N. Katal, S. K. Singh: "Multi-objective optimisation of PID controller for DC servo motor using genetic algorithm", *Eng. Intell. Syst*, Vol. 23, No. 1, 2015, pp. 7-16

[24] Nasseer K. Bachache, Jinyu Wen: "Multi Objective Swarm Optimization Design Fuzzy Controller to Adjust Speed of AC Motor Drive", *International Conference in Swarm Intelligence,* Springer, Berlin, Heidelberg, 2013

[25] Stefano Leonori, et al.: "Multi objective optimization of a fuzzy logic controller for energy management in microgrids", *IEEE Congress on. Evolutionary Computation (CEC)* 2016, DOI: 10.1109/CEC.2016.7743811

[26] Longda Wang, et al.: "Multi-objective Optimization Improved GA Algorithm and Fuzzy PID Control of ATO System for Train Operation", *Intelligent Computing, Networked Control, and Their Engineering Applications, (ICSEE 2017), (LSMS 2017) Communications in Computer and Information Science*, Vol. 762. Springer, Singapore 2017

[27] G. Fadel, I. Haque, V. Blouin, M. Wiecek, "Multi-criteria multi-scenario approaches in the design of vehicles", *6th World Congresses of Structural and Multidisciplinary Optimization* (2005) DOI:10.1.1.74.3818

[28] R. Marijt: "Multi-objective robust optimization algorithms for improving energy consumption and thermal comfort of buildings", *Master's thesis*, Leiden Institute for Advanced Computer Science, Leiden University, 2009 http://liacs.leidenuniv.nl/assets/Masterscripties/2009-20RobertMarijt.pdf

[29] L. F. Wang: "Controller design for DC motor drives using multi-objective optimization evolutionary algorithms", Proceedings of the 2004 International Symposium on Micro-Nanomechatronics and Human Science and The Fourth Symposium Micro-Nanomechatronics for Information-Based Society, 2004, DOI: 10.1109/MHS.2004.1421273

[30] Sanjay Kr Singh, et al.: "Multi-objective optimization of PID controller for temperature control in centrifugal machines using genetic algorithm", *Research Journal of Applied Sciences, Engineering and Technology,* Vol. 7, No. 9, 2014, pp. 1794-1802

[31] Yazmin Maldonado, Oscar Castillo, Patricia Melin: "A multi-objective optimization of type-2 fuzzy control speed in FPGAs", *Applied Soft Computing*, Vol. 24, 2014, pp. 1164-1174

[32] Margaret M. Wiecek, Vijay Singh, Vincent Blouin: "Multi-scenario multi-criteria optimization in engineering design", *Report Documentation Page*, Clemson Univ Sc Dept Of Mathematical Sciences, Form Approved: OMB No. 0704-0188, 2007

[33] Francesco Rossi, et al.: "Multi- scenario robust online optimization and control of fed- batch systems via dynamic model- based scenario selection" *AIChE Journal*, Vol. 62, No. 9, 2016, pp. 3264-3284

[34] Marco C. Campi, Simone Garatti, Maria Prandini: "The scenario approach for systems and control design", *Annual Reviews in Control,* Vol. 33, No. 2, 2009, pp. 149-157

[35] Ling Zhu, Kalyanmoy Deb, Sandeep Kulkarni: "Optimization of Multi-Scenario Problems Using Multi-Criterion Methods: A Case Study on Byzantine Agreement Problem", IEEE Congress on Evolutionary Computation (CEC 2014) 2014, DOI: 10.1109/CEC.2014.6900637

[36] Karl Iagnemma, Steven Dubowsky: "Traction Control of Wheeled Robotic Vehicles in Rough Terrain with Application to Planetary Rovers", *The International Journal of Robotics Research,* Vol. 23, No. 10-11, 2004, pp. 1029-1040

[37] G. Carbone: "Stiffness analysis and experimental validation of robotic systems", *Frontiers of Mechanical Engineering* vol Vol. 6, No. 2, 2011, pp. 182-196

[38] Irfan Ullah et al: "Integrated tracking and accident avoidance system for mobile robots", *International Journal of Control Automation and Systems*, Vol. 11, No. 6, 2013, pp. 1253-1265

[39] Zoltan Pap, Istvan Kecskes, Ervin Burkus, Fulop Bazso, Peter Odry: "Optimization of the hexapod robot walking by genetic algorithm" *IEEE 8th International Symposium on Intelligent Systems and Informatics (SISY)* 2010, DOI: 10.1109/SISY.2010.5647242

[40] I. Kecskés, P. Odry: "Fuzzy Route Control of Dynamic Model of Four-Wheeled Mobile Robot", *4th IEEE International Symposium on Logistics and Industrial Informatics (LINDI)* 2012, pp. 215-220, DOI: 10.1109/LINDI.2012.6319490

[41] I. Kecskés, E. Burkus, Z. Király, Á. Odry, P. Odry: "Competition of motor controllers using a simplified robot leg PID vs fuzzy logic", *4th International Conference on Mathematics and Computers in Sciences and Industry (MCSI)* Corfu, 2017, DOI: 10.1109/MCSI.2017.16

[42] I. Kecskes, E. Burkus, P. Odry: "Swarm-based optimizations in hexapod robot walking", in: *IEEE 9th International Symposium on Applied Computational Intelligence and Informatics (SACI)* 2014, pp. 123-127, DOI:10.1109/SACI.2014.6840048

[43] Particle swarm toolbox for MATLAB, http://code.google.com/p/psomatlab/

[44] Matlab code of MSMO optimization framework, http://appl-dsp.com/wp-content/uploads/2014/03/optimization-methods.zip

[45] Maurizio Melluso: "A Theoretical and Experimental Approach of Fuzzy Adaptive Motion Control for Wheeled Autonomous Nonholonomic Vehicles", *ISRN Robotics*, Volume 2013, 2013, 18 pages, Article ID 621067, DOI: 10.5402/2013/621067

[46] Á. Odry, J. Fodor, and P. Odry: "Stabilization of a two-wheeled mobile pendulum system using LQG and fuzzy control techniques", *International Journal On Advances in Intelligent Systems*, Vol. 9, No. 1-2, 2016, pp. 223-232

[47] I. Kecskés, P Odry: "Protective Fuzzy Control of Hexapod Walking Robot Driver in Case of Walking and Dropping." *Computational Intelligence in Engineering*, Springer Berlin Heidelberg, 2010, pp. 205-217, DOI: 10.1007/978-3-642-15220-7_17

[48] Stanley Rylander, Gotshall Bart: "Optimal population size and the genetic algorithm", *Population,* Vol. 100, No. 400, 2002, p. 900

[49] Tianshi Chen, et al.: "A large population size can be unhelpful in evolutionary algorithms" *Theoretical Computer Science,* Vol. 436, 2012, pp. 54-70

[50] S. Mirjalili, A. Lewis: "Novel frameworks for creating robust multi-objective benchmark problems", *Information Sciences,* Vol. 300, 2015, pp. 158-192, DOI:10.1016/j.ins.2014.12.037

[51] O. B. Augusto, F. Bennis, S. Caro, "Multiobjective engineering design optimization problems: a sensitivity analysis approach", *Pesquisa Operacional,* Vol. 32, No. 3, 2012, pp. 575-596, DOI: 10.1590/S0101-74382012005000028

Abstraction-enriched Formal Methods Integration

Slavomír Šimoňák[1], Matúš Uchnár[1], Peter Feciľak[1], Eva Chovancová[1], Martin Chovanec[2]

[1]Department of Computers and Informatics, Faculty of Electrical Engineering and Informatics, Technical University of Košice, Letná 9, 042 00 Košice, Slovakia

[2]Institute of Computer Technology, Technical University of Košice, B. Němcovej 3, 042 00 Košice, Slovakia

e-mails: slavomir.simonak@tuke.sk, matus.uchnar@tuke.sk, peter.fecilak@tuke.sk, eva.chovancova@tuke.sk, martin.chovanec@tuke.sk

Abstract: The paper presents the results of our research in the field of combining process algebra and Petri nets. To provide better support for design and analysis of larger-scale systems by means of abstraction mechanism, the method itself and the tools allowing its practical application have been enhanced significantly. The theoretical aspects and implementation of enhancements are discussed in detail. Careful testing, along with the process of implementing the new functionality into one of the involved tools, helped us to disclose its certain hidden imperfections, which are subsequently addressed.

Keywords: process algebra; Petri nets; formal methods integration; abstraction

1 Introduction

Formal methods offer a mathematically-based framework, allowing for a systematic specification, development, and analysis of systems. When applying formal methods to the design and analysis of real-life-sized systems, the usage of different methods and different verification techniques can be very useful. It might be either because a particular formalism is most suitable for the design of an individual component or the designer is interested in different system properties to investigate, or to cope with the complexity of the system [1].

The existence of successful series of conferences on Integrated Formal Methods (iFM), refers to the importance of formal methods integration. The conferences cover all aspects of the integration from language design, through the analysis to the tools and their application in software engineering practice [1]. In September

2017, 13th International Conference of this kind (iFM 2017) was organized in Torino, Italy.

Formal methods integration, in this particular case, is based on the transformation of process algebra ACP [6] specifications into the corresponding Petri net representations. Source algebraic specification of a system, supplied by using XML-based PAML language [31], is processed by the ACP2Petri tool, which produces corresponding Petri net based representation of the system in PNML [21] format.

1.1 Motivation

Despite the large number of existing formal methods, new methods are currently being developed. In such a situation, it is actually very fruitful to study various combinations of several methods with different characteristics and complementary strengths [7]. Petri nets have an intuitive graphical representation, they allow to describe both the states and the actions of the considered system and offer many analytical techniques [11] for investigation of structural as well as the behavioral properties of a model. Process algebra is a symbolic formalism, which is focused on the dynamic behavior of a system. Algebraic specification usually has no explicit representation of states and available proof techniques are generally aimed at investigating the equality of behavioral descriptions [7]. So we can conclude that Petri nets and process algebra can be considered complementary in several aspects.

According to our experience, it is very useful to build the specification of the system once and to obtain the corresponding specification in different formalisms, after automatic transformation, with almost no effort. For the purposes of the analysis, both models can be used and according to the properties of interest, we can choose the best one.

In many cases, the intuitive graphical representation offered by Petri nets, supports a better understanding of the structure and operation of the system under consideration [15]. In the case of modeling larger systems, however, benefits of graphical representation are less evident with an increasing size and complexity of a system. Algebraic specification in such situations is often much more compact than the corresponding Petri net. On the other hand, the main source of motivation for transforming algebraic specifications into the Petri net formalism is the access to analytical techniques and the results available for Petri nets [18]. The design and analysis of communication protocols can serve as an example of application of the approach, mentioned above [32]. We believe that, in many cases, it is simpler to create a specification for a particular communication protocol using process algebra, rather than Petri nets. It can be done by specifying the communicating entities and the communication medium separately and composing them together by the means of process algebra's parallel composition operation. When it comes to analysis, the powerful analytical apparatus of Petri nets, including automatic generation of system invariants, is highly appreciated.

After years of using the method [32] and the set of tools associated with it, we recognized the need for a major update. The need was connected with the inability of processing abstraction [17] within specifications of bigger systems. The last significant update was oriented towards a graphical user interface [3] and fixing some shortcomings found within the ACP2Petri tool [34]. Such an update not only provided a better user experience, when using the application, but also allowed for tracing the progress of transformation, in a visual way. This enabled a better understanding of how the process of transformation is implemented and it resulted in disclosure of some shortcomings, which were repaired subsequently.

The fact that one of the most advanced toolsets for the mCRL2 specification language [20], based on process algebra ACP, still does not support recursive parallelism [27], can be perceived as a limitation in some cases. Therefore, it can be considered as another source of motivation.

1.2 Related Work

Research in the field of relating both process algebra and Petri nets, two fundamental concurrency theories, is not new and many influential works have been published [13, 26, 29]. On the other hand, the research is still active and it produces new and interesting results. In [18] a calculus (Finite-net Multi-CCS), inspired by CCS, is introduced and provided by a labeled transition system as well as Petri net semantics. The ability to represent finite, statically reduced, P/T nets by well-formed finite-net Multi-CCS processes is shown in [19]. A framework is introduced in [9] where a net encoding can be constructed for calculi using different communication patterns.

A simple process calculus of Petri nets (Petri calculus) is defined in [30]. The main motivation here is to provide the compositional approach for defining the semantics of Petri nets. Within the paper, a compositional extension of Condition/Event nets is introduced. A net is associated with interfaces to which its transitions can be connected. Composition of such nets along a common interface is performed by synchronization of transitions. It is shown that the class of nets with boundaries has the same expressiveness as a simple process calculus.

The relations between the Petri Box Calculus and a class of P/T Petri nets are considered in [10]. PBC terms are carefully designed in order to define the transformation producing P/T nets preserving the structural operational semantics of the terms. In such way a composition of P/T nets is allowed. A unique algebraic semantics for Petri nets, based on process algebra ACP, is introduced in [8]. Actions of the PTNA (Place/Transition-Net Algebra) correspond to production and consumption of tokens by Petri net transitions. It is shown, that both Petri net and its corresponding algebraic representation have identical operational behavior. The results are further enhanced to hierarchical P/T nets.

Compared to the existing approaches, mentioned above, our approach differs in several aspects. We use widely-adopted formalisms without defining their special extensions, as is the case in many available solutions. This fact implies a reasonable support by existing tools and contributes to its practical application. Process algebra ACP has been selected as a part of our integration framework in this case, as we believe it has its own advantages compared to other well-known process algebras such as CCS and CSP. Compared to the other two, ACP emphasizes the algebraic aspect, more. The equational theory is the central point here. It can be equipped with a range of semantical models [5]. The communication scheme of ACP is also more general, since in CCS communication is combined with abstraction and it is combined with restriction in case of CSP. Last, but not least, there is a software toolset for the implementation of our transformation, therefore, it is much more available, for practical utilization.

2 Theoretical Background

Previous enhancements were connected mainly with the changes within the main transformation tool - the ACP2Petri. The current extension, on the other hand, is more profound and it affects both the theoretical foundations and the supporting tools. The theoretical foundations of the transformation were published in [35] and are only shortly summarized here and extended by the new properties.

Elementary nets represent the basic building blocks of more complex specifications and they correspond to the notion of atomic actions of process algebra ACP. Except those, we defined also the elementary nets corresponding to the empty process (ε) and the deadlock (δ).

Let a process Q be represented by the term a ($Q = a$). Then corresponding elementary net ($N(Q) = N_a$) is given by: $N_a = (P, T, pre, post)$, where $P = \{Q, Q'\}$, $T = \{a\}$, $pre(Q, a) = 1$, $post(Q', a) = 1$, $I(P) = \{Q\}$, and $F(P) = \{Q'\}$. Here P, T stand for sets of places and transitions respectively. $pre()$ and $post()$ represent pre- and post- transition relation, giving the structure of the net. $I(P)$ and $F(P)$ are the sets of initial and final places of the given Petri net, respectively. Here, *N*() stands for the mapping from the process term to the corresponding Petri net. In Table 1, Petri net configurations are summarized for all elementary net types, together with their graphical representations.

Table 1

Elementary nets

$Q = a$		$Q = \varepsilon$		$Q = \delta$	
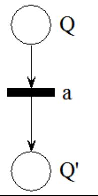	$P = \{Q, Q'\}$ $I(P) = \{Q\}$ $F(P) = \{Q'\}$	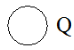	$P = \{Q\}$ $I(P) = \{Q\}$ $F(P) = \{Q\}$		$P = \{Q\}$ $I(P) = \{Q\}$ $F(P) = \{\}$
a)		b)		c)	

The net operations are defined, corresponding to the operators of process algebra ACP, which are necessary for expressing the net semantics, of more complex algebraic terms.

Table 2

Petri net composition operations

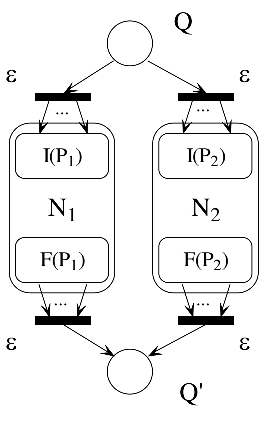

a)

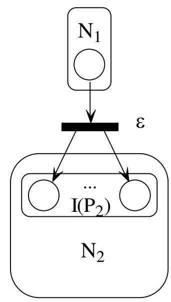

b)

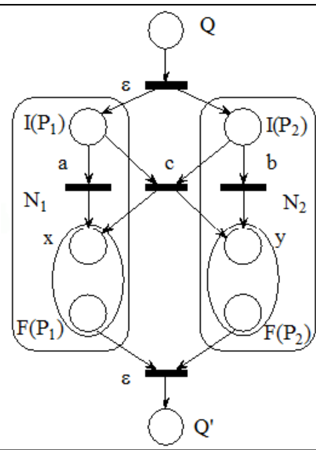

c)

The net operations defined correspond to alternative composition (+), sequential composition (·), parallel composition with communication (‖) and encapsulation operation (∂) of the process algebra ACP. The net operations mentioned above are only briefly discussed here. They are depicted in Table 2 and explained deeper in [35]. The alternative composition (case a) in Table 2) of two Petri nets is constructed by enhancing a set of places (given by union of sets of places of composed nets) by two additional places (Q, Q'), where Q will be the initial place and Q' the final place of the composition. In the case of sequential composition (case b) in Table 2), the final place of the first of composed nets (N_1) is connected to the initial place(s) of the second of nets (N_2) by the new, ε-labeled transition.

As we can observe, the set of final places in the elementary net corresponding to deadlock (δ) is empty, meaning that there is no possibility to append another Petri net to such net by operation of sequential composition, which corresponds to the desired behavior.

The parallel composition of two Petri nets can be slightly more complicated, especially when the communication of the processes represented by the Petri nets is considered. Figure depicted in c) of Table 2 illustrates the situation, where two actions *a* and *b* are able to communicate and the result of such communication is the action *c*. Within the process algebra ACP such communication possibility can be expressed by means of communication function $\gamma(a,b)=c$. In the situation depicted by the figure, a Petri net denoted by *x* represents the net obtained from the net N_1 by removing its initial place, transition *a*, and corresponding arcs. Petri net denoted by *y* can be obtained analogically. Petri net corresponding to the application of the encapsulation operation is constructed in such way that transitions labeled by the actions from the encapsulation set (*H*) are removed from the net as well as the arcs connected to those transitions. For expressing the Petri net semantics of APC terms inductive rules were defined:

$$N(Q+R)=N(Q)\mathbf{+}N(R) \tag{1}$$

$$N(Q\cdot R)=N(Q)\boldsymbol{\cdot}N(R) \tag{2}$$

$$N(Q\,\|\,R)=N(Q)\,\boldsymbol{\|}\,N(R) \tag{3}$$

$$N(\partial_H(Q))=\boldsymbol{\partial_H}(N(Q)) \tag{4}$$

While on the left side of equations (1) – (4), there are operators (+, ·, ||, ∂) of process algebra ACP, operators on the right side of the equations refer to their equivalents on Petri nets. To distinguish them, the Petri net operators are emphasized using the bold face text.

Abstraction [24] is a fundamental mechanism in the design of hierarchical systems. Such mechanism allows us to abstract away from the internal operation of modules from which larger systems are composed. Without such a mechanism, it would be virtually impossible to specify anything useful, except in a very small system [4].

If we want to abstract from certain actions, it does not mean that we can simply remove those actions, because we want to preserve the behavior of original process apart from the abstracted actions [6, 17]. So, the silent step (τ), is introduced, which can be removed in some cases, but cannot be removed in other cases. In [6] two τ-laws are formulated, giving the exact behavior of the silent step (Table 3).

Table 3

Behavior of silent step

$x\tau = x$	B1
$x(\tau(y+z)+y) = x(y+z)$	B2

So the abstraction essentially represents a renaming of given actions into τ. The abstraction operator (τ_I) is introduced, which renames all actions from the set I into τ. As a consequence, additional axioms (Table 4) are included to the axiom system of process algebra ACP. It holds that $\delta \notin I$, since $\delta \notin A$ and $I \subseteq A$, so δ is never renamed into τ. In the Table 4 it is assumed that $a \in A \cup \{\delta, \tau\}$.

Table 4

Axioms for abstraction

$\tau_I(a) = a \quad \text{if } a \notin I$	TI1
$\tau_I(a) = \tau \quad \text{if } a \in I$	TI2
$\tau_I(x+y) = \tau_I(x) + \tau_I(y)$	TI3
$\tau_I(xy) = \tau_I(x) \cdot \tau_I(y)$	TI4

The silent step is not allowed to communicate with other actions and therefore it is defined (5) that communication involving τ results in deadlock [17, 6].

$$\tau \mid a = \delta, \quad \text{for} \quad a \in A \cup \{\delta, \tau\} \tag{5}$$

The complete axiom system for process algebra ACP extended by the notion of silent step (ACP^τ) including axioms B1, B2 and TI1-TI4 can be found in [6].

3 Adding Abstraction Support within the Toolset

A new unary operation was added to the existing set of net operations, which corresponds to the application of the abstraction operator (τ_I) of process algebra ACP. The result is a Petri net where the transitions with labels from the set *I* are renamed to the silent action τ. So the new operation can be expressed more formally in a following way:

$$N(\tau_I(Q)) = \boldsymbol{\tau_I}\,(N(Q)) \tag{6}$$

While the left side of equation (6), τ_I represents the abstraction operator of process algebra ACP, $\boldsymbol{\tau_I}$ and the right side refers to its equivalent in Petri nets. The toolset including the PATool, as well as, the ACP2Petri needed update and incorporate the new transformation possibilities.

3.1 Updating the PATool

The PATool [31] provides some useful functionality supporting the integration of process algebra and Petri nets. It is able to work with the various formats used in algebraic specifications, provides valuable capabilities of conversion and serves as an interface to additional transformation tools, including the ACP2Petri. PATool in this case is used to translate a text based ACP specification to the PAML format, which is suitable for processing by the ACP2Petri. New elements allowing for use of abstraction within specifications were added to the input (text-based) as well as the output (XML-based) language. The input language enhancements include two new statements: `tauset`, for specifying the set of actions to be abstracted away and the `tau` for applying the abstraction renaming to a particular process. The updated DTD specification of the output language can be found in Table 5. Within the table, updated parts are emphasized using the bold face text.

Table 5
Updated DTD specification

```
<!-- ACP tau DTD for process specifications -->
<!ELEMENT ACPSPEC (GAMMA*,ENCSET*,TAUSET*,ACPEQUATION+)>
<!ELEMENT ACPEQUATION (VAR,ACPTERM)>
<!ATTLIST ACPEQUATION INIT CDATA #REQUIRED>
<!ELEMENT ACPTERM (ALTCMP|SEQCMP|PARCMP|ACTION|VAR|ENCAPS|TAU)>
<!ELEMENT ALTCMP ((ALTCMP|SEQCMP|PARCMP|ACTION|VAR|ENCAPS|TAU),
(ALTCMP|SEQCMP|PARCMP|ACTION|VAR|ENCAPS|TAU))>
<!ELEMENT SEQCMP ((ALTCMP|SEQCMP|PARCMP|ACTION|VAR|ENCAPS|TAU),
(ALTCMP|SEQCMP|PARCMP|ACTION|VAR|ENCAPS|TAU))>
<!ELEMENT PARCMP ((ALTCMP|SEQCMP|PARCMP|ACTION|VAR|ENCAPS|TAU),
(ALTCMP|SEQCMP|PARCMP|ACTION|VAR|ENCAPS|TAU))>
<!ELEMENT ENCAPS (ALTCMP|SEQCMP|PARCMP|ACTION|VAR|ENCAPS|TAU)>
<!ATTLIST ENCAPS ENCID CDATA #REQUIRED>
<!ELEMENT TAU (ALTCMP|SEQCMP|PARCMP|ACTION|VAR|ENCAPS|TAU)>
<!ATTLIST TAU TAUID CDATA #REQUIRED>
<!ELEMENT ACTION EMPTY>
<!ATTLIST ACTION NAME CDATA #REQUIRED>
<!ELEMENT VAR EMPTY>
<!ATTLIST VAR NAME CDATA #REQUIRED>
<!ELEMENT GAMMA EMPTY>
<!ATTLIST GAMMA ACT1 CDATA #REQUIRED ACT2 CDATA #REQUIRED RES CDATA #REQUIRED>
<!ELEMENT ENCSET (ACTION*)>
<!ATTLIST ENCSET ENCID CDATA #REQUIRED>
<!ELEMENT TAUSET (ACTION*)>
<!ATTLIST TAUSET TAUID CDATA #REQUIRED>
```

To illustrate a text-based ACP specification and a corresponding PAML specification we provide an example in Table 6 and Table 7 respectively.

Table 6

Example of text-based ACP specification

```
gamma(a,b)=c
encset[H](b)
tauset[I](d)
X = encaps[H](tau[I](Y || Z))
Y = b.e
Z = b.d
```

Within the example, `gamma(a,b)=c` represents the definition of communication function, where two actions *a*, *b* are able to communicate and the result of such communication is the action *c*. `encset[H](b)` defines the set of actions (*H*) to be encapsulated, while encapsulation itself is applied by the `encaps[H]` operator. Similarly, `tauset[I]` defines the set of actions (*I*) for renaming to silent step. Abstraction renaming is applied by `tau[I]` to the parallel composition of processes *Y* and *Z*.

Table 7

Example of corresponding PAML specification

```
<ACPSPEC>
   <GAMMA ACT1="a" ACT2="b"
RES="c"></GAMMA>
   <ENCSET ENCID="H">
      <ACTION NAME="b"></ACTION>
   </ENCSET>
   <TAUSET TAUID="I">
      <ACTION NAME="d"></ACTION>
   </TAUSET>
   <ACPEQUATION INIT="true">
      <VAR NAME="X"></VAR>
      <ACPTERM>
         <ENCAPS ENCID="H">
            <TAU TAUID="I">
               <PARCMP>
               <VAR NAME="Y"></VAR>
               <VAR NAME="Z"></VAR>
               </PARCMP>
            </TAU>
         </ENCAPS>
      </ACPTERM>
   </ACPEQUATION>
   <ACPEQUATION INIT="false">
      <VAR NAME="Y"></VAR>
      <ACPTERM>
         <SEQCMP>
            <ACTION NAME="b"></ACTION>
            <ACTION NAME="e"></ACTION>
         </SEQCMP>
      </ACPTERM>
   </ACPEQUATION>
   <ACPEQUATION INIT="false">
      <VAR NAME="Z"></VAR>
      <ACPTERM>
         <SEQCMP>
            <ACTION NAME="b"></ACTION>
            <ACTION NAME="d"></ACTION>
         </SEQCMP>
      </ACPTERM>
   </ACPEQUATION>
</ACPSPEC>
```

With respect to new elements of the language to be processed by the PATool, the core functionality of the tool has been updated to reflect the changes. Now the tool provides conversion of text-based ACP specifications, including the abstraction related elements, to the PAML format, suitable for further processing by the ACP2Petri.

3.2 Enhancing the ACP2Petri Tool

The ACP2Petri also required substantial updates to reflect the new transformation properties. It was necessary to create sets of actions defined by the `TAUSET` element of source specification and identified by `TAUID` attribute in order to apply abstraction renaming performed by `TAU` operation to correct actions of the particular process.

Special attention has been paid to more complicated cases, like the nested application of abstraction operator, or its combination with recursion and parallelism, as it is illustrated in Figure 1, while the full specification of example is provided in Table 8.

Table 8

Specification with application of abstraction operator

```
tauset[I](a)
tauset[J](b)
tauset[K](c)
X = tau[I](tau[J](tau[K](a.b.c.d.(X || X))))
```

Within the specification in Table 8, all the actions (*a*,*b*,*c*) except the action *d* are renamed to silent action by the means of nested application of abstraction operator.

However, not all actions renamed to silent action τ can be simply removed from the resulting Petri net. The reasons were discussed in section 2 of this paper and are connected with the effort to preserve the behavior of the original process apart from the abstracted actions. To remove those silent actions, which can be removed safely, we implemented a special "Tau removing mode" functionality within the tool for the case the system designer wishes to remove them. This functionality can be switched on using the command line option (`-t`) when starting the ACP2Petri tool.

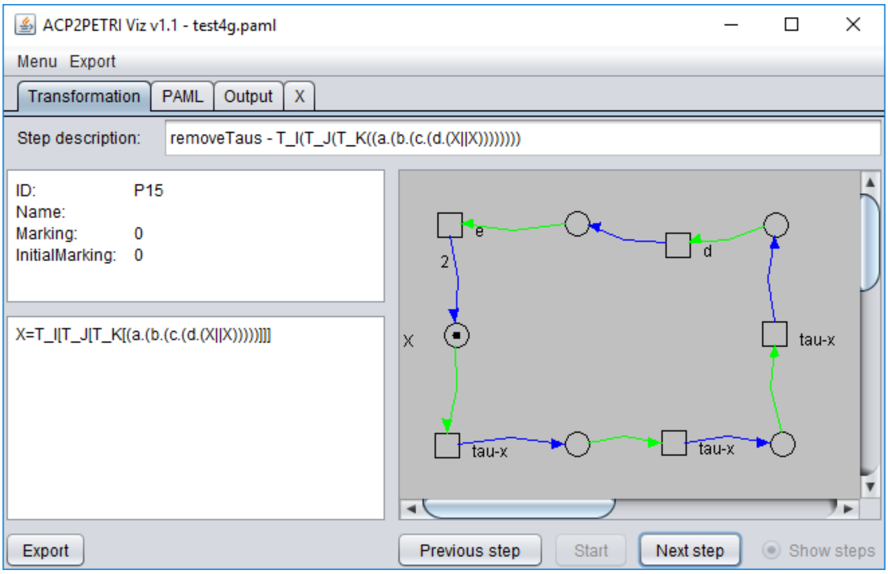

Figure 1
Application of abstraction operator in ACP2Petri

Since the program has been started with the `-t` option for removing silent actions, all three of them (named *tau-x* in Figure 1) are removed in the next step and the resulting Petri net is depicted in Figure 2. As it was stated above, not all of the silent actions can be removed automatically.

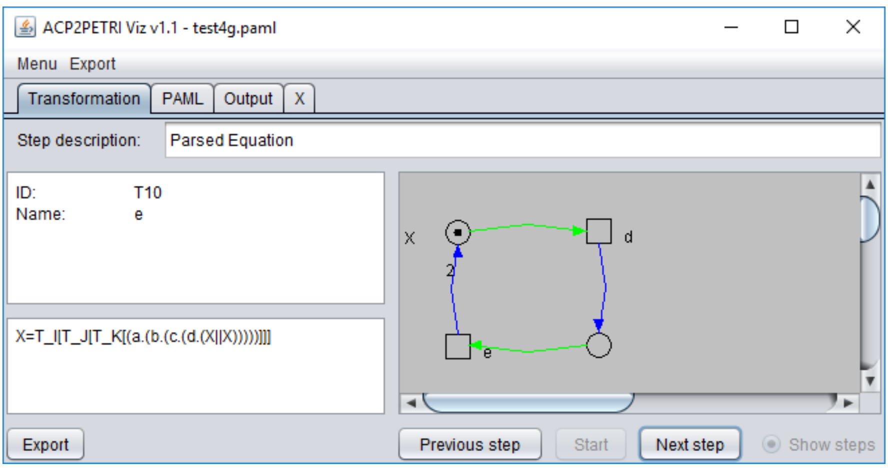

Figure 2
Removing silent actions in ACP2Petri

To illustrate the difference, we provide another example (Table 9) containing also the silent action which will not be automatically removed by the tool.

Table 9
Specification containing abstraction operator

```
tauset[I](b)
X = tau[I](b.(a.b + b.a))
```

According to the specification above the set *I* contains single action (*b*) to be abstracted away within the process *X* by the application of the abstraction operator. All three occurrences of the action *b* are renamed to silent action τ, but only two of them are scheduled to be removed by the tool automatically and denoted by *tau-x* label, as it is shown in the Figure 3.

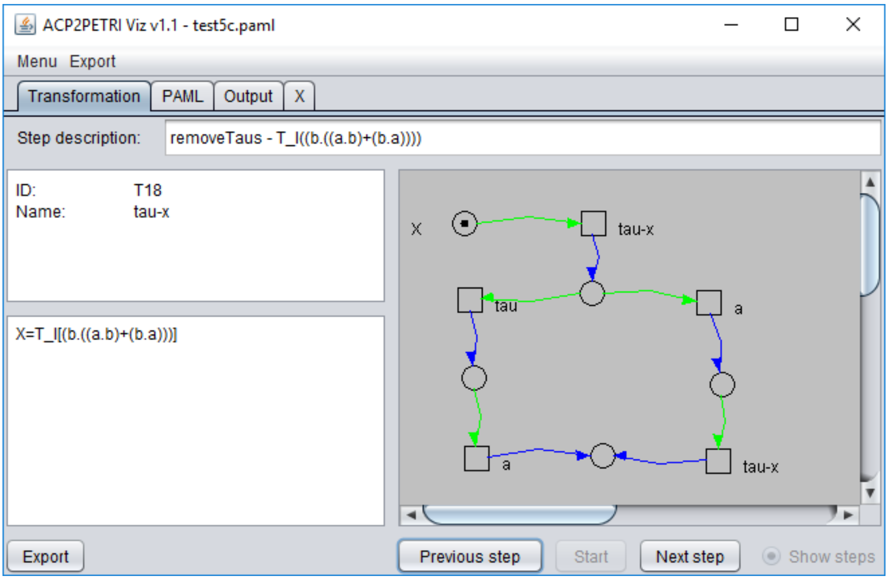

Figure 3
Silent actions in Petri net

As it can be observed, only two of three silent actions have been removed (described as *tau-x* in the Figure 3) by the tool, while one (described as *tau*) has been retained. The resulting Petri net is shown in Figure 4, containing two *a*-labeled actions and one silent action *tau*.

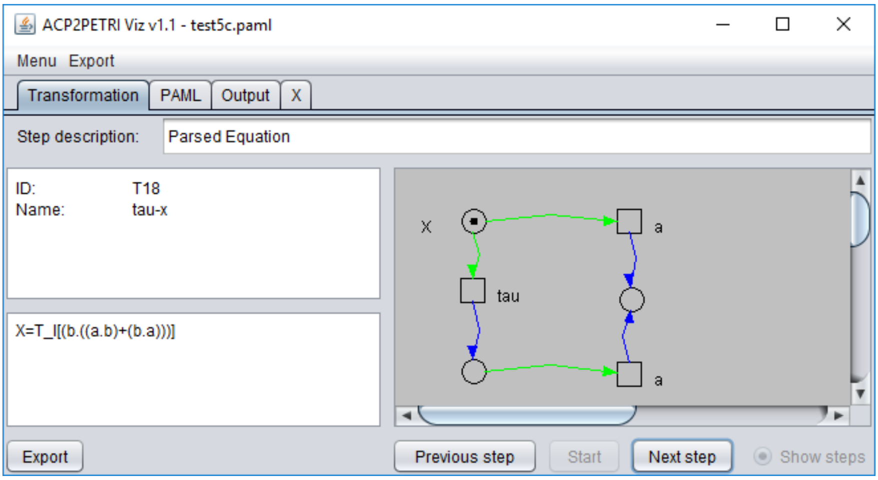

Figure 4
Removing selected silent actions by the ACP2Petri tool

The most important extensions of the tool were described within this section; however, some of the less apparent, but still very useful updates are described in the following one.

4 Additional Improvements

Updates we are discussing within the paper, not only introduced the abstraction as a fundamental design mechanism, but lead also to some additional corrections to the process of transformation. An extensive testing of newly implemented extensions allowed us to uncover certain hidden imperfections within some of the older functionality of the ACP2Petri tool. One of such imperfections is illustrated by small example given in Table 10, where recursion and encapsulation are used together.

Table 10
Repairing imperfections present in older version of the tool

```
gamma(a,b) = c
encset[H](c)
X = encaps[H](a.b.X)
```

The older version of the tool (Figure 5) was not able to handle this combination of operations correctly and did not identify the place holding a token with the place marked by *X*. In such form the resulting Petri net does not reflect the full behavior of the process *X*. It is easy to spot the difference in a small system like this, and adjust it eventually, but for larger-scale systems it could induce serious problems.

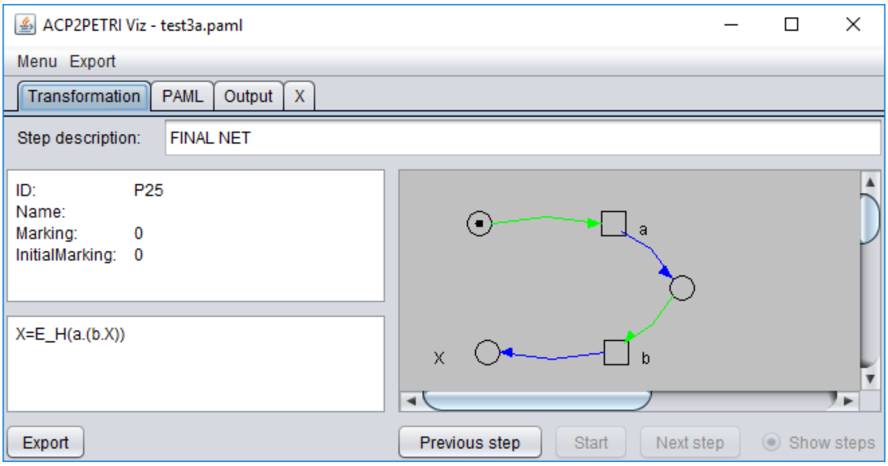

Figure 5
Incorrect Petri net produced by the older version of the tool

The correct Petri net representation of the process, produced by the current version of the tool, is shown in Figure 6. In some rare, more complicated cases, we even found that the transformation was not finished successfully and the exception was generated. Regardless of our current effort, only a further, more practical exploitation of the tool can show if there are some additional shortcomings.

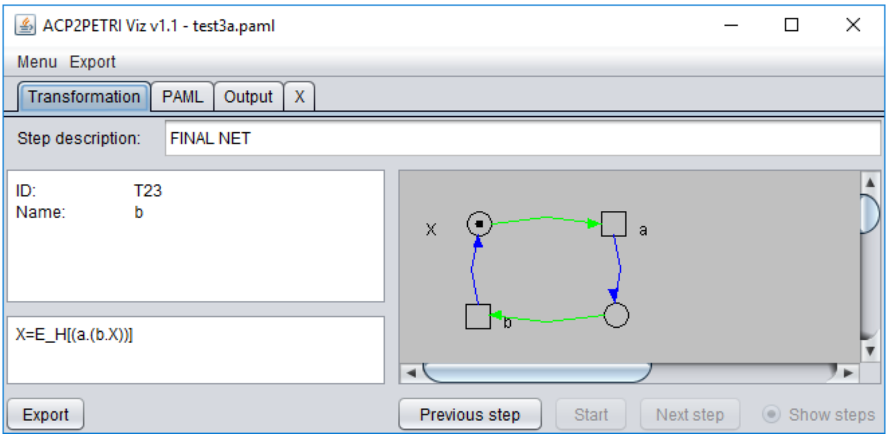

Figure 6
Correct Petri net produced by the current version of the tool

The additional improvement is connected with the ability to further simplify the Petri net generated by the tool in case if it is possible. The Petri net of CB system (Figure 7) can serve as an example, whose operation will be detailed within the next section of the paper. Here the place *X* and the *e*-labeled transition, representing the empty action, are present within the net, for the purpose of distributing tokens to the places B_{12} and B_{23}, representing the initial places of concurrently working components of the system.

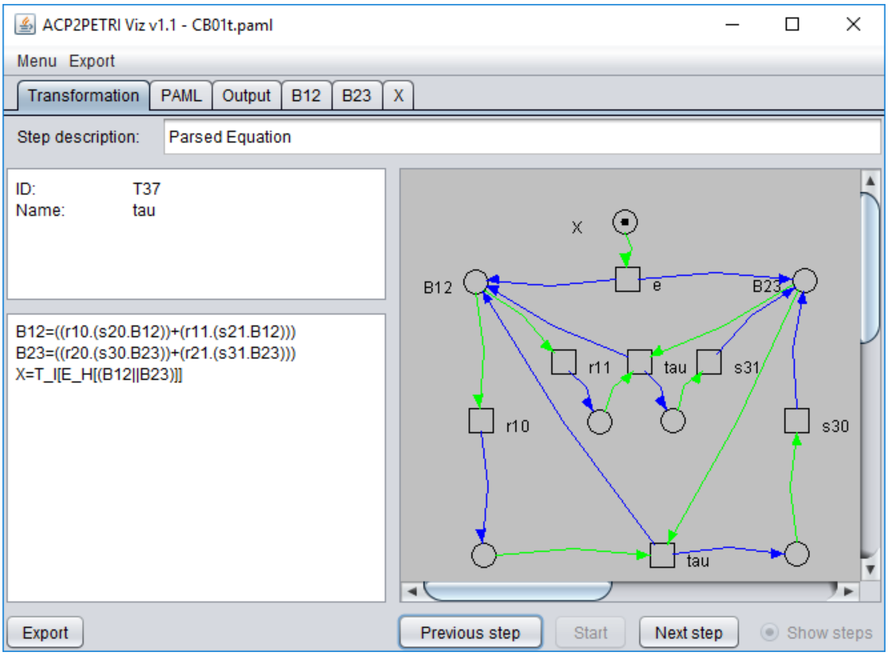

Figure 7

Petri net of the CB system

When places B_{12} and B_{23} are marked, then the place *X*, the *e*-labeled transition that is connected to the place and the corresponding arcs are not required for the correct operation of the system and can be removed. Such functionality was incorporated into the ACP2Petri tool and can be activated using the `-i` command line option. The resulting Petri net can be found in Figure 10.

5 Illustrating Example

In this section, there is a small practical example exposing also the newly adopted properties of the transformation presented. We have chosen a Coupling buffers (CB) system adapted from [6], which is depicted in Figure 8. The system represents the buffer with a capacity for two items, composed from two one-element buffers (B_{12} and B_{23}).

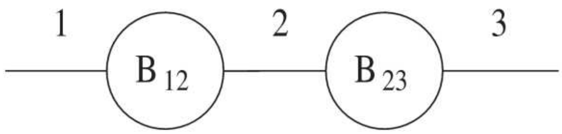

Figure 8
Coupling buffers system

Ports 1 and 3 of the system represent input and output ports, respectively, whereas port 2 is the internal one, allowing for communication between the two buffers (B_{12} and B_{23}). The algebraic specification of the CB system is given in Table 11.

Table 11
Specification of the CB system

```
gamma(s20,r20) = c20
gamma(s21,r21) = c21
encset[H](r20,s20,r21,s21)
tauset[I](c20,c21)

B12 = r10.s20.B12 + r11.s21.B12
B23 = r20.s30.B23 + r21.s31.B23
X = tau[I](encaps[H](B12||B23))
```

According to the specification, one-element buffer can read element 0 or 1 at its input port and send the read element to its output port. In case of the buffer B_{12}, the input port is port 1, so action reading element 0 from this port is named `r10` and `r11` in case of reading the element 1. The buffer can then send the element that is just read to output port 2. Two buffers are composed using the parallel composition operator and they can communicate over internal port 2, which is expressed by the means of communication function (`gamma`). Internal actions of the system (`r20`, `s20`, `r21`, `s21`) are further encapsulated by the encapsulation operator (`encaps`). In this way, the communication between buffers B_{12} and B_{23} over internal port 2 is expressed by actions `c20` and `c21`. Since we are interested only in an external behavior of the CB system, the actions just mentioned, are abstracted away using the `tau` operator.

A simulation of the CB system operation was performed using the PSF Toolkit [14]. Actions executed by the system (recorded in the TRACE window) are indicated by *atom* prefix, and the internal (hidden) actions are indicated by *com. skip* prefix as it is illustrated in Figure 9. The specification of the system, using the PSF language, based on process algebra ACP, is given in the PSF window of the figure.

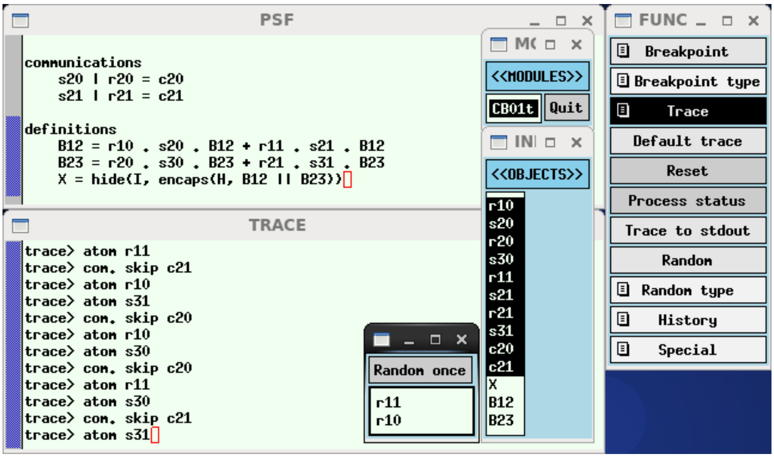

Figure 9

Simulation of the CB system using the PSF Toolkit

After processing the specification from Table 11, by the tools described within the paper, the resulting Petri net can be imported by the variety of available Petri net tools for further processing. Wolfgang Petri net editor [36] e.g. allows us to display the execution trace (Figure 10), which can be easily compared to the trace we got by simulating the algebraic specification using the PSF Toolkit. After removing silent actions we can observe that we were able to simulate the same sequences of actions. In general, for the CB system we can conclude that the ordering of elements entering the system on its input port 1 is the same as ordering of elements leaving the system via the output port 3. Our simulation-based observations correspond to this behavior.

A further analysis can be done by e.g. means of the structure theory of Petri nets [11], which investigates what behavioral properties of particular Petri net can be deduced from its structural properties. By means of instruments like reachability graph, coverability graph, S-Invariants, and T-invariants, many important properties of the system considered can be investigated. The petri net of the CB system, depicted in Figure 10, according to the analysis performed using the tool Netlab [28] is reversible, live, bounded and it has no deadlock.

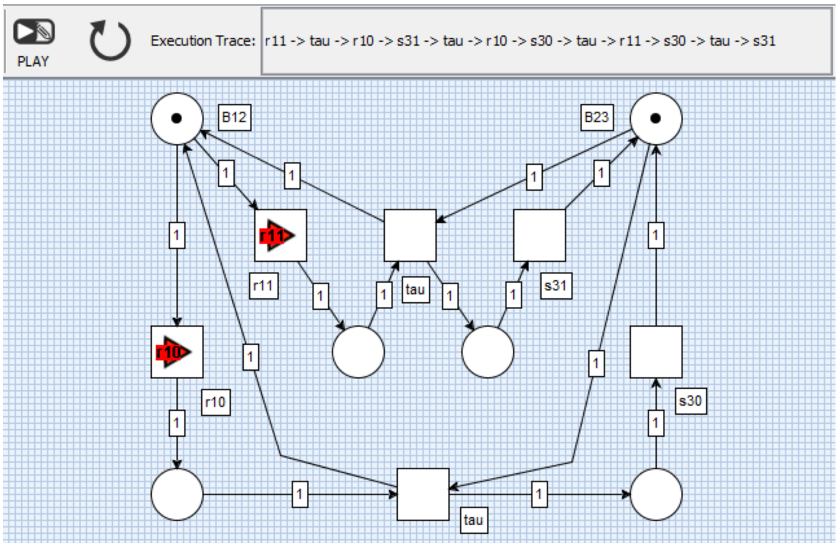

Figure 10
Simulation of the CB system using the Wolfgang tool

Conclusions

Within the paper we described our latest effort in the field of combining process algebra and Petri nets. The method has been updated by the means required for utilizing the benefits of the abstraction mechanism in order to provide better support for a convenient design and analysis of larger-scale systems.

Except the method itself, the tools allowing the practical application of its benefits were also extended, in order to support the new features. The PATool has been updated to reflect the new enhancements available for use in ACP specifications. The transformation tool, ACP2Petri, now supports abstraction mechanism too, together with the possibility to remove the silent actions, which can be removed safely. The extensive testing within the process of implementing new functionality helped us to uncover some hidden imperfections, which have been subsequently addressed too.

Comparing our method to other integration approaches combining Petri nets and process algebra we consider the availability of its software implementation to be a real benefit allowing for its practical utilization. We can mention its successful application in the field of communication protocols [32, 33], and we believe there will be further promising areas of application after the current update.

We consider support for handling data as one of future extensions, since processes can be understood as mechanisms for the data manipulation [16]. There are process algebras with data support available [12] as well as high-level Petri nets [22] giving such idea a real outline.

Including the notion of time into the process of transformation would also allow us to integrate some of the time-enabled process algebras [12] and Petri nets [37, 38] in order to model and study time-critical systems.

Another extension possibility is connected with the integration of additional formal method allowing for precisely determined and well defined development process, such as the B method [2]. The method allows for developing a system specification in form of a collection of components called B-machines with formally proven properties. It enables to refine an abstract specification into the concrete realm, which can then be translated into programming language [25]. Some activities have been done [23] in this area and it would be very interesting to continue in this direction, in order to utilize the new results in the area of software engineering. It would help to take important steps on the way to generating implementations of verified software components.

References

[1] Ábrahám, E., Huisman, M. (Eds.): Integrated Formal Methods, 12th International Conference, IFM 2016, Reykjavik, Iceland, June 1-5, 2016, Proceedings

[2] Abrial, J. R.: Modeling in Event-B: System and Software Engineering, Cambridge University Press, New York, NY, USA, 2010

[3] Bačíková, M., Porubän, J., Lakatoš, D.: Defining Domain Language of Graphical User Interfaces, Slate 2013: 2nd Symposium on Languages, Applications and Technologies, June 20-21, 2013, Porto, Portugal. Wadern: Schloss Dagstuhl - Leibniz-Zentrum fuer Informatik, 2013 pp. 187-202

[4] Baeten, J. C. M. (ed.): Applications of process algebra, Cambridge University Press, 1990

[5] Baeten, J. C. M.: A Brief History of Process Algebra, Theoretical Computer Science 335, 2005, pp. 131-146

[6] Baeten, J. C. M., Weijland, W. P.: Process Algebra, Cambridge University Press, 1990

[7] Basten, T.: In Terms of Nets: System Design With Petri Nets and Process Algebra, Eindhoven University of Technology, 1998

[8] Basten, T., Voorhoeve, M.: An Algebraic Semantics for Hierarchical P/T Nets, Computing Science Report, Eindhoven University of Technology, 1995

[9] Baldan, P., Bonchi, F., Gadducci, F., Monreale, G., V.: Asynchronous Traces and Open Petri Nets, In Programming Languages with Applications to Biology and Security, Volume 9465 of the series Lecture Notes in Computer Science, pp. 86-102, Springer International Publishing, 2015

[10] Best, E., Devillers, R., Koutny, M.: Petri Nets, Process Algebras and Concurrent Programming Languages, Lectures on Petri Nets II: Applications, Volume 1492 of the series Lecture Notes in Computer Science, Springer Berlin Heidelberg, 1998, pp. 1-84

[11] Best, E., Wimmel, H.: Structure Theory of Petri Nets, In Transactions on Petri Nets and Other Models of Concurrency VII, Volume 7480 of the series Lecture Notes in Computer Science, pp. 162-224, Springer Berlin Heidelberg, 2013

[12] Cranen S. et al.: An Overview of the mCRL2 Toolset and Its Recent Advances. In: Piterman N., Smolka S. A. (eds) Tools and Algorithms for the Construction and Analysis of Systems. TACAS 2013. Lecture Notes in Computer Science, Vol. 7795. Springer, 2013

[13] Desel, J., Juhás, G., Lorenz, R.: Process Semantics of Petri Nets over Partial Algebra, Proceedings of ICATPN 2000, 21st International Conference on Application and Theory of Petri Nets, Vol. 1825 of LNCS, pp. 146-165, Springer-Verlag, 2000

[14] Diertens, B.: Software Engineering with Process Algebra, Ph.D. Thesis, University of Amsterdam, 2009

[15] Ermel, C., Bardohl, R., Ehrig, H.: Specification and Implementation of Animation Views for Petri Nets, Proceedings of 2nd International Colloquium on Petri Net Technologies for Modelling Communication Based Systems, Berlin, Germany, 2001

[16] Fokkink, W.: Modelling Distributed Systems, Protocol Verification with μCRL, 2nd edition, Springer, 2011

[17] Fokkink, W.: Introduction to Process Algebra, 2nd edition, Springer-Verlag, 2007

[18] Gorrieri, R., Versari, C.: A Process Calculus for Expressing Finite Place/Transition Petri Nets, Proceedings of 17th International Workshop on Expressiveness in Concurrency, EXPRESS'10, Paris, France, 2010

[19] Gorrieri, R.: Language Representability of Finite P/T Nets, In Programming Languages with Applications to Biology and Security, Volume 9465 of the series Lecture Notes in Computer Science pp. 262-282, Springer International Publishing, 2015

[20] Groote, J. F., Keiren, J. J. A., Stappers, F. P. M., Wesselink, J. W., Willemse, T. A. C.: Experiences in developing the mCRL2 toolset. In Software: Practice and Experience, 41(2): 143-153, 2011

[21] Hillah, L. M., Kindler, E., Kordon, F., Petrucci, L., Trèves, N.: A primer on the Petri Net Markup Language and ISO/IEC 15909-2, Petri Net Newsletter Vol. 76, pp. 9-28, October 2009

[22] Hostettler, S. P., et al.: High-Level Petri Net Model Checking with AlPiNA. Fundamenta Informaticae, 2011, Vol. 113, No. 3-4, pp. 229-264

[23] Hudák, Š., Zaitsev, D. A., Korečko, Š., Šimoňák, S.: MFDTEPntool - a tool for the rigorous design, analysis and development of concurrent and time-critical systems, Acta Electrotechnica et Informatica, Vol. 7, No. 4, 2007, pp. 5-12

[24] Kollár, J., Pietriková, E., Chodarev, S.: Abstraction in Programming Languages According to Domain-Specific Patterns, Acta Electrotechnica et Informatica, Vol. 12, No. 2, 2012, pp. 9-15

[25] Korečko, Š., Sobota, B.: Petri nets to B-language transformation in software development, Acta Polytechnica Hungarica, Vol. 11, No. 6, 2014

[26] Lodaya, K.: A regular viewpoint on processes and algebra, Acta Cybernetica 17, 751-763, 2006

[27] mCRL2 language reference, Technische Universiteit Eindhoven, http://www.mcrl2.org/web/user_manual/language_reference/process.html

[28] Netlab, https://www.informatik.uni-hamburg.de/TGI/PetriNets/tools/db/netlab.html

[29] Olderog, E. R.: Nets, Terms and Formulas, Cambridge University Press, 1991

[30] Sobocinski, P.: Representations of Petri net interactions, CONCUR 2010 - Concurrency Theory, Volume 6269 of the series Lecture Notes in Computer Science, pp. 554-568, 2010

[31] Šimoňák, S., Peťko, I.: PATool – A Tool for Design and Analysis of Discrete Systems Using Process Algebras with FDT Integration Support, in Acta Electrotechnica et Informatica, Vol. 10, No. 1, 2010, pp. 59-67

[32] Šimoňák, S.: Verification of Communication Protocols Based on Formal Methods Integration, Acta Polytechnica Hungarica, Vol. 9, No. 4, 2012

[33] Šimoňák, S., Hudák, Š., Korečko, Š.: Protocol Specification and Verification Using Process Algebra and Petri Nets, Proceedings of CSSim 2009, pp. 110-114

[34] Šimoňák, S., Šolc, M.: Enhancing Formal Methods Integration with ACP2Petri. Journal of Information and Organizational Sciences. Vol. 40, No. 2 (2016) pp. 221-235

[35] Šimoňák, S., Hudák, Š.: Petri net semantics for ACP terms, Acta Electrotechnica et Informatica, Vol. 4, No. 1, 2004 (in Slovak)

[36] Wolfgang - Tool Documentation, BPSec group, Department for Telematics, Institute for Computer Science and Social Studies, University of Freiburg, Germany. Available at: http://doku.telematik.uni-freiburg.de/wolfgang

[37] Zaitsev, D.: Clans of Petri Nets: Verification of protocols and performance evaluation of networks. LAP LAMBERT Academic Publishing, 2013

[38] Zhang, X., Yao, S.: Bank switching performance verification with object-oriented timed Petri nets, Proceedings of the 2013 IEEE 8th Conference on Industrial Electronics and Applications, ICIEA 2013, Melbourne, Australia, pp. 1664-1669

Factual Results of an Eight Year Application of the SOL Safety Event Analysis Methodology in a Hungarian Nuclear Power Plant

Miklós Antalovits[a], Lajos Izsó[a], Sándor Suplicz[b]

[a] Department of Ergonomics and Psychology, Budapest University of Technology and Economics, Magyar tudósok körútja 2, 1117 Budapest, Hungary, antalovits@erg.bme.hu , izsolajos@erg.bme.hu

[b] Ágoston Trefort Centre for Engineering Education, Óbuda University, Népszínház utca 8, 1081 Budapest, Hungary, suplicz.sandor@tmpk.uni-obuda.hu

Abstract: The objective of this paper is to summarize the factual results of eight year application of the SOL safety event analysis methodology for the period of 2007-2015 in a nuclear power plant in Hungary. After putting the SOL analyses into a wider context, 531 particular contributing factors were identified and classified into the 20 broad standard SOL contributing factor categories. It turned out that a 28 item "toplist" of the particular contributing factors altogether contains 236 out of the total of 531 – corresponding to about 44% – and their highest frequency socio-technical system component category was the "Organization" (118.50%), closely followed by the "Individual" (98.41%). Based on the identified contributing factors and their relative weights, the corrective measures taken could prevent these – or similar other – events from recurring.

Keywords: SOL; safety event analysis methodology; nuclear power plant

1 Introduction

1.1 Background

This paper is the first of two related papers providing the most fundamental parts of the experiences gained during the latest eight year use of the SOL (*Safety through Organizational Learning*) safety event analysis methodology in the MVM Paks Nuclear Power Plant Ltd. (hereafter Paks NPP) in Hungary. The Paks NPP is still the only nuclear power plant in Hungary, and it has four units in operation with VVER-440 reactors.

The fundamentals of the SOL methodology have already been published elsewhere in many journal articles and books, e.g. refer to [31], [14], [30], and

[12]. Apart from scientific publications listed above, some IAEA (International Atomic Energy Agency) and EC (European Commission) technical documents also review the SOL, refer e.g. to [17] and [11].

In short, the SOL is a sophisticated event analysis methodology for learning from events that already have happened. This is clearly an "analysis methodology" to facilitate organizational learning in a well-structured way, and not an "investigation methodology" for finding some persons to blame. This is a very effective in-depth methodology, especially capable of identifying organizational and leadership related problems. It has also to be mentioned, however, that applying the SOL is also relatively costly. It requires a thoroughgoing preparation (collecting all the relevant documents and facts concerning the given event), involving independent external experts (as moderators of SOL sessions), and taking out from duty the most involved 10–14 NPP employees, independently from their positions, for two and a half consecutive working days and providing them the necessary working conditions in a hotel as well.

The father of SOL was late prof. Bernhard Wilpert of the TU Berlin, with whom the first two authors of this paper had the possibility to cooperate in adapting the SOL to the conditions of the Paks NPP in the years 2000-2005. In 2006 we already presented the very first application experiences [23], and later published some of the experiences gained since then [1]. Nevertheless, the present paper is the first comprehensive and detailed summary of our results in English on applying the SOL in the Paks NPP.

After carrying out several pilot SOL analyses, and having convinced the top management of the Paks NPP, the safety director decided in 2006 on introducing the SOL methodology. The original idea was to compare the results gained by the SOL with the results of the usual routine event analysis methodology – called PRCAP (*Paks Root Cause Analysis Procedure*) – of the Paks NPP. The main features of the PRCAP can be found in [17] and in [11].

The SOL methodology finally was introduced into the organization of the Event Analysis Group of the Safety Directorate in 2007 on a regular basis, 3-4 analyses per year, as part of the efforts increasing safety. Already the first experiences had shown that the SOL is not simply an alternative to the PRCAP, but it is rather a powerful complementary approach especially capable of identifying organizational "contributing factors" and thus supporting individual and organizational learning, increasing safety attitude and awareness.

Always only such events have been selected for SOL analysis that previously had already been analyzed and officially closed by the PRCAP. Therefore the SOL is a kind of "posterior" methodology, to be used quite independently from the PRCAP. This way the goal of applying the SOL has never been finding someone to blame, but only learning from the experiences. The moderators of the SOL sessions have always been invited independent external experts – actually the three authors of this paper – having both NPP related technological and psychological qualification and experience. Selecting events for SOL analyses is done by the Safety Directorate, usually consulting with independent SOL experts.

As the leader of the Event Analysis Group of the Safety Directorate at the Paks NPP, Gergely, – from an internal NPP perspective focusing on the specific local circumstances – [15] compiled a summary of guidelines for applying the SOL at the Paks NPP. The most important guidelines that have been proven significant concerning the selection of participants:

- The directly involved persons should participate (to ensure direct experiences and memories be taken into account)
- The involved organizational units should be represented proportionally (to ensure the appropriate content of the SOL working group)
- Manager (if possible top manager) should always be participating (to ensure the presence of real decision makers)
- All the participants should be professionally competent concerning the given event (to ensure the widest possible sources of relevant knowledge and experiences be at service)
- The total number of participants should not exceed 15 (to ensure the optimal number of participants for the best possible group dynamics)

Further requirements for preparing the invited participants prior to SOL analyses:

- Take part in a preparatory SOL meeting organized by the Safety Directorate
- Study the PRCAP analysis protocol of the given event
- Collect all relevant written materials (documents, memos, warrants, etc.)
- In order to identify minor details that could later turn out to be important, diccuss the event with colleagues of the organizational unit
- Study several earlier SOL protocols available on the NPP intranet portal

In the Paks NPP the instruction and training of employees is of high priority, the instruction and training system is diversified and multilevel. Based on the SAT (*Systematic Approach to Training*) concept of the IAEA the activity spectrum covers areas from general basic courses for new employees via professional basic education and refresher training, full scope simulator training for the control room crew, to practical training for the maintenance personnel.

The Paks NPP has a large Training Center under the Human Resource Directorate employing about 60 staff. In addition to the professional instructors, there is a network of so-called “qualified instructors”, who are outstanding specialists with high reputation in their own fields. These “qualified instructors” have acquired the pedagogical, psychological and communicational skills necessary for effective instruction and training in the frame of special adult education.

In the dissemination of the SOL results the Training Center is the key actor. Since the introduction of SOL, the Training Center has gradually become active in transmitting the results of SOL analyses toward the production, technology and maintenance areas. Utilizing the results via instruction and training is now a high priority expectation from the top management toward the Training Center. All the protocols of completed SOL analyses are continuously available for the employees on the intranet portal.

The initial disapproval because of the skepticism and relatively high costs has already disappeared. Since 2015 all the results of the SOL analyses have also to be discussed at the meetings of the Operational Review Committee. By this time the SOL analyses have been built into the internal regulation system of the Paks NPP.

Applying the SOL this way has been a real success story: since its introduction in 2007 till now altogether 32 SOL analyses have already been completed, revealing many organizational and leadership related problems that – as confirmed by the experiences – could not have been identified by the usual PRCAP analysis methods. The PRACP method, even if applied more thoroughly, could not have the capability of yielding more insights into organizational and leadership related problems, because of the inner limits of this method. The PRACP is a very useful, but much simpler, more routine and cheaper method in comparison with SOL which was designed mainly to identify organizational and leadership related problems.

In 2013 the WANO (*World Association of Nuclear Operators*) declared the SOL application practice in the Paks NPP as a "good practice" and proposed adapting this methodology for the nuclear communities of the world.

Based on this, among many others, the IAEA OSART (*Operational Safety Review Team*) in its 2014 report on the Kozloduy Nuclear Power Plant, Bulgaria, contains proposals for introducing the SOL [18].

1.2 Research Questions

The goal of this paper is to present the main factual results of the 27 SOL analyses — and the related four SOL meta-analyses — completed in the period of March 2007 – May 2015, totaling up to about 8 years.

Before focusing on this SOL target period of 2007-2015, we first place the main recorded safety characteristics of this period into a wider context in terms of time and also in terms of deviation types, professional areas of deviations, organizational areas responsible for treating deviations, and corrective measure types taken. It was hoped that this way we could get a more realistic picture about the "sampling basis" for selecting events for deeper SOL analyses.

Commencing with the introduction of SOL in 2007, in every second year SOL meta-analyses have been carried out aiming at identification of the most relevant particular contributing factors for these respective sub-periods. The 20 broad factor categories of possible contributing factors are precisely defined in the SOL terminology and are the following:

(1) Technological components, (2) Information presentation, (3) Communication, (4) Working conditions, (5) Personal performance, (6) Rule violation, (7) Operation scheduling, (8) Responsibility, (9) Control and supervision, (10) Group influence, (11) Rules, procedures and documents, (12) Personal qualification, (13) Training, (14) Organization and management, (15) Feedback of experience, (16) Safety principles, (17) Quality management, (18) Maintenance, (19) Regulatory and consulting bodies, (20) Environmental influence.

The main research questions, concerning the target period for applying the SOL, were to determine the frequency distributions of the identified contributing factors and how to interpret them.

2 Methods

2.1 Approach

The theoretical frame of the SOL methodology was developed basically from the widely known so called “Swiss-Cheese Model” [26], and from the “socio-technical system model” specifically designed for the nuclear industry [4]. These two event causation models were combined with the organizational learning approach. This frame serves at the same time as the theoretical basis of this research too, presented here in this paper.

The “Swiss Cheese” metaphor is an expressive accident causation model using the concept of layered security (defense in depth). It likens the different sub-systems of the “socio-technical system” to multiple slices of Swiss cheese, stacked side by side, in which the hazards (potentially harmful effects) could – or could not – pass through the holes of these slices as defense layers. The main components of the “socio-technical system” are the “Individual”, the “Group”, the “Organization”, the “Technology” and the “Environment” domains. The relevant defense layers could be in the areas of any sub-sub-systems of these main components. More details on Reason’s views about these topics can be found in [27] [28] [29].

Learning from (especially negative) experiences (like accidents, incidents, errors, etc.) is an essential determinant of successful operation in high-risk socio-technical systems. This learning is a human activity that can take place in the domain of “Individual”, or/and “Group”, or/and “Organization” socio-technical system components. As an example, we, in cooperation with Paks NPP, also developed and operated a practical computer-supported method for fostering individual and group (team) level learning in situations immediately after simulator training sessions: [2] [21]. The SOL, however, targets directly the learning at organization level, which is far the most important domain.

By the SOL terminology, events (occurrences of unexpected, undesirable system states) can be described as causal and temporal chains of elementary sub-events called “event building blocks”. Events occur through interaction of different contributing factors working on the domains of any socio-technical system components.

A SOL event analysis is the later reconstruction of the occurrence of an event as well as of its causes in the sense of a root-cause analysis. For root-cause analysis in a NPP, refer to [19].

The SOL was especially designed to identify organizational (including management, leadership, procedures, documentation, etc. related) problems, and the practice has shown that the SOL is really very capable of doing this.

Our view is rather radical concerning the organizational factors: we believe that, in a wider sense, the final root-causes are very often – almost always – located within the domain of the “Organization” socio-technical system component. If this causal relationship cannot be proven, the analysis probably has not delved deep enough. After such a statement, one could question the role of the “Individual”, “Group”, “Technology” and the “Environment” components. Actually, these can be considered as some kind of intermediate or transition components that would sooner or later lead to the Organization component. The key in the SOL methodology to labeling a problem domain as “Individual”, “Group”, “Organization”, “Technology” or “Environment” is the answer to the question: “*Given the present state of the art, can the prevention of this very problem/failure/flow be expected from this very organization?*”. The main aspect is “sooner or later”: what cannot be expected from an organization today, can well be expected tomorrow.

There are many examples in the literature for cases that first clearly seemed to be associated with individual, group or technology level error, but a deeper analysis later revealed that in reality it is – at least partly – an organization level error.

A good example is the case of the disaster of freight ferry Herald of Free Enterprise in 1987, when the assistant bosun – although it was his duty – did not close the bow doors, since at this time he was asleep in his cabin instead. This fact, however, gets a quite different judgment if we get to know that before falling asleep the assistant bosun was already on duty for about 24-hours, and therefore suffered from sleep deprivation [16, page 61].

This way the label “individual error” suddenly was transformed into mainly “organization error”: the company required him to be for 24 hours on duty. Literally the following can be found in the corresponding judicial document [10, page 14]: “At first sight the faults which led to this disaster were the aforesaid errors of omission on the part of the Master, the Chief Officer and the assistant bosun, and also the failure by Captain Kirby to issue and enforce clear orders. But a full investigation into the circumstances of the disaster leads inexorably to the conclusion that the underlying or cardinal faults lay higher up in the Company.”

In this same disaster, the balancing group in the ship's bottom inappropriately balanced the weight, and the embarking group carelessly counted the passengers that led to a serious 13% overload. At first sight these seemed to be group level errors, but later it turned out that these are predominantly also organization level errors, since the management tacitly accepted and tolerated this risky behavior already for a long time.

Similarly, the facts that the ferry had a top-heavy design, her body was not subdivided into watertight compartments, and there was an uncorrected leaning to the right, first seemed to be associated with technological (design or equipment) level errors. The deeper analysis, however, revealed again that these are predominantly also organization level errors, since the management knew these technological problems but tolerated them without taking any corrective measures. Further details are available e.g. in [24, page 129] and in [25].

Another example from our own practice for causing or preventing human errors at "Individual" level by means of "Organization" level regulation is presented in [22]. We found that NPP control room operators during normal – and therefore relatively uneventful – shifts experience a kind of rather strong "arousal compensation tendency" that influences their subjective well-being. We concluded that it is safer to allow for operators certain kinds of not directly task-related voluntary activities (like not task-related conversation, listening to the radio, etc., of course within reasonable limits) than expect them strictly doing nothing and being under stimulated during long eventless periods of operation.

This view, concerning human error (should it be at "Individual", "Group", or "Organization" level), is in perfect agreement with Dekker's "New View of Human Error", refer to [6]. In this book (page 159) Dekker states that "A human error problem is an organizational problem. Not because it creates problems for the organization. It is organizational, because a human error problem is created, in large part, by the organization in which people work."

Right in the preface of this book (Table 0.1, page xi) Dekker summarizes the characteristics of the "Old View" and the "New View" of Human Error in the following way (direct quotations):

The Old View of Human Error on what goes wrong	**The New View of Human Error on what goes wrong**
Human error is a cause of trouble.	Human error is a symptom of trouble deeper inside a system.
To explain failure, you must seek failures (errors, violation, incompetence, mistakes).	To explain failure, do not try to find where people went wrong.
You must find people's inaccurate assessments, wrong decisions, and bad judgments.	Instead, find how people's assessments and actions made sense at the time, given the circumstances that surrounded them.

The Old View of Human Error on how to make it right	**The New View of Human Error on how to make it right**
Complex systems are basically safe.	Complex systems are not basically safe.
Unreliable, erratic humans undermine defenses, rules and regulations.	Complex systems are trade-offs between multiple irreconcilable goals (e.g. safety and efficiency).
To make systems safer, restrict the human contribution by tighter procedures, automation, and supervision.	People have to create safety through practice at all levels of an organization.

More details on Dekker's views about these topics can be found in [5] [7] [8] [9].

It has also to be stressed that behind the "Technology" and the "Environment" related contributing factors a thorough analysis usually (but, of course, not always) also reveals the "Organization" level root causes.

If e.g. a faulty piece of machinery represents a "Technology" related contributing factor of a particular event, the causal chain can be followed backwards and the questions rightfully arise:

- Why has the "Organization" purchased this particular piece of machinery?
- If it went wrong only after a longer use, why the "Organization" has not provided appropriate and effective preventive maintenance?

Similarly, if e.g. a sudden unexpected weakening of the market position of the company represents an "Environment" related contributing factor of an event, the following questions are appropriate:

- Why was this concrete loss of position a surprise for the "Organization"?
- Why the "Organization" has not prepared itself for such economic turbulences?

2.2 Applied Methods

We share Dekker's opinion [6] that simply counting human errors cannot be a valid and meaningful approach in NPP safety research, because it is hard to agree what an "error" really is. Instead of identifying and counting human errors we are focusing on identifying and counting deviations and contributing factors.

Therefore our basic methods were

- Studying of the event analysis data gained by the PRCAP methodology during the period of 1999-2014 in broad terms of deviation types, professional areas of deviations, organizational areas responsible for treating deviations, and measure types taken as functions of time.

- Detailed analysis of the results gained by the SOL methodology in the period of 2007-2015 via focussing on identified contributing factors.

These analyses are based on the PRCAP and SOL data bases and basically comprise comparing frequencies in different categories derived from deviations and contributing factors. Because of the nature of these data, either merely descriptive statistics were considered, or simple nonparametric statistical tests were applied.

3 Results

3.1 The Wider Context

Before focusing on the target period of March 2007 – September 2015, this period was taken into a wider context in terms of time, deviation types, professional areas of deviations, organizational areas responsible for treating deviations, and measure types taken. These pieces of information can be seen in Figures 1, 2, 3 and 4.

This way we could get a more realistic picture about the "sampling basis" for selecting events for SOL analysis. In the period of January 1999 – November 2014 the Safety Directorate of the Paks NPP altogether investigated 624 events, including a total of 2236 deviations.

A deviation is defined as any shift from standard practice or parameter value. A violation is a deliberate deviation from standard practice, carried out to maintain safe operation.

The number of deviations per event is quite steadily 3.58 throughout this period (min=1, max=26, SD=2.97).

Root causes are the fundamental causes of a deviation in a causal chain that if corrected, will prevent recurrence of this deviation.

Direct causes are the latent weaknesses that allow or cause the observed cause of an initiating event to happen, including the reasons for the latent weakness.

Contributing cause (factor): a condition that may have affected the occurrence of a deviation.

It can be observed in all the Figures 1, 2, 3 and 4 that from 2005 there is a radical decrease in the number of events, and consequently also in the number of deviations. Its reason is very probably – in accordance with the opinions of the leading safety experts of the Safety Directorate of the Paks NPP – that following the INES (*International Nuclear Event Scale*) level 3 event that occurred in 2003 certain severe safety measures have been taken step by step and simultaneously the general awareness for preventing human errors has also increased. It has also to be taken into account that the deviation reporting criteria significantly changed in August 2013.

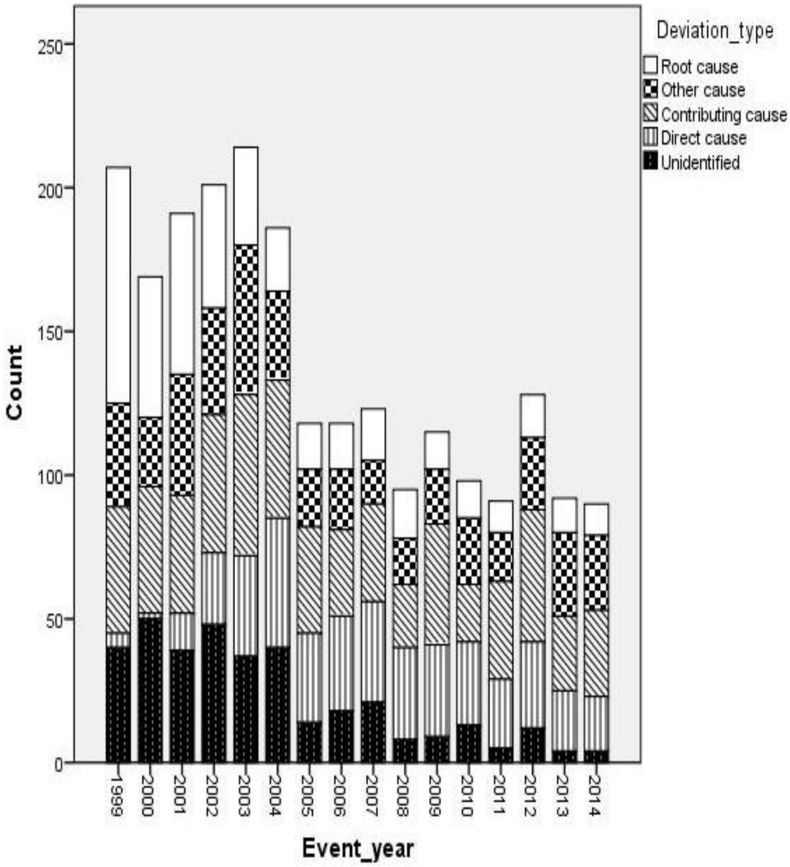

Figure 1

Frequencies of different deviation types as a function of time in years

It is also clear from the Fig. 1 that the number of identified root causes continuously decreases along the whole time period. Simultaneously, the number of identified direct causes steeply increases till 2004, and after that slightly decreases. Important background information is that each event has at least one identified direct cause. Complex events may even have two direct causes, but more than two usually cannot be found.

A more detailed analysis has shown that this changing pattern is true not just for the absolute numbers of root causes (and of direct causes), but also for the ratio of root cause numbers to total cause numbers (and for the ratio of direct cause numbers to total cause numbers).

The total number of identified root causes for this period was 428, which means that it was possible to find root causes only for about 68% of the events.

It was found that the ratio of total number of causes to the number of root causes starts at about 2 in 1999, and after a slight continuous increase, in 2004 jumps to about 7, and its final value is about 9 in 2014.

Our interpretation is that after the INES level 3 event in 2003, as a result of the new and rather severe safety measures taken, (1) a smaller number of such events occurred that had to be investigated by the PRCAP methodology, and (2) the analysis have become more thorough. These are reflected in the fact, that with one root cause an increasing number of other causes are associated.

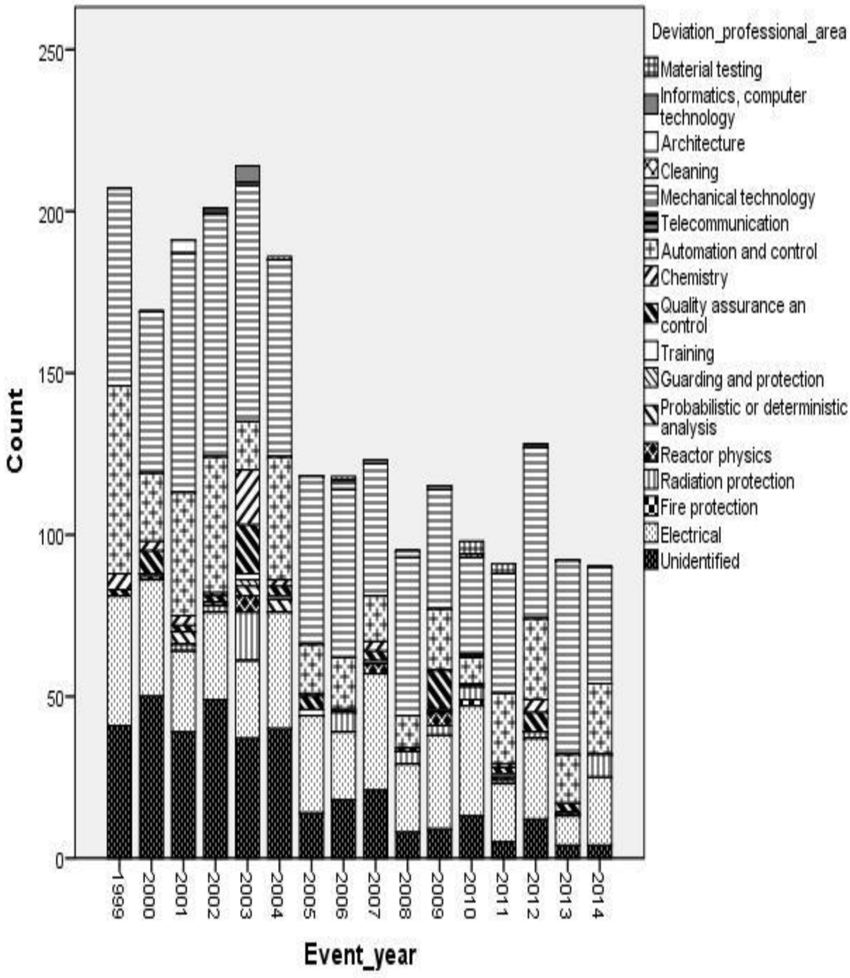

Figure 2

Frequencies of different professional areas of deviations as a function of time in years

It can be seen that the most involved professional area is the mechanical technology, which is followed by the electrical technology and by the automation and control.

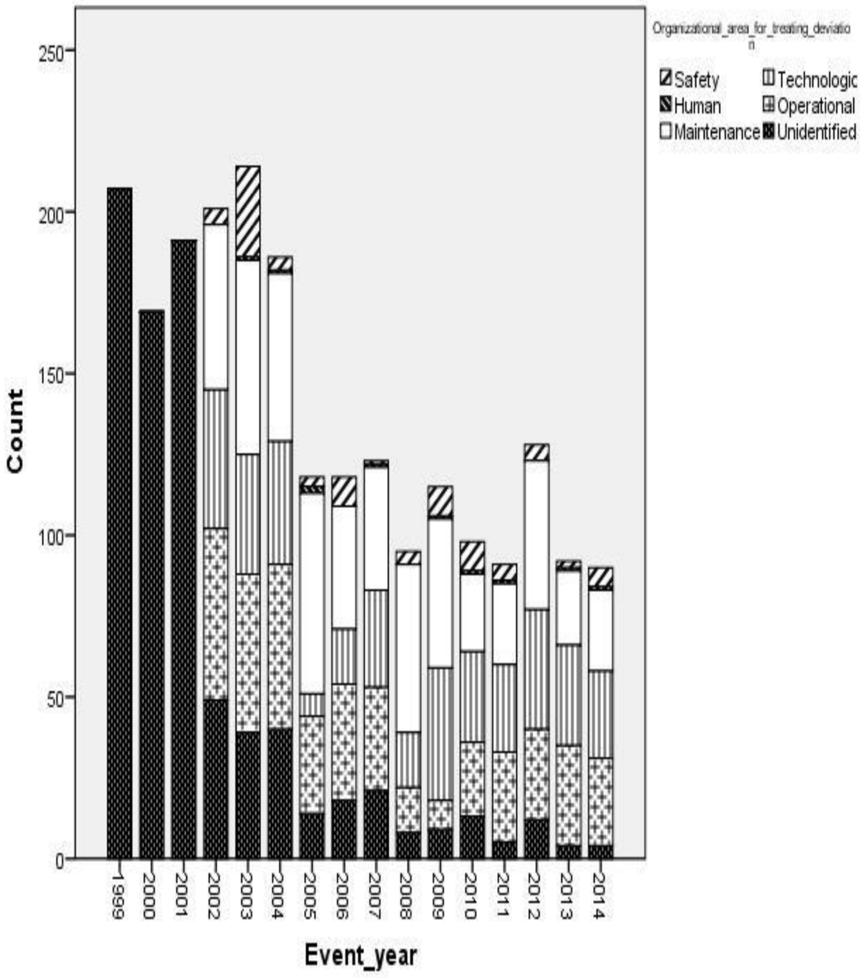

Figure 3

Frequencies of different organizational areas responsible for treating deviations as a function of time in years

It can be seen that the most frequently involved organizational area is the maintenance, which is followed by the operation and by technology.

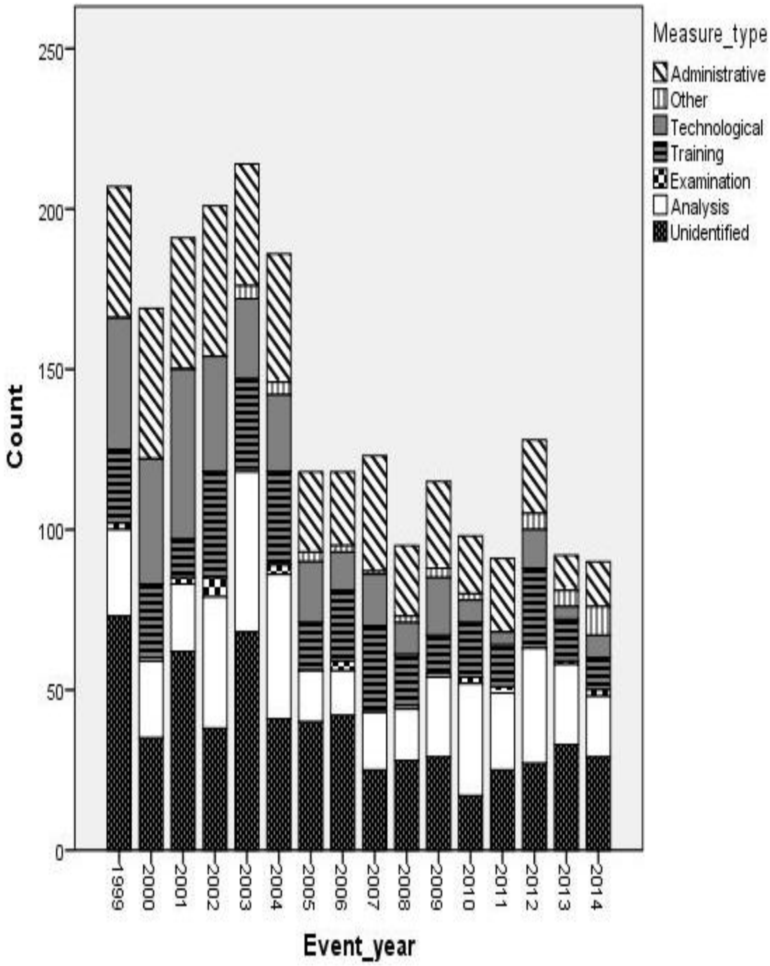

Figure 4

Frequencies of measure types taken by the organization as responses for the deviations as a function of time in years

In this figure we can see that the most frequently involved measure type taken is administrative, which is followed by technological, analysis and training measures.

3.2 Results Gained by the SOL Methodology in the Period of 2007-2015

From the above it follows that within our whole target period of interest (2007-2015) the selection of events for SOL analysis during the first three two-year sub-periods (2007-08, 2009-11, 2011-13) had been done from among events investigated by the same criterion system. During the last sub-period (2013-15), however, different criteria were used for the analysis – which although directly surely have not influenced the process of selecting events for SOL analysis – for only the order's sake the results of this last sub-period were analyzed separately. As the results later showed, and as expected, there were really no differences.

From the above it can also be seen that in the period of January 1999 – November 2014 (for which the Safety Directorate of the Paks NPP had final processed event analysis data at the time of closing the manuscript of this paper) altogether 624 events were investigated. From these events 218 occurred and were investigated in the period of 2007-2014. Of these 218 events – of which only a very small fraction was officially labeled as "safety relevant" – 25 were selected for the deeper SOL analysis, corresponding to about 11%. This percentage has always to be kept in mind while trying to generalize SOL results.

The frequency distribution of the 531 contributing factors identified in the period of 2007-2015 along the four sub-periods of the corresponding SOL meta-analyses can be found in Table 1, while the distribution of these contributing factors along the 20 broad factor categories can be seen in Table 2.

Table 1
The frequency distribution of the 531 contributing factors identified in the period of 2007 – 2015 along the four sub-periods of the SOL meta-analyses

Sub-period of SOL meta-analyses	**2007-2008**	**2009-2011**	**2011-2013**	**2013-2015**	**Total**
Number of SOL analyses completed	8	8	6	5	27
Number of identified contributing factors	182	135	129	85	531

Taking into account that the deviation reporting criteria changed in August 2013, the statistical analysis first compared only the first three sub-periods by the chi-square test. This analysis, however, has not revealed any time effects: there were no significant differences between the numbers of identified contributing factors of the first three sub-periods. It has also been proven, that – despite the change of reporting criteria in August 2013 – there were no statistically significant differences between the frequencies of identified contributing factors of the first three sub-periods (taken together) and of the fourth sub-period.

This time-independence was also true not just for the total numbers of identified contributing factors (as presented in Table 1), but also separately for each of the 20 broad factor categories (as presented in Table 2). This means, that even if in reality there do exist some increasing numbers of time-dependent deviations as was originally presupposed by us due to the ageing of the NPP, it was not possible to prove it during this relatively short eight year period by our relatively incomplete and insensitive methods. We have also to recall, that the SOL sampling rate was only about 11% of the all events of the target period.

Notwithstanding, during the SOL sessions we sporadically have heard such pieces of information that support the hypothesis of increasing number of age-related deviations. Examples: to certain older soviet made equipment certain documents or component parts, accessories and fittings are not always available in time. In some cases even the original manufacturers of these components are not available either.

Table 2
The frequency distribution of the 531 contributing factors identified by the SOL methodology in the period of 2007 – 2015 along the 20 broad contributing factor categories and the 5 socio-technical system components

ID code	Broad contributing factor category	Total frequency of 2007-2015	%	Socio-technical system component
1	Technological components	48	9.04	Technology
2	Information presentation	17	3.20	Technology
3	Communication	35	6.59	Individual - Group
4	Working conditions	37	6.97	Organization
5	Personal performance	95	17.89	Individual
6	Rule violation	49	9.23	Individual
7	Operation scheduling	16	3.01	Organization
8	Responsibility	17	3.20	Organization
9	Control and supervision	16	3.01	Organization
10	Group influence	3	0.56	Group
11	Rules, procedures and documents	59	11.11	Organization
12	Personal qualification	3	0.56	Organization
13	Training	6	1.13	Organization
14	Organization and management	91	17.14	Organization
15	Feedback of experience	13	2.45	Organization
16	Safety principles	3	0.56	Technology
17	Quality management	6	1.13	Organization
18	Maintenance	5	0.94	Organization
19	Regulatory and consulting bodies	7	1.32	Environment
20	Environmental influence	5	0.94	Environment
Sum total		531	100.00	All

Table 3
The "top list" of particular contributing factors identified by the SOL methodology in the period of 2007-2015

	Concrete particular contributing factors of the highest total frequencies identified in the period of 2007-2015	**Socio-technical system component**	**Total frequency of 2007-2015 (at least 5)**
1	Omitted activity	Individual	25
2	Lack of following procedures	Individual	18
3	Incomplete documentation	Organization	13
4	Documentation not necessarily detailed	Organization	10
5	Time pressure or performance urge	Organization	10
6	Design error of technical component	Technology	10
7a	Incomplete or unsatisfactory communication*	Group	9 (5)
7b	Incomplete or unsatisfactory communication*	Individual	9 (4)
8	Unsatisfactory attention for details	Individual	9
9	Important information delayed to forward or lost	Individual	8
10	Not recognizing the real importance of task	Individual	8
11	Tolerating general practice that - at least partly - violate rules	Organization	8
12	Unsatisfactory control and supervision	Organization	8
13	Missing resources (human, financial, time, etc.) for achieving goals	Organization	8
14	No organizational level regulation concerning identified problems	Organization	7
15	Disturbing working conditions, significant workload	Organization	7
16	Complacency based on past experiences	Organization	7
17	Error in performing a task	Individual	7
18	Work performance that – at least partly – violates rules	Individual	7
19	Not observing procedures	Individual	7
20	Unsatisfactory change management	Organization	7
21	Missing documentation	Organization	6
22	Missing warning signal before safety intervention	Organization	6
23	Management does not treat a problem according to its importance	Organization	6
24	Making an error or misjudgment	Individual	5
25	Unsatisfactory briefing before performing tasks	Group	5
26	Unsatisfactory human resource allocation	Organization	5

27	Preferring production or economic aspects against safety	Organization	5
28	Not introducing necessary measures against known problems	Organization	5
Sum total		All	236

Comments:

(1) * The frequency of 9 of the "Incomplete or unsatisfactory communication" contributing factor was divided between the "Group" and "Individual" socio-technical system component categories.

(2) Since there were no statistically significant differences between the frequencies of the identified contributing factors during the four sub-periods, here the whole period of 2007-2015 is treated together.

The following bar chart presents the distribution of these 236 contributing factors along the socio-technical system components.

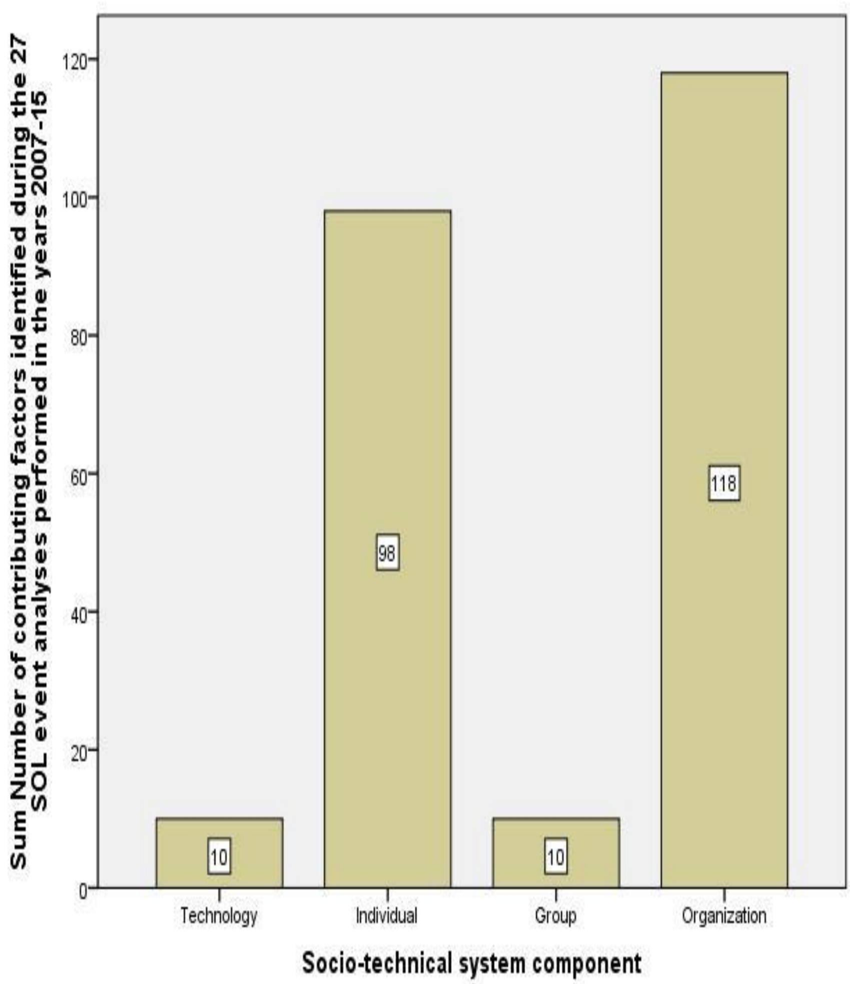

Figure 5
Bar chart of the frequencies of the identified 236 particular contributing factors of the highest total frequencies belonging to different socio-technical system components for the SOL analyses period of 2007-2015

The frequencies in the different socio-technical system component categories in Fig. 5 were calculated from the "top list" frequencies of particular contributing factors shown in Table 3.

Important to note, that from the data in Table 2 a bar chart very similar to Fig. 5 could have been constructed, but since the "top list" in Table 3 (and the related Fig. 5) contains much fewer items, it is also much easier to interpret.

4 Discussion

The "top list" shown in Table 3 is considered to be the main and practically most usable summary results of the SOL analyses. It presents those concrete particular contributing factors the total frequencies of which are at least 5. These 28 particular contributing factors altogether contain 236 out of the total of 531, corresponding to about 44%. These contributing factors indicate those identified problems for the elimination (or at least mitigation) of which corrective measures had to be taken. The big majority of these measures really have been taken. Concerning the perceived utilization efficiency of these measures please refer to the continuation of this paper titled "*Impact assessment of eight year application of the SOL safety event analysis methodology in a nuclear power plant*" published in the same issue of this journal.

Not surprisingly, the highest frequency socio-technical system component category was the "Organization", closely followed by the "Individual". Although half of all the identified contributing factors fell into the "Organization" category, on principal basis we have good reasons to think that even deeper SOL analyses could have categorized an even greater part of "Individual" factors into "Organization".

On the other side, in the practice there is no need for such "even deeper SOL analyses", because the applied SOL analysis in its present form is deep enough for all practical purposes. Our radical view that the final root-causes are almost always located within the domain of the "Organization", in itself, is not concrete enough and therefore is useless in the practice. The real practical strength of this view during SOL analysis lays in encouraging the attitude of:

- Fact-finding (not searching for scape-goats)
- Avoiding premature or insufficient generation of hypotheses
- Avoiding mono-causal thinking and truncated search strategies

If doing so, apart from that the overwhelming a majority of final root-causes, almost always, will be located within the "Organization" domain. The analyzed concrete events will be correctly reconstructed and deeply understood in more detail. This way, based on the identified contributing factors and their relative weights, the corrective measures taken, could prevent these or similar other events from recurring.

Acknowledgements

The authors first of all would like to acknowledge the support from Gábor Volent, safety director of Paks NPP, who had made us available the data base of events investigated in the period of 1999-2014, and the documentation of the results of 27 SOL analyses performed in the period of 2007-2015. Similarly, special thanks go to József Gergely of the Safety Directorate who shared with us his valuable experiences gained during all the 27 SOL analyses. We are also indebted to Tibor

Sárközi of the Safety Directorate, for helping us to interpret certain parts of the content of the data base. Finally, we express our gratitude to Dr. Antal Kovács communication director for his practical remarks and giving permission for publishing this paper.

References

[1] Antalovits, M., Izsó, L. (2013) Increasing safety through Organizational Learning in high-risk systems. The methodology and application experiences of the SOL (*Safety through Organizational Learning*) method (In Hungarian) Munkavédelem és Biztonságtechnika. 2013/3 3-11

[2] Antalovits, M., Izsó, L. (1999) Self-assessment and learning in NPP simulator training. In: Misumi, J., Wilpert, B., Miller, R. (eds) Nuclear Safety: A Human Factors Perspective, ISBN 0-7484-0818-5, pp. 243-256, Taylor and Francis, London

[3] Antalovits, M., Izsó, L. (2003) Assessment of Crew Performance and Measurement of Mental Effort in a Cognitively Demanding Task Environment. In: Hockey, G. R. J., Gaillard, A. W. K., Burov, O. (eds) Operator Functional State, NATO Science Series, pp. 284-290, ISBN 1-58603-362-X, IOS Press

[4] Becker, G., Hoffmann, S., Wilpert, B., Miller, R., Fahlbruch, B., Fank, M., Freitag, M., Giesa, H., Schleifer, L. (1995) Analyse der Ursachen von "menschlichen Fehlverhalten" beim Betrieb von Kernkraftwerken (BMU-1996-454) Budesministerium für Umwelt, Naturschutz and Reaktorsicherheit, Bonn

[5] Dekker, S. (2002) The Field Guide to Human Error Investigation. Ashgate Publishing Company

[6] Dekker, S. (2006) The Field Guide to Understanding Human Error. Ashgate Publishing Company

[7] Dekker, S. (2011) Drift into Failure. Ashgate Publishing Company

[8] Dekker, S. (2012) Just Culture: Balancing Safety and Accountability. Ashgate Publishing Company

[9] Dekker, S. (2014) Safety Differently. Human Factors for a New Era. CRC Press

[10] Department of Transport, (1987) The Merchant Shipping Act 1894. mv Herald of Free Enterprise. Report of Court No. 8074. Formal Investigation. London, Her Majesty's Stationery Office

[11] European Commission (Ziedelis, S., Noel, M.), 2011. Comparative Analysis of Nuclear Event Investigation Methods, Tools and Techniques. Interim Technical Report. European Commission, Joint Research Centre, Institute for Energy

[12] Fahlbruch, B., Schöbel, M. (2011) SOL - Safety through organizational learning: A method for event analysis. Safety Science, 49 (2011) 27-31

[13] Fahlbruch, B., Wilpert, B., (1997) Event analysis as a problem solving process. In: Hale, A., Wilpert, B., Freitag, M. (Eds.) After the Event from Accident to Organizational Learning. Pergamon, Oxford, pp. 113-130

[14] Fahlbruch, B., Wilpert, B., (1999) System safety - an emerging field for I/O psychology. In: Cooper, C.L., Robertson, I.T., (Eds.) International Review of Industrial and Organizational Psychology, Vol. 14, Wiley, Chichester, pp. 55-93

[15] Gergely, J. (2011) A review of the SOL methodology (in Hungarian) Paks NPP, Hungary

[16] Grech, M., Horberry, T., Koester, T. (2008) Human Factors in the Maritime Domain. CRC Press, Taylor & Francis Group, London, New York

[17] IAEA (2002) Review of methodologies for analysis of safety incidents at NPPs. Final report of a co-ordinated research project 1998-2001, TECDOC-1278, Vienna, Austria

[18] IAEA (2014) Report of the Operational Safety Review Team (OSART) to the Kozloduy Nuclear Power Plant Bulgaria. 26th November to 13th December 2012, Follow up Mission 23-27 June 2014

[19] IAEA (2015) Root Cause Analysis Following an Event at a Nuclear Installation: Reference Manual. TECDOC-1756. Vienna, Austria

[20] Institute of Nuclear Power Operations (INPO), 2013. Traits of a Healthy Nuclear Safety Culture. INPO 12-012, Rev. 1 (April 2013)

[21] Izsó, L. (2001) Fundamentals of the Model Behind the COSMOS Methodology Used for Team Assessment in Simulator Training. Journal of Occupational Safety and Ergonomics, Volume 7, No. 2, pp. 163-178

[22] Izsó, L., Antalovits, M. (1997) An Observation Method for Analyzing Operators' Routine Activity in Computerized Control Rooms. Journal of Occupational Safety and Ergonomics, Volume 3, No. 3, pp. 173-189

[23] Izsó, L., Antalovits, M. (2006) Implementation of "SOL" as a tool for better event analysis at Paks Npp Ltd. (The first experiences) IEAE Workshop, June 26-30, 2006, Balatonfüred, Hungary

[24] Murray, S. L. and Thimgan, M. S. (2016) Human Fatigue Risk Management: Improving Safety in the Chemical Processing Industry. Academic Press. ISBN: 978-0-12-802412-6

[25] O'Meara, C. (2016) "Herald of Free Enterprise" - lessons for management. An edited versionof addressto theVictorian Branch of the Association on the "Herald of Free

Enterprise"http://www.austlii.edu.au/au/journals/ANZMarLawJl/1989/3.pdf (Sept. 2016)

[26] Reason, J. (1983, 1990, 1994) Human Error. Cambridge University Press, Cambridge

[27] Reason, J. (1997) Managing the Risks of Organizational Accidents. Ashgate, Aldershot

[28] Reason, J. (1998) Achieving a Safe Culture: Theory and Practice, 12th ed. Taylor, Manchester

[29] Reason, J. (1999) Are we casting the net too widely in our search for the factors contributing to errors and accidents? In: Misumi, J., Wilpert, B., Miller, R. (eds) Nuclear Safety: A Human Factors Perspective, pp. 199-208, Taylor and Francis, London

[30] Wilpert, B. and Meimer, H. (2001) Computer supported Event Analysis (SOL - Safety through Organisational Learning). Berlin University of Technology

[31] Wilpert, B., Miller, R. & Fahlbruch, B. (1997) SOL: Sicherheit durch Organisationales Lernen. Technische Überwachung, 38 (4), 40-43

A Priori Cost of the Energy to Perform Movement on a Predefined Path

Mădălin Costin[1, 2, 3], Ion Voncilă[2, 3], Ion Bivol[2]

[1]Faculty of Automatic Control and Computer Science, "Gheorghe Asachi" Technical University of Iaşi, Iaşi, România

[2]Faculty of Automatic Control, Computer Science, Electrical and Electronics Engineering, "Dunărea de Jos" University of Galaţi, Galaţi, România

[3]Energy Conversion Integrated Systems and Advanced Control of Complex Processes Research Centre, Galaţi, România, "Dunărea de Jos" University of Galaţi, Galaţi, România

Madalin.Costin@ugal.ro, Ion.Voncila@ugal.ro, Ion.Bivol@ugal.ro

Abstract: The object of the paper is a priori energy cost estimation for the motion work performed by electric drive systems. We tested an original method for finding the efficiency of motion along a pre-specified path. Two mathematical models: the classic point-to-point trajectory planning and the interpolation model for the efficiency of the energy conversion process provide the data for energy cost estimation. First, the interpolation model was built using the electric drive actuator's data specifications. These data are the torque, speed, and efficiency for scattered steady-state operation points. The interpolation model builds the efficiency surface vs. torque and speed, which passes through all specification points of the actuator. If the required trajectory is superposed on the efficiency surface, we can find the incremental values of the efficiency which correspond to trajectories speed and torque. These quantities are necessary and sufficient for energy cost estimation of the motion along the desired trajectory. The a priori calculation of energy costs for electromechanical motion processes is an important means of preventing the energy wastage by adopting the minimum cost trajectory based on execution time, command law and load torque.

Keywords: Electromechanical servo system; trajectories planning; minimum time and minimum RMS torque control; scattered points interpolation; interpolation model; energy efficiency of the motion

1 Introduction

1.1 Literature Review

In any area of activity, it is necessary to perform useful mechanical work by means of electromechanical energy conversion systems. In this paper, we refer to the conversion systems with electric machines powered by static converters and advanced motion control systems. Currently, electromechanical energy conversion systems are widely used for various processes of mechanical motion (robots, electric vehicles, industrial and residential processes etc.). The conventional electromechanical energy conversion systems, realize a wide variety of trajectories of movement at the highest level of quality (accuracy, response time, efficiency). The selection of a particular trajectory becomes a design problem because the same useful work can be obtained with various energy costs and different levels of motion quality.

The interest in the issue of the a priori cost estimation of the electromechanical movement systems has increased due to the rapid progress in the field of the motion planning as discussed in robotics literature and self-driving vehicles. The topics of the motion planning are very extensive and hence only a description of the selected approach is done. See [1]-[5] for surveys on this subject. In the motion planning, the following components must be identified: finding a feasible path, discover the safest maneuvers and determine the optimal trajectory. The actual self-driven vehicles motion planning algorithms originate primarily from the field of mobile robotics. Three categories of path planning methodologies were adopted for autonomous vehicles: graph search based planners, sampler based planners, interpolation curve planners. The last method uses a previous set of points that describes a global road map and on this base generate a new set of data for the trajectory [6]. The interpolating curve planners implement different techniques for path smoothing: lines and circles, clothoid curves, polynomial curves, Bezier curves, spline curves.

The problem of feasible and optimal path planning has been studied extensively over the past few decades [7]. Feasible path planning referees to the problem of determining a path that satisfies given problem constraints.

Optimal path planning refers to the problem of finding a path that optimizes some quality criteria subject to given constraints. Assuming that the cost functional is the arc-length of the path, it is well known that the sufficient family of time-optimal paths for both Dubins', as well as, Reeds-Shepp's car models [8] consist of the concatenation of circular arcs with maximum curvature and straight line segments, all tangentially connected. We consider that shortest obstacle free path is not enough for mitigation of the vehicles effects on the environment. The functional cost to be optimized must take into account the cost of the energy involved in the motion process.

A first step in the strategy of choosing the minimum cost path is the determination of the a priori cost. A direct method of determining a priori energy cost consists of assessing the losses. The total cost is obtained by summing up the cost of the required useful energy and the estimated losses costs.

Many papers have been written on the time optimal and, respectively, the minimum energy criteria for the motion trajectories generation, in electrical drive systems. There is the detailed references analysis in the domain, e.g. in [9]. A realistic design of the motion path was obtained in [10], [11], by minimizing an indicator that takes into account the tracking time, the energy consumption, the restrictions and system nonlinearities. A survey of the electromechanical control systems for electric vehicles (EV) has been written in [12]. The evaluation of the cost of the different dissipative energy losses especially in dynamic regimes poses a complex problem. The dissipative energy components are depended on the electrical machines material's properties (copper and iron losses), mechanical friction and load nonlinearities and so on. Minimizing a cost function, subject to various constraints, taking into account all the dissipative components of the analytic model, is quite laborious.

In robotic manufacturing systems, much energy is wasted due to an adopted minimum time policy for robot operations. [13]. Energy optimal trajectories for robot applications, is now an enormous research field in and of itself, see e.g. [14]-[17].

1.2 The Idea of the Paper

The efficiency of the energy transfer in the various physical processes like electrical, mechanical or thermal is univocally characterized by a pair of variables: the effort $e(t)$ and flow $f(t)$.

The inner product of these generalized variables is the instantaneous power. In the electromechanical process, when the electric machine operates as motor, the energy transfer are characterized by the following power variables: the input voltage $u(t)$ and the current $i(t)$ and the output mechanical force $f(t)$ or the corresponding torque $\tau(t)$ and velocity $v(t)$ or the corresponding angular velocity $\omega(t)$. The instantaneous efficiency of the energy transfer is the ratio of the output and input instantaneous power. The cost of the energy transfer in the interval 0 to t_1 is described by relationship:

$$E(t) = \int_0^{t_1} \frac{efdt}{\eta(e,f)}. \tag{1}$$

The output power variables $e(t)$ and $f(t)$ are known because these are desired variables.

The novelty of the paper, is to build the surface of the process efficiency in terms of the output power variables with an aim to estimate the instantaneous values of the efficiency in the interval 0 to t_1. Thus, we can determine the a priori cost necessary to obtain the desired dynamics of the power variables (effort and flow) by minimizing the wasted energy.

Starting with a relatively small number of experimental data, an interpolation model of the actuator efficiency, as a function of torque and angular velocity, was build up. Motion trajectories are transformed from the explicit form (in the time domain) into the implicit form (in the ngular velocity and torque domain). Thus, the implicit motion trajectories were projected on the surface of the efficiency in order to obtain the discrete values of the efficiency, corresponding to the discrete torque and angular velocity values. As a result, the discrete values of the cost and then the total cost can be calculated. The novelty of the developed method is that it can provide the possibility of predetermining the energy costs both in the steady-state regime and in the dynamic regimes, starting from a relatively limited experimental database of the efficiency in the steady-state regimes.

The paper is structured as follows. Section 2 presents the point to point trajectories planning method, under the minimal time or minimal RMS torque control laws. Section 3 describes the strategies applied for building an interpolation model which estimate the efficiency of the energy conversion process. Section 4 introduces the numerical tests and based on these, simulations are performed and analyzed. Finally, section 5, concludes the paper.

2 Problem Formulation

In the following, the electromechanical conversion process, which is the object of the a priori energy costs estimation, is briefly described. Currently, most of the physical processes that are subject to human activities require adequate control by computer means. The purpose of these processes is to achieve useful goals. The desired objectives are obtained by means of power actuators powered by primary energy sources. The actuators are controlled by means of informatics systems according to quality and energy criteria in order to obtain real objectives as close as possible to the desired ones. The most widespread actuators elements in electromechanical systems are the electric machines driven by power static converters. The torque τ obtained through the air gap electromagnetic field of electric machine, and the angular velocity ω are transmitted to the mechanical load. The mechanical load transforms the internal rotational quantities ω and τ in external quantity (Cartesian representation) by means of the kinematics specific to the application domain. There is a large variety of mechanical loads. For the generalization of the mechanical motion equations, the external quantities were rated to the motor shaft. In the case of an electric vehicle, for example, the mere traveled distance x at velocity $\dot{x}$, and acceleration $\ddot{x}$ are the external quantities. These quantities are rated to the following internal quantities at the motor shaft: the angular position θ rad, angular velocity $\dot{\theta}$ and the acceleration $\ddot{\theta}$. The fundamental kinematic model is based on the motor torque τ, the load torque τ_r, and the dynamic torque. The balance equation on the motor shaft is the following:

$$M_d = \left\{ (\omega, \tau, \theta) \left| \begin{array}{l} \dot{\omega} = K_m \tau - K_m \tau_r \\ \dot{\theta} = \omega \\ \tau_r = f(\omega, \theta) \end{array} \right. \right\} \tag{2}$$

The constant K_m is defined by $K_m = \tau_R / J\omega_R$. If the electric machine operate as motor $\tau_r \geq 0$ else if the electric machine operate as generator (braking mode), $\tau_r \leq 0$.

The mechanic load torque τ_r was considered dependent on position and velocity. All the quantities in equations system (2) are expressed in per-unit [pu] values and τ_R Nm, ω_R rad/s are the rated motor torque and speed, J kgm^2 is the total moment of inertia. The electromechanical system (2) reaches the desired speed ω and position θ controlling the motor torque τ.

We consider that the movement is planned as a point-to-point motion. Each motion sequence begins from the conditions known initially and reaches the desired final conditions in a given motion time T_f.

The planning of the trajectory means the design of the variation for the torque τ_{ff}, velocity ω_{ff} and position θ_{ff} according to the required objective with fixed initial and final conditions. These trajectories are imposed in a feed forward (ff) manner to the torque, velocity and position controllers. The feed forward control generates the required torque command to move the mechanical load in accordance to the desired trajectory. The desired trajectory must be such that the required torque and speed are in accordance with the actuating device limitations. The required torque command τ_{ff} is determined at every sampling time $t_k = kT_s$.

The sampling period of the motion trajectory is T_s. The required torque is adopted as piecewise linear:

$$G_{\tau ff} = \{(\tau_k) | \tau_k = C_1(k) + C_2(k) t_k, \quad k = 1,\dots,N\} \tag{3}$$

The parameters $C_1(k)$ and $C_2(k)$ of torque τ_k are computed at every sampling time step k for the next initial condition:

$$\begin{cases} t = 0 \\ \theta = \theta_i \\ \omega = \omega_i \end{cases} \tag{4}$$

and finally:

$$\begin{cases} t = T_f \\ \theta = \theta_f \\ \omega = \omega_f \end{cases} \tag{5}$$

The set of the C parameters were obtained by solving the mathematical model of equation (6):

$$C = \left\{ (C_1(k), C_2(k)) \left| \begin{array}{l} Find \;\; C_1(k) \;\; and \;\; C_2(k) \;\; by \;\; solving: \\ \begin{cases} \omega = K_m \int_0^{T_f} (C_1(k) + C_2(k)t - \tau_r(k))dt \\ \theta = \int_0^{T_f} \omega dt \end{cases} \\ under \;\; initial \;\; and \;\; final \;\; conditions. \end{array} \right| k = 1,..,N \right\} \tag{6}$$

The load torque $\tau_r(k)$ depends on the performed applications. For example, the load torque imposed by an Electric Vehicle (EV) may be described by:

$$M_{\tau r} = \{(\tau_{rk}) | \tau_{rk} = \tau_{r0} + C_w(k)\omega^2(k), \quad k = 1,\dots, N\} \tag{7}$$

The initial torque is τ_{r0}, while C_w is a global coefficient that takes into account different resistive torque effects [18].

The set of discrete values of the trajectories of the velocity and the position results from the mathematical model (2) after the parameters $C_1(k)$ and $C_2(k)$ was calculated.

$$G_{\omega_{ff}} = \left\{ (\omega_k) \middle| \begin{array}{l} \omega(k) = \omega(k-1) + (C_1(k) + C_2(k)t_k - \tau_r(k))T_s K_m \\ \omega(0) = \omega_i \\ k = 1,\ldots,N \end{array} \right\} \tag{8}$$

$$G_{\theta_{ff}} = \left\{ (\theta_k) \middle| \begin{array}{l} \theta(k) = \theta(k-1) + \omega(k)T_s \\ \theta(0) = \theta_i \\ k = 1,\ldots,N \end{array} \right\} \tag{9}$$

A start-stop motion, for example, with the steady-state regime has three sequences: starting, steady-state and braking regimes. If the control law is the minimum time $C_2 = 0$ and the velocity profile is trapezoidal, otherwise, the control law is the minimum RMS torque and the starting and braking velocity profiles are parabolic [19]. The continuity of position, velocity and acceleration (torque) for each sequence of the movement is fulfilled by the fact that final conditions of the past sequence are the initial conditions of the current sequence. The initial and final torque gradient (jerk) is implicitly limited by the torque controller. The requested trajectories were obtained from (2, 7, and 8) in implicit (10) or explicit (11, 12) forms:

$$G = \left\{ (\omega_k, \tau_k, \theta_k) \middle| \theta_k = \theta_{k-1} + T_s\omega(k), k = 1,\ldots,N \right\} \tag{10}$$

$$G_\omega = \left\{ (\omega_k, \tau_k) \middle| t_k = kT_s, \quad k = 1,\ldots,N \right\} \tag{11}$$

$$G_\tau = \left\{ (\tau_k, t_k) \middle| t_k = kT_s, \quad k = 1,\ldots,N \right\} \tag{12}$$

The a priori energy cost of the trajectory G (11) is completely determined if are known the set of efficiency values $\eta_k (k = 1,..N)$ which corresponds to the discrete values of speed ω_k and torque τ_k.

3 Determination of the a Priori Energy Cost Using the Interpolation Model

The efficiency of the energy conversion process through electric machines and power converters is determined by velocity and torque. The measurements by experimental methods of the power quantities (velocity and torque), as well as the corresponding efficiency, allows knowing a limited number of values, usually with a scattered distribution in the admissible range. The interpolation model has as input the velocity and the torque, the output quantity being the corresponding value to the efficiency. The following set of experimental data in the steady-state operation is considered:

$$\{X, Y, Z\} = \{(\omega_m, \tau_m, \eta_m) | m = 1, \ldots, M_{obs}\} \tag{13}$$

Where, M_{obs} are the observation number of points.

The problem formulation of the interpolation model is the following:

Starting from a given data set of irregularly (scattered) distributed points over space $\mathbb{R}^2$ described by:

$$P_m = \{(\omega_m, \tau_m) | m = 1, \ldots, M_{obs}\} \tag{14}$$

Considering the scalar values of efficiency $\eta_m, m = 1,..M_{obs}$ associated with each point P_m, satisfying:

$$\eta_m = F(\omega_m, \tau_m) \tag{15}$$

Denoting the unknown function by $F(\omega, \tau)$, look for an interpolating function $\tilde{F}$, such that for every observation points P_m, the interpolating function fulfills the condition:

$$\tilde{F}(\omega_m, \tau_m) = \eta_m \tag{16}$$

We assume that all points P_m, also referred as nodes, or "support points" are distinct and not collinear. Due to the intrinsic inertial nature of involved conversion process, the function *F* is geometrically represented as a continuous differentiable surface which allows finding the desired function $\tilde{F}$ that passes exactly through each M_{obs} observation points. Consequently, the ill-posed problem is avoided, no regularization being necessary for an adequate approach.

The main objective of the paper is not to approach, in details, the current methods used for approximation of the surfaces. However, it can be that noted that the scattered data interpolation methods may be divided into two important classes:

- *Local methods*, where the interpolated value depends only on the "nearly" points
- *Global methods*, where the value of the interpolate at a point P depends on all data points used

Two methods, which are most widely used in different application fields (in areas such as computer graphics, physical modeling, geographic information systems, medical imaging, and more), have been adopted. These methods are:

- *Delaunay triangulation* and related methods
- *Radial Basis Function* (RBF) networks interpolation

Local methods usually need a triangulation of the set of points (support points).

The interpolated value of a point, other than support points:

$$\{x, z, y\} \notin \{X, Y, Z\} \tag{17}$$

is obtained by local interpolation techniques with the three nearby points. One widely used approach is Delaunay triangulation of data and the Voronoi diagram of a set of points which is the dual of the first approach.

The interpolation technique by the RBF neural networks is based on the theory of learning systems. The function $\tilde{F}(\omega,\tau)$ to be interpolated is, in a pragmatic consideration, represented as a linear combination of the non-linear basis functions weighted by a learning process based on the data points $\{X, Y, Z\}$.

The interpolation error of the energy conversion process efficiency was estimated using two sets of the experimental data: a learning set $\{X, Y, Z\}$ and an assessing set $\{U, V, W\}$ such that $\{U, V, W\} \notin \{X, Y, Z\}$.

Let be the assessing experimental data set as

$$\{U, V, W\} = \{(\omega_n, \tau_n, \eta_n) | n = 1, \ldots, N_{obs}\} \tag{18}$$

The assessing points were:

$$P_n = \{(\omega_n, \tau_n) | n = 1, \ldots, N_{obs}\} \tag{19}$$

and the interpolation values of efficiency was

$$\tilde{\eta}_n = \tilde{F}(\omega_n, \tau_n) \tag{20}$$

A Root-mean-square error (RMS-error) of interpolation is given by:

$$RMS - error = \sqrt{\left(\sum_{n=1}^{Nobs} \frac{(\tilde{\eta}_n - \eta_n)^2}{N_{obs}} \right)} \tag{21}$$

The error of the above method adds experimental data measurement errors.

Several papers have studied the comparative assessment of performances of the RBF networks to approximate nonlinear static characteristics accurately [20]. The techniques adopted in the paper has been shown that the surface of the efficiency vs. velocity and torque was interpolated (reconstructed) with an error less than 2% by means of a reasonable volume of experimental data. The absolute error is about one order of magnitude larger near the boundary, than it is in interior of the domain. By including points on the boundary the error is much smaller.

The Matlab function used in the paper for local scattered data interpolation was:"griddata", "griddatan" and the "scatteredInterpolant" class in 3D space.

The energy cost of the electromechanical conversion processes is completely determined by the so-called energy quantities: the torque τ , the velocity ω , and the actuator efficiency η . The discrete values of the speed ω_k and torque τ_k are known due to the fact that these are requested quantities. These requested quantities were obtained by the trajectories planning system (11). The efficiency values $\eta_k (k = 1,..N)$ which corresponds to the discrete values of speed ω_k and torque τ_k was obtained from the interpolation model:

$$E = \left\{ (\tilde{\eta}_k) \middle| \tilde{\eta}_k = \tilde{F}(\omega_k, \tau_k), \ \ k = 1,\ldots,N \right\} \tag{22}$$

The final cost may be expressed in the implicit or respectively explicit forms:

$$W_N = \sum_{k=1}^{N} \frac{\theta_k \tau_k}{\tilde{\eta}_k} \tag{23}$$

$$W_N = \sum_{k=1}^{N} \frac{\omega_k \tau_k T_s}{\tilde{\eta}_k} \tag{24}$$

Thus, the discrete values of final cost are:

$$W = \left\{ (w_k) \middle| w_k = \sum_{k=1}^{N} \frac{\omega_k \tau_k T_s}{\tilde{\eta}_k} \right\} \tag{25}$$

In Figure 1 was represented the flowchart of the main functions of the a priori cost estimation technique of the electromechanic motion process. The learning database in the Figure 1 contains the M_{obs} of the measurements points (13).

These points generate the surface $\tilde{F}(\omega_m, \tau_m) = \eta_m$ (16) by the interpolation model. Once the surface $\tilde{F}$ was built, we can estimate the efficiency $\tilde{\eta}_k$ for any point (τ_k, ω_k) by assessing the interpolation model. The a priori cost estimation for a required motion trajectory (11) was accomplished based on discrete points (τ_k, ω_k) of the G considered trajectory and the corresponding efficiency $\tilde{\eta}_k$.

The same technique can be used for a posteriori cost calculation of the motion. In these case, the measurement quantities we need are the actual value of the velocity ω and the feed forward torque value τ_{ff}. The actual value of the torque τ may be considered very close to the required torque τ_{ff} because the error of the torque controller usually is very small.

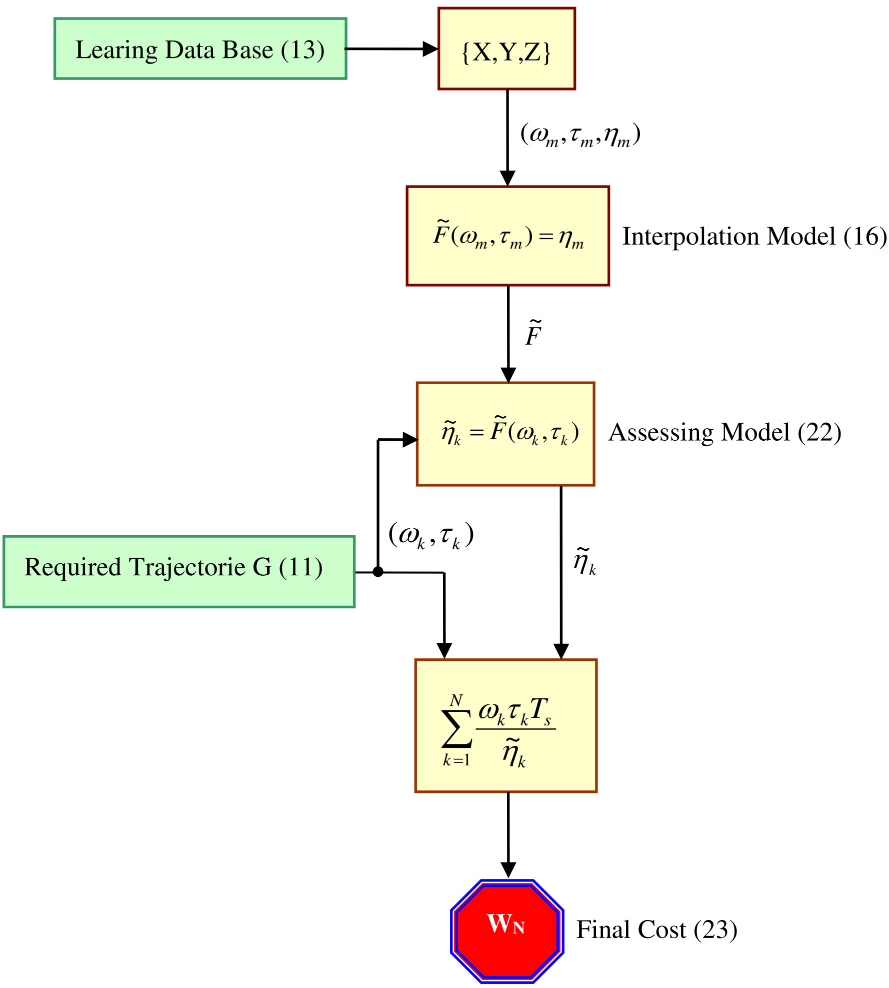

Figure 1
The flowchart of the a priori cost estimation technique of the electromechanic motion process

The test of the above cost estimation method was achieved with an electrical drive system with the permanent magnet synchronous motor. The actuator is a general-purpose power electronic converter. The power electronic converter is provided with control loops for the electromagnetic and mechanical quantities. The main electromagnetic controlling quantity is the motor torque. The mechanical controlling quantities are the angular velocities ω, the angular position θ and eventually angular acceleration $\dot{\omega}$ and jerk $\ddot{\omega}$.

The tests were based on experimental data obtained with the device UQM PowerPhase 220 HD (UQM Technologies, Inc., www.uqm.com).

In Figure 2 are represented some experimental data of the device efficiency vs. mechanical load torque at constant speeds.

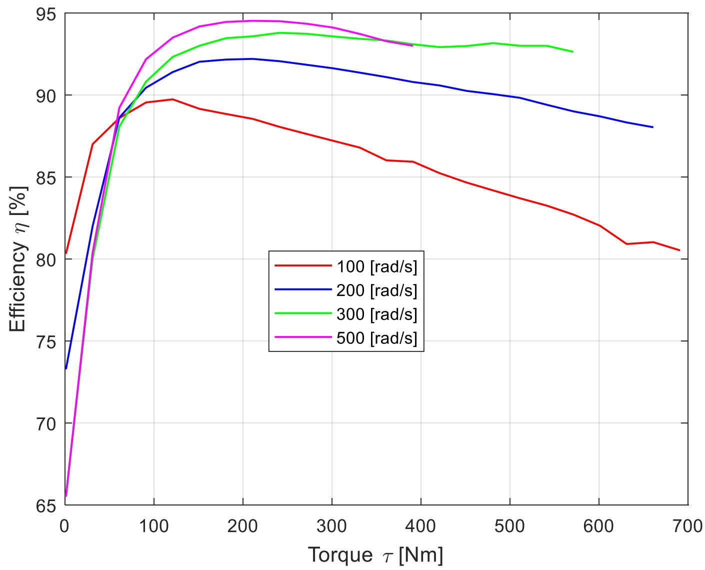

Figure 2
Some experimental data regarding efficiencies vs. torques
at constant velocity of the UQMHD220 device

The coordinates of the steady-state operating points are represented by $(\tau_m, \omega_m), m = 1,..M_{obs}$ with restrictions: $\tau_m \le \tau_{\max}$ and $\omega_m \le \omega_{\max}$. In the paper, the set of the M_{obs} experimental points (τ_m, ω_m) and the corresponding values η_m has been passed to the Matlab function *scatteredInterpolant*, and it has returned the surface $\widetilde{F}(\omega, \tau) = \eta$. This surface passes through the sample values at the point locations. We can evaluate this surface at any query point $(\tau_i, \omega_i), i \ne m$, to produce an interpolated value:

$$\tilde{\eta}_i = \tilde{F}(\omega_i, \tau_i) \tag{26}$$

Interpolation technique used in the paper was *Delaunay interpolation of points*. The set of points obtained by sampling the implicit trajectory of the motion $g(\omega, \tau) = 0$ is $G_{\omega ff}$ and $G_{\tau ff}$ (3)-(8).

The set E of the efficiency values corresponding to the set $G_{\omega ff}$ and $G_{\tau ff}$ are obtained by the interpolation model (22).

The cost W_N of the movement in tracking the trajectory $g(\omega, \tau) = 0$ is computed according to relationships (23)-(24) and depends on the geometry of the trajectory $g(\omega, \tau) = 0$ lying on the surface $\tilde{\eta}_i = \tilde{F}(\omega_i, \tau_i)$. For the same useful work, the same displacement θ_f can be achieved with different control laws and different final execution time T_f, at different energy costs.

The informatics system (Figure 1) offers the possibility of choosing the minimum cost trajectory depending on the required mechanical load, the desired execution time and the control law. Consider an EV under the conditions of the UQM220HD device specifications. The mechanical rated load torque is $\tau_R = 300Nm$ and the angular rated velocity is $\omega_R = 314 rad/s$.

The electromechanical coupling system converts the motor rotational motion in the EV translational motion with position x. We consider a requested longitudinal distance traveled $x_f = 200m$ which correspond to the motor shaft angle $\theta_f = 3000rad$. The moment of inertia corresponding to the total kinetic energy (rotational and translational) is $J = 1Kgm^2$. A possible load torque for EV has the following expression:

$$\tau_r = \tau_{r0} + C_w \omega^2 \tag{27}$$

The initial mechanical load torque was adopted at value $\tau_{r0} = 0.8[pu]$ and the global load coefficient $C_w = 0.3$.

The different motion trajectories were considered for cost estimation tests, keeping the same traveled distance. Hereinafter, we present some experimental results under the following conditions:

- Case 1 when the control law is the minimum time
- Case 2 when control law is the minimum RMS torque

Final time and maximum speed are set to the required values. Acceleration is limited by default via the torque controller.

Figure 3 illustrates the explicit form of the torque and speed trajectories generated under cases 1 and 2.

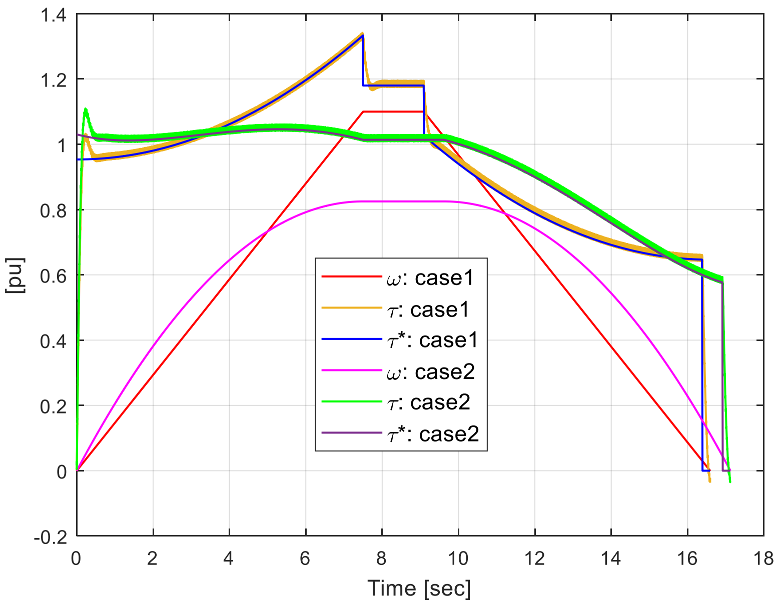

Figure 3

Torque and velocity vs. time in case 1 (minimum time) and 2 (minimum copper energy losses) for UQM device

Both trajectories have the same final required time $T_f = 15s$ but, the execution time was higher because of the speed limit $\omega_{\max} = 1.1[pu]$. In case 1 the control law was the minimum time and resulted $T_f = 16.57s$ and torque $\tau_{RMS} = 1.0189[pu]$. In case 2 the control law was the minimum RMS torque and resulted $T_f = 17.08s$ and torque $\tau_{RMS} = 0.9893[pu]$. In both cases the tracking error of the actual electromagnetic torque vs. the requested one is negligible.

Figure 4 shows how torque vs. speed implicit trajectories is performed on the energy conversion efficiency map. The same movement on two different paths leads to different costs.

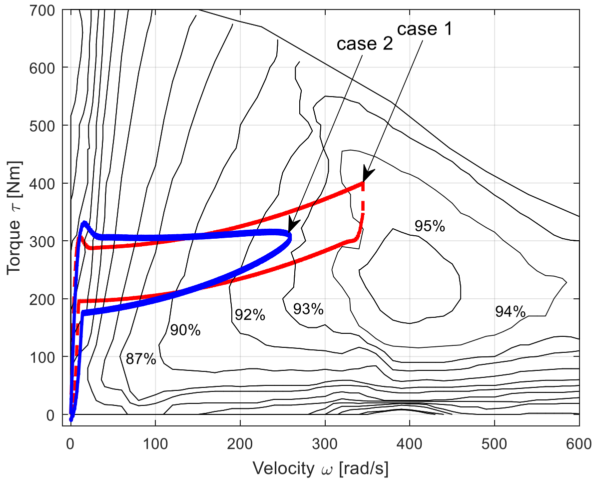

Figure 4

The implicit trajectories of the torques vs. velocities in cases 1 (minimum time) and 2 (minimal copper loss) projected on the efficiency map

Figure 5 shows the energy conversion efficiency based on the distance x travelled. It can be seen that during start-up and braking, the efficiency of the movement is reduced.

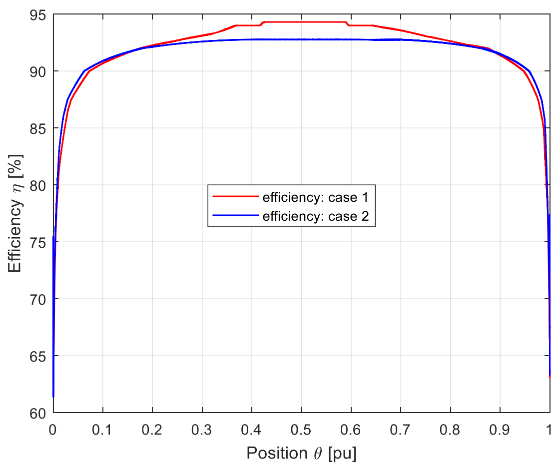

Figure 5

Efficiencies vs. traveled position in cases 1 (minimum time) and 2 (minimum copper energy losses) for UQM device

Figure 6 shows the variation of the a priori cost as a function of the execution time needed to complete a requested distance for an automotive load torque. Two control laws were applied: minimum time and minimum RMS torque control.

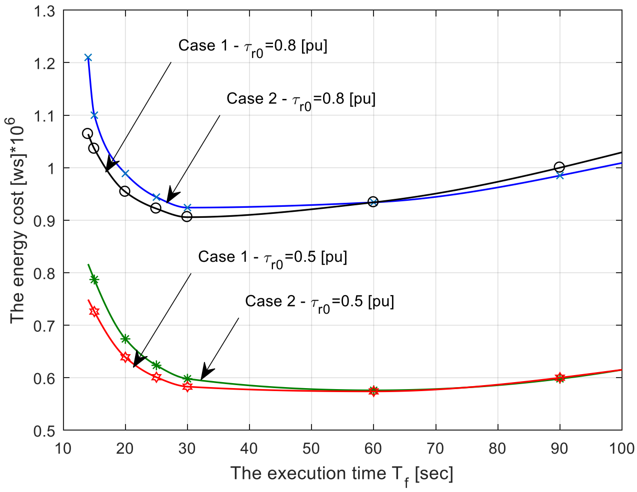

Figure 6
Variation of the cost of movement over a 200 m distance
depending on the final execution time and the control law

The influence of the execution time on the energy cost is predominant, in relation to the control law. This outcome is consistent with [19]. For an EV with the initial data specified above, the $200m$ distance is done at a minimum cost if the travel time is $T_f = 30s$ as shown in Figure 5. For example, if the travel time is $T_f = 20s$, the energy cost increases with 7.5% for minimum time command law and with 6.5% for the minimum RMS torque control law.

Similar analysis can be performed for various motion processes, the method is generalized and not dedicated, since the motion variables are rated to the internal shaft of the motor.

Conclusions

The paper discusses a method of estimating the energy cost for electromechanical motion system. The tested solution is based on a set of experimental data in the steady-state regime for the efficiency, speed and torque of a servo motor with permanent magnet powered by a static converter with the feed forward control system. The experimental data are interpolated to all the allowable range by building the surface for efficiency in terms of speed and torque. Thus, we can evaluate the efficiencies values for each sample of the trajectory, and calculate the cost and overall efficiency of the movement. It was confirmed experimentally that the same useful work can be performed at different levels of cost and efficiency, which proved the existence of an optimal operation. The advantage of the method developed in the paper is that it eliminates the uncertainties related to the analytical evaluation of the losses of the energy conversion system. Future research will aim to predetermine the optimal trajectories of the movement in both motor and generator operation modes of the electric machine. The presented method can be extended relatively easily for on-line applications, where the load torque needs to be estimated based on the total moment of inertia, motor torque and speed. The a priori calculation of energy costs for electromechanical energy conversion processes provides additional information to the end user, with the aim of avoiding energy waste.

References

[1] B. Paden, M. Cap, S. Z. Yong, D. Yershov, E. Frazzoli: A Survey of Motion Planning and Control Techniques for Self-Driving Urban Vehicles, IEEE Transactions on Intelligent Vehicles, Vol. 1, No. 1, 2016, pp. 33-55

[2] D. González, J. Pérez, V. Milanés, F. Nashashibi: A Review of Motion Planning Techniques for Automated Vehicles, IEEE Transactions on Intelligent Transportation Systems, Vol. 17, No. 4, 2015, pp. 1135-1145

[3] C. Katrakazas, M. Quddus, W. H. Chen, L. Deka: Real-Time Motion Planning Methods for Autonomous on-Road Driving: State-of-the-Art and Future Research Directions, Transportation Research Part C, Vol. 60, 2015, pp. 416-442

[4] J. T. Betts: Survey of Numerical Methods for Trajectory Optimization, Journal of Guidance, Control, and Dynamics, Vol. 21, 1998, pp. 193-207

[5] E. Polak: An Historical Survey of Computational Methods in Optimal Control, Society for Industrial and Applied Matematics Review, Vol. 15, No. 2, 1973, pp. 553-584

[6] J. A. Storer, J. H. Reif: Shortest Paths in the Plane with Polygonal Obstacles, Journal of the Association for Computing Machinery, Vol. 41, 1994, pp. 982-1012

[7] O. Wigström, B. Lennartson: Energy Optimization of Trajectories for High Level Scheduling, IEEE Conference on Automation Science and Engineering, 2011, pp. 654-659

[8] J. Reeds, L. Shepp: Optimal Paths for a Car that Goes Both Forwards and Backwards, Pacific Journal of Mathematics, Vol. 145, 1990, pp. 367-393

[9] Y. Wang, K. Ueda, S. A. Bortoff: A Hamiltonian Approach to Compute an Energy Efficient Tajectory for a Servomotor System, Automatica, Vol. 49, No. 12, 2013, pp. 3550-3561

[10] M. Yazdani, G. Gambleb, G. Hendersonc, R. Hecht-Nielsen: A Simple Control Policy for Achieving Minimum Jerk Trajectories, Neural Networks, Vol. 27, 2012, pp. 74-80

[11] P. Lambrechts, M. Boerlage, M. Steinbuch: Trajectory Planning and Feedforward Design for Electromechanical Motion Systems, Control Eng. Pract, Vol. 13, 2005, pp. 145-157

[12] Z. Preitl, P. Bauer, J. Bokor: Cascade Control Solution for Traction Motor for Hybrid Electric Vehicles, Acta Polytechnica Hungarica, Vol. 4, No. 3, 2007, pp. 75-88

[13] E. S. Sergaki, G. S. Stavrakakis, A. D. Pouliezos: Optimal Robot Speed Trajectory by Minimization of the Actuator Motor Electromechanical Losses. Journal of Intelligent and Robotic Systems, Vol. 33, 2002, pp. 187-207

[14] A. Chatterjee, R. Chatterjee, F. Matsuno: Augmented Stable Fuzzy Control for Flexible Robotic Arm Using LMI Approach and Neuro-Fuzzy State Space Modeling, IEEE Transactions on Industrial Electronics, Vol. 55, No. 3, 2008, pp. 1256-1270

[15] T. Haideggera, L. Kovácsa, R. E. Precup, B. Benyóa, Z. Benyóa, S. Preitl: Simulation and Control for Telerobots in Space Medicine, Acta Astronautica, Vol. 181, No. 1, 2012, pp. 390-402

[16] A. Ürmös, Z. Farkas, M. Farkas, T. Sándor, L. T. Kóczy, Á. Nemcsics: Application of Self-Organizing Maps for Technological Support of Droplet Epitaxy, Acta Polytechnica Hungarica, Vol. 14, No. 4, 2017, pp. 207-224

[17] J. Saadat, P. Moallem, H. Koofigar: Training Echo State Neural Network Using Harmony Search Algorithm, International Journal of Artificial Intelligence, Vol. 15, no. 1, 2017, pp. 163-179

[18] D. A. Ord: Advanced Vehicle Powertrain Design Using Model-Based Design, Master thesis, Virginia Polytechnic Institute, Blacksburg, 2014

[19] I. Ioslovich, P. O. Gutman, A. Berger, S. Moshenberg: On Energy-Optimal and Time-Optimal Precise Displacement of Rigid Body with Friction, Journal of Optimization Theory and Applications, Vol. 172, No. 2, 2017, pp. 466-480

[20] H. Wendland, Scattered Data Approximation, Cambridge University Press, Cambridge, 2005

[21] M. Milovanović, D. Antić, M. Spasić, S. S. Nikolić, S. Perić, M. Milojković: Improvement of DC Motor Velocity Estimation Using a Feedforward Neural Network, Acta Polytechnica Hungarica, Vol. 12, No. 6, 2015, pp. 107-126

[22] S. Cuomo, A. Galletti, G. Giunta, L. Marcellino: A Novel Triangle-Based Method for Scattered Data Interpolation, Applied Mathematical Sciences, Vol. 8, No. 134, 2014, pp. 6717-6724

[23] W. Leonhard: Trajectory Control of a Multi-Axes Robot with Electrical Servo Drives. IEEE Conference on Industrial Electronics, Philadelphia, USA, 6-10 November 1989, pp. 1-9

[24] A. Šabanovic´, K. Ohnishi: Motion Control Systems. Wiley & Sons, Singapore, 2011

[25] H. Bouvier, G. Colin, Y. Chamaillard: Determination and Comparison of Optimal Eco-Driving Cycles for Hybrid Electric Vehicles, Proceedings of the European Control Conference (ECC), Linz (Austria), 2015, pp.142-147

[26] X. Wang, J. Stoev, G. Pinte, J. Swevers: Classical and Modern Methods for Time-Constrained Energy Optimal Motion - Application to a Badminton Robot, Mechatronics, Vol. 23, No. 6, 2013, pp. 669-676

[27] H. N. Koivo: Neural Network Toolbox, February 1, 2008